Karlsruhe Institute of Technology

Interannual to Decadal Rainfall Variability over Greater Horn of Africa: Non-Stationary Teleconnections, Physical Mechanisms, and Predictability

Zur Erlangung des akademischen Grades eines

DOKTORS DER NATURWISSENSCHAFTEN

von der KIT-Fakultät für Physik des Karlsruher Instituts für Technologie (KIT)

genehmigte

DISSERTATION

von M.Sc. Titike K. Bahaga aus Äthiopien

Tag der mündlichen Prüfung: **28.06.2019**
Referent: **Prof. Dr. Andreas H. Fink**
Korreferent: **Prof. Dr. Peter Knippertz**

Abstract

The main objectives of this thesis are to understand the drivers of interannual-to-decadal rainfall variability over the Greater Horn of Africa (GHA), to detect non-stationary teleconnections, to investigate the physical mechanisms, and to assess the skill of the MiKlip decadal forecast systems. To address these objectives, interannual to decadal teleconnections influencing the three GHA major rainy seasons are examined using observational datasets for 1901–2013. Sea Surface Temperature (SST)-based climate indices known to influence Short, Kiremt and Long Rains are used in a comprehensive statistical analysis to detect non-stationary behaviour in teleconnections and to split them into interannual and decadal times scales. Interannual variability in the October–December Short Rains is predominantly influenced by the Indian Ocean Dipole (IOD) with percent variance explained (PVE) of up to 80% in recent years. However, abrupt shifts in this teleconnection are found around 1918, 1951, 1987, and 1994. The Short Rains also correlate strongly with El Niño-Southern Oscillation (ENSO). However, the ENSO influence on Short Rains is mediated by in-phase fluctuation of IOD. Decadal variations in Short Rains are more directly explained by low-frequency variability in the Pacific Ocean (PO). A hitherto undocumented non-stationary relation was found between Atlantic Niño 3 and June–September (JJAS) Kiremt Rains. The non-stationarity seems to be related to a decadal regime shift of the West African monsoon in the late 1960s. The variability of Kiremt Rains is also strongly associated with ENSO, though the recently increased correlation was not a multidecadal change. Consistent with recent studies, the post-1998 March–May Long Rains decline is strongly associated with decadal variability in the PO. The PVEs in the stable correlations with the Pacific Decadal Oscillation (PDO) and the Interdecadal Pacific Oscillation (IPO) indices range from 25–64%, mostly due to low-frequency variability (>8 years).

The recent increase in ENSO influence on Kiremt Rains raises questions about the physical mechanisms. This motivated a modeling study, and the Kiremt Rains interannual variability analyzed using observational data and higher-resolution SST-forced Icosahedral Nonhydrostatic (ICON) experiments for the period of 1981–2017. Such fine-grid global and two-way nests over the GHA were carried out here for the first time. The physical mechanisms that link ENSO influence on the Kiremt Rains in the model and the ERA-Interim reanalysis were also investigated. It is found that the model reasonably simulates the main features of the JJAS rainfall climatology over

GHA and also reproduces horizontal wind intensity and patterns at $150, 600, 850, 925 - hPa$ levels over Africa. It is shown that there is a substantial skill in reproducing the leading modes of Kiremt Rains interannual variability ($r = 0.64$) given the SSTs are known. The result suggests that the majority ($> 50\%$) of Kiremt Rains anomalies are driven by equatorial Pacific SST variability, while the SST effects from other regions counteract the ENSO impact in the model. Consistent with previous studies, it is found that the El Niño phase of the ENSO drives a corresponding large-scale circulation anomaly, which weakens the monsoon trough over the Arabian Peninsula, enhances descending motion, and upper-level convergence right over Ethiopia. The subsidence over the GHA region induces upper (lower) level westerly (easterly) wind anomalies over North Africa leading to weakening the Tropical Easterly Jet, Somali Low-Level Jet, and reducing the moist westerlies from the Atlantic and Congo basin, and thus lead to a reduction of Kiremt Rains over Ethiopia. The opposite pattern is observed during La Niña events with enhanced surface westerlies leading to a wetter Kiremt Rains. This mechanism represents an anomalous Walker-type circulation for the ENSO-Kiremt Rains teleconnection.

Finally, the skill of MiKlip decadal forecast systems was assessed over GHA. The predictability of climate drivers at seasonal to decadal time-scale and observed teleconnection patterns were evaluated. It is shown that Atlantic Multidecadal Oscillation (AMO) is predictable within a time-scale that depends strongly on the particular MiKlip experiments, ranging from 2 up to 10 years, while the SST interannual variability in the North Atlantic basin appears to be skillfully reproduced at 1 year lead. Nonetheless, overall performance of the MiKlip prediction skill for PDO is found to be lower than that for AMO. The predictive skill for ENSO is dependent on the lead time. It is shown that the January–March El Niño 3.4 (N34) index has considerable prediction skill ($r > 0.85$) for 1 year lead, but the skill for the JJAS N34 index is substantially decreased. Moreover, the MiKlip decadal hindcasts failed to reproduce ENSO-Kiremt Rains teleconnection patterns during the JJAS season, and in general, the prediction skill for SST and rainfall is weak over most parts of the tropical regions.

The results of this PhD thesis, therefore, have provided useful insights on the drivers of interannual to decadal rainfall variability, non-stationary teleconnections, physical mechanisms, and predictability over the GHA. The ramifications of the results of this thesis go beyond seasonal-to-decadal forecasting. They are also useful when analyzing the persistent of seasonal-to-decadal teleconnections under anthropogenic climate change.

Preface

The PhD candidate confirms that the research presented in this thesis contains significant scientific contributions by himself. This thesis reuses material from the following publications:

Bahaga, T. K., Fink, A. H., Knippertz, P. Revisiting interannual to decadal teleconnections influencing seasonal rainfall in the Greater Horn of Africa during the 20th century. *International Journal of Climatology*. 2019; 39: 2765–2785. https://doi.org/10.1002/joc.5986

The abstract, Chapters 3, Chapters 4, and the appendix A.1 reuse material from Bahaga *et al.* (2019).

In all cases, the design, implementation of the research, data analysis, interpretation of the results, and manuscript preparation was the responsibility of the candidate. Andreas H. Fink and Peter Knippertz played a prominent role in assisting with valuable insight, direction, guidance, and supervision in all aspects of the PhD thesis and with help producing a publishable quality manuscript.

Contents

Glossary

AEJ	African Easterly Jet
AIOGA	Atlantic, Indian Ocean–Global Atmosphere
AMIP	Atmospheric Model Intercomparison Project
AMO	Atlantic Multidecadal Oscillation
CHIRPS	Climate Hazards Group InfraRed Precipitation with Station data
DMI	Dipole Mode Index
DWD	Deutscher Wetterdienst
ECMWF	European Centre for Medium-Range Weather Forecasts
EEA-SR-SPI	Equatorial East African Short Rains SPI
ENSO	El Niño-Southern Oscillation
EOF	Empirical Orthogonal Function
ERA-20C	ECWMF 20^{th} Century Re-Analysis
ERA-40	40-yr ECMWF Re-Analysis
ERAI	ECMWF Interim Re-Analysis
ERSSTv4	Extended Reconstructed SST version 4
ETH-KR-SPI	EThiopian Highland Kiremt Rains SPI
GECCO2	German contribution to Estimating the Circulation and Climate of the Ocean 2
GHA	Greater Horn of Africa
GHACOF	Greater Horn of Africa Climate Outlook Forum
GHA-LR-SPI	GHA Long Rains SPI
GOGA	Global Ocean–Global Atmosphere
GPCC	Global Precipitation Climatology Center
HadISST	Hadley Centre Sea Ice and Sea Surface Temperature
ICON	Icosahedral Nonhydrostatic
IOD	Indian Ocean dipole
IPO	Interdecadal Pacific Oscillation
ITCZ	Intertropical convergence zone
JJAS	June–July-August–September
MAM	March–April–May

MiKlip	Mittelfristige Klimaprognosen
MPI-ESM-MR	Max Planck Institute Earth System Model, medium resolution
MPI-ESM-LR	Max Planck Institute Earth System Model, low resolution
MSL	Mean Sea Level
N34	El Niño 3.4
NCEP-NCAR	National Centers for Environmental Prediction–National Center for Atmospheric Research
NOAA	National Oceanic and Atmospheric Administration
NWP	Numerical Weather Prediction
OND	October–November–December
PDO	Pacific Decadal Oscillation
POGA	Pacific Ocean–Global Atmosphere
SLLJ	Somali Low Level Jet
SLP	Sea level pressure
SPI	Standardized Precipitation Index
SST	Sea surface temperature
SSTA	Sea surface temperature anomaly
TEJ	Tropical Easterly Jet
WAM	West African monsoon

List of Figures

List of Tables

Chapter 1

Introduction

1.1 Motivation and Objectives of the Thesis

Greater Horn of Africa (GHA) is one of the regions most vulnerable to recurrent extreme climate events (IPCC, 2007). This is mainly attributed to the fact that most of the socioeconomic activities are rain dependent. Interannual to decadal rainfall variability has a large impact on the livelihoods of millions with roughly 75% of the labor force in the region involved in a smallholder, rain-fed agriculture (Salami *et al.*, 2010). The frequent occurrence of climate extreme such as drought or flood events also affect the Gross National Product (GDP) of countries in this region (Conway *et al.*, 2011). For instance, the impact of rainfall on the Ethiopian economy is well demonstrated in Figure 1.1, showing rainfall variability and GDP growth over time (World-Bank, 2006), with rain-fed agriculture accounting for 40% of GDP (Äthiopien Wirtschaft, 2018).

In the current and previous decades, this part of the world experienced a series of severe droughts as for example in 2010/11, 2015, and 2016/2017 (FEWS-NET, 2011; Lyon and DeWitt, 2012; FEWS-NET, 2015; FEWS-NET and WFP, 2016). The 2010/2011 drought in Kenya, Somalia, and southeastern Ethiopia, for example, affected some ten million people, was by some measures the worst drought in 60 years, and contributed to more than 250 000 fatalities in Somalia alone (UN-OCHA, 2011; Checchi and Robinson, 2013). Moreover, some recent studies have noted significant changes in the frequency and intensity of sever weather events, onset, and cessation of rainfall season (Pohl and Camberlin, 2011), and climate extremes (Conway *et al.*, 2011; IPCC, 2007).

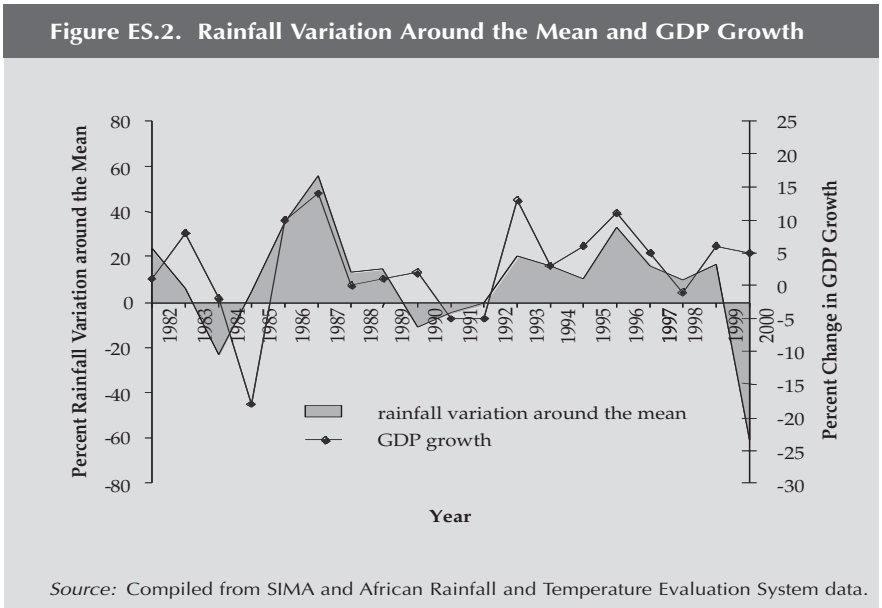

Figure 1.1: Rainfall variability and fluctuations in GDP Growth Rates for Ethiopia (from World-Bank, 2006).

Changes are also being observed in the patterns of many socioeconomic sectors. For example, the highland that were previously free of malaria epidemics have now become malaria high risk areas (Zhou *et al.*, 2004; IPCC, 2007).

These extreme events and rainfall variability in the GHA are dominated by changes on the large scale, with a clear link to tropical ocean-atmosphere variability. Given the uncertainty of climate projections in the region, the inevitability of drought and associated socio-economic distress, understanding the mechanisms that produce this variability and developing both dynamical and statistical approaches for extended-range forecasts and climate information is urgently needed. In this regard, the Greater Horn of Africa Climate Outlook Forum (GHACOF) has been issuing seasonal consensus forecasts for GHA since 1998 (Ogallo *et al.*, 2008). The GHACOF seasonal forecast skill is generally derived from teleconnections with slowly evolving ocean variability, particularly Sea Surface Temperature (SST) anomalies. The persistence of SST anomalies forms the basis of seasonal forecasts either as a predictor in a statistical model or as boundary conditions to dynamic seasonal forecasts using general circulation models. The GHACOF seasonal forecasts based on empirical data might be constrained by overfitting, usage of unphysical predictors, and non-stationary teleconnections. One way to improve these forecasts is to check the validity of the statistical predictors used, as the teleconnections may change over time, and better define them accordingly.

Additionally, despite numerous studies on teleconnections between GHA seasonal rains and remote climate anomalies, apparent disagreements among them regarding attribution arise from consideration of different seasons, datasets, and varying analysis periods due to non-stationarity of climate drivers (Nicholson, 2015, 2017). Although few studies exist on the non-stationarity and multidecadal changes of teleconnections, the dynamical processes driving the non-stationary behavior in interannual teleconnections has not been addressed. Furthermore, there is, to the best of our knowledge, no study that identifies the GHA seasonal teleconnections to interannual or/and decadal time-scales and examines the role of multidecadal SST background in driving the non-stationarity of interannual teleconnections. Several such studies exist for the West African monsoon (WAM) teleconnections (Diatta and Fink, 2014; Suárez-Moreno *et al.*, 2018). Furthermore, in recent decades, a drying trend in precipitation is observed (e.g., Liebmann *et al.*, 2014). This drying appears to contradict the projected wetting under global warming in Coupled Model Intercomparison Project phase 5 (CMIP5) models (e.g., Rowell *et al.*, 2015). Much work is still required to understand the reasons for the drying trend, particularly as models were shown to have biases (Yang *et al.*, 2014).

Therefore, the primary objective of the first part of this dissertation is to fully understand the drivers of interannual to decadal rainfall variability over GHA, to detect non-stationary teleconnections, and to explore the dynamical processes instigating multidecadal changes. The specific objectives are:

- To statistically test the non-stationarity of previously identified teleconnections for 11- and 31-year windows during the whole investigation period 1901–2013.
- To consider SST indices in all ocean basins and examine the evolution of a statistical relationship over both varying time window lengths for fixed starting years, as well as over changing starting years for fixed time window length in a triangle representation.
- To understand a physical mechanism for identified significant non-stationary teleconnections.
- To identify and assign GHA seasonal teleconnections to interannual or/and decadal time-scales.
- To investigate the influence of internal Pacific multidecadal variability on the recent increased frequency of droughts in GHA.

Strong interannual variations of the Ethiopian rainfall are shown in Figure 1.1, and these variations can cause significant socio-economic problems as outlined in the beginning of this section. Generally, these rainfall variations are associated with El Niño-Southern Oscillation (ENSO) events (e.g., Camberlin, 1997; Gissila *et al.*, 2004; Diro *et al.*, 2011b). El Niño (La Niña) episodes were shown to be associated with less (more) summer rainfall across much of the country. Although there is general agreement that SST variability in the central eastern tropical Pacific plays a significant role in driving the interannual rainfall variability in Ethiopia (Diro *et al.*, 2011b), the key features which characterize the ENSO-rainfall teleconnection and the physical mechanisms have rarely been investigated. On the other hand, the role of the Atlantic and Indian Oceans in forcing climate anomalies is less well understood than the effects of ENSO-related forcing. Therefore, understanding what extent does the Pacific Ocean interfere with the Atlantic and Indian Oceans is important.

The second part of this thesis explores the atmospheric responses to the SST-forced Icosahedral Nonhydrostatic (ICON) experiments over Ethiopia. It also investigate the physical mechanism for the Kiremt Rains interannual variability associated with the Pacific SSTs, and in particular, the following questions are addressed:

- How well can the SST-forced ICON represent the climatology and interannual variability of rainfall and large-scale circulation patterns during the Kiremt Rains season?
- What are the key features which characterize the ENSO-Kiremt Rains teleconnection?
- How and to what extent does the Pacific Ocean interfere with the Atlantic and Indian Ocean-forced Kiremt Rains' variability?
- What are the physical mechanisms by which the SST anomalies in the Pacific Ocean impact on the Ethiopian Kiremt Rains, with a focus on the implication for seasonal predictability?

While there has been practical and relevant capacity building to generate skillful seasonal prediction in the GHA, no attempt has been made to develop similar capacity and skill for decadal predictions. Nonetheless, at the same time

information of extreme climate variations at decadal timescale is becoming useful for decision makers in diverse areas from water management to public health experts, medium- and long-term national development plans among many other sectors that are sensitive to climate variability and changes. In order to accommodate these demand for reliable information up to a decade, different national and international initiatives have been launched. CMIP5 (Taylor and Stouffer, 2012) offers a platform to approach decadal predictions on a common basis via hindcast experiments for the period 1960–2010. In this context, the German Mittelfristige Klimaprognosen (MiKlip) project, funded by the Federal Ministry of Education and Research in Germany (BMBF), has developed model systems to produce a skillful decadal climate prediction (Pohlmann *et al.*, 2009; Marotzke *et al.*, 2016). A process and teleconnection evaluation of the MiKlip decadal forecast system has not been performed over GHA.

Thus, the third part of the study focuses on teleconnection evaluation of the MiKlip decadal systems, and the following questions are addressed:

- How well do the Miklip systems predict the principal drivers of seasonal to decadal climate variability?
- How well do the MiKlip decadal predictions represent the observed teleconnection patterns?

1.2 Thesis Outline

As extension of the concepts discussed in this Chapter, a comprehensive review of existing literature on GHA seasonal rainfall climatology, large-scale atmospheric circulation climatology, and interannual to decadal rainfall variability and predictability are presented in Chapter 2. The employed data, methods, and ICON configuration and experimental setups are described in Chapter 3.

A brief discussion on interannual and decadal variability during the three major rainy seasons over GHA is given in Chapter 4. This continues with comprehensive statistical analysis on non-stationary teleconnections, and Chapter 4 further the dynamical processes behind multidcadal changes in the teleconnections. Chapter 4 has previously been published (Bahaga *et al.*, 2019), and minor adjustments have been made before its inclusion here.

In Chapter 5, the ability of ICON to simulate the climatological features of the summer rainfall over the GHA and the atmospheric circulation over the regions surrounding Africa is evaluated. In this Chapter, SST-forced higher-resolution ICON experiments are performed to identify the extent to which the Pacific Ocean interferes with the Atlantic and the Indian Ocean-forced summer rainfall variability over Ethiopia. It also explores the responses of the atmosphere for individual ICON experiments and large-scale circulation anomalies associated with the leading mode of Ethiopian rainfall interannual variability, and Chapter 5 further investigates the physical mechanisms that link the ENSO influence on the Ethiopian rainfall in the model and reanalysis datasets.

Next, in Chapter 6, the MiKlip decadal hindcast experiments are assessed on their ability to predict the observed teleconnection patterns, and the predictability of climate drivers providing interannual and decadal skill is evaluated.

Conclusions to the thesis and an outlook are given in Chapter 7.

Chapter 2

Background Literature Review

In this Chapter, the scientific background necessary to understand the research is reviewed. GHA climate and geographical features will be covered in section 2.1, while annual cycle and seasonal rainfall climatology will be described in sections 2.2. The regional atmospheric circulation features and a coupled tropical ocean-atmosphere phenomenon will be detailed in sections 2.3 and 2.4, respectively. Interannual to decadal seasonal rainfall variations and teleconnections will be covered in section 2.5, and finally, decadal climate variability and prediction will be discussed briefly in section 2.6.

2.1 GHA Topography and Climatological Features

This study focuses on the GHA, which includes the countries Kenya, Uganda, Tanzania, Ethiopia, Eritrea, Djibouti, Somalia, Sudan, South Sudan, Rwanda, and Burundi (see Fig. 2.1). This region is characterized by complex topography, land surface heterogeneity, and diverse spatio-temporal rainfall fluctuations. GHA encloses both the highest and the lowest points of the African continent. This wide altitudinal range, from Lake Assal in Djibouti (153 m below Mean Sea Level (MSL)) to Mount Kilimanjaro in Tanzania (5,895 m above MSL), is emblematic of a region of strong elevation gradients and highly diverse topographical environments (Camberlin, 2018). The north-south highland barrier is interrupted by a major gap, the Turkana gap, between the Ethiopian and the Kenyan High-

lands (Fig. 2.1). It is a 300-km wide depression, lower than 700 meters except for some isolated mountains. This gap is of great climatic significance and connects two major low-lying areas. The first one, to the northwest, corresponds to the Nile Plains, west of the Ethiopian Highlands, covering most of Sudan and South Sudan at an altitude between 300 and 500 meters. The second one, to the south-east, are the plains and low plateaus bordering the Indian ocean, from Tanzania to eastern Kenya, eastern Ethiopia, and Somalia.

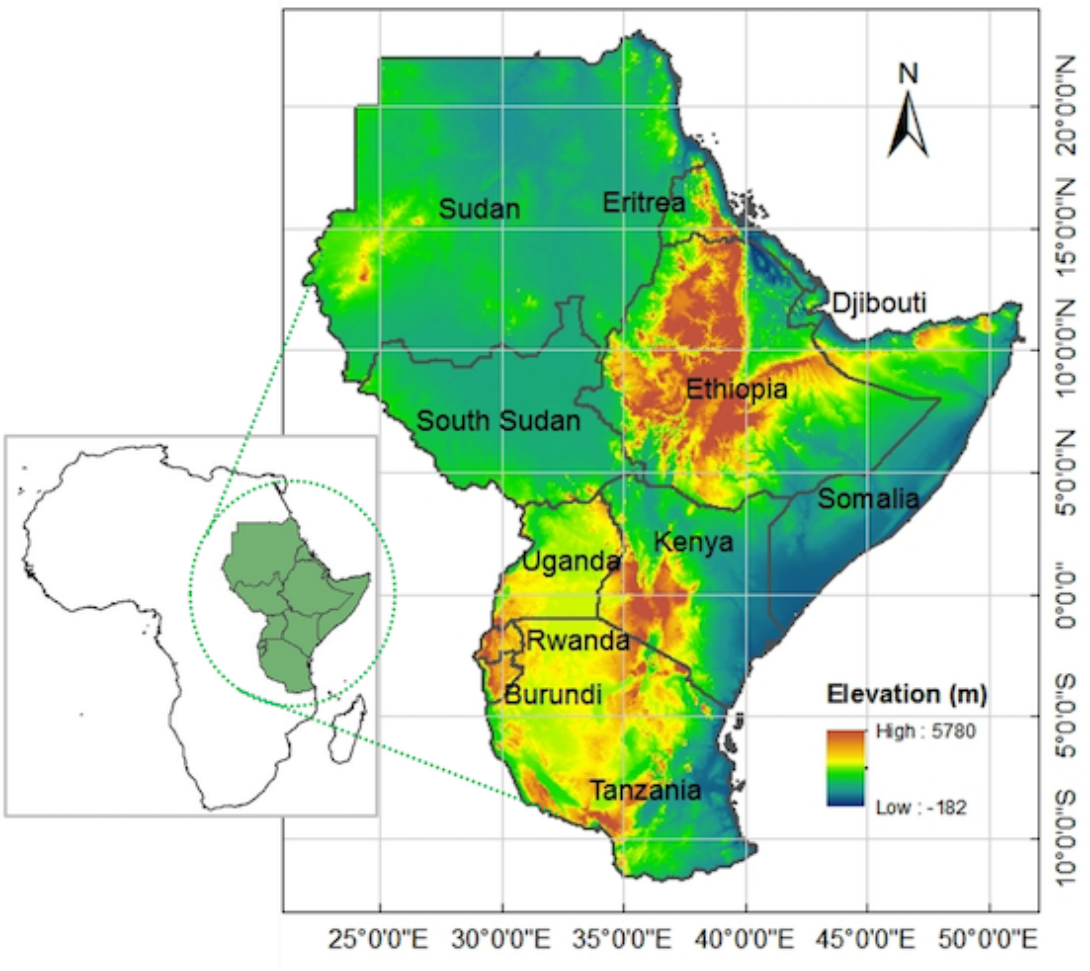

Figure 2.1: Topographic elevation map and countries of GHA. The insert shows the location of the GHA region on the map of the Africa continent.

The climate of the GHA shows considerable spatial heterogeneity owing in large part to substantial topographic variations across the region (e.g., Hession and Moore, 2011). In the tropical belt, most part of this region stands out as a relatively dry area, despite its equatorial location. Between 12^{o}S and 12^{o}N, it is actually the driest land area (Yang *et al.*, 2015). There are likely several factors

contributing to the general aridity of the region (Nicholson, 1996), one being a generally divergent large-scale flow, particularly over the low-lying, eastern regions (Yang *et al.*, 2015; Nicholson, 2018). Average annual rainfall nonetheless varies by an order of magnitude between the northeastern coastal regions of Somalia and the western Highlands of Ethiopia, where orographic rainfall is substantial (Fig. 3.1). Even in highland areas spatial variations in rainfall can be substantial over distances of tens of kilometers given orographic variations and the seasonally varying direction of the low-level wind flow (Nicholson, 1996). Orography also controls important features of the atmospheric circulation, an example being the gap between the Ethiopian and Kenyan Highlands leading to the formation of the Turkana low level jet, which channels the southeasterly flow from over the Indian ocean inland (Viste and Sorteberg, 2013; Nicholson, 2016). As a whole the complex regional terrain presents an environment within which local and large scale climate systems frequently interact to create highly variable climate in both space and time.

2.2 Annual Cycle and Seasonal Rainfall Climatology

2.2.1 Sasonal rainfall climatology

Besides orographic effects and other factors, the seasonal rainfall climatology over GHA is highly influenced by the north-south displacement of the tropical rainbelt, often, but inadequately termed ITCZ (Nicholson, 2018). In the following, the traditional motion of ITCZ is used for tropical rainbelt region. Figure 2.2 shows seasonal mean rainfall derived from the CHIRPS climatology for the period 1981–2017 (for a brief description of this rainfall dataset see Chapter 3). Throughout January–February (JF; Fig. 2.2a) most parts of the GHA are dry, and the northeast monsoon brings dry continental air into the region, and consequently, the rainfall during these months is low (Yang *et al.*, 2015), except heavy rainfall occur in southern hemisphere sector. Much of the northern Ethiopian Highlands and northwestern parts of the GHA have boreal summer monsoon regimes with maximum rainfall during the period of June–September (JJAS; Fig. 2.2c), known in Ethiopia as "Kiremt Rains". This season accounts for some 50 to 80% of the rainfall over Ethiopian agricultural regions (Korecha and Barnston, 2007). The

equatorial part of GHA has two rainy seasons; the bimodal patterns are experienced over many parts of GHA during the "Long Rains" of March–May (MAM; Fig. 2.2b) and the "Short Rains" of October–December (OND, Fig. 2.2d). During the Long Rains, the precipitation rate over the coastal areas to the east of the Highlands peaks and in general exceeds 1 $mm(day)^{-1}$ except in the northeastern extreme of the Horn. The Short Rains show a similar precipitation pattern to the Long Rains but with a slightly weaker magnitude.

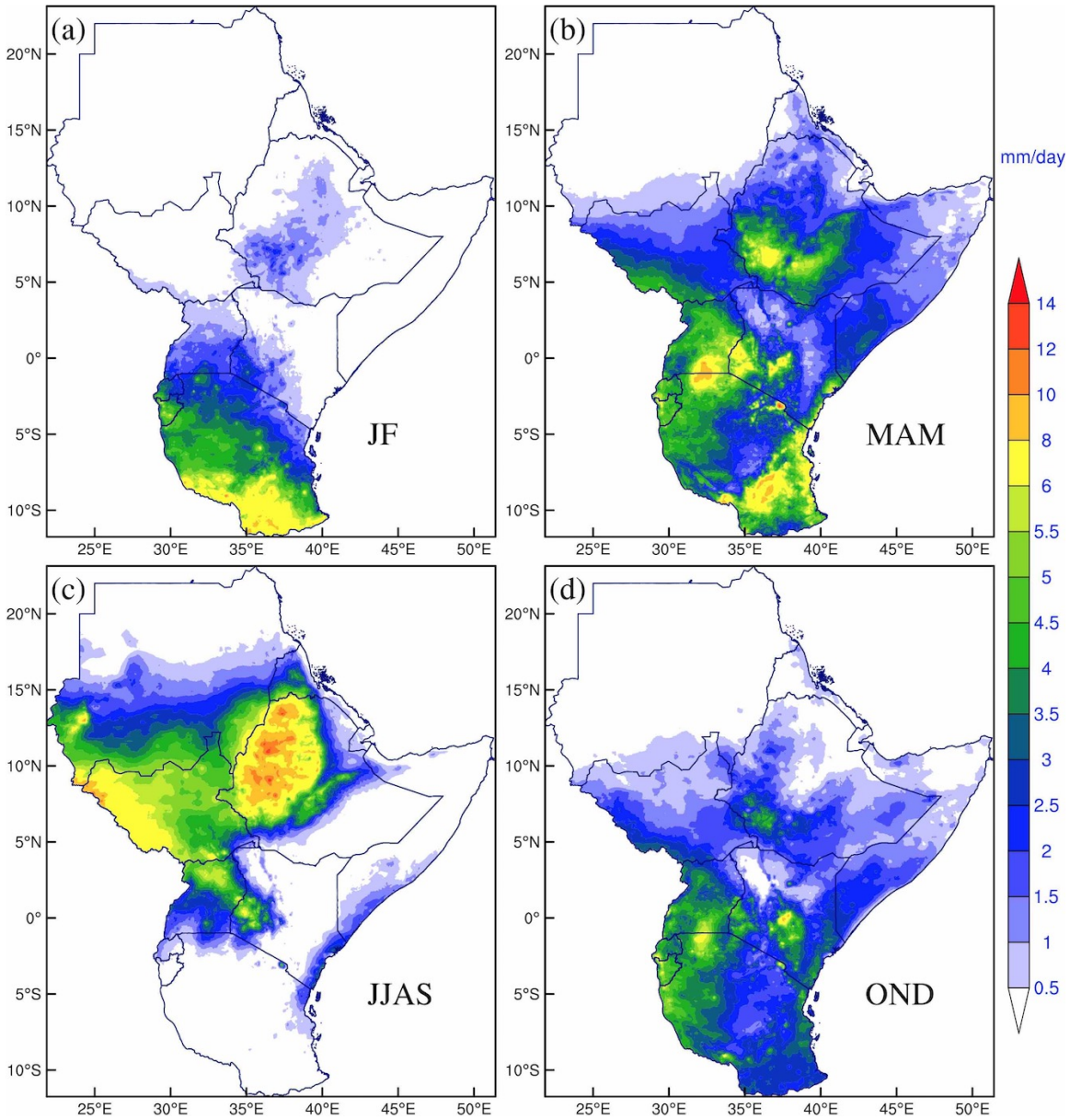

Figure 2.2: Seasonal mean CHIRPS rainfall distribution over GHA averaged from 1981 to 2017. (a) January–February (JF), (b) MAM, (c) JJAS and (d) OND. Unit is given in $mm(day)^{-1}$.

These bimodal rainfall distribution is related to the movement of the ITCZ, which migrates between 15^{o}S and 15^{o}N between January and July respectively, and by the Indian and WAM circulations. The amount of rainfall is larger during the Long Rains, as compared to that of the Short Rains (Hastenrath *et al.*, 1993). Moreover, the Long Rains bring several weeks of heavy rainfall associated with the relatively slow northward movement of the ITCZ. In contrast, during the core of the Short Rains, the southward migration of the ITCZ is more rapid (Black *et al.*, 2003) and exhibits more intense variability (Hastenrath *et al.*, 2007). These rainy seasons occur during the transitions between the winter and summer monsoons, when air in both hemispheres confluence near the equator (Hastenrath *et al.*, 2004). On the other hand, the southwest monsoon starts in June and persists until September, during JJAS the moisture influx from the Atlantic and Indian oceans results in high rainfall over the Ethiopian Highlands (Diro *et al.*, 2011a; Segele *et al.*, 2009b, 2015). However, during southwest monsoon season the southern, southeastern and horn part of the GHA is dry because this region is convectively stable year round (Yang *et al.*, 2015). Divergence in the lower troposphere appears to play a role as well.

2.2.2 Annual cycle of rainfall climatology

The annual cycle of precipitation over much of the GHA shows a bimodal distribution although in some regions a unimodal distribution dominates. Figure 2.3 shows some example of mean seasonal precipitation variations for the period 1981–2017, derived from CHIRPS and averaged over four representative regions. Since the GHA lies in the tropics, each region has a distinct annual cycle rainfall driven by the motion of the sun and associated changes in oceanic and atmospheric circulation caused by a degree of solar insolation (Black *et al.*, 2003; Yang *et al.*, 2015). In addition, the seasonal cycle of rainfall in the GHA is controlled by large-scale monsoon circulations, the migration of the ITCZ, and by regional orography (Nicholson *et al.*, 1988; Black *et al.*, 2003). It is clearly seen that there is a marked contrast in the seasonal cycle between the northernmost region and the other three, reflecting the strong influence of the southwest monsoon circulation on rainfall in Ethiopian Highlands during JJAS (Fig. 2.3a). The other regions are dry during the southwest monsoon and instead show a bimodal distribution to the rainfall, which is particularly marked for the equatorial East Africa and Horn of Africa (Fig. 2.3c and 2.3d). On the other hand, southern

GHA is dry throughout both southwest monsoon and equatorial transition period, this region receives significant amount of rain during boreal winter (Fig. 2.3d). In general, the bimodal distribution dominates to the east of the Highlands and near the equator while the unimodal distribution dominates over the southern and northwestern parts of the GHA. In addition to the mean monthly rainfall, Figure 2.3 shows the interannual standard deviation. It is clear that the Short Rains are highly variable at interannual timescale (Black *et al.*, 2003; Hastenrath *et al.*, 1993). Indeed, in percentage terms, they are more variable than the Long Rains. The possible reasons for this are discussed later in the context of the interannual variability.

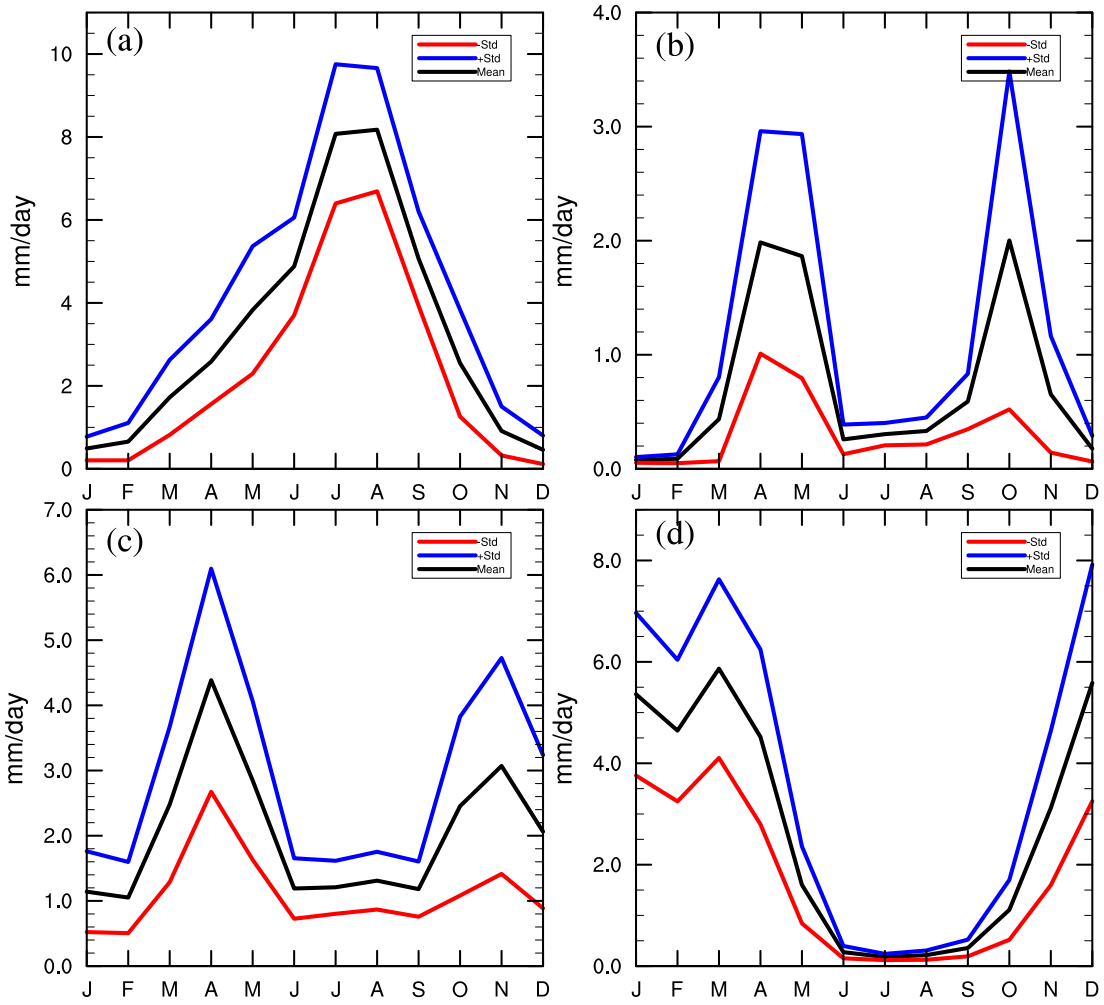

Figure 2.3: The annual cycle of area-averaged monthly precipitation in GHA. (a) Ethiopian Highlands (6–14^{o}N, 35–40^{o}E), (b) Horn of Africa (2–12^{o}N, 40–50^{o}E), (c) Equatorial East Africa (5^{o}S–5^{o}N, 35–46^{o}E), and (d) Southern East Africa (5^o–12^{o}S, 32–42^{o}E. The black curve denotes the climatological mean, and the blue and red curve show ± one standard deviation of the interannual variability. Rainall is derived from CHIRPS for the period 1981–2017. The units are given in $mm(day)^{-1}$.

2.3 Large-scale Atmospheric Circulations Climatology

The seasonal climate of GHA is dominated by planetary scale features such as the meridional overturning of the Hadley and Walker circulations, the influences of the Atlantic and Indian ocean monsoons, large-scale teleconnections, subtropical anticyclons, tropical cyclones, jet-streams, ITCZ, and easterly/westerly wave perturbations (Glantz, 1988; Nicholson *et al.*, 1988; Hastenrath, 1991; Segele *et al.*, 2009b). In addition, the GHA climate is directly linked to regional factors, including topography, lakes, and the maritime influence (Camberlin, 2018). This sub-sections gives an overview of the regional and large-scale circulation features and systems that influence the seasonal climate variability and patterns in the GHA.

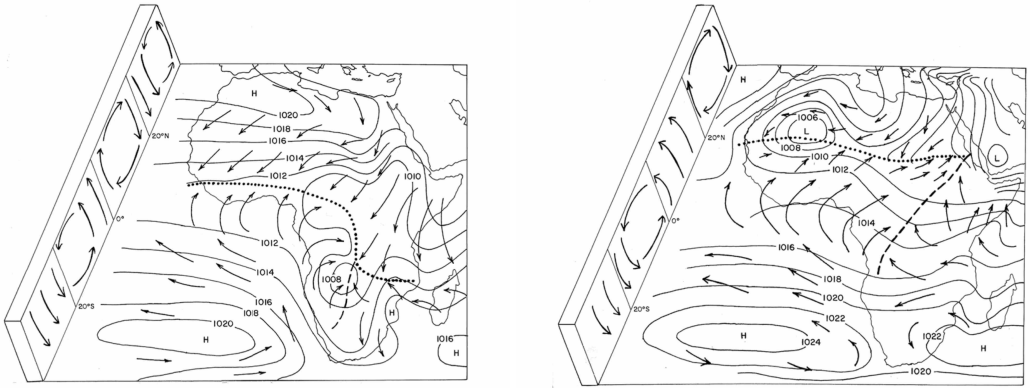

(a) January Circulation **(b)** July/August Circulation

Figure 2.4: Schematic of the general pattern of mean wind and pressure fields over Africa in (a) January and (b) July/August (after Nicholson *et al.*, 1988). The dotted and dashed lines represent the ITCZ and Congo air boundary, respectively.

2.3.1 Intertropical convergence zone (ITCZ)

The ITCZ is the main synoptic scale system that controls the intensity and migration of the seasonal rainfall over the GHA. It is a boundary of confluence of hemispheric winds near the surface as a result of inter-hemispheric monsoon wind systems over the region. Due to the complex effects of topographic diversity on low-level synoptic circulation, the convergence zone is difficult to locate at low levels over the GHA. However, the classic explanation of the seasonal cycle of precipitation over the GHA is the seasonal migration of the ITCZ. Dur-

ing the southern hemisphere summer from November to March, the ITCZ has two unique components i.e the east-west orientation called the zonal component and the north-south oriented component referred to as the meridional component (Fig. 2.4a). The converging northeasterly and southwesterly trades form the zonal component. This branch of the ITCZ during northern summer is located in Eritrea and appears as an asymptotic wind confluence between the moist south-westerlies and the much drier north-westerly winds. Accordingly, the wind convergence over Eritrea and extreme northern Ethiopia is believed to be associated to Kiremt Rains (Segele *et al.*, 2009b). In addition, during July/August, the meridional branch of the ITCZ (Fig. 2.4b) shifted farthest northeast which causes large part parts of Ethiopia and south Sudan to be under a moist westerly monsoonal winds from Atlantic ocean and the moist Congo basin (Flohn, 1987; Kassahun, 1987; Segele *et al.*, 2009a; Diro *et al.*, 2011a). This eastward displacement of the meridional arm of ITCZ is often associated with the influx of the moist westerly and southwesterly airmass which is locally known as "Congo Airmass".

On the other hand, the north-south oscillation of the zonal component is primarily responsible for both the Long and the Short Rains seasons over the GHA (Fig. 2.2b and 2.2d). The strength of ITCZ during this period depends on the intensity of the northeasterly and southeasterly trade winds, which in turn are driven by the subtropical anticyclones (Camberlin, 2018). The meridional component is formed by the convergence between the easterly wind from the Indian and the moist westerly from the Atlantic ocean and Congo basin. It oscillates roughly between longitudes 25^o and 36^oE. While north-south migration of ITCZ twice a year significantly influence the rainfall regimes based on the onset, spatial-temporal evolution, and withdrawal pattern (Camberlin *et al.*, 2009). Because the ITCZ encompasses the region where rain-producing system occur in the GHA, interannual fluctuation in rainfall amount and distribution have in the past been generally attributed to anomalies in the large-scale factors that influence the characteristics of the ITCZ in the region. For instance, the 1984 drought was associated with the non-establishment of the zonal arm of the ITCZ as a result of a series of a tropical cyclone in the Indian ocean that rendered the low-level flow over the region diffluent as it was diverted to the low pressure systems over the ocean (Anyamba, 1984). Moreover, the 1961/62 flood, the worst experienced in the region this century, were associated with a very strong low-level westerly wind anomaly attributed to the meridional branch of ICTZ (Anyamba, 1984; Anyah

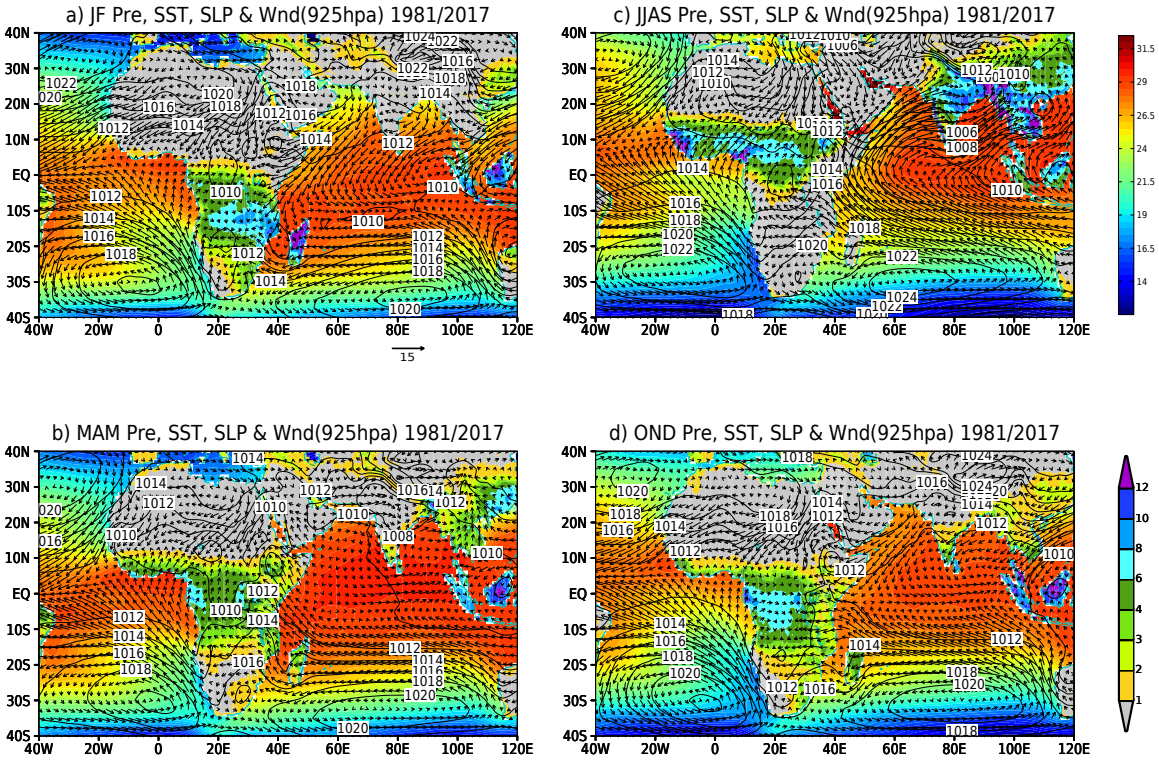

Figure 2.5: Seasonal mean low level wind (vector), SST (colors), sea level pressure (contour), and rainfall (colors over land) climatologies for the period 1981–2017. (a) January–February (JF), (b) MAM, (c) June–September (JJAS), and (d) OND. Sea level pressure (hPa) and wind (ms^{-1}) fields are derived from ERA-Interim reanalysis data. The SST (^0C) and rainfall ($mm(day)^{-1}$) data are from HadISST and CHIRPS respectively. Further descriptions of these datasets are given in Chapter 3.

and Semazzi, 2006).

2.3.2 African and Indian monsoons

The annual cycle in the tropics is driven by the motion of the sun and associated changes in surface and atmospheric heating caused by the degree of solar insolation. Maximum heating moves from the northern hemisphere in boreal summer to the southern hemisphere in winter. The large heat capacity of water means that SST maxima normally lag the solar cycle by around two months, and this differential heating over the land and the ocean leads to temperature gradients and associated flow patterns throughout the tropics. Monsoons are defined as the seasonal reversal of the cross-equatorial winds that follow such meridional temperature and pressure gradient. Among others, West African and Indian monsoons, are accompanied by changes in the rainfall regime, from very dry to very wet periods. The GHA is located at the interface between these two

monsoon systems: the WAM to the west and the Indian monsoon to the east. The East African Highlands are actually a major north-south barrier that both separates and connects the two systems. The climate of GHA region is particularly influenced by the northeast and southeast monsoons which are experienced during southern and northern summer (Findlater, 1971; Camberlin *et al.*, 2009)

Figure 2.5 shows low-level winds and SLP derived from the ERA-Interim reanalysis, HadISST, and CHIRPS rainfall climatologies for the period 1981–2017. The winter monsoon is characterized by high pressure over the Asian land mass (Fig. 2.5a); the winds are northeasterly over the GHA, the Arabian Sea and the Bay of Bengal. During the northern summer the key factor in the intensity of the Indian monsoon winds is the Tibetan Plateau, which acts as an elevated heat source and hence low SLP, and has a profound influence on the establishment and maintenance of the Asian summer monsoon circulation (Figure 2.5c). Research has been done to investigate link between the Ethiopian Highlands Kiremt Rains and summer monsoons. For instance Camberlin (1997) has shown a strong connection between East African summer rainfall and Indian monsoon. He suggested that strong monsoon conditions (low SLP over Mumbai) correspond to a west-east pressure gradient and therefore to abnormally strong westerly winds advecting moisture from the Congo basin to the GHA. Another potential link is through the change of the Somali Low Level Jet (SLLJ) over the Indian ocean (Fig. 2.6). The SLLJ occurs during boreal summer over northern Madagascar and off the coast of Somalia. The jet is most intense from June to August with average monthly maximum surface speeds of 18 ms^{-1} even though daily speeds can reach 50 ms^{-1} (Krishnamurti *et al.*, 2013). The negative summer rainfall anomalies over India often implies the weakening of the monsoon circulation, especially the SLLJ which is also associated with dry Kiremt Rains as well as warm east equatorial Pacific SST (Diro *et al.*, 2011a).

During the intermediate equatorial seasons MAM (Fig. 2.5b) and OND (Fig. 2.5d) both monsoonal wind systems are present with one withdrawing while the other is advancing. Figure 2.5 also shows the climatological values of SSTs over the Indian and Atlantic oceans and it is clear that the seasonal rainfall during monsoon transition co-varies with the near-coast SSTs in the Indian ocean. SSTs are highest during the Long Rains season (greater than 28.5 ^0C) and are around 1.5 ^0C cooler, yet with a similar pattern, during the Short Rains season (Fig. 2.5b and 2.5d). SSTs are coolest during boreal summer due to southwesterly

wind stresses over the GHA coast, and the Arabian Sea. During boreal winter, a relatively strong north-south SST gradient is evident and there is an associated gradient in rainfall between the north and the south (Fig. 2.5a) consistent with findings in Yang *et al.* (2015).

2.3.3 SLP

At the lower levels, the subtropical high pressure zones in the vicinity of Africa influence moisture fluxes and hence rainfall over the GHA. Figure 2.5 further shows the seasonal change in the distribution of surface pressure, primarily associated with seasonal variations in the position of the Sun. The southeasterly trades that blow across the southern Indian ocean and represent the northern side of the Mascarene High migrate equator wards and strengthen as the Asian summer monsoon develops in JJAS. The Mascarene High moves from its position over the southeastern Indian ocean centered near 85^{o}E, 35^{o}S in JF, to lie over the southwestern Indian oceans centered near 60^{o}E, 30^{o}S in JJAS. In addition, the low level moisture sources during the Kiremt Rains are the Atlantic and the Indian ocean and the flux of moisture depends on the intensity and position of the St. Helena and Mascarene Highs (Kassahun, 1987; Segele *et al.*, 2009a). On the contrary, the Tibetan High generates stronger north-easterlies during the Short Rains period than the south-easterlies from the relatively weaker Mascarene High. Since the north-easterlies do not have long trajectory over the ocean, as compared to south-easterlies which have a longer trajectory over the southwest Indian ocean the ITCZ yields lesser rainfall during the OND period (Fig. 2.5d). Meanwhile, during the MAM season, the Mascarene High drives stronger and moister south-easterlies into GHA. Convergence of southeasterly and northeasterly results into Long Rains season (Fig. 2.5b). Furthermore, intensification in the strength of the St. Helena High implies stronger moist westerlies over Atlantic ocean and Congo basin, and therefore a stronger meridional arm of ITCZ, attributed to more rainfall during the MAM period.

2.3.4 Low level flow

In boreal winter the northeast dry monsoon winds sweep over the northern Indian ocean, cross the equator, and recurve to meet the southeast trade winds in a confluence zone around 10^{o}S overlying a band of warmest SSTs (Fig. 2.5a). In boreal summer the southeast trade winds cross the equator and curve back to

become the southwest monsoon penetrating into the southern part of the Asian continent (Fig. 2.5c and 2.6). Several studies examined the relationship between the JJAS rainfall and near surface circulation anomalies (e.g., Segele *et al.*, 2009a; Diro *et al.*, 2011a). They showed very robust relationships between the Kiremt Rains and low-level westerlies over western and central Africa and the SLLJ. Evidence suggests that the enhanced westerlies are associated with high pressure over the Gulf of Guinea and an anomalously deep monsoon trough over the Arabian Peninsula. Besides, the surface winds are easterlies south of the equator in the eastern and central Indian ocean but turn northwestward toward the GHA during both transition seasons of MAM and OND (Figs. 2.5b, 2.5d). The regional turn coincides with development and retreat of the boreal summer monsoon and leads to moisture convergence over Equatorial East Africa, enhancing the atmospheric convection and rainfall there (Hastenrath *et al.*, 1993; Behera *et al.*, 2005). Another important aspect is the zonal circulation over the Indian ocean (Hastenrath *et al.*, 2011; Pohl and Camberlin, 2011; Nicholson, 2015). During most of the year the prevailing equatorial circulation is westerlies at low levels (Fig. 2.5).

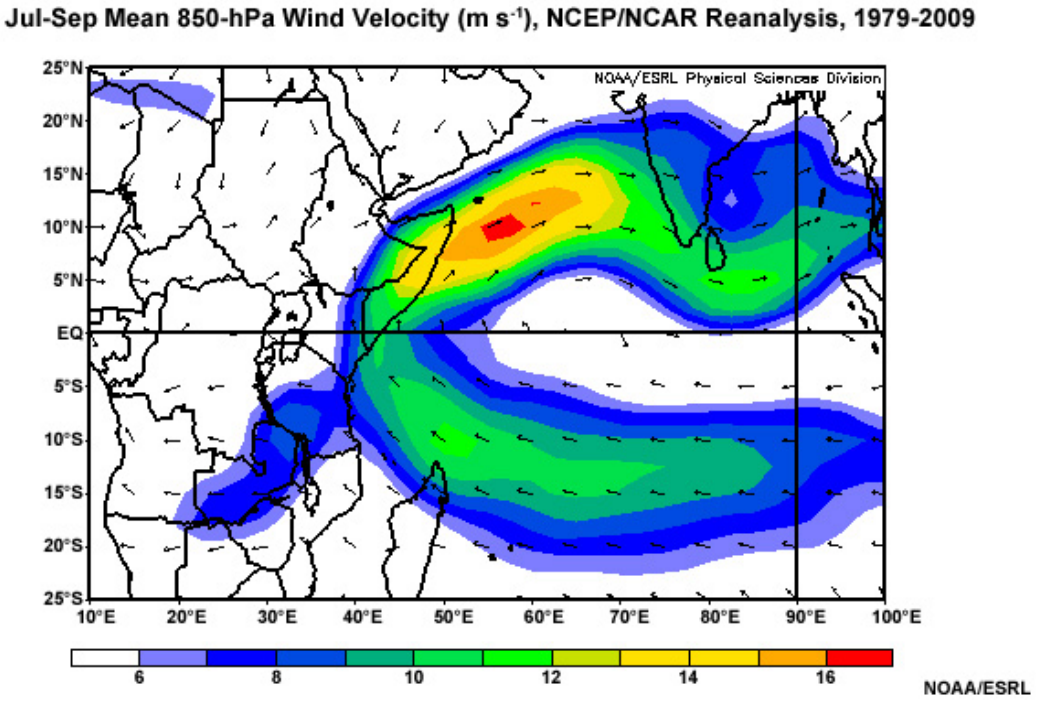

Figure 2.6: Mean wind speed at 850 mb for July to September over northern Madagascar and off the coast of Somalia. The filled contour represents the magnitude of the wind speed (ms^{-1}) and the vectors indicate the direction. Plot adapted from https://www.meted.ucar.edu/

2.3.5 AEJ

The AEJ is a mid-tropospheric jet (at around 600 mb) located over tropical north Africa during northern hemisphere summer (Fig. 2.7). The AEJ over west Africa during the northern hemisphere summer results from the north-south gradient between the relatively cooler temperatures to the south and the hot Sahara to the north (Cook, 1999). In addition, Thorncroft and Blackburn (1999) suggested that the AEJ is maintained by two diabatically forced meridional circulation patterns: The circulation associated with the dry convection in the Saharan heat low regions; and the one associated with deep moist convections in the ITCZ. Burpee (1972) showed that the AEJ is both barotropically and baroclinically unstable resulting in easterly waves which grow at the expense of the jet. This implies that the observed AEJ results from the combination of the diabatically forced meridional circulation that maintains it, and the easterly waves that weaken it (Thorncroft and Blackburn, 1999).

The fluctuations of the position and strength of the AEJ induce rainfall variability at the intraseasonal and interannual time-scales in the Sahel. For example, a more equatorward position of the AEJ corresponds to dry conditions over the Sahel (Nicholson, 2008). Similarly, Diro *et al.* (2011b) suggested that the southward shift of the AEJ related to warm SST anomalies in the Pacific ocean and Ethiopian Kiremt Rains. They argue that the weaker (stronger) jet or the northward (southward) shift of the jet means less (more) moisture is taken away from east Africa and hence to more (less) rainfall.

2.3.6 Tropical Easterly Jet (TEJ)

In the upper troposphere, the TEJ is one of the most prominent features occurring at the height of the summer monsoon circulation, lasting from late June into early September (Hastenrath, 1991). A band of strong easterlies extends from south East Asia across the Indian ocean and Africa as shown in Figure 2.8. The development of the TEJ is connected with the more zonally symmetric north-south differential heating of the upper troposphere between the elevated Tibetan Plateau and the Indian ocean surface to the south (Hastenrath, 1991). Off-equatorial zonal jets induce a secondary meridional circulation at jet entrance (exit) to balance the acceleration (deceleration) of zonal geostrophic wind (Holton and Hakim, 2013). Ethiopia is located at the east exit region of the TEJ core and according to this theory, the jet induces upper-level divergence

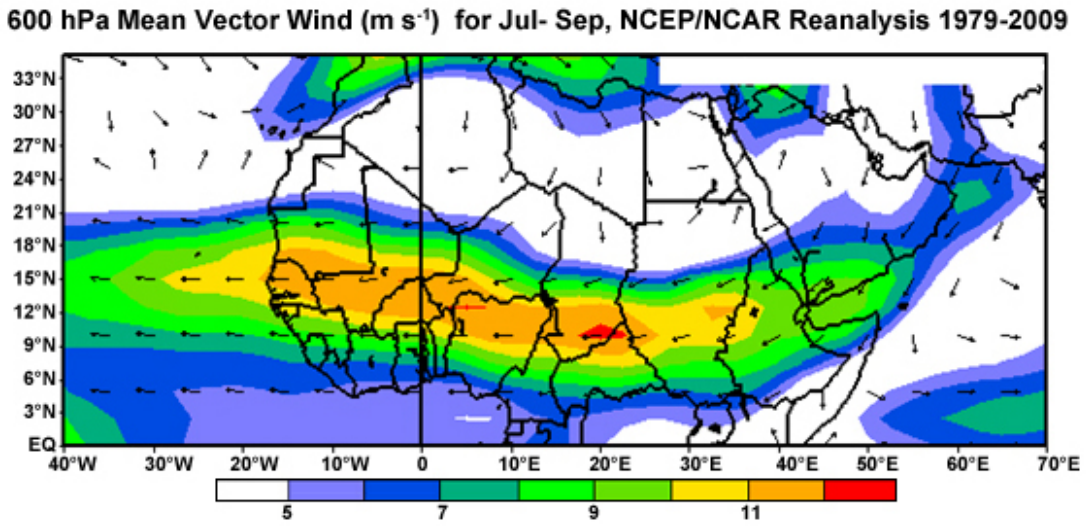

Figure 2.7: Mean wind speed at 600 mb for July to September over northern tropical Africa and the tropical Atlantic ocean. The filled contour represents the magnitude of the wind speed (ms^{-1}) and the vectors indicate the direction. Plot adapted from https://www.meted.ucar.edu/

over Ethiopia. Observations show a divergence maximum at 100 mb (Segele *et al.*, 2009a). Upper-level divergence facilitates convection and therefore rainfall. This theory links the strength of the TEJ to Kiremt Rains via vertical motion (Berhane *et al.*, 2014; Camberlin, 1997; Diro *et al.*, 2011a; Segele *et al.*, 2009a). Diro *et al.* (2011b) further suggests that warm SST anomalies in the Central Pacific weaken the TEJ via upper-level equatorial Rossby waves and thereby weaken upper-level divergence over Ethiopia.

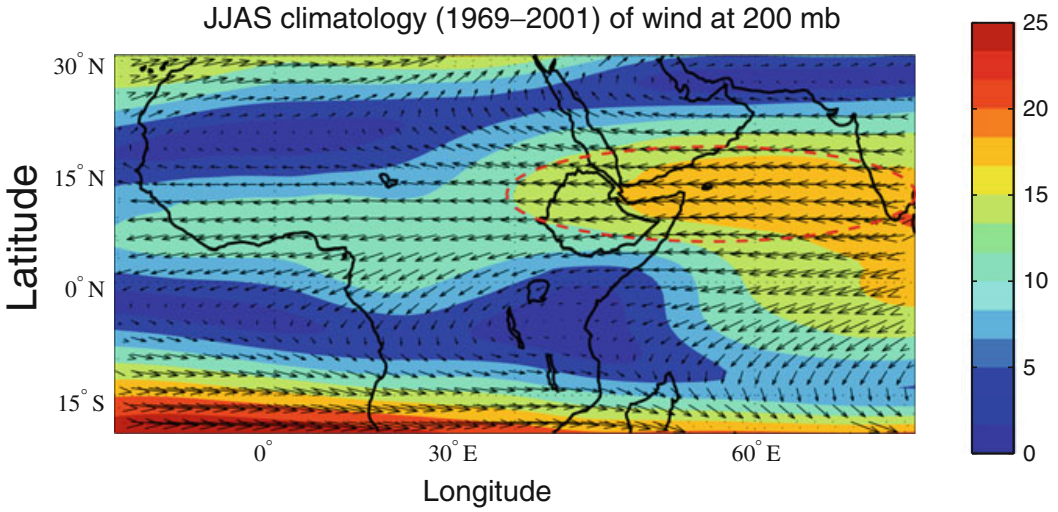

Figure 2.8: JJAS climatological wind at 200mb. The filled contour represents the magnitude of the wind speed (ms^{-1}) and the vectors indicate the direction. The red broken lines indicates the location of maximum wind speed region of TEJ (after Diro *et al.*, 2011a).

2.4 Tropical Ocean-Atmosphere Variability

Tropical oceans play major roles in the natural variability of the world climate. It is a well-established fact that anomalous coupled ocean-atmosphere phenomena generated in the tropical oceans produce global atmospheric and oceanic circulation changes that influence regional climate conditions even in remote regions. On the interannual time scale, ENSO in the tropical Pacific ocean is known as one typical example of such phenomena and has so far received worldwide attention because of its enormous climate and societal impact in areas far distant from its origin in the equatorial Pacific ocean. The GHA is one of those regions, in which ENSO is considered as the primary driver for Short Rains' interannual variability with El Niño/La Niña resulting in anomalously wet/dry conditions. While El Niño/La Niña episodes are associated with dry/wet Kiremt Rains. This section provides a brief description of tropical ocean-atmosphere interaction known to influence the interannual to decadal variability of three major rainy seasons over GHA. For the definition of El Niño and other SST-based climate indices and further information, see Chapter 3.

2.4.1 Pacific Ocean: El Niño-Southern Oscillation (ENSO)

The ENSO is the most significant mode of interannual ocean-atmosphere coupled phenomena in the global climate system (e.g., Philander, 1990). It is also an irregular phenomenon that tends to reoccur every 2–7 years (Diaz and Markgraf, 2000) alternating between its two extremes: El Niño and La Niña. An El Niño (La Niña) occurs when warm (cool) SST anomalies are observed in the central and/or eastern equatorial Pacific ocean (Glantz, 2001). During an El Niño event, SLP tends to be lower in the eastern Pacific and higher in the western Pacific while the opposite occurs during a La Niña. This see-saw in atmospheric pressure between the eastern and western tropical Pacific is called the Southern Oscillation (Walker, 1924).

Schematic diagrams of normal, El Niño, and La Niña conditions are shown in Figures 2.9a, 2.9b, and 2.9c respectively. Under normal climatic state in and over the Pacific ocean (shown for boreal winter in Figure 2.9a), a tropical Pacific-wide circulation proceeds westward at the surface and rises over the west Pacific warm pool, where there is persistent convective rainfall. This region of rising motion is characterized by a surface low pressure. As it rises, it reaches the tropopause

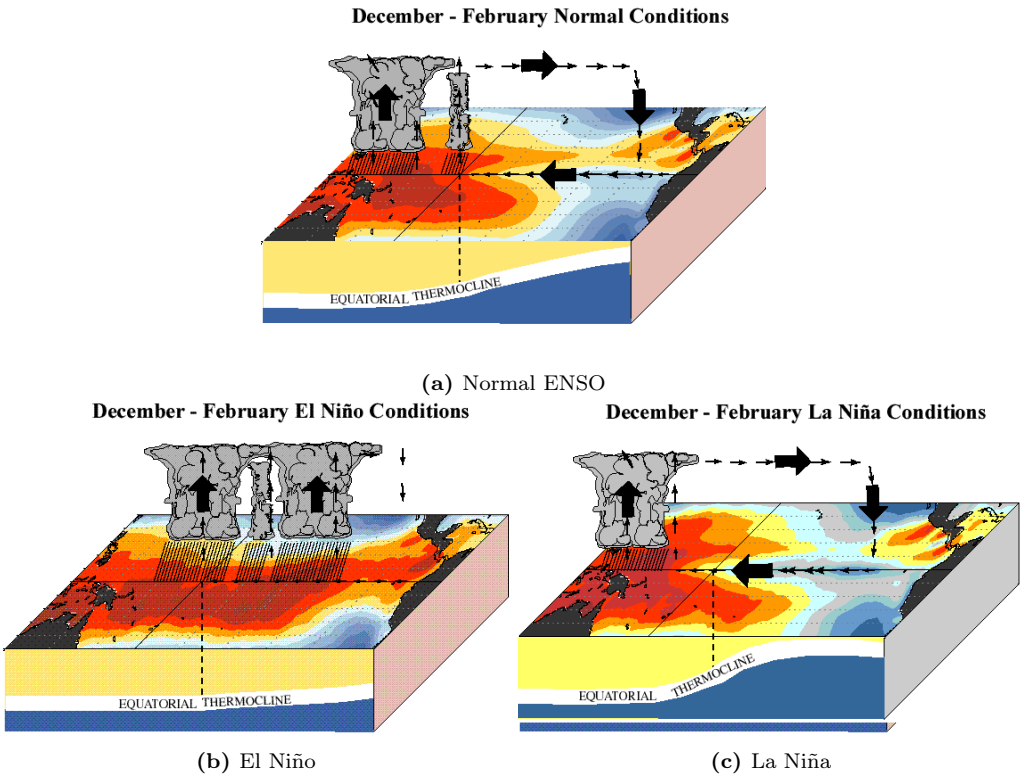

(a) Normal ENSO

(b) El Niño

(c) La Niña

Figure 2.9: Schematic diagrams of (a) Normal, (b) El Niño, and (c) La Niña in the equatorial Pacific and sub-surface waters during boreal winter. Plot adapted from *http* : *//www.pmel.noaa.gov/*.

and returns eastward aloft, completing the circulation by descending over the cool eastern Pacific, leading to high pressure at the surface. This phenomena is called the Walker circulation (Gill, 1982). The easterly winds cause increased sea-surface height in the west, as warm waters pile up there. The thermocline (the interface at which there is maximum vertical gradient in the subsurface ocean temperature, separating the warm upper ocean from the deep ocean, preventing vertical mixing) features a mean west-to-east tilt under normal conditions as shown in Figures 2.9a. Typical behaviour during El Niño conditions is shown in Figures 2.9b. The coupled response to east Pacific warming involves longitudinal shifts in the tropical Walker circulation. During El Niño , the rising arm of the Walker cell, normally over the west Pacific, shifts toward the warmer central and eastern waters, taking with it atmospheric convection. During La Niña, the opposite phase to El Niño, features cooling in the central to east Pacific region, associated with enhanced easterly trade winds and a steeper thermocline with more upwelling in the east (Fig. 2.9c).

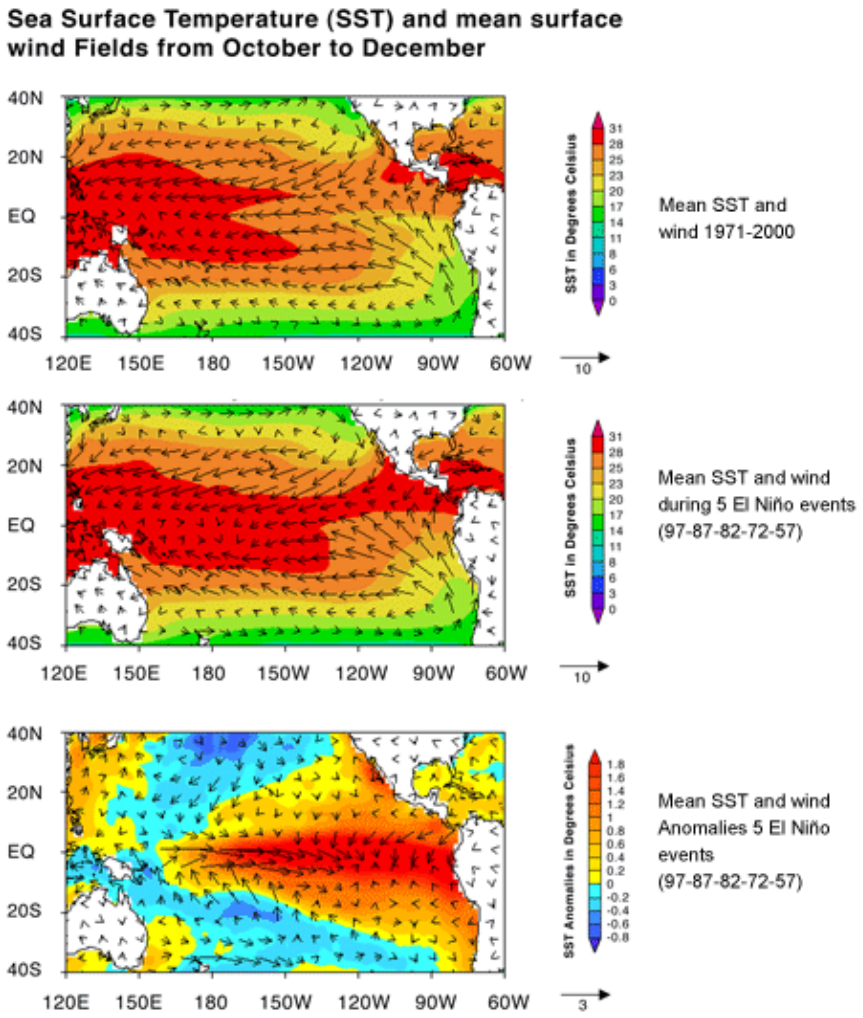

Figure 2.10: October-December seasonal mean and anomalies of observed SST and low level wind over Pacific ocean basin for 30-year average during 1971–2000. Plot adapted from *https* : *//ctl.columbia.edu/*.

To further demonstrate ENSO phenomena with observed data, Figure 2.10 shows the tropical Pacific climatology for 30-year averaged SSTs and low level wind observed during OND seasons (upper panel), the average SST and low level wind observed during the five warmest years (middle panel), and the observed anomaly during the five warmest years (bottom panel). The climatology shows an asymmetry in the SST and wind distribution, with the ITCZ and warmest SSTs being located in the western part of the basin (Fig. 2.10 top panel). The easterlies drive Ekman divergence along the equator and coastal upwelling along the coasts of South America, resulting in the formation of the east Pacific "cold tongue" and Peruvian coastal upwelling. During an El Niño event (Fig. 2.10 bottom panel), equatorial trade winds weaken, as does the Walker Circulation (Bjerknes,

1969), a direct thermodynamic circulation in the longitude-height plane over the equatorial Pacific ocean. SSTs in the central-eastern tropical Pacific become anomalously high and the subsurface thermocline across the equatorial Pacific flattens as a result of less upwelling cold water in the eastern Pacific as well as more eastward warm water migrating from the west Pacific warm pool (Bjerknes, 1966).

The oscillations between two ENSO phases involve great changes of SST/precipitation amplitude and distribution in the tropical Pacific ocean. In addition, ENSO can modulate the weather and climate in other parts of the world, even those that are far from the tropical Pacific, via Rossby wave propagation and energy transport (Ropelewski and Halpert, 1987; Trenberth *et al.*, 1998). Some of these severe ENSO-related heavy rainfall, droughts, wildfires, and off-shore warming can have damaging socioeconomic impacts on the societies in the entire tropics and the western coastline of the Americas (Philander, 1985; Ropelewski and Halpert, 1987; Hsiang *et al.*, 2011). Numerous studies have found a significant correlation between the GHA seasonal rainfall and the ENSO, with the impact, sign of the correlation, and its variance depending on the precise region and season. For further discussion and literature review for the influence of ENSO on interannual to decadal rainfall variability over the GHA see section 2.5.

2.4.2 Indian Ocean: Indian Ocean Dipole (IOD)

The IOD is a coupled ocean-atmosphere phenomenon in the Indian ocean characterized by an anomalous cold SSTs in the south-eastern equatorial Indian ocean and and anomalous warming of the western equatorial Indian ocean. This anomalous pattern was first described as a "dipole" or "zonal" mode independently in two studies in 1999, by groups from the USA (Webster *et al.*, 1999) and Japan (Saji *et al.*, 1999). Both studies suggested that the IOD is a native mode of the Indian ocean that exists independently from the Pacific ocean. The term IOD itself was introduced by Saji *et al.* (1999). It reflects a zonal structure of the phenomena with two maxima of different "polarity". This anomaly can be found not only in SSTs but also in other oceanic and atmospheric fields over the Indian Ocean, such as sea surface heights, wind, pressure, rainfall, and outgoing longwave radiation. Later, some authors referred the anomalous pattern to the Indian ocean Zonal Mode (IOZM, e.g., Black *et al.*, 2003; Clark *et al.*, 2003) as

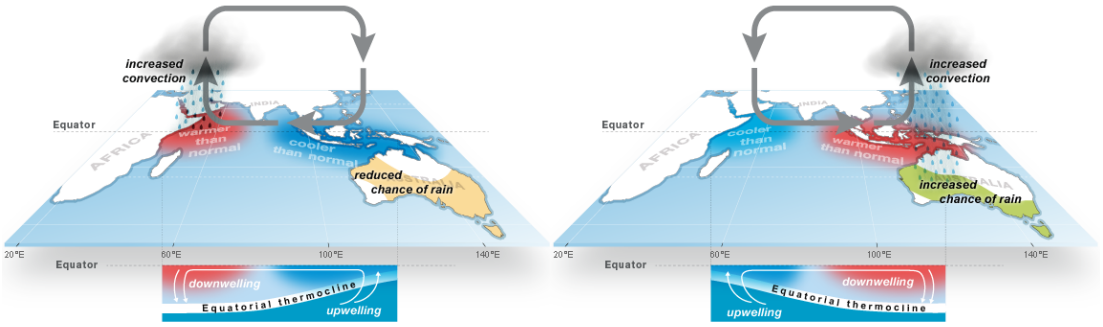

Figure 2.11: Schematic diagram of the IOD phases. (left) Positive IOD phase, and (right) Negative IOD phase. Clouds and precipitation indicate areas of increased convection activity. Surface and upper level zonal wind direction is denoted by the gray arrows. Plot adapted from *http* : *//www.bom.gov.au/climate/iod/*.

proposed by Webster *et al.* (1999), or Indian ocean Dipole Zonal Mode (IODZM, Annamalai *et al.*, 2005) because it matches the out-of-phase development of the SST extremes in the east and west Indian ocean. During a positive IOD event, cooler than normal SSTs are observed in the equatorial eastern Indian ocean and warmer than normal in the equatorial western Indian ocean (Fig. 2.11a). Conversely, during a negative IOD event, negative (cooler) SST anomalies are observed in the western tropical Indian ocean with positive (warmer) anomalies in the eastern tropical Indian ocean (Figure 2.11b). Behera *et al.* (2005) and others showed that a positive IOD event drives an atmospheric circulation with westward low-level winds. Rising motion is enhanced over warmer SSTs (positive anomalies) in the tropical western Indian ocean. Convective activity and rainfall amounts are enhanced in this area, including parts of the GHA, with a deficit in the equatorial eastern Indian ocean (Yamagata *et al.*, 2004; Behera *et al.*, 2005). During negative phase, opposite ocean-atmosphere conditions are observed; leading to enhanced subsidence over parts of GHA which results in the Short Rains reduction (Hastenrath *et al.*, 2004).

To further substantiate the Indian ocean variability with observed data, Figure 2.12 demonstrates the leading EOFs spatial pattern over the Indian ocean computed for the period of 1950–2012. EOF1 explains about 59% of variation and represent the basin wide uniform distribution of SSTAs and it is associated with forced mode due to ENSO (Fig. 2.12 top panel; Saji *et al.*, 1999; Xie and Annamalai, 2002), the corresponding PC1 indicates the warming trend over central Indian ocean (Fig. 2.13 top panel). On the other hand, EOF2 explains 13.3% of the variation which shows the dipole mode pattern (Fig. 2.12 bottom panel),

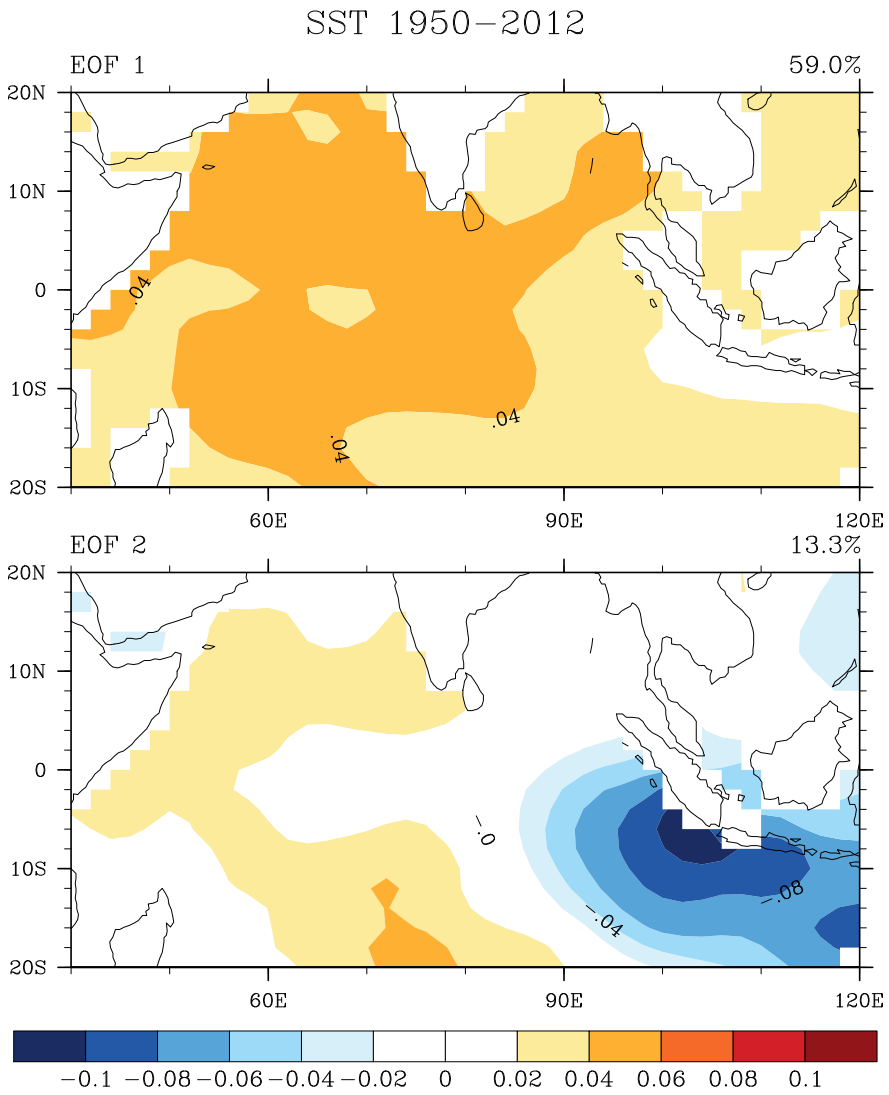

Figure 2.12: Spatial distribution of leading empirical orthogonal functions mode of average OND HadISST anomalies over the Indian ocean basin. EOF1 (top panel), and EOF2 (bottom panel).

and the corresponding PC2 has a similar trend with IOD index and explains the IOD which is strongly associated with the Short Rains' interannual variability (Fig. 2.13 bottom panel; Saji *et al.*, 1999; Black *et al.*, 2003; Behera *et al.*, 2005; Bahaga *et al.*, 2015). Further review on the influence of IOD towards the Short Rains will be discussed in section 2.5, while for the quantitative description see Chapter 3.

2.4.3 Relation between ENSO and IDO

Several studies showed that although the IOD may sometimes evolve without ENSO external forcing, it does on some occasions interact with ENSO (Baquero-

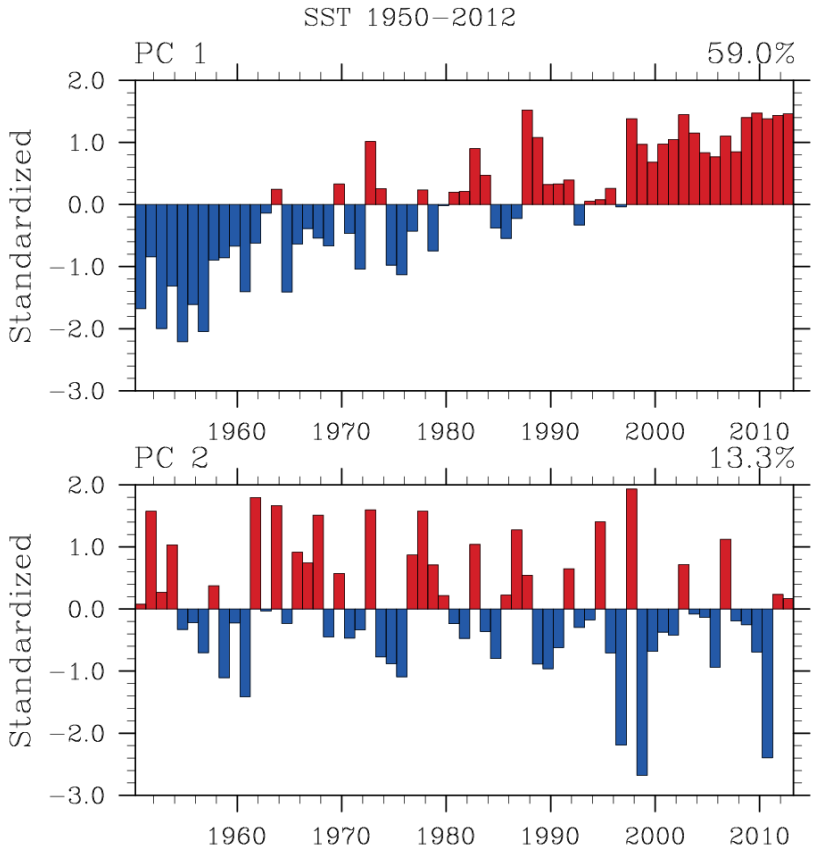

Figure 2.13: The two leading modes of Principal Components (PCs) computed from average OND HadISST anomalies over Indian ocean basin. Year-to-year variation of standardized PC1 (top panel), and PC2 (bottom panel).

Bernal *et al.*, 2002). Figure 2.14 demonstrate SST anomalies representative of the central and eastern equatorial Pacific (Niño 3 region) against the IOD index time series. Note the significant dipole mode events of 1961, 1967 and 1994 coinciding with no ENSO, La Niña and a weak El Niño respectively (Saji *et al.*, 1999). There are years in which dipole mode events coincide with strong ENSO events as in 1972 or 1997. During IOD events, the surface wind field over the tropical Indian ocean experiences large changes, especially in its zonal east-west component over the Equator. Figure 2.14 also demonstrate area-averaged equatorial zonal wind anomalies (Ueq) over (70^o–90^oE and 5^oS–5^oN) region. It is clear that the intensity of the SST dipole mode and the strength of the zonal wind anomaly over the Equator are strongly dependent on each other.

There is a controversy going on about their relationship in the literature, with the scientific community split between the IOD being dependent on ENSO (Baquero-Bernal *et al.*, 2002; Xie and Annamalai, 2002) and independent of

ENSO (Saji *et al.*, 1999; Saji and Yamagata, 2003). Previous work suggests that IOD and ENSO seem to be linked to some extent. Baquero-Bernal *et al.* (2002) questioned the independence of an IOD event from ENSO. They found out that an oscillatory dipole mode exists in the tropical Indian ocean. Their conclusion was that this dipole-like variability can be explained as an oscillatory mode only in the context of ENSO. Based on their data analysis, Xie and Annamalai (2002) conclude that most of the Indian ocean variability is due to downwelling Rossby waves that propagate from the east to the west and are forced by ENSO. The oceanic Rossby waves are thought to interact with the atmosphere after reaching the western tropical Indian ocean.

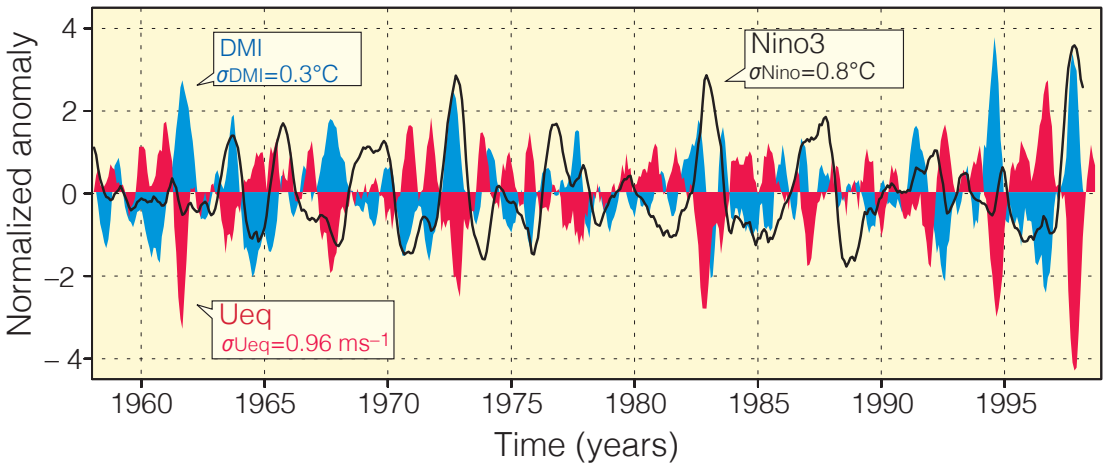

Figure 2.14: Dipole mode and El Niño events since 1958. Plotted in blue, the dipole mode index (DMI) exhibits a pattern of evolution distinctly different from that of the El Niño is represented by the Nino3 SSTAs (black line). On the other hand, equatorial zonal wind anomalies Ueq (plotted in red) coevolves with the DMI. All the three time series have been normalized by their respective standard deviations (after Saji *et al.*, 1999).

On the other hand, after analyzing observations, Saji and Yamagata (2003) concluded that 11 out of 19 episodes occurred independently of ENSO. Studies undertaken by Black *et al.* (2003) and Behera and Yamagata (2003) suggest that IOD events may sometimes evolve without ENSO external forcing. Although there are IOD events that do not coincide with ENSO, such as 1961, the authors agree that there are instances when it does interact with ENSO, possibly through the Walker Circulation to the west and/or via the associated flow of the warm tropical ocean waters from the Pacific into the Indian ocean (i. e., the Indonesian through-flow). Moreover, Behera and Yamagata (2003) add to the debate by suggesting that the IOD can be induced by both ENSO and local Indian ocean circulations, although the resulting spatial IOD structures may be slightly different. This idea is supported by Xie and Annamalai (2002) and Black

et al. (2003) who put forward that the occurrence of IOD events with no ENSO, such as in 1961, may suggest that the IOD can be triggered by factors other than ENSO. However, there is no intention to provide a detailed analysis of the relation between ENSO and IOD which is beyond the scope of this thesis.

2.4.4 Atlantic Ocean: Atlantic Niño 3 (ATL3)

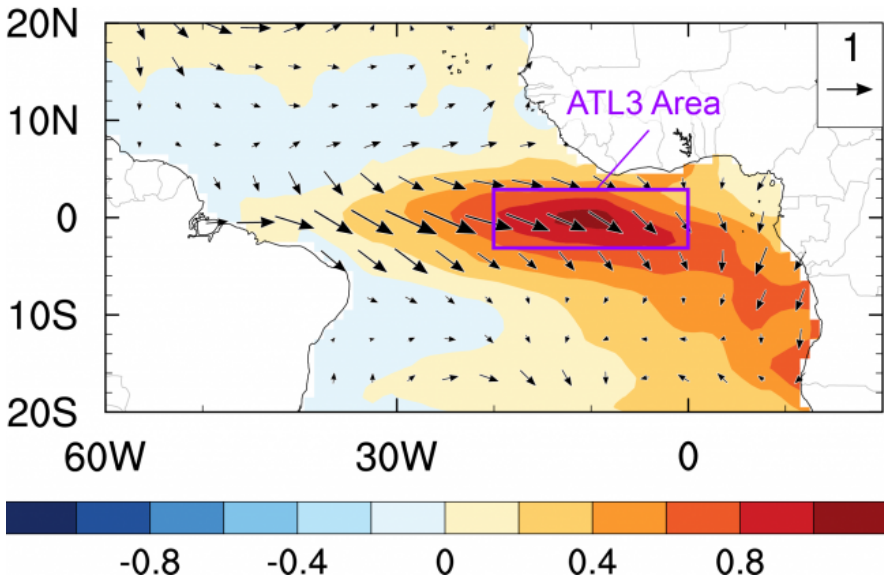

Figure 2.15: A composite Atlantic Niño event (i.e. an average over several Atlantic Niño years, namely 1988, 1991, 1995, 1996, 1999, 2008) based on Optimally Interpolated SST (OISST) and ERA-Interim reanalysis. The figure shows SST anomalies and surface wind anomalies averaged over the months May–July (MJJ). The temperature anomalies are ^oC, and the surface wind anomalies in ms^{-1}. The Atlantic Niño 3 (ATL3) region is shown by the purple box. Plot adapted from $http://www.jamstec.go.jp/$.

In the equatorial Atlantic ocean, the main mode of interannual variability results from ENSO-like ocean-atmosphere interaction (Zebiak, 1993; Keenlyside and Latif, 2007; Xie and Carton, 2013; Ding *et al.*, 2010), and is termed the "Atlantic zonal mode" or "Atlantic Niño". Nonetheless, in the Atlantic ocean, the variability has a different seasonality, and anomalous events in SST often reach their mature phase during boreal summer (Keenlyside and Latif, 2007). Figure 2.15 shows a composite of observed SST and surface wind anomalies constructed based on Atlantic Niño years and averaged over the months May–July (MJJ). The two salient features are that the SSTs in the eastern equatorial Atlantic ocean become anomalously warm and the westerly wind anomalies cover most of the equatorial region. The average total winds in the equatorial Atlantic

blow from east to west, so a westerly anomaly means a weakening of the prevailing easterly winds.

Interannual SST variations in the eastern tropical Atlantic ocean are known to be related with a dipole response in WAM rainfall; warm SSTs tend to enhance (reduce) rainfall over the Guinea Coast (Sahel) and vice versa during cold SSTs (e.g., Losada *et al.*, 2010; Diatta and Fink, 2014). The Sahel rainfall reduction during anomalously warm eastern Atlantic SST is attributed to a decreased meridional surface temperature gradient and weakened surface confluence over the Sahel. Additionally, the tropical Atlantic ocean seems to influence the Tropical Pacific variability through an atmospheric bridge (e.g., Keenlyside and Latif, 2007; Rodríguez-Fonseca *et al.*, 2009). Recent studies have also shown a significant simultaneous association between the Kiremt Rains and the Atlantic Niño after the 1970' (Segele *et al.*, 2015; Bahaga *et al.*, 2019).

2.5 Interannual to Decadal Rainfall Variability in the GHA

Interannual to decadal rainfall fluctuations threaten the livelihood of millions and this has become an inescapable feature of the underprivileged national economies of the GHA. In the current and previous decades, this part of the world experienced a series of severe droughts as for example in 2010/11, 2015, and 2016/2017 (FEWS-NET, 2011, 2015; Lyon and DeWitt, 2012; FEWS-NET and WFP, 2016). These extreme events and rainfall variability in GHA are dominated by changes on the large-scale, with a clear link to tropical ocean-atmosphere variability. Given the uncertainty of climate projections in the region, the inevitability of drought and associated socio-economic distress, understanding the mechanisms that produce this variability and developing both dynamical and statistical approaches for extended-range forecasts and climate information is urgently needed. In this section, the literature relevant to interannual to decadal teleconnections associated with three major rainy seasons in GHA is reviewed.

2.5.1 The Short Rains

The GHA region experiences an extreme interannual variability during Short Rains season (Hastenrath *et al.*, 1993; Black *et al.*, 2003; Clark *et al.*, 2003; Nicholson, 2015). Several studies have investigated the relationship between the Short Rains and the ENSO (Ropelewski and Halpert, 1987; Ogallo, 1988; Hastenrath *et al.*, 1993; Mutai *et al.*, 1998; Nicholson, 2017). These statistical studies find a strong connection between ENSO and East African rainfall. Contrarily, atmospheric general circulation models suggest that the Indian ocean SSTs exert a greater influence on the East African short rains than the Pacific SSTs (Goddard and Graham, 1999; Latif *et al.*, 1999). This has resulted in considerable controversy concerning the primary driver of the Short Rains interannual variability. Consequently, other studies tried to compare the fractional influence of IOD and ENSO on Short Rains (Saji *et al.*, 1999; Clark *et al.*, 2003) and suggested that IOD is a major contributor to the variability of the Short Rains. In view of these finding, the focus has been shifted to the IO for understanding the variability of the Short Rains (Black *et al.*, 2003; Yamagata *et al.*, 2004; Behera *et al.*, 2005; Ummenhofer *et al.*, 2009; Bahaga *et al.*, 2015; Nicholson, 2015; Endris *et al.*, 2016). The conclusion is that rainfall over East Africa (Indonesia) is increased (decreased) during a positive IOD event and reverse ocean-atmosphere condition happen in negative IOD events. The physical mechanism for the IOD influence on Short Rains is explained by a Gill-type response (Gill, 1980) to the western warm pool of the IO and the modulation of the IO Walker circulation (Webster *et al.*, 1999; Latif *et al.*, 1999; Bahaga *et al.*, 2015).

Another aspect of the Short Rains' interannual variability is its coupling to a zonal vertical circulation cell in the central equatorial Indian ocean (Hastenrath *et al.*, 1993, 2011; Pohl and Camberlin, 2011; Nicholson, 2015, 2017). This is frequently referred to as a Walker cell or a Walker-type circulation (Fig. 2.16). Under normal climatic state at low levels, westerly winds prevail, a result of a steep eastward pressure gradient. At 200 hPa easterly flow prevails. Rising motion in the east and subsidence in the west, near eastern Africa, complete the cell. However, during a positive IOD, warm SSTs in the west and cold SSTs in the east are associated with a weakened Walker circulation over the Indian ocean, while the reverse SST pattern of the IOD's negative phase acts to enhance the Walker circulation over the Indian ocean.

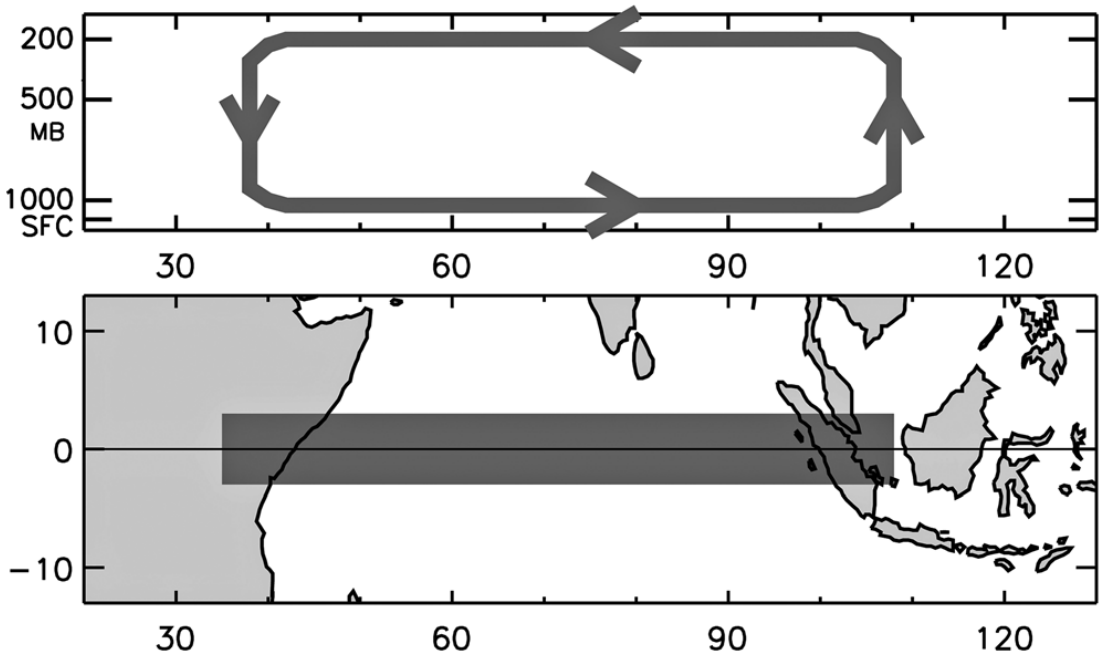

Figure 2.16: Schematic of the zonal circulation cell over the Indian ocean during OND. The shaded box in the bottom diagram shows the approximate geographical location of this cell (after Nicholson, 2017).

While there are substantial pieces of evidence of Short Rains' interannual variability, only a handful of studies examined modes of decadal signal and associated drivers (Clark *et al.*, 2003; Omondi *et al.*, 2012; Bahaga *et al.*, 2015). Especially, few studies exist on non-stationarity and multidecadal changes of teleconnections (Nakamura *et al.*, 2009; Manatsa and Behera, 2013; Nicholson, 2015, 2017; Bahaga *et al.*, 2019). The most comprehensive study of the multidecadal changes of teleconnections is that of Bahaga *et al.* (2019). They demonstrate that the western Indian ocean is a major driver of interannual variability, while the low-frequency variability in eastern Indian and the Pacific ocean are highly associated with Short Rains' decadal variability.

2.5.2 The Kiremt Rains

Focusing on the Ethiopian Kiremt Rains, some studies identified large-scale forcings important for seasonal prediction (Camberlin, 1997; Gissila *et al.*, 2004; Korecha and Barnston, 2007; Diro *et al.*, 2008; Segele *et al.*, 2009a; Diro *et al.*, 2011a,b; Nicholson, 2014; Degefu *et al.*, 2016). These studies have shown a significant simultaneous association between the summer

rainfall over the Ethiopian Highlands and ENSO indices. El Niño (La Niña) episodes were shown to be associated with less (more) summer rainfall across much of the country. Other studies found an association between Ethiopian JJAS rainfall and SST anomalies over the southern Atlantic ocean (AO), Gulf of Guinea, and IO (Segele *et al.*, 2009b; Diro *et al.*, 2011a; Williams *et al.*, 2012) also suggesting that the transport of moist air from the Congo Basin plays a role in the interannual variability of boreal summer rainfall in GHA. Although southern AO, Gulf of Guinea, and Congo air masses have long been assumed to be a source of moisture for summer rainfall over the Ethiopian Highlands, the role of the south AO on the interannual variability is still disputed. Segele *et al.* (2009b) and Segele *et al.* (2015) suggest that the south AO has an influence on the interannual variability of Kiremt Rains. In addition, Lyon (2014) discusses the climate characteristics of the Ethiopian severe drought of 1982–84 during the JJA season and point to a role of AO forcing. On the other hand, there have only been a few studies conducted on decadal summer rainfall variability and its relationship to global SSTs. Jury (2010) found a modest association between areas of summer rainfall over Ethiopia and SST variability associated with the Atlantic Atlantic Multidecadal Oscillation (AMO), while rainfall variability over the bimodal southern and eastern zone of the Ethiopian Highlands are associated with the cool phase of the PDO.

2.5.3 The Long Rains

Unlike the short rains, understanding interannual variability and predictability of the Long Rains has been a challenge for researchers and forecasters, since no strong oceanic or atmospheric forcing has been identified (Hastenrath *et al.*, 1993; Camberlin and Philippon, 2002; Liebmann *et al.*, 2014; Nicholson, 2017). Moreover, the variability of MAM rainfall reflects the net influence of factors operative on intraseasonal, interannual, decadal, and multidecadal timescales (e.g., Pohl and Camberlin, 2011; Omondi *et al.*, 2013; Lyon *et al.*, 2014; Nicholson, 2017; Vigaud *et al.*, 2017; Ummenhofer *et al.*, 2018). Motivated by increased frequency of drought in the last decade, some studies emphasized the recent downward trend of the Long Rains over parts of GHA (Funk *et al.*, 2008; Williams and Funk, 2011). Lyon and DeWitt (2012) further examined these persistent droughts and suggested that the decline started abruptly around 1999. They also demonstrate that the

decline is part of a large-scale precipitation anomaly pattern that extends across the Indian and Pacific oceans.

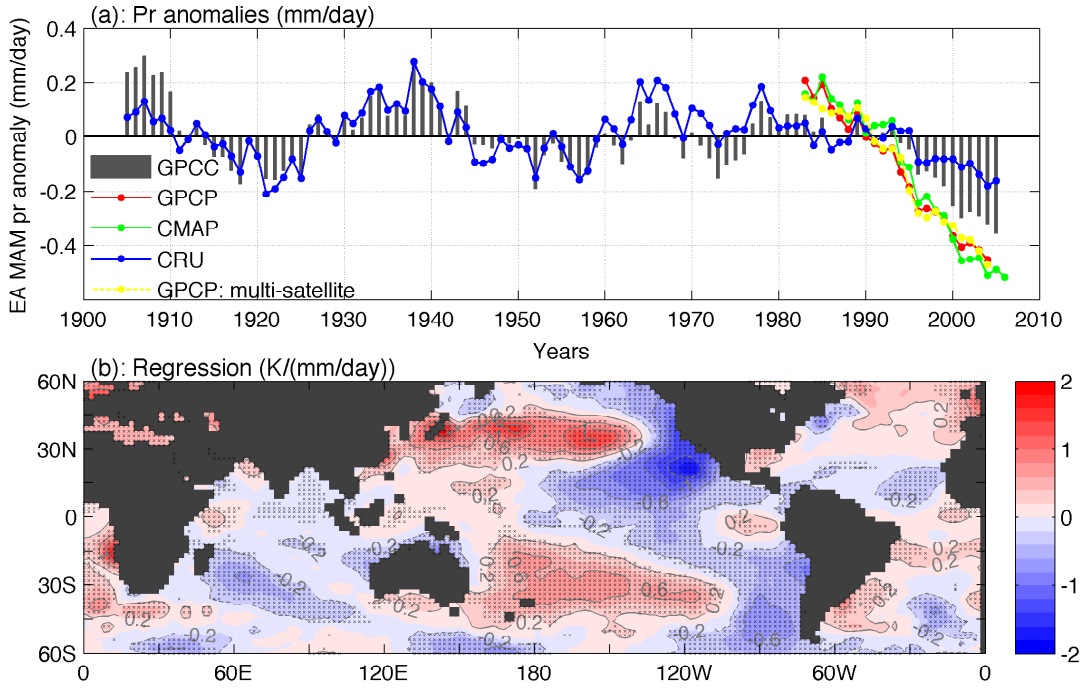

Figure 2.17: (a): GHA(30^o–52^oE, 10^oS–12^oN) MAM precipitation rate anomaly relative to the 1979–2000 base period in observations. Nine-year running average has been applied to all the time series. (b): Regression of SST anomaly on the negative of GHA precipitation rate anomaly (i.e. b as in $sst_a = -b \times pr_a$) in MAM over the period of 1901–2009. (after Yang *et al.*, 2014)

Figure 2.13a shows the nine-year-running-averaged anomalies (relative to the 1979-2000 base) of the GHA Long Rains in four observational datasets: GPCC, GPCP, CMAP and CRU. The four datasets are consistent in showing drying over the most recent decades when all have data. The longer GPCC and CRU datasets suggest that the drying trend in the most recent decades is part of the decadal variability of climate over East Africa. Further studies provide evidence that the decline in GHA Long Rains is associated with a shift of warmer SSTs over the western tropical Pacific and cooler SSTs over the central and eastern tropical Pacific (Lyon and DeWitt, 2012; Lyon, 2014; Lyon *et al.*, 2014; Yang *et al.*, 2014; Vigaud *et al.*, 2017; Ummenhofer *et al.*, 2018) and the PO multidecadal variability (Fig. 2.13b; Lyon, 2014; Yang *et al.*, 2014; Bahaga *et al.*, 2019). Similarly, Vigaud *et al.* (2017) suggest that a more frequent dry regime in May since 1998/99, associated with an earlier onset of the summer monsoon and SLLJ, could account for a recent abrupt shift observed in GHA Long Rains. In contrast, other studies

link the drying trend to anthropogenic and aerosol forced Indo-Pacific ocean warming, resulting in the westward extension of the Indo-Pacific warm pool, causing a westward shift of the Walker circulation and a subsidence anomaly and drying over East Africa (Williams and Funk, 2011; Liebmann *et al.*, 2014; Funk *et al.*, 2014; Funk and Hoell, 2015; Hoell *et al.*, 2017). Alternatively, Hoell *et al.* (2017) suggest that human-induced changes in tropical SST exacerbated the effect of natural Pacific decadal variability, enhancing GHA drying during the Long Rain season. Additional modeling studies examined several hypotheses related to the decline of the Long Rains and concluded that anthropogenic aerosol emissions played a role (Rowell *et al.*, 2015; Tierney *et al.*, 2015).

Despite the above-referenced numerous studies on teleconnections between the GHA seasonal rains and remote climate anomalies, apparent disagreements amongst them regarding attribution arise from consideration of different seasons, datasets, and varying analysis periods due to non-stationarity of climate drivers (Nicholson, 2015, 2017; Bahaga *et al.*, 2019). Especially, few studies exist on non-stationarity and multidecadal changes of teleconnections. These studies only deal with changes of Short Rains teleconnections over time (Camberlin and Philippon, 2001; Clark *et al.*, 2003; Manatsa *et al.*, 2012; Manatsa and Behera, 2013; Nakamura *et al.*, 2009; Nicholson, 2015, 2017). Camberlin and Philippon (2001) also suggested that the change in large-scale circulation anomalies, background climate, and duration of the period under which regional convection forced by remote signals as the possible explanation for non-stationary teleconnections. Furthermore, there is, to the best of our knowledge, no study that assigns the GHA seasonal teleconnections to interannual or/and decadal timescales. Several such studies exists for the WAM (Diatta and Fink, 2014; Suárez-Moreno *et al.*, 2018). To fill these gaps, Chapter 4 of this thesis provides a comprehensive statistical analysis considering the three major rainy seasons at the GHA. While Chapter 5 extends the results of an assessment of ICON simulation in representing the Atmospheric processes that control the Ethiopian Kiremt Rains' mean state, modes of the interannual variability, and the underline physical mechanisms.

2.6 Decadal Climate Variability and Prediction

Several studies have demonstrated evidence of strong decadal pattern of climate variability (e.g., Trenberth and Hurrell, 1994; Deser *et al.*, 2004; Meehl *et al.*, 2009c). Other studies suggest, in addition to interannual ENSO fluctuations, the Indo-Pacific exhibits decadal and multi-decadal climate variability (Mantua *et al.*, 1997; Zhang *et al.*, 1997). The leading of monthly SST anomalies over the North Pacific (after removing the global mean SST anomaly) and its associated PC time series are termed the Pacific PDO after Mantua *et al.* (1997). The PDO has also been termed the Interdecadal Pacific Oscillation (Power *et al.*, 1999b) in recognition of its extension to the South Pacific. Likewise, SSTs in the North Atlantic undergo slow variations with a period on the order of 65–80 years (Kushnir, 1994; Enfield *et al.*, 2001). This phenomenon has been termed the AMO (Enfield *et al.*, 2001). For more details on the quantitative description of PDO, IPO, and AMO (see Chapter 3).

Although the primary drivers remain unclear (e.g., Keenlyside *et al.*, 2015), as one of the most important climate modes, the AMO has been widely linked to prominent regional climate anomalies that can have tremendous socioeconomic consequences. The AMO can modulate Atlantic hurricane activity (Goldenberg *et al.*, 2001), disrupt the North American and European summer climate (Sutton and Hodson, 2005), and change rainfall over the United States (Enfield *et al.*, 2001), the Sahel (Folland *et al.*, 1986; Zhang and Delworth, 2006), Brazil (Knight *et al.*, 2006), and the Ethiopian Highlands (Jury, 2010). Similarly, the linkages between the PDO and interdecadal variations in rainfall have been found in many parts of the globe, including southwestern United States and Indian monsoon (Meehl and Hu, 2006), the Sahel (Mohino *et al.*, 2011), Australia (Power *et al.*, 1999a), and the GHA (Yang *et al.*, 2014; Bahaga *et al.*, 2019). Climate conditions in these regions show contrasting patterns during warm and cold phases of the IPO. For example, Bahaga *et al.* (2019) showed that during the warm phases of PDO, the GHA received above normal precipitation, while cold phases PDO coincide with below normal rainfall.

In recent years, there have been signs of progress in the field of decadal climate prediction (Smith *et al.*, 2007; Keenlyside *et al.*, 2008; Pohlmann

et al., 2009; Taylor and Stouffer, 2012). The primary goal of decadal climate predictions are to produce a skillful and reliable forecast of the actual evolution of both externally forced and internally generated variations of the climate system. The decadal climate predictions are based on coupled ocean-atmosphere models run for 10 years forced by the observed and projected changes in the external forcing and initialized from an observed state at the beginning of the simulation (Taylor and Stouffer, 2012). Such predictions have been shown to have skill over a period of several years (Smith *et al.*, 2007; Meehl *et al.*, 2009a, 2014).

In the context of international and national efforts, the German MiKlip project, funded by the Federal Ministry of Education and Research in Germany (BMBF), has developed model systems to produce a skillful decadal climate prediction (Pohlmann *et al.*, 2009; Marotzke *et al.*, 2016). In Chapter 6 the skill of different versions of the MiKlip decadal climate prediction system are assessed over Africa, and the climate drivers (e.g., ENSO, IPO, AMO, and IOD) providing interannual and decadal skill are also analyzed. For more details on the MiKlip experiments and initialization see Chapter 3.

Chapter 3

Datasets, Models, and Methods

This Chapter briefly describes the various datasets used in this thesis, observed precipitation and SST from different sources; ERA-Interim and ERA-20C from ECMWF, ICON-AMIP type simulations, and MIKLIP decadal ensemble forecast systems. In addition, the statistical and analysis methods employed are concisely summarized.

3.1 Observed Datasets

3.1.1 Precipitation

In order to select a good quality precipitation dataset with a long and recent record that represents rainfall characteristics over the GHA seven widely used rain gauge-based, satellite-based, and gauge-satellite merged precipitation estimates are evaluated. These products are compared in terms of seasonal cycle, spatial and temporal variability. However, only three best precipitation datasets are selected and used in this thesis, and briefly described hereafter.

To assess the long-term rainfall fluctuations over GHA, we use:

- Version 7 of Global Precipitation Climatology Center (GPCC) gridded monthly precipitation (Schneider *et al.*, 2014), this is a gauge-based, global, land-surface dataset at 0.5^o x 0.5^o latitude/longitude spatial grids and monthly temporal resolution for the period 1901–2013.

- The recently released Centennial Trends Greater Horn of Africa precipitation archive (CenTrends), which is developed by scientists at U.S. Geological Survey (USGS) and Florida State University (FSU), and offers seasonal rainfall products on high-resolution a 0.1^o x 0.1^o latitude/longitude grid covering 15^oS–18^o N; 28^o–54^o E from 1900 to 2014 (Funk *et al.*, 2015b).

- In addition, satellite and satellite-gage derived precipitation estimates are compared with respect to their spatial and temporal scale representation over GHA in recent periods (not shown). Climate Hazards group InfraRed Precipitation with a Station dataset version 2 (CHIRPS2) was selected for further analysis. This dataset is a quasi-global (50^oS–50^oN) daily, pentad, and monthly precipitation product from a combination of in-situ station observations and satellite precipitation estimates based on Cold Cloud Duration (CCD) observations to represent sparsely gauged regions. CHIRPS2 was developed by the Climate Hazards Group (CHG) at the University of California at Santa Barbara (UCSB) in collaboration with the U.S. Geological Survey (USGS) Earth Resources Observation and Science (EROS) center (Funk *et al.*, 2015a).The high-resolution dataset on a 0.05^o X 0.05^o latitude/longitude grid, version 2.0, and monthly rainfall information for the 1981–2017 period was downloaded from ftp://ftp.chg.ucsb.edu/.

The GPCC and CentTrends selected for further analysis based on substantially better observational coverage, having a long period record for the whole 20^{th} century, and relatively better representation of interannual variability of seasonal rainfall over GHA. Our analysis also shows that CHIRPS2 has a high correlation of greater than 0.8 with GPCC over East Africa and the Ethiopian Highlands. Therefore, CHIRPS2 has been selected to compare precipitation datasets in representing the GHA rainfall climatology in recent times, to evaluate the performance of the Deutscher Wetterdienst numerical weather prediction Icosahedral Nonhydrostatic (ICON) simulation, and to provide a description of Ethiopian summer rainfall variability.

3.1.2 Rainfall indices in the Greater Horn of Africa

In order to re-assess the interannual to decadal changes in the association between seasonal rainfall over GHA and indices of remote ocean-atmosphere

variability we have used observed precipitation and SST datasets. To investigate long-term rainfall fluctuations in the investigation period we have used GPCC. To validate GPCC and to show GHA rainfall climatology in recent times, gridded monthly rainfall estimates from CHIRPS2 were also utilised. In addition, the GPCC dataset was compared with CenTrends. The GPCC and CenTrends datasets were used to construct area-average Standardized Precipitation Index (SPI; McKee *et al.*, 1993) time series for the three major rainy seasons over GHA. The result, discussion and conclusions are given in Chapter 4.

The Standardized Precipitation Index (SPI) is used to drought detection and monitor short-term water supplies (e.g., meteorological, soil moisture) and long-term water resources (e.g., groundwater supplies, stream-flow and lake and reservoir levels). Moreover, the SPI is spatially consistent (invariant) and its probabilistic interpretation makes it useful to be used in risk and decision making analyses. McKee *et al.* (1993) have given mathematical derivation and physical interpretation of SPI and reviewed here in brief. Computation of the SPI involves fitting a gamma probability density function to a given frequency distribution of precipitation totals for a station or areal averaged index. The gamma distribution is defined by its frequency or probability density function:

$$g(x) = \frac{1}{\beta^{\alpha}\Gamma(\alpha)} x^{\alpha-1} e^{\frac{-x}{\beta}} \qquad for \quad x > 0 \tag{3.1}$$

where: $\alpha > 0$, α is a shape parameter; $\beta > 0$, β is a scale parameter; $x > 0$, x is the precipitation amount; and $\Gamma(\alpha) = \int_0^{\infty} y^{\alpha-1} e^{-y} dy$, $\Gamma(\alpha)$ is the gamma function.

The alpha and beta parameters of the gamma probability density function are estimated for each station, for each time scale of interest (β= 3, 6, 9, 12, 48 months) and for each month of the year. From Thom (1966); the maximum likelihood solutions are used to optimally estimate α and β:

$\hat{\alpha} = \frac{1}{4A}\left(1 + \sqrt{1 + \frac{4A}{3}}\right)$, $\hat{\beta} = \frac{\bar{x}}{\hat{\alpha}}$ where: $A = \ln(\bar{x}) - \frac{\sum \ln(x)}{n}$ and n=number of precipitation observations.

The resulting parameters are then used to find the cumulative probability of an observed precipitation event for the given month and time scale

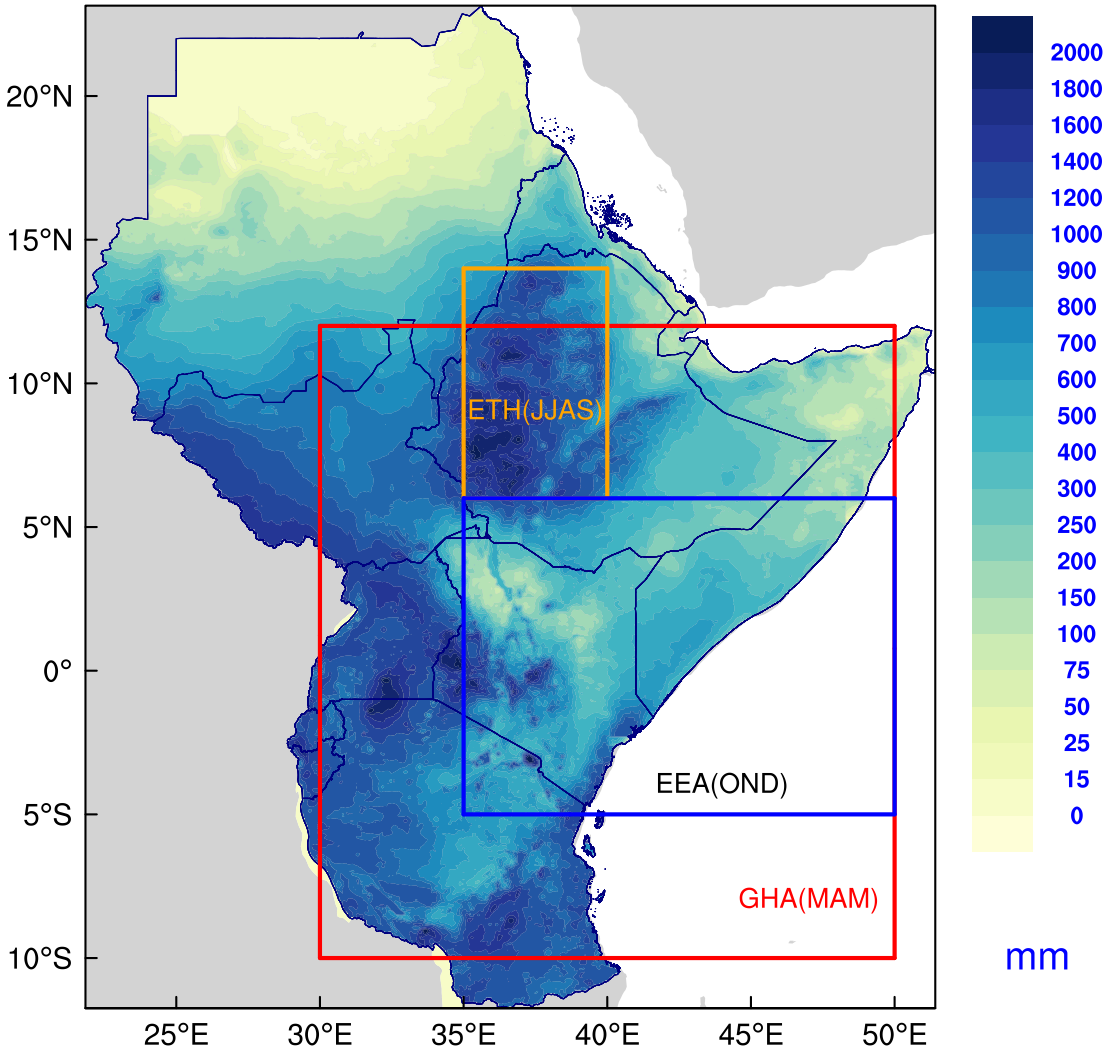

Figure 3.1: Annual mean precipitation from 1981 to 2013 in mm, derived from Climate Hazard Infra-Red Precipitation with station version 2 (CHIRPS2). The boxes represent regions for which seasonal standardized precipitation indices are created: MAM precipitation over GHA (red), OND precipitation over equatorial East Africa (blue), and JJAS precipitation over the Ethiopian Highlands (orange). From Bahaga *et al.* (2019). © 2019 Bahaga et al. International Journal of Climatology published by John Wiley & Sons Ltd on behalf of the Royal Meteorological Society.

for the station in question. The cumulative probability is given by:

$$G(x) = \int_0^x g(x)dx = \frac{1}{\hat{\beta}^{\hat{\alpha}}\Gamma(\hat{\alpha})} \int_0^x x^{\hat{\alpha}-1} e^{\frac{-x}{\hat{\beta}}} dx \tag{3.2}$$

Letting $t = \frac{-x}{\hat{\beta}}$, his equation becomes the incomplete gamma function:

$$G(x) = \frac{1}{\Gamma(\hat{\alpha})} \int_0^x t^{\hat{\alpha}-1} e^{-t} dt \tag{3.3}$$

Since the gamma function is undefined for $x = 0$ and a precipitation distribution may contain zeros, the cumulative probability becomes: $H(x) = q + (1 - q)G(x)$ where q is the probability of a zero. If m is the number of zeros in a precipitation time series, Thom (1966) states that q can be estimated by $\frac{m}{n}$. Then the cumulative probability ($H(x)$) is transformed to the standard normal random variable Z with mean zero and variance of one, which is the value of the SPI .

$$Z = SPI = -\left(t - \frac{c_0 + c_1 t + c_2 t^2}{1 + d_1 t + d_2 t^2 + d_3 t^3}\right) \qquad for \quad 0 < H(x) \leq 0.5 \qquad (3.4)$$

$$Z = SPI = +\left(t - \frac{c_0 + c_1 t + c_2 t^2}{1 + d_1 t + d_2 t^2 + d_3 t^3}\right) \qquad for \quad 0.5 < H(x) < 1.0 \qquad (3.5)$$

where: $t = \sqrt{\ln\left(\frac{1}{(H(x))^2}\right)} \qquad for \quad 0 < H(x) \leq 0.5$

$t = \sqrt{\ln\left(\frac{1}{(1.0-H(x))^2}\right)} \qquad for \quad 0.5 < H(x) < 1.0$

$c_0 = 2.515517, \qquad c_1 = 0.802853, \qquad c_2 = 0.010328$

$d_1 = 1.432788, \qquad d_2 = 0.189269, \qquad d_3 = 0.001308$

In this thesis, SPI employed over the GHA region, which comprises of eleven countries: Kenya, Ethiopia, Eritrea, Somalia, Djibouti, Uganda, Tanzania, Rwanda, South Sudan, Sudan, and Burundi and includes areas with bimodal and unimodal rainfall distributions. The GHA region is divided into three subregions based on seasonal rainfall climatologies (Fig. 3.1). Our analysis particularly focuses on three well-defined rainfall regimes in the respective sub-regions, which cover most parts of GHA and are named as follows: the EEA-SR-SPI is represented by the area-averaged OND rainfall over the land grid boxes of the region 5^oS–6^oN, 35^o–50^oE (blue box in Fig. 3.1). EEA covers most of Kenya, the southern parts of Ethiopia and Somalia, and northern Tanzania. It is characterized by a bimodal rainfall distribution with the major rainfall season in MAM. ETH-KR-SPI is defined by the area-averaged JJAS rainfall over the land grid boxes of the region 6^o–14^oN, 35^o–40^oE (orange box in Fig. 3.1). ETH covers most of the northern Ethiopian Highlands and some parts of Sudan. It has a rainfall maximum during boreal summer and a pronounced dry season in boreal winter. The GHA-LR-SPI is designated by the area-averaged MAM rainfall over the land

grid boxes of the region 10^{o}S–12^{o}N, 30^o–50^{o}E (red box in Fig. 3.1). Thus, throughout the paper the terms Long Rains, Short Rains, and Kiremt Rains will correspond to specific locations within the study domain (i.e., the red, blue and orange boxes; Fig. 3.1). We have verified that the results presented in Chapter 4 are robust with respect to small variations in size and position of these regions. The SPI indices were computed for the entire investigation period.

3.1.3 Sea surface temperature (SST)

Gridded monthly SST datasets were obtained from the Extended Reconstructed SST version 4 (ERSSTv4) of the National Oceanic and Atmospheric Administration (NOAA) National Climate Data Center (NCDC) (Huang *et al.*, 2015). The ERSSTv4 dataset has a spatial resolution of 2^o x 2^o and covers the period from 1854 to the present. This dataset can be accessed at http://www1.ncdc.noaa.gov/pub/data/cmb/ersst/v4/netcdf/. For comparison we have also used the Hadley Centre Sea Ice and Sea Surface Temperature (HadISST) dataset (Rayner *et al.*, 2003). This dataset consists of gridded monthly average SST with a resolution of 1^o x 1^o. HadISST temperatures are reconstructed using an optimal interpolation procedure in addition to gridded observations. The HadISST dataset, and further information about it, can be found at http://www.metoffice.gov.uk/hadobs/hadisst/.

3.1.3.1 SST-based indices of remote climate states

In Chapter 4 of this thesis, various previously identified SST-based climate teleconnection indices were utilized to explore their impacts on interannual to decadal seasonal rainfall fluctuations over GHA. In addition, these indices were also used to investigate and understand the multidecadal changes in the teleconnections. Observed SST datasets described above are implemented to construct the indices. SST-based indices fall into the geographical sectors shown in Fig. 3.2. A brief summary of how indices of remote climate anomalies are defined, created, and relevant previous works suggesting climate indices-rainfall relationships is given in Table 3.1. Unless otherwise noted, all indices were computed for the entire investigation period 1901–

2013 and the 1950–1979 climatological base was used for computing anomalies. More details on the indices and their definitions, the readers are referred to the relevant literature cited in the Table 3.1.

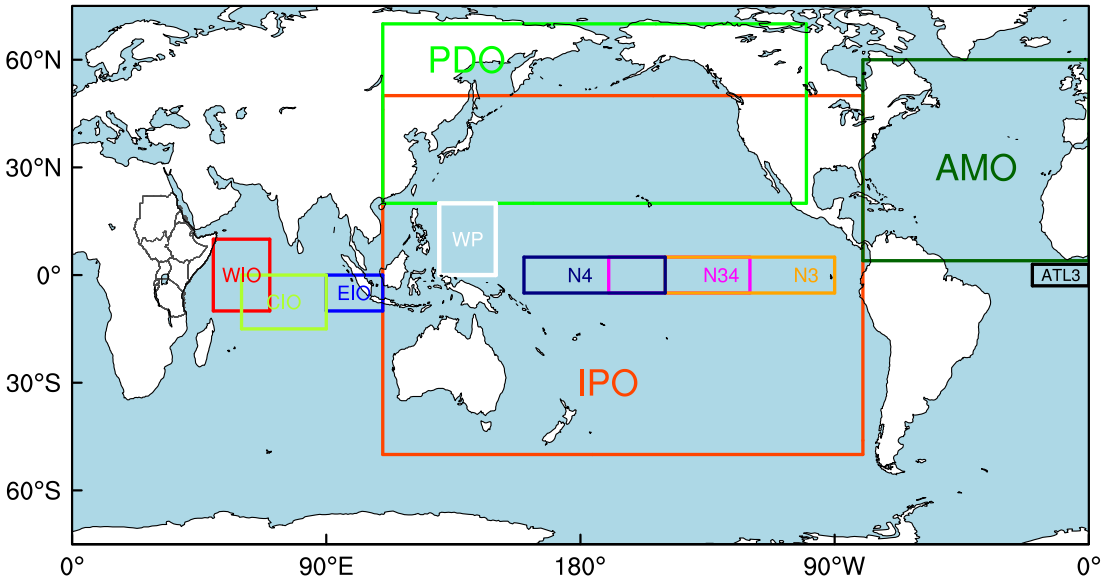

Figure 3.2: Locations of remote climate anomalies used in this study as predictors for GHA seasonal mean rainfall. The indices and corresponding geographical areas are detailed in Table 3.1. From Bahaga *et al.* (2019). © 2019 Bahaga et al. International Journal of Climatology published by John Wiley & Sons Ltd on behalf of the Royal Meteorological Society.

3.1.3.2 Further description of climate indices

There are several indices used to monitor the tropical and subtropical oceans, all of which are based on SST anomalies computed across a given region. N34 region is used to characterize the state of ENSO. In an ENSO warm event (i.e., El Niño), the index is positive, whereas it is negative during ENSO cold events (i.e., La Niña). We adopted the definition of ENSO from Trenberth (1997) to compute the N34 index. The Standardized N34 anomaly index used here was then created with respect to the 1950-1979 mean. Other ENSO measures used in this study are the El Niño 3 (N3) index created in a similar way.

PDO is the leading EOF of monthly SST anomalies in the North Pacific Ocean. To create the PDO index, monthly mean SST anomalies are detrended before computation of the EOF analysis to separate the pattern of variability from any global warming signal that may be present in the data; more details can be found in Zhang *et al.* (1997). The PDO spatial

Table 3.1: Definition of climate indices used in this study and the corresponding relevant works suggesting potential relationships between climate indices and GHA seasonal rainfall.

Index	Reference	Definition	Impact on GHA rainfall
PDO	Mantua *et al.* (1997)	Pacific Decadal Oscillation created as leading Empirical Orthogonal Function (EOF) mode of monthly SST anomalies after removing global mean SSTs anomalies; EOF is computed over 20^o–65^oN and 120^o E–100^oW.	Long Rains (e.g., Lyon, 2014), Short Rains (e.g., Omondi *et al.*, 2012), and Kiremt Rains (e.g., Jury, 2010)
IPO	Deser *et al.* (2004)	Interdecadal Pacific Oscillation created as the second EOF mode of monthly SST anomalies after removing global mean SSTs; EOF is computed over 50^oS–50^oN and 120^oE–100^oW.	Short Rains (e.g., Omondi *et al.*, 2012; Bahaga *et al.*, 2015)
CIO	Funk *et al.* (2014)	Central IO as standardized SST anomalies averaged over 0^o–15^oS, 60^o–90^oE.	Long Rains (e.g., Funk *et al.*, 2014)
WPG	Funk *et al.* (2014)	Western Pacific Gradient as a gradient between standardized SST anomalies in the El Niño 4 region (**N4**; 5^oS–5^oN, 160^oE–150^o) and the western Pacific (**WP**; 0^o–20^oN , 130^o–15^oE).	Long Rains (e.g., Funk *et al.*, 2014)
ATL3	Diatta and Fink (2014)	Tropical Atlantic Niño3 as standardized SST anomalies averaged over 0^o–20^oW, 3^o S–3^oN.	Kiremt Rains (e.g., Diro *et al.*, 2011a)
DMI	Saji *et al.* (1999)	Dipole Mode Index as difference between standardized SST anomalies over the western Indian Ocean (**WIO**; 10^oS–10^oN, 50^o–70^oE) and eastern IO (**EIO**; 10^o–0^oS, 90^o–110^oE).	Short Rains (e.g., Behera *et al.*, 2005; Bahaga *et al.*, 2015).
N34	Trenberth (1997)	El Niño 3.4 (N34) as standardized SST anomalies averaged over 5^oS–5^oN ; 170^o–120^oW.	Short Rains (Ropelewski and Halpert, 1987) and Kiremt Rains (e.g., Korecha and Barnston, 2007)
N3	Trenberth (1997)	El Niño 3 as standardized SST anomalies averaged in region bounded by 5^oS–5^oN, 150^o–90^oW.	Short Rains and Kiremt Rains (e.g., Jury *et al.*, 2002)
AMO	Enfield *et al.* (2001)	Atlantic Multidecadal Oscillation as standardized SST anomalies for the North Atlantic region 0–60^oN, 0–80^oW after removing global mean SST anomalies.	Kiremt Rains (e.g., Jury, 2010)

pattern, obtained by regressing global SST anomalies onto the normalized leading principal component time series, has a typical horseshoe shape connecting tropical and extratropical anomalies. In its "warm phase," the PDO is characterized by cold SST anomalies in the western North Pacific encircled by warm SST anomalies in the eastern part of the basin extending to the central and eastern tropical regions (Deser *et al.*, 2012; Farneti, 2017). The cold phase is characterized by opposite anomalies with negative equatorial SST anomalies. The IPO index is computed in a similar way (Table 3.1). The first leading EOF mode represents interannual variability most likely related to ENSO pattern and the second EOF mode depicts the IPO. When SSTs in the entire Pacific basin are considered, the emerging IPO pattern is roughly symmetric across the equator (Power *et al.*, 1999b). The PDO and IPO essentially have the same interdecadal variability (Deser *et al.*, 2004), with the PDO traditionally defined within the North Pacific, while the IPO covers the whole Pacific basin.

The Indian Ocean Dipole (IOD) is a coupled ocean-atmosphere phenomenon in the Indian Ocean. Anomalous cooling of SSTs in the southeastern equatorial Indian Ocean and anomalous SST warming in the western equatorial Indian Ocean characterize a warm or positive IOD phase. During the warm phase, the climatological equatorial surface westerlies blowing towards the Maritime Continent are weakened or reversed. The intensity of the IOD is represented by an anomalous SST gradient between the western equatorial Indian Ocean (WIO) and the south eastern equatorial Indian Ocean (EIO); this gradient is named Dipole Mode Index (DMI); Table 3.1).

Atlantic Multi-decadal Oscillation (AMO) is a basin-scale mode of multidecadal climate variability with alternating warm and cool phases over large parts of the North Atlantic Ocean, where the AMO signal is most pronounced (Enfield *et al.*, 2001). The HadISST and ERSSTv4 datasets were also used to calculate other indices, which are standardized SST anomalies in the respective regions (Table 3.1). Unless otherwise noted, all indices were computed for the entire investigation period 1901–2013 and the 1950–1979 climatological base was used for computing anomalies. For more details of the indices, the readers are referred to the relevant literature cited in Table 3.1.

3.1.4 Reanalysis

To estimate the performance of ICON simulation in reproducing the mean climate systems and observed circulation changes associated to ENSO induced Ethiopian summer rainfall anomalies, the European Centre for ECMWF Interim Re-Analysis (ERAI) (Dee *et al.*, 2011) was used, which extends from 1 January 1979 to present date. The ERAI configuration has a spectral T255 horizontal resolution 0.75^o x 0.75^o latitude/longitude grids with 37 vertical levels from 1000 to 1 hPa. The data assimilation system is based on a 2006 release of the Integrated Forecasting System (IFS) and the system includes a 4D-Var analysis with a 12 h analysis window [http://www.ecmwf.int/en/research/climate-reanalysis/era-interim]. In Chapter 5 of this thesis, we use monthly averaged horizontal and vertical wind, mean sea level pressure, and geopotential height to evaluate the performance of ICON for the period of 1981–2017.

In addition, we use the latest European Centre for Medium-Range Weather Forecasts (ECMWF) 20^{th} Century Reanalysis product (ERA-20C; Poli *et al.*,

2016). Monthly averaged fields at 1^o x 1^o latitude/longitude grids horizontal resolution were considered. The analysis spans 111 years, from January 1900 to December 2010. This product is used in Chapter 4 of this thesis as an input for our composite analysis to understand the mechanism for multidecadal changes in the interannual teleconnections.

3.2 ICON Model Description

In this thesis the ICON model is used to understand the large-scale influences and the underpinning physical mechanism of summer rainfall variability over the Ethiopian Highlands. ICON (Zängl *et al.*, 2015) is a seamless modeling system for Numerical Weather Prediction (NWP) and climate studies that allows for an explicit representation of nonhydrostatic processes and can be applied across a wide range of scales. It has been developed as a collaboration between the Max Planck Institute for Meteorology and the Deutscher Wetterdienst (DWD), where it is used to produce global operational weather forecasts since 2015. In the following section, a brief description of the dynamical core, the grid-nesting approach, the physics packages, and the ICON configuration and experimental setups applied in this thesis are summarized.

3.2.1 ICON dynamical core

The ICON dynamical core consists of systems of non-linear partial differential equations. The formulations of these equations and further details on ICON is given in Zängl *et al.* (2015). The dynamical core solves the fully compressible nonhydrostatic atmospheric equations of motion, using the set of prognostic variables suggested by Gassmann and Herzog (2008), but a two-dimensional rather than a three-dimensional Lamb transformation to convert the nonlinear momentum advection into a vector-invariant form. After Zängl *et al.* (2015) the energy, local mass, and potential vorticity conservation properties of ICON were improved compared to the previous operational weather prediction model GME and the regional Consortium for Small scale Modelling (COSMO) system. ICON allows for static local grid refinement with the options of one- and two-way nesting. Two-way nesting results in a more precise simulation of atmospheric processes, computational

time step reduction and feedback of higher resolved prognostic variables from the nesting domains to the global scale

3.2.2 ICON physical parameterizations

The ICON configuration, in this study, have adopted the same physics packages as implemented in the operational ICON NWP at DWD. The fast-physics parametrizations have been inherited from COSMO model (Doms and Schättler, 2004). The cloud microphysics scheme is a slightly extended version of the COSMO-EU five-category prognostic scheme (Doms and Schättler, 2004). The turbulence scheme (Raschendorfer, 2001) is based on a prognostic equation for turbulent kinetic energy (TKE) and has undergone some revision for ICON in order to improve the numerical stability under extreme conditions. The TERRA land-surface scheme (Heise *et al.*, 2006) has recently been extended with a multilayer snow scheme and an option for a tile-based approach accounting for subgrid-scale land-cover variability. Likewise, the slow physics parametrizations have mostly been imported from the Integrated Forecasting System (IFS) of ECMWF. The Bechtold *et al.* (2008) convection scheme considered which is an improved version of the Tiedtke (1989), with some tuning applied to the Convective Available Potential Energy (CAPE) to improve the diurnal cycle of precipitation over tropical land (Stratton and Stirling, 2012). In addition, the subgrid-scale orography scheme (Lott and Miller, 1997), the nonorographic gravity-wave drag scheme (Orr *et al.*, 2010), and the Rapid Radiation Transfer Model (RRTM) radiation scheme (Mlawer *et al.*, 1997) is used in a similar version as in the IFS.

3.2.3 ICON grid structure

The set of partial differential questions that are in the dynamical core could be solved using a Cartesian coordinate or spherical coordinate systems. In both systems, singularities can occur, e.g. at the Earth's poles. Both, spherical and Cartesian grids, represent regular grids. In regular grids the cells are aligned in a fixed pattern. The second type is an irregular grid type which allows to overcome the singularity problem as well as problems with boundary conditions, e.g. coastlines. In this grid type, the cells are not aligned in

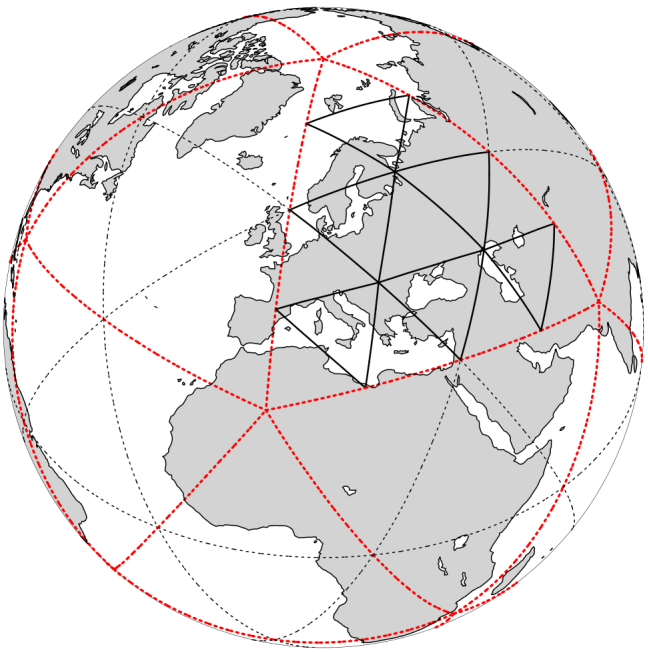

Figure 3.3: Illustration of the ICON grid construction procedure. The original spherical ahedron is shown in red. The initial division ($n = 2$; black dotted), followed by one subsequent edge bisection ($k = 1$) yields an $R2B01$ grid (solid lines).

a fixed lattice. In ICON, an icosahedral-triangular C grid is used (e.g., Staniforth and Thuburn, 2012). This grid is an unstructured triangular grid and allows a very natural way of implementing local grid refinement. A spherical icosahedron is refined in a successive way, to construct the horizontal grid structure of ICON. For the root division (termed R_n), following Sadourny *et al.* (1968), the triangle edges are divided in n equal parts. The connection of the division points constructs new triangles. This step is followed by k bisection steps (termed B_k), where each triangle is recursively subdivided into 4 smaller triangles (Fig. 3.3). The total number of cells (n_{cell}) can be calculated by

$$n_{cell} = 20n^2 4^k \tag{3.6}$$

The resulting grid is called $R_n B_k$ grid and the effective grid resolution $\overline{\Delta x}$ is defined as:

$$\overline{\Delta x} = \sqrt{\overline{a_c}} = \sqrt{\frac{\pi}{5}} \frac{r_e}{n2^k} \tag{3.7}$$

with $\overline{a_c}$ the average cell area and r_e the Earth's radius. An overview for the effective horizontal grid resolution used in the Global (parent, R3B04 gird)

and GHA (two nest, R3B05 and R3B06) domains used in this thesis is given in Table 3.2.

Table 3.2: The total number of cells and effective grid resolution applied in ICON configuration to simulate climate variability over the Greater Horn of Africa.

Domain	**Grid** (R_nB_k)	**Number Cell** (n_{cell})	**Effective grid resolution** ($\overline{\Delta x}$) [km]
DOM01	R3B04	46080	105.2
DOM02	R3B05	10544	52.6
DOM03	R3B06	12428	26.3

Like most atmospheric modelling systems, the vertical coordinate system in ICON is chosen to be terrain following. More precisely, the SLEVE system (smooth level vertical) is used, based on Schär *et al.* (2002) and Leuenberger *et al.* (2010). To ovoid intersection of model levels at steep orography regions, a lower boundary for the model level distance is defined to be 400 m. For the operational NWP configuration 90 terrain-following model levels extending from the surface to a height of 75km are used.

3.2.4 ICON grid nesting

The grid-nesting approach adopted in ICON is a classical two-way nesting. To circumvent the problem of unphysical wave reflections at the nest boundaries, the mesh-size ratio is fixed to a value of 2, which means that one large triangular cell (denoted as parent cell in the following) is subdivided by edge bisection into four small triangular (child) cells. To ensure numerical stability with explicit time stepping, the time step in nested domain(s) is reduced in proportion to the mesh refinement ratio- i.e. a factor of 2. In addition, vertical nesting is available, which means that a nested domain may have a lower top level than the parent domain. The basic workflow at model runtime is thus as follows: Integrate one physics time step in the parent domain; compute the lateral boundary conditions for the nested domain(s); integrate two physics time steps in the nested domain(s); provide feedback for prognostic variables from the nested domain(s) to the parent domain.

The number of cells and the effective resolution used is summarized in Table 3.2. There is a tightly coupled two-way interaction between the ICON

regional model and the ICON. Similar to operational NWP configuration 90 terrain-following model levels extending from the surface to a height of 75 km are used, while the nesting domains comprise 60 levels up to a height of 22.5 km. DOM03 in ICON covers most part of GHA, representing the area bounded by the coordinates 10.5^{o}S–15^{o}N, 30^{o}W–52.5^{o}E (Fig. 3.4). The integration time step for the dynamics routines is chosen to be 600s; convection time step set to be 1200s; while radiation time step selected to be 2400s for DOM01.

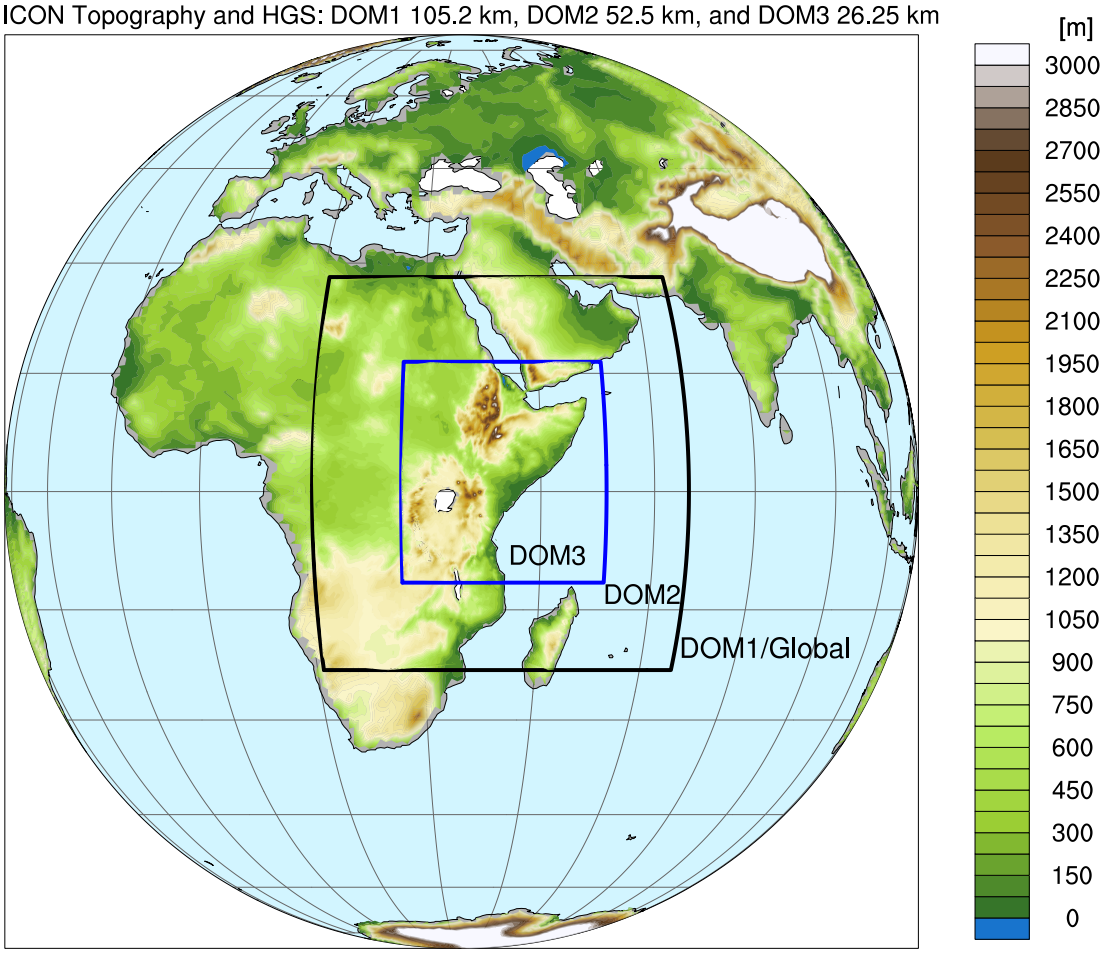

Figure 3.4: Horizontal extent of the ICON and model topography in (m) for the global model domain with the coarsest grid-point distance (105.2 km) and two nested domains with high resolution over GHA (52.5 and 26.25 km grid distance for middle and inner domain respectively).

3.2.5 AMIP experimental design and forcing data

In this thesis, ICON is configured as an Atmospheric Model Intercomparison Project (AMIP)-like experiment (Gates *et al.*, 1999). In AMIP simulations,

SSTs are specified, based on observations, which guarantees that the occurrences of simulated historical El Niño events coincide with observations. In these runs, it is possible to directly compare a model's atmospheric manifestations of El Niño conditions with observations, but agreement will still be limited by atmospheric variability not tightly coupled to SSTs. These AMIP experiments aim at simulating the mean climate processes and SST's forced Kiremt rainfall interannual variability over Ethiopian Highlands. One control run and two experiments are configured with a global grid R3B4 as DOM01 and two nesting domains over the GHA region named DOM02, and DOM03, respectively (Fig. 3.4).

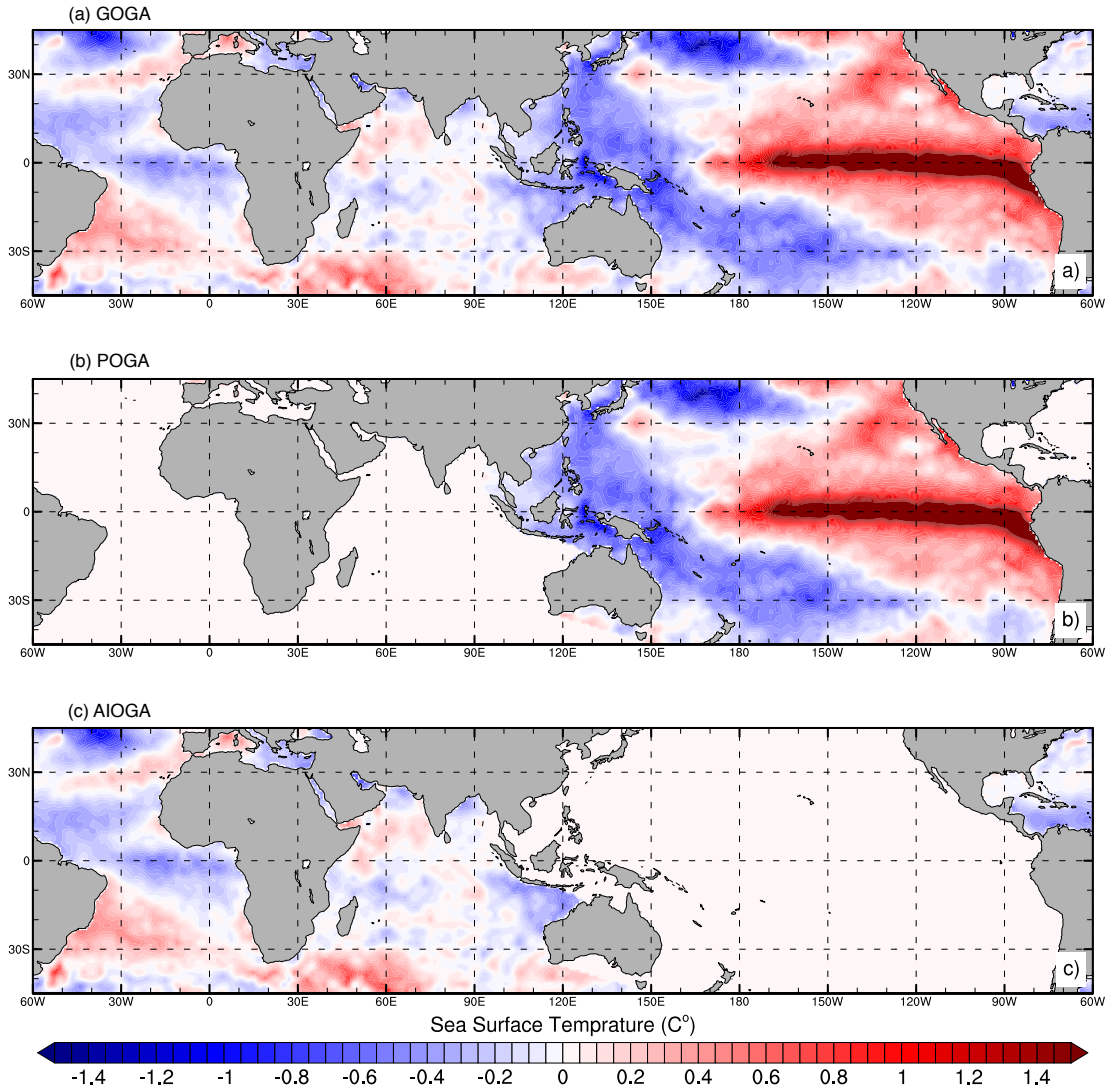

Figure 3.5: SST anomaly patterns (^oC) used to prescribe the three ICON experiments. (a) GOGA, (b) POGA, and (c) AIOGA. SST anomaly used are derived from HadISST from 1981 to 2017 relative to 1981–2010 base period.

The monthly mean SST and sea ice boundary conditions for the ICON simulations were obtained from the HadISST data set (Rayner *et al.*, 2003). Three separate sets ICON experiments were performed, for "control" run where the model was forced with observed, global SSTs, while the two experiment has been forced with observed SSTs over the ocean basin of interest and set to monthly varying climatology elsewhere. The three experiments are described as follows:

- In the control simulation (GOGA: Global Ocean–Global Atmosphere), a simulation of ICON was carried out by forcing the global ocean with observed time-varying SSTs (Fig. 3.5a).
- In the first experiment (POGA: Pacific Ocean–Global Atmosphere), the Pacific Ocean basin bounded by 60^oN to 60^oS were forced with time-varying SSTs, while elsewhere the climatological annual cycle of SSTs was prescribed (Fig. 3.5b).
- In contrast, the second experiment (AIOGA: Atlantic, Indian Ocean–Global Atmosphere), the climatological annual cycle of SSTs was prescribed only in the Pacific Ocean, while other parts of the global ocean basin bounded by 60^oN to 60^oS were forced by time-varying observed SSTs.(Fig. 3.5c).

All ICON simulations start from an initialized state derived from ECMWF ERA-Interim (Dee *et al.*, 2011) reanalysis (e.g., pressure, temperature, water vapour and horizontal wind fields). Simulations are initiated on November 1^{th} 1979 and run up to 16^{th} April 2018 based on the availability of observed SST and sea ice data.

Output of the global domain is remapped to regular 0.75^o x 0.75^o latitude/longitude grid in order to compare with ERA-Interim, while output of DOM03 is remapped to a 0.25^o x 0.25^o grid for comparing model precipitation with high resolution observations. In the vertical, both parent and nests are interpolated to the 20 pressure levels of 100, 150, 200, 250, 300, 350, 400, 450, 500, 550, 600, 650, 700, 750, 800, 850, 900, 925, 950, and 1000 hPa. Pressure level and surface output is written every 6 hours, total precipitation is accumulated every day and radiation flux variables are written out every 3 hours. Further post-processing of model output, analysis details, and discussion of results are given in Chapter 5 of this thesis.

3.3 MiKliP Decadal Prediction Systems

In Chapter 6 of this thesis decadal prediction systems developed by the German national project Mittelfristige Klimaprognosen (MiKlip), funded by the Federal Ministry of Education and Research in Germany (BMBF; Marotzke *et al.*, 2016) are utilized. Miklip aims at investigating and understanding the climate system controlling decadal climate variability and predictability, then incorporate these processes to establish and improve a decadal climate prediction system, that eventually will be transferred to DWD for operational use. The MiKlip development is based on the Max Planck Institute Earth System Model (MPI-ESM; Giorgetta *et al.*, 2013) together with initialization strategies (see Table 3.3).

Table 3.3: Experiments performed in MiKlip. In MPI-ESM-LR, LR stands for low resolution, in MPI-ESM-MR, MR stands for mixed resolution and in MPI-ESM-HR, HR stands for high resolution (Marotzke *et al.*, 2016).

	Baseline0	**Baseline1**	**Prototype**	**Preop**	**Preop-DCPP**
Models	Max Planck Institute Earth System Model, low resolution (MPI-ESM-LR) Max Planck Institute Earth System Model, medium resolution (MPI-ESM-MR)	MPI-ESM-LR MPI-ESM-MR	MPI-ESM-LR	MPI-ESM-LR MPI-ESM-HR	MPI-ESM-HR
Initialization ocean	3D temperature (T)-salinity (S) anomalies from MPIOM forced with National Centers for Environmental Prediction–National Center for Atmospheric Research (NCEP-NCAR) reanalysis	3D $T-S$ anomalies from ORAS4	3D $T-S$ (full field) from German contribution to Estimating the Circulation and Climate of the Ocean 2 (GECCO2) and from ORAS4	3D $T-S$ anomalies from ORAS4	3D $T-S$ anomalies from ORAS4
Initialization atmosphere	Assimilation run	40-yr ECMWF Re-Analysis (ERA-40) and ERA-Interim; vorticity, divergence, log (p), T; full field	ERA-40 and ERA-Interim; vorticiy, divergence, log (p), T; full field	ERA-40 and ERA-Interim; vorticity, divergence, log (p), T; full field	ERA-40 and ERA-Interim; vorticity, divergence, log (p), T; full field; prescribed **CMIP6** historical values of atmospheric composition and emissions (and other conditions including volcanic aerosols).
Ensemble size	LR: 3 (10); MR: 3	LR: 10; MR: 5	30 (15 each with initialization from GECCO2 and ORAS4)	LR: 10; HR: 5	HR: 10
Start years	LR: 1961–2013; yearly for 3 realizations	LR: 1961–2013: yearly; MR: 1961–2013: yearly	1961–2013: yearly	LR: 1961–2013: yearly; HR: 1961–2013: yearly	HR: 1961–2018: yearly

The skill of different sets of simulation including baseline0, baseline, prototype, and preop MiKlip decadal forecasts and preop postprocessed hindcasts are analyzed and evaluated against the observed climate over Africa, and the climate drivers (e.g., ENSO, IPO, AMO, and IOD) providing interannual and decadal skill are also analyzed. Table 3.3 provides an overview of the experiments analyzed. A detailed introduction into the MiKlip predic-

tion system can be found in Marotzke *et al.* (2016). In this thesis, the main focus is on the skill of individual model ensembles mean, min, and the max throughout the common hindcast period. These models have retrospective forecasts (hindcasts) with 10 years integration and are initialized in every year starting from 1961 to 2013. Besides probabilistic postprocessing, we have identified and applied standard forecast verification tools to measure and quantify the skill of the MiKlip decadal forecast systems over Africa. Further analysis details and discussion of results are presented in Chapter 6.

3.4 Statistical Methods

In this thesis, different statistical methods are employed to investigate and quantify large-scale influences on interannual to decadal variability during the three major rainy seasons over GHA. These methods are used (a) to explore the dominant modes of variability, (b) to compute the linear association and multidecadal variations in the interannual teleconnections, (c) to separate the unique contribution of one climate index to precipitation variability independent of other, and (d) to understand the underlying physical mechanism for the effect of SST on precipitation and evaluate potential predictability. Brief descriptions of the methods used are given subsequently.

3.4.1 Correlation, regression and composite analysis

To quantify the linear association between remote indices of ocean-atmosphere climate anomalies and GHA rainfall shown in later sections, several statistical methods were used. The Pearson's linear correlation and percentage of variance explained (PVE) are employed to evaluate the link between the remote climate indices and GHA seasonal rainfall. The triangle representations used in Fink *et al.* (2010) and Diatta and Fink (2014) was chosen to illustrate the correlation coefficient over all possible combinations of starting dates and time window lengths (Fig. 3.6). The critical values of the significance levels for Pearson's linear correlations are calculated by an F-test (Taubenheim, 1969). We have then used both the standard degree of freedom (hereafter SDOF) based on the total number of data pairs that enter the correlations and the effective degree of freedom (hereafter EDOF) as described in Fink

and Speth (1997), which takes autocorrelations into account.

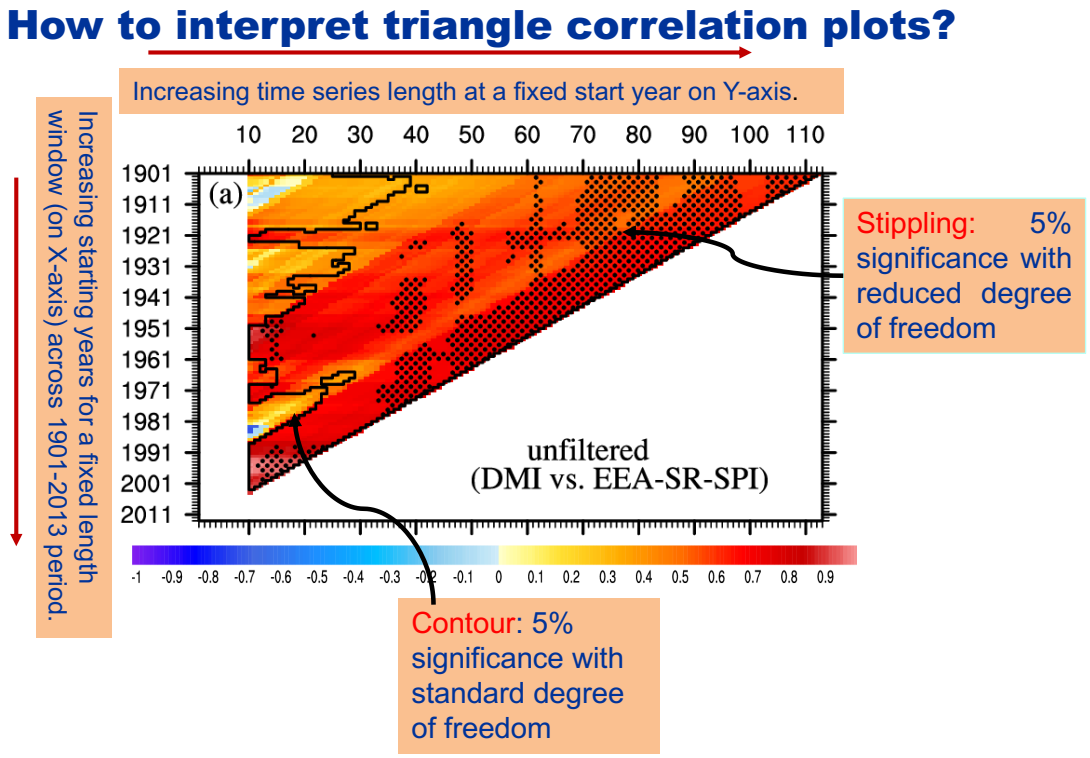

Figure 3.6: Schematic diagram for the evolution of correlation over both varying time window lengths for fixed starting years, as well as over changing starting years for fixed time window length in the triangle representations.

3.4.2 Non-stationarity significance test

The non-stationarity significance test proposed by Van Oldenborgh and Burgers (2005) applied to check the significance of multidecadal changes. This method uses Monte Carlo techniques to generate synthetic time series under constant regression coefficients and approximates the weather noise with a normal distribution. One thousand of precipitation indices (termed p_{MC}) are generated with the real observations replaced by synthetic observations with the same 113-year regression with the SST-base climate indices (e.g., N34). Then the running correlations of the synthetic times series with observed rainfall indices are calculated using a window length of 11 and 31 years.

A normal distribution is a good approximation to the distribution of the observed residues:

$$\log p_{MC}(t) = a_0 + a_1 N_{3.4}(t) + \sigma_{\log p}\sqrt{1-r^2}\eta_p(t), \tag{3.8}$$

with standard deviation $\sigma_{\log p}$ and fit parameters a_0 and $a_1 = r\sigma_{\log p}$ estimated from the observations, and noise $\eta_p(t)$ drawn from a normal distribution $N(0,1)$ with zero mean and unit variance. As the autocorrelation between seasonal rainfall in successive years t and $t+1$ is small, the noise is uncorrelated in time. Neglecting serial correlations underestimates statistical fluctuations. The difference between the highest and lowest of the running correlation is expressed in z-values with $z = \log(\frac{1+r}{1-r})\frac{1}{2}$. This quantity is unbounded, estimates are more normally distributed around the true value, and the variance is to a first approximation independent of correlation coefficient r. Over the 113 years with data in rainfall and SST indices, the fluctuations in running correlation can be calculated as: $\Delta z = z_{max} - z_{min}$.

To quantify the statistical significance of the observed decadal variations, Δz is computed for each synthetic series. Then the running correlations of the synthetic times series with the observed rainfall indices are calculated using a window length of 11 and 31 years. The null hypothesis of constant correlation is tested, and if rejected, the teleconnection is considered to be non-stationary over the 113-year period.

3.4.3 Partial correlations

Besides the simple linear correlations, we use partial correlations to separate the possible competing impacts of SSTA indices on seasonal rainfall. The partial correlation technique (e.g., Yule, 1907) is used to examine relationships between three variables, e.g. the partial correlation between DMI and Short Rains, while excluding the influence that arises owing to the correlation between N34 and Short Rains. The definition of the partial correlation is:

$$pr_1 = \frac{r_{y1} - r_{y2}r_{12}}{\sqrt{(1-{r_{12}}^2)(1-{r_{y2}}^2)}} \tag{3.9}$$

where r_{y1} is the simple correlation of the dependent variable, Y, and the causative variable X_1 (e.g., N34). Similarly, r_{y2} is the simple correlation

between Y and X_2 (e.g., DMI), and X_{12} that between X_1 and X_2.

pr_1 is the correlation between Y from which X_2 has been partialled out and X_1 from which X_2 has been partialled out. The square of the quantity, ${pr_1}^2$, answers the question of how much of the Y variance that is not associated with X_2 in the equation is estimated by X_1.

Moreover, regression and composite analysis techniques are performed to understand the driver of interannul variability of Kiremt Rains over the Ethiopian Highlands and to investigate potential physical mechanisms. Furthermore, we have identified and applied standard forecast verification tools to measure and quantify the skill of the MiKlip decadal forecast systems.

3.4.4 Empirical Orthogonal Function (EOF) analysis

Empirical Orthogonal Function (EOF) analysis is widely used in climate research to highlight the potential physical mechanisms associated with climate variability (von Storch and Zwiers, 1999). Conceptually, EOF analysis determines a spatio-temporal pattern of variability that accounts for the maximum covariance between e.g. SST anomaly time series at all pairs of grid points in the dataset. Then, the remaining covariability is subject to the same decomposition with the added constraint that the second spatio-temporal EOF pattern is orthogonal (e.g., uncorrelated) in both time and space to the leading EOF pattern. This procedure is repeated until all n EOF patterns have been computed, where n is equal to the number of grid points. In practice, only the first few leading modes are robust as a result of the orthogonality constraint. Each EOF pattern is associated with a principal component (PC) time series, which describes the temporal evolution of an EOF pattern. The PC time series may be obtained by projecting the EOF pattern onto the original SST anomaly field at each time step so as to find the sign and amplitude of the pattern at any given time.

In this thesis, EOF analysis is applied to create the POD time series, which is the leading EOF of monthly SST anomalies in the North Pacific Ocean (See section 1.1 and Table 3.1). An analogous analysis applied on the detrended monthly mean SST anomalies to define the IPO. To refine previous interpretation on physical mechanism associated with the spatio-temporal SST patterns in the Indian Ocean, the EOF method (Dommenget

and Latif, 2002) is performed to isolate the dominant modes of the interannual variability. Furthermore, the rainfall variability over Ethiopia during the Kiremt Rains season and its possible link to SST were analyzed using EOF analysis (see Chapter 5). The analysis is performed over the larger domain (32^o–49^oE, 4^o–15^oN), covering most parts of Ethiopia. Here, EOF analysis is applied to JJAS averaged monthly anomalies of CHIRPS2 and ICON simulated rainfall to extract the temporal variability that maximizes the fraction of total variability that they represent.

3.4.5 Spectral analysis and filtering

Our analysis in Chapter 4 uses of both unfiltered and filtered data. In order to filter our time series we have employed spectral analysis, which is concerned with estimating the unknown spectrum of the process from the data and with quantifying the relative importance of different frequency bands to the variance of the process. The spectrum of a time series is the distribution of variance of the series as a function of frequency. Apart from providing the spectral composition of a signal, spectral analysis also makes it possible to filter the signal in a selected band (or bands) and analyse the filtered signal, as well as to estimate qualitatively the relative contribution of the variance of the signal in a particular band to the total variance of the signal. Applications of spectral analysis in practice are commonly based on the Fourier Transform. Here low- and high-pass Butterworth filters (Butterworth, 1930) with a half power period of 8 years were applied to both time series before the calculation of linear correlations. The low-pass filtered time series are thus representing fluctuations of 8 years and longer (i.e., decadal timescales) and the high-pass filtered data are reflecting interannual variability.

This Chapter provides only a brief description of some of the data analysis methods used, whereas detailed discussion of the remaining statistical methods and tools used in this thesis are given in the Chapters where they are applied. Along with this thesis, interannual and multidecadal variability are extracted by means of a Butterworth filter

Chapter 4

Interdecadal Changes in the SST-Driven Teleconnections with the Seasonal Rainfall in the GHA

4.1 Introduction

This Chapter presents and discuss the observed teleconnections for three major rainy seasons at the GHA for the period 1901–2013. Sea surface temperature-based climate indices known to influence Short, Kiremt, and Long Rains are used (see Table 3.1). Besides, a comprehensive statistical analysis are applied to detect non-stationary behaviour in teleconnections and to split them into interannual and decadal time scales. Physical mechanisms are also proposed for identified significant non-stationary teleconnections.

The various methods used to address the goal of this study are given in Chapter 3. While Chapter 2 reviews scientific backgrounds that were necessary to understand this research. Despite those numerous studies on teleconnections between GHA seasonal rains and remote climate anomalies, apparent disagreements amongst them regarding attribution arise from consideration of different seasons, datasets, and varying analysis periods due to non-stationarity of climate drivers (Nicholson, 2015, 2017). Especially, few studies exist on the non-stationarity and multidecadal changes of teleconnections. These studies only deal with changes of Short Rains teleconnec-

tions over time (Camberlin and Philippon, 2001; Clark *et al.*, 2003; Manatsa *et al.*, 2012; Manatsa and Behera, 2013; Nakamura *et al.*, 2009; Nicholson, 2015, 2017). Furthermore, there is, to the best of our knowledge, no study that assigns the GHA seasonal teleconnections to interannual or/and decadal timescales. Several such studies exists for the WAM (Diatta and Fink, 2014; Suárez-Moreno *et al.*, 2018). To fill these gaps, this Chapter provides a comprehensive statistical analysis considering all three major GHA rainy seasons. The specific objectives of this Chapter are:

- To statistically test the non-stationarity of previously identified teleconnections for 11- and 31-year windows during the whole investigation period 1901–2013.

- Here for the first time, to consider SST indices in all ocean basins and examine the evolution of a statistical relationship over both varying time window lengths for fixed starting years, as well as over changing starting years for fixed time window length in a triangle representation (Diatta and Fink, 2014), indicating potential non-stationary behavior of GHA rainfall teleconnections in all possible combinations,

- To propose a physical mechanisms for identified significant non-stationary teleconnections.

- To identify and assign the teleconnections to periodicities below or/and above 8 years.

- To revisit and attribute the recent increased frequency of Long Rains droughts in GHA as part of the natural decadal variability driven by Pacific multidecadal variability.

This Chapter is organized as follows. In section 2, the GHA interannual and decadal variabilities during the three major rainy seasons are briefly discussed. Section 3 presents multidecadal changes in the teleconnections with some of the physical mechanisms for non-stationary correlation also explored. Finally, the results are summarised and discussed in section 4.

4.2 GHA Rainfall Interannual and Decadal Variability

In this section, the 1901–2013 year-to-year and low-frequency evolution of the three major GHA seasonal rainfall indices are examined. Figure 4.1a shows interannual variability and low-pass filtered SPI of the Short Rains based on GPCC data. Compared with the Long Rains (Fig. 4.1c), there is recent evidence of strong interannual variability of Short Rains, with the years of 1961 and 1997 standing out as the wettest years (Fig. 4.1a). Moreover, there is a clear phase shift in the decadal variability. For instance, the dry Short Rains decadal signals during 1935–1943 and 1981–1989 occurred during wetter Long Rains, while during 1921–1927 and 1999–2010 wetter Short Rains occurred with persistent Long Rains drought.

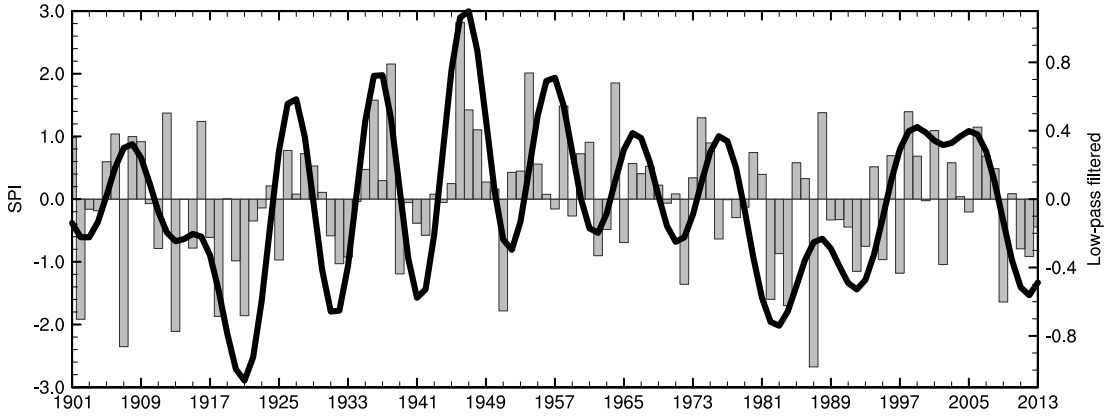

Figure 4.1: Interannual and low-frequency variability of the seasonal mean standardized precipitation indices for 1901–2013: (a) EEA-SR-SPI, (b) GHA-LR-SPI, and (c) ETH-KR-SPI. The smooth curves are low-pass filtered by applying a Butterworth filter with a half power period of 8 years. The three regions are represented in boxes in Fig. 3.1. Note that the right and left Y-axes scales are different. From Bahaga *et al.* (2019). © 2019 Bahaga et al. International Journal of Climatology published by John Wiley & Sons Ltd on behalf of the Royal Meteorological Society.

For ETH Kiremt Rains, Figure. 4.1b indicates large interannual variations but also characteristics that are reminiscent of the Sahel multidecadal variability, with comparatively wet conditions during the 1940s, 1950s, and 1960s, then a downward trend with increased drought in the 1980s and 1990s and a recent recovery, albeit between 2009 and 2013 JJAS rainfall was quite low (Fig. 4.1b). Although JJAS rainfall over ETH shows multidecadal behaviour similar to West Africa, the involved mechanisms responsible might

vary substantially, since features such as the Somali low-level jet play a role (Segele *et al.*, 2009a).

Unlike the Short Rains, interannual variability of the Long Rains shows a clear persistent decline in recent decades (Fig. 4.1c). Moreover, the low-frequency SPI variations suggest that the drying trend since about 1998 is part of the decadal variability of climate over GHA. Furthermore, there are other periods where the time series of Long Rains shows upward and downward trends. This is consistent with recent studies that the post-1998 Long Rains decline in MAM is a manifestation of decadal variability (Lyon, 2014; Yang *et al.*, 2014). In general, it is important to note that in marked contrast to the declining trend in the Long Rains after 1980, the Short Rains show a weak upward trend (Figs. 4.1a, 4.1c; Rowell *et al.*, 2015; Nicholson, 2017).

4.3 Interdecadal Changes in the SST-Driven Teleconnections with the GHA Seasonal Rainfall

4.3.1 Changes associated with Short Rains teleconnections

In this subsection, the dominant teleconnections for the Short Rains and their multidecadal changes are analysed. Figure 4.2 shows the time evolution of the correlation coefficients between mean EEA-SR-SPI and four SST-based remote climate indices for a 31-year sliding window. It is clear from Fig. 4.2 that there are non-stationary correlations to different degrees. One good example is the eastern IO index (EIO), which reflects the time variations of the eastern node of the DMI. It changed from insignificant correlations in the early 1940s to significantly negative correlations of about -0.7 in the late-1960s. Based on the non-stationarity significance test, the changes in the running correlation between the EIO index and the Short Rains are significant. A similar change in the link over time, but opposite in correlation, is that between EEA-SR-SPI and DMI. For the 31-year windows centred on years between mid-1920 and 1967, the linear correlation coefficient rose from

statistically insignificant values of 0.3 to significant values of around 0.75, but for the DMI did not pass the significant test of non-stationarity. Besides, the change in the correlation with the western IO index (WIO) shows a fairly similar trend compared with DMI except that the evolution of correlations in WIO are lower than DMI after the 1950s (Fig. 4.2).

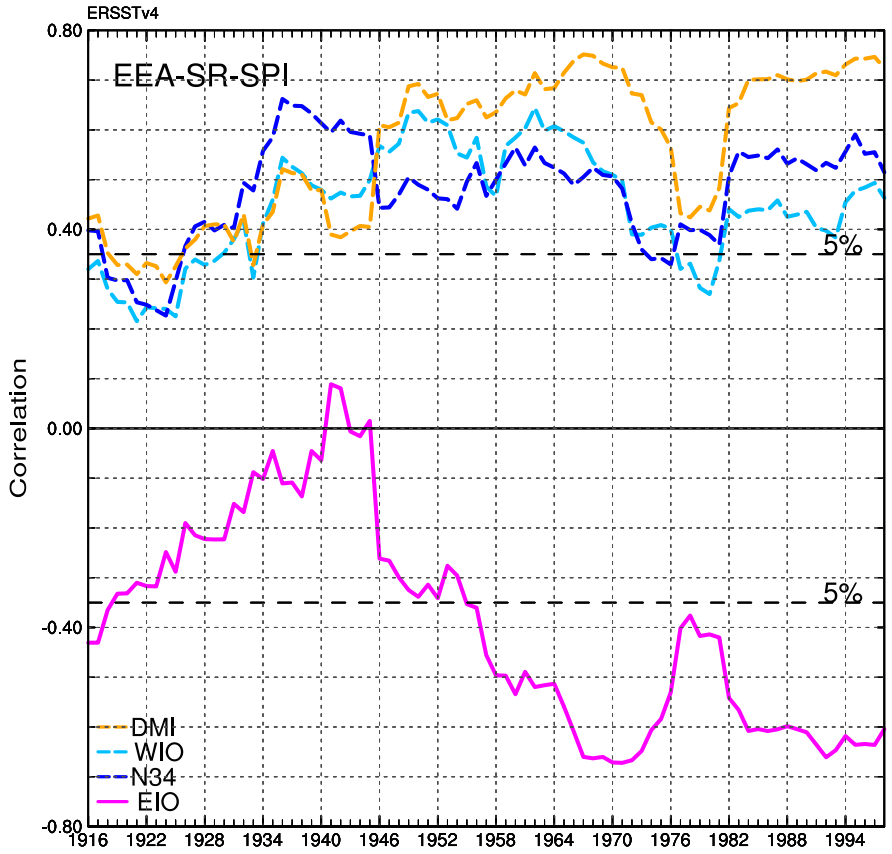

Figure 4.2: Time evolution of the correlations between OND EEA-SR-SPI and DMI (*orange dashed*), WIO (*light blue dashed*), N34 (*blue dashed*) and EIO (*magenta solid*). Correlations are created over a 31-year moving window. The value for 1916, for instance, relates to the period 1901–1931. The horizontal dashed lines represent the 5% significance level according to the F-test using the standardized degree of freedom (SDOF). All correlation coefficients are calculated with linearly detrended time series. The changed in relation with EIO passed the significant test of non-stationarity. From Bahaga *et al.* (2019). © 2019 Bahaga et al. International Journal of Climatology published by John Wiley & Sons Ltd on behalf of the Royal Meteorological Society.

On the other hand, the correlation coefficient between EEA-SR-SPI and N34 changes from a statistically insignificant correlation of nearly 0.2 in mid-1920s to a significant correlation of 0.65 in mid-1930s, then remains significant throughout most of the investigation period, despite an abrupt decrease below the significance level around 1976 (Fig. 4.2). This sudden change was presumably related to a Pacific or global climate shift (Trenberth and Hur-

rell, 1994; Zhang *et al.*, 1997; Meehl *et al.*, 2009c). The recent increase in N34 and EEA-SR-SPI relation could be an interference of ENSO in the EEA-SR-SPI and IOD relation as discussed by Goddard and Graham (1999) and others, finding that the Pacific forces the changes in the IO that are linked to the interannual variability of Short Rains. Another possible explanation is that increased coupling between the tropical Pacific and IO during the ENSO cycle since the mid-1970s resulted in frequent co-occurring IOD and ENSO events (Annamalai *et al.*, 2005). To disentangle this competing influence, a partial correlation analysis between DMI and Short Rains anomalies after removing/partialling out the Niño-3.4 control applied. Positive and significant correlations across East Africa indicate that excessive rains during OND are preferentially linked to concurrent IOD (Fig. A1.1a). However, a similar analysis with Niño-3.4 index and rainfall anomalies for the same season after removing/partialling out IOD indicate that the ENSO anomaly leads to a spatially non-coherent negative correlation over parts of East Africa (Fig. A1.1b). Corresponding modelling studies (e.g., Goddard and Graham, 1999; Bahaga *et al.*, 2015) and observation studies (e.g., Black *et al.*, 2003; Behera *et al.*, 2005) revealed viable evidence of the dominant role of the tropical IO in modulating the Short Rains interannual variability (Hastenrath *et al.*, 2011; Nicholson, 2015). Though there are still some disagreements among scientist, it has now become clearer that the association between the Short Rains in East Africa and ENSO is actually more the result of an indirect forcing by the PO on the IO (Black *et al.*, 2003; Annamalai *et al.*, 2005).

Collectively, the centred correlations of all remote climate indices were insignificant for the period up to the late-1930s. This weaker Short Rains correlation in first half of the 20th century might be linked to SST data quality issues. However, this is notably altered in the early 1950s and after, particularly with EIO (Fig. 4.2; Camberlin and Philippon, 2001; Manatsa and Behera, 2013; Nicholson, 2015). In addition, all remote indices indicate a change in the relation with EEA-SR-SPI around the mid-1970s, most likely related to a 'climate shift' in this period, with global consequences (Meehl *et al.*, 2009c). The possibility that such abrupt changes in the Short Rains teleconnections are due to inclusion/exclusion extreme years of 1961 and 1997 (Fig. 4.1a) was tested by replacing the mean (i.e., a zero anomaly) and redoing the correlations. Overall, such replacement does not affect the significant shift in the mid-1970s and multidecadal changes in the relationship

between the Short Rains and DMI for short time windows (not shown). This is consistent with Nicholson (2015).

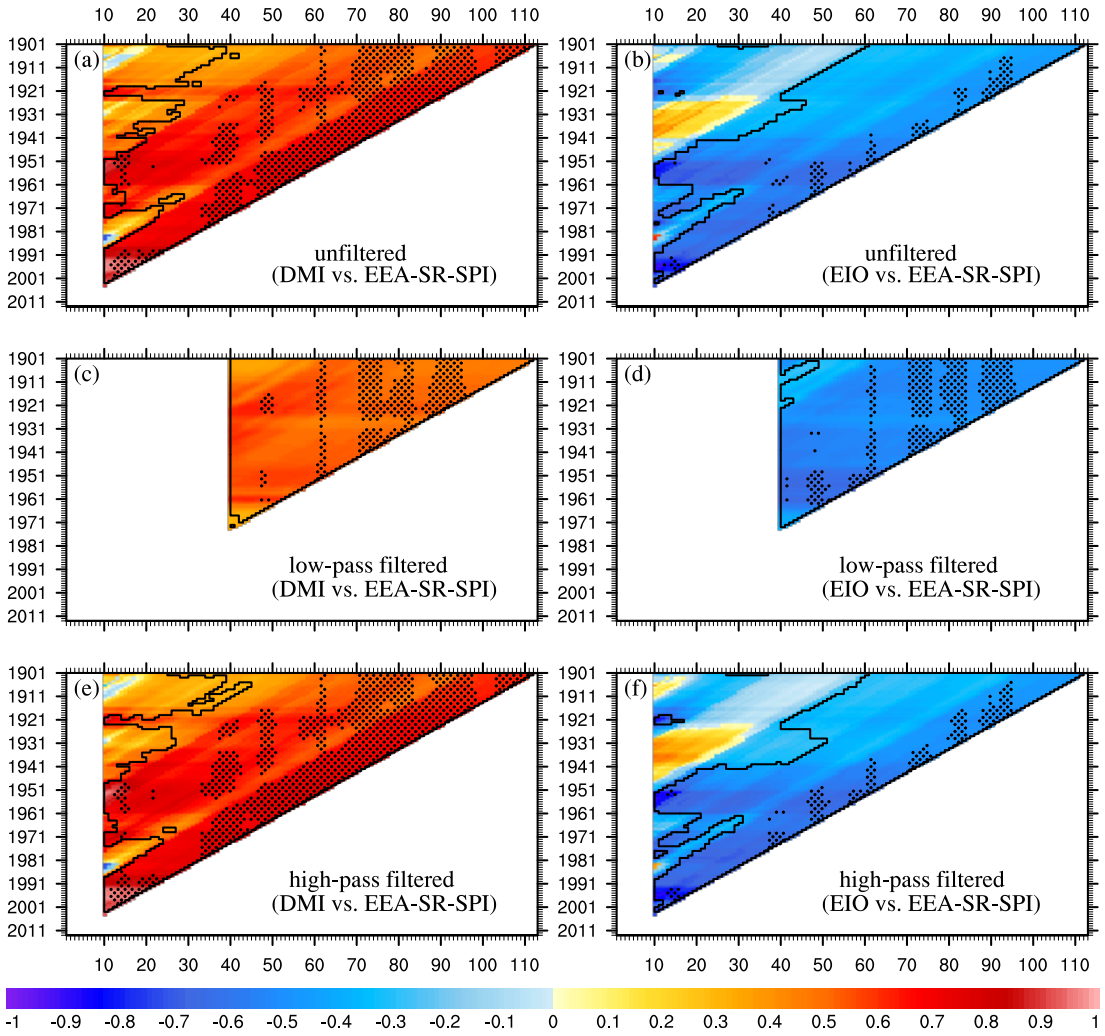

Figure 4.3: Linear correlation coefficients between EEA-SR-SPI and standardized EIO index (right panels) and DMI (left panels) for the period 1901–2013 using a combination of all starting years (ordinate) and time window lengths (abscissa). (a, b) The unfiltered components, (c, d) low-frequency components, i.e., longer than 8 years with only window lengths of ≥40 years displayed, and (e, f) High-frequency components, i.e., shorter than 8 years. Significance at 5% level based on the standard degree of freedom (SDOF) and effective degree of freedom (EDOF) is indicated by contours (stippling). All correlation coefficients are calculated with linearly detrended time series. From Bahaga *et al.* (2019).

4.3.2 Changes associated with Short Rains teleconnections in triangle representation

It is evident from Fig. 4.2 that the correlations are non-stationary to different degrees. To further examine such non-stationary associations, the statistical relationship over both various time window lengths for fixed starting years and starting years for fixed time window length in triangle representations are explored. The first analysis is performed for DMI and EIO indices representing IOD and related to interannual variability in the tropical IO. Figure 4.3 demonstrates the linear correlation coefficients between EEA-SR-SPI and the two indices for the period 1901–2013. The triangle representation of the correlations can be interpreted as follows: firstly, moving from the starting year on the left ordinate horizontally to the right represents correlations at the starting year with increasing time window length. Secondly, moving from the top vertically downward yields correlations for starting years with a fixed moving time window denoted on the lower and upper abscissa. All correlations with 5% significant level based on SDOF (EDOF) are indicated by contours (stippling).

No significant connection was found between the DMI and the Short Rains for time series of less than 20 years for starting years between 1901 and 1951, with an exception of starting years near 1918 (Fig. 4.3a). However, a relatively strong coupling between the two occurred after 1951 until 1978. Another abrupt shift in correlation occurred around 1983, signalling a significant change in the relationship. However, the relation reversed again near 1987 to the recently observed even stronger coupling. Our non-stationarity test applied to an 11-year window length further confirmed that the change in Short Rains and IOD link is significant at the 1% significance level. Previous studies also mention a similar change in the relation between the Short Rains/IOD, particularly during 1918, 1961, 1983, and 1997 (Clark *et al.*, 2003; Manatsa and Behera, 2013; Nicholson, 2015, 2017). These periods have already been confirmed as times when significant shifts occurred in the IO (Manatsa *et al.*, 2012). However, a significant positive correlation for windows longer than 30 years is seen for starting years after 1918. East Africa receives above (below) normal rainfall during + (-) IOD years (Fig. 4.3a). The PVE for such long sample periods is greater than 16%; particularly in recent years with a short length of the time window the PVE increased

to 80%. An analogue pattern is identified for high-pass filtered time series (Fig. 4.3e). A similar analysis is shown for low-pass filtered data with a half power period of 8 years (Figs. 4.3c). For this, window lengths equal or longer than 40 years are used. The correlation coefficients must be interpreted with caution due to the very few cycles of decadal variations that can occur in a 40–113 year-long time series. Positive correlations significant at 5% confidence level between low-pass filtered time series of DMI and the Short Rains are revealed in Fig. 4.3c. This decadal link between DMI and the Short Rains is most likely a signal of decadal timescale PO influence on the eastern IO (Fig. 4.3d, 4.4c). In fact, some previous studies have suggested that the PO decadal variability is related to the interdecadal variability of Short Rains (Omondi *et al.*, 2013; Bahaga *et al.*, 2015).

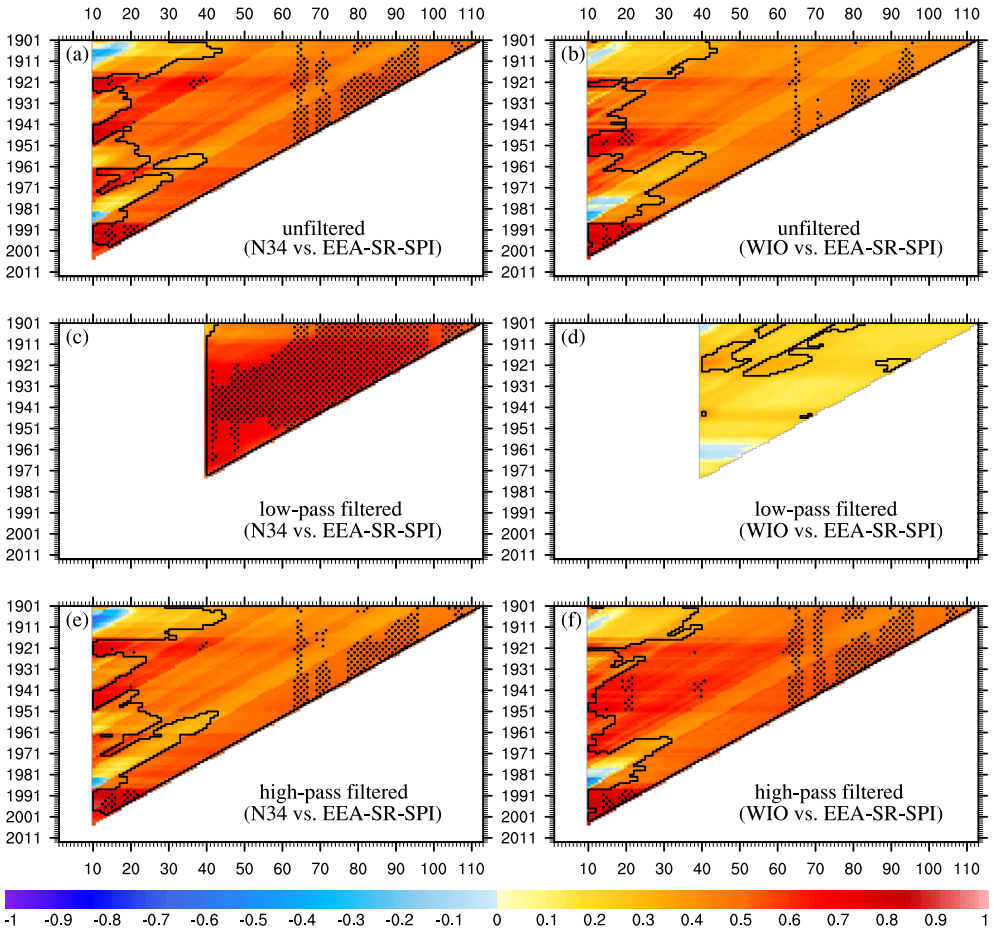

Figure 4.4: As Fig. 5, but for correlation coefficients between EEA-SR-SPI and standardized N34 index (left panels) and WIO (right panels). From Bahaga *et al.* (2019). © 2019 Bahaga et al. International Journal of Climatology published by John Wiley & Sons Ltd on behalf of the Royal Meteorological Society.

A comparable but negative correlation between EIO index and EEA-

SR-SPI is presented in Fig. 4.3b. However, no significant correlations are found for time windows less than 60 years and for starting years until 1951. For a shorter time window, a shift in the relationship occurred around 1931, where the relationship changed to an insignificant positive correlation, then reversed to a significant negative correlation around 1951 and after 1991 (Fig. 4.3b). The DMI (EIO) show positive (negative) significant correlations to low-pass filtered EEA-SR-SPI (Fig. 4.3c, 4.3d), but no significant connections are found for WIO (Fig. 4.4d), which signals that low-frequency association between DMI (Fig. 4.3c) and EEA-SR-SPI is most likely explained by interaction between western Pacific and eastern Indian Oceans on a decadal timescales (Xie and Annamalai, 2002; Black *et al.*, 2003). These studies suggest the dynamics behind ENSO and IO teleconnections, an interaction which goes beyond the scope of this study.

In order to investigate the variation of EEA-SR-SPI teleconnection to N34 and WIO, further analyses are performed. Figure 4.4a shows the correlation patterns between the N34 index and EEA-SR-SPI. N34 is positively correlated with East African Short Rains for long sample periods. The PVE is greater than 16%, which is low but statistically significant. This suggests that N34 plays a role in the interannual variability of this Short Rains, but that the N34 influence is mediated through a concurrent warming in the western IO as extracted by partial correlation analysis (Fig. A1.1b). Figure 4.4a further reveals multidecadal changes in the relationship between N34 and EEA-SR-SPI. For time windows of less than 20 years prominent changes occurred for starting years around the 1920s, in the late 1940s, and around the early 1970s. Another abrupt shift in correlation occurred in recent decades. These changes coincide with the negative phase of Interdecadal Pacific Oscillation (IPO, e.g., Fig. 4.10) and might point to a multidecadal change in Pacific SSTs in 1998–1999, which is consistent with Figure 7c of Lyon *et al.* (2014); that is akin to the Pacific climate shift during 1976–1977 (Trenberth and Hurrell, 1994; Deser *et al.*, 2004; Meehl *et al.*, 2009c). Thus, the statistically significant correlation between N34 and EEA-SR-SPI largely stems from the low-frequency fluctuations (Fig. 4.4c).

To further substantiate the role of IPO on Short Rains variability, the correlation between EEA-SR-SPI and IPO index is shown in Fig. 4.5. For time windows of less than 20 years, a clear decadal change in the relation is

evident around the early 1920s, the late 1940s, around 1970s, and in recent decades (Fig. 4.5a), consistent with previously reported changes in the PDO (e.g., Mantua *et al.*, 1997). In addition, while there are some differences, this correlation pattern is similar to N34, with N34 having the most pronounced signal (Fig. 4.4a). This is further confirmed by a significant association between IPO and EEA-SR-SPI in the low-pass filtered data (Fig. 4.5b). The evidence presented here indicates strong connections between the East African Short Rains with EIO, N34 and IPO on the decadal timescales, corresponding to a decadal interactions between the western Pacific and eastern Indian Ocean (Xie and Annamalai, 2002; Black *et al.*, 2003). Furthermore, the result found here reaffirms that as previous studies which showed the association between the East African Short Rains and ENSO on the interannual timescale is actually more the result of an indirect forcing by the PO on the IO. On the other hand, the Short Rains decadal variability is mainly driven by decadal variability in the PO (Figs. 4.4c, 4.5b). Overall, it is shown that the western Indian Ocean is a primary driver of East Africa Short Rains interannual variability, while the low-frequency variability in eastern Indian and the Pacific Ocean are highly associated with Short Rains decadal variability.

4.3.3 Changes associated with Kiremt Rains teleconnections

In this study, the relation between SST-based remote climate anomalies and Kiremt Rains over the Ethiopian Highlands are revisited. An in-depth analysis was executed to examine the non-stationary nature of Kiremt Rains teleconnections. Figure 4.6 shows the 20^{th} century time evolution of the correlation coefficients between mean ETH-KR-SPI and three SST-based remote climate indices for a 31-year sliding window. It is evident from Fig. 4.6 that there are non-stationary correlations to different degrees. One salient example is the ATL3 index. It changed from significant negative correlations of nearly -0.6 in the late 1940s to a nearly significant positive correlation of about 0.35 in the recent decade. Based on the non-stationarity significance test, the changes in the running correlation between the ATL3 index and ETH-KR-SPI are significant. This suggests a change from a simultaneous occurrence of a warm tropical east Atlantic and dry Kiremt Rains in

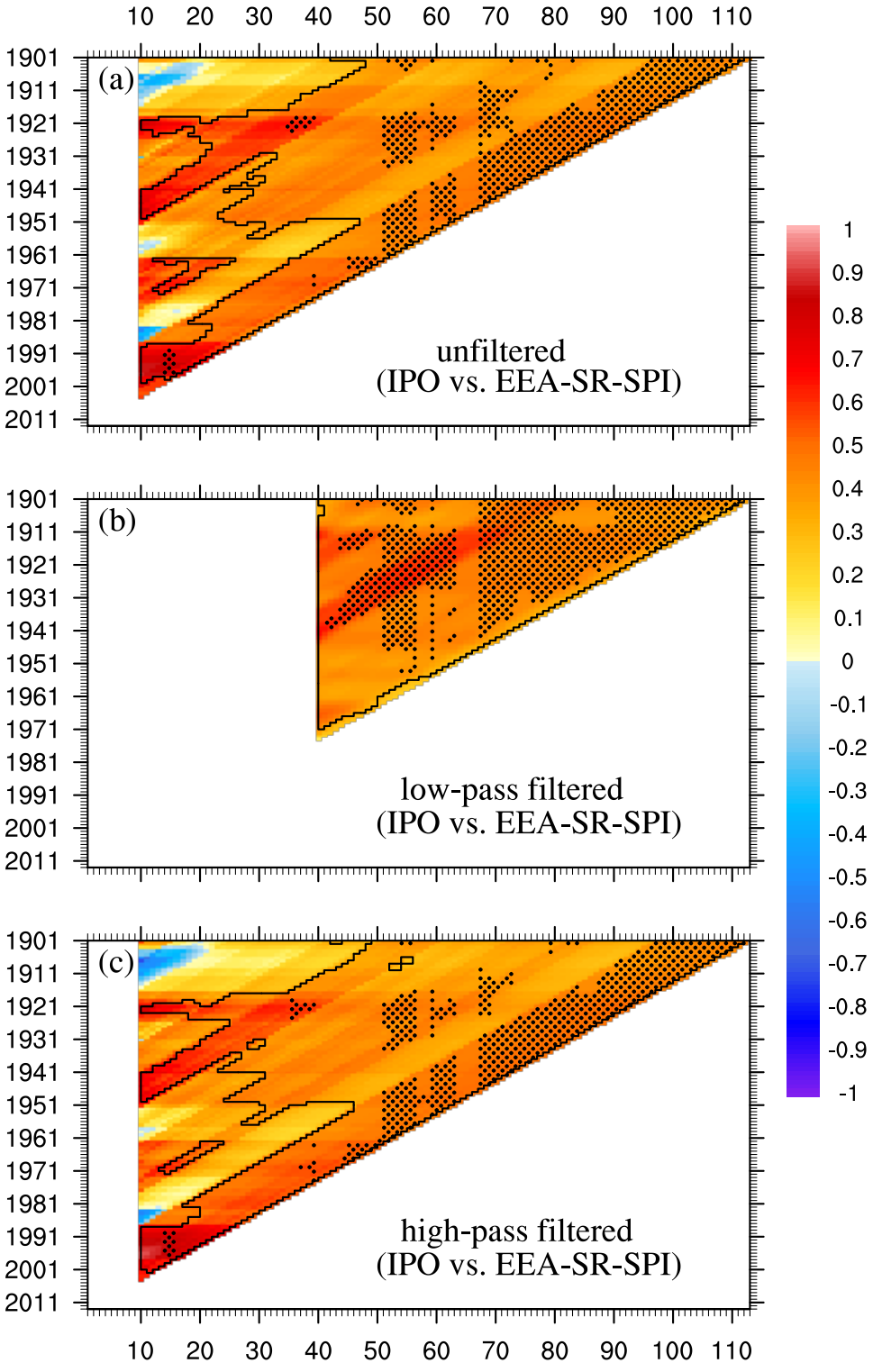

Figure 4.5: As Fig. 5, but for correlation coefficients between EEA-SR-SPI and standardised IPO index. From Bahaga *et al.* (2019). © 2019 Bahaga et al. International Journal of Climatology published by John Wiley & Sons Ltd on behalf of the Royal Meteorological Society.

the early part of the investigation period to an opposite behaviour in recent decades (Fig. 4.6). The latter is consistent with Segele *et al.* (2015) based on modelling experiments for the period of 1971–2000, who showed that warmer Atlantic Ocean SSTA generally brought wetter conditions to northern Ethiopia. In addition, Srivastava *et al.* (2018) found similar multidecadal evolution in the teleconnection between ATL3 and WAM rainfall. They showed that after 1980, El Niño (La Niña) tend to occur simultaneously with negative (positive) ATL3 and this in turn reduced (enhanced) WAM by increased south-westerly moisture flux.

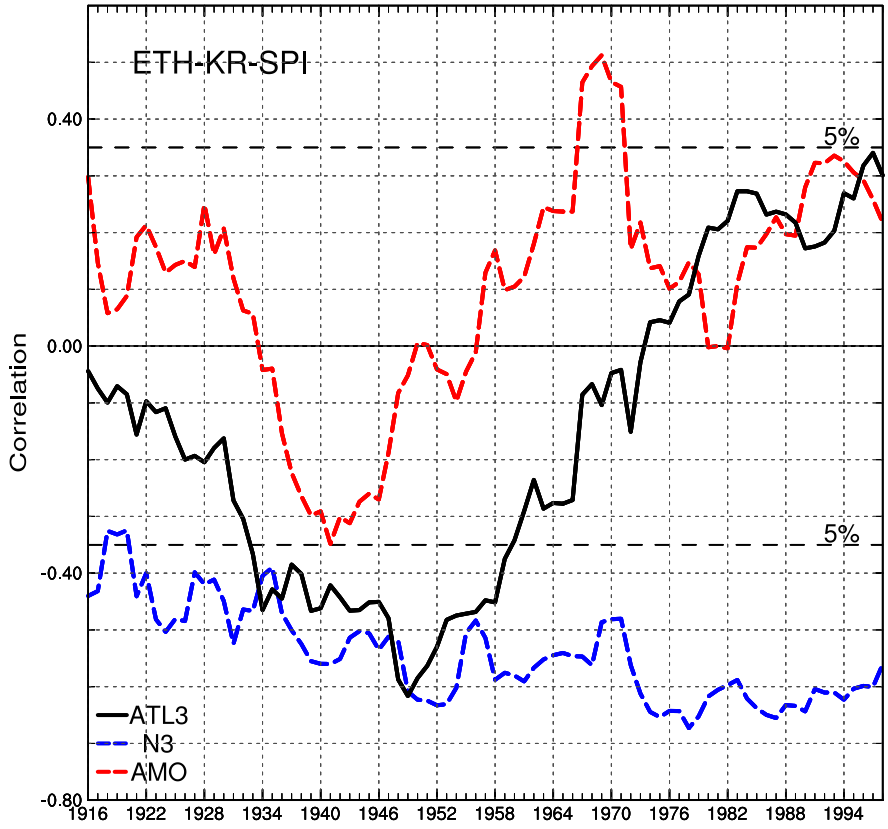

Figure 4.6: As Fig. 4, but for the evolution of the correlations between JJAS ETH-KR-SPI and ATL3 (*black solid*), N3 (*blue dashed*), and AMO (*red dashed*). The changed in relation with ATL3 passed the significant test of non-stationarity. From Bahaga *et al.* (2019). © 2019 Bahaga et al. International Journal of Climatology published by John Wiley & Sons Ltd on behalf of the Royal Meteorological Society.

A second insignificant but non-stationary correlation is that between the AMO index and ETH-KR-SPI. For 31-year windows, it changes from significant negative correlations of nearly -0.35 in the early 1940s to the significant positive correlation of about 0.5 in the late 1960s (Fig. 4.6). For the given window length of 31 years, the index cannot represent the AMO

which fluctuates on timescales of about 60 years (Enfield *et al.*, 2001; Diatta and Fink, 2014). Thus, this non-stationary correlation might reflect the changes in the covariability between interannual SST anomalies in the North Atlantic and JJAS rainfall over the Ethiopian Highlands. As indicated by Fig. 4.1, summer rainfall over the Ethiopian Highlands has a fingerprint of Sahel multidecadal variability. This is consistent with the changes in the running correlation between AMO and ETH-KR-SPI (Fig. 4.6), suggesting that a fraction of the JJAS multidecadal rainfall variability is associated with SST changes in the Northern Hemisphere Atlantic Ocean. Jury (2010) also found a modest association between areas of the summer rainfall over Ethiopia and SST variability associated with the AMO. Nonetheless, this requires further modelling experiments.

The sliding correlation coefficient between the Kiremt Rains and N3 (used here instead of N34 due to somewhat stronger correlations) also varies over the study period between statistically insignificant values of nearly -0.32 to the robust and significant correlation value of nearly -0.67 for 31-year windows centred around the late-1970 (Fig. 4.6). Nonetheless, it may be noted that the significant but lower correlation before 1930s may be related to data quality issues both in SST and Ethiopian rainfall data sets. In general, the observed relations reveal that the interannual variability of the Kiremt Rains is strongly associated with eastern Pacific SST anomalies. However, the time evolution of correlation coefficients did not pass the significance test of non-stationarity. It is evident that the occurrence of drought (excessive rainfall) over this region is associated with El Niño (La Niña) events (Fig. 4.6). This is consistent with the findings reported in previous studies (e.g., Korecha and Barnston, 2007; Segele *et al.*, 2009a,b; Diro *et al.*, 2011a). In addition, it is important to underline increasing influence of ENSO on Kiremt Rains over Ethiopian Highlands in the recent period (Fig. 4.6). This is consistent with Suárez-Moreno *et al.* (2018) who suggested that the non-stationary teleconnection between WAM and ENSO is likely due to the varying amplitude of the latter. Some recent decades have seen strong ENSO variations which would suggest an enhancement of teleconnections in our case. However, our results show that such an enhancement cannot be statistically proven in the period under study.

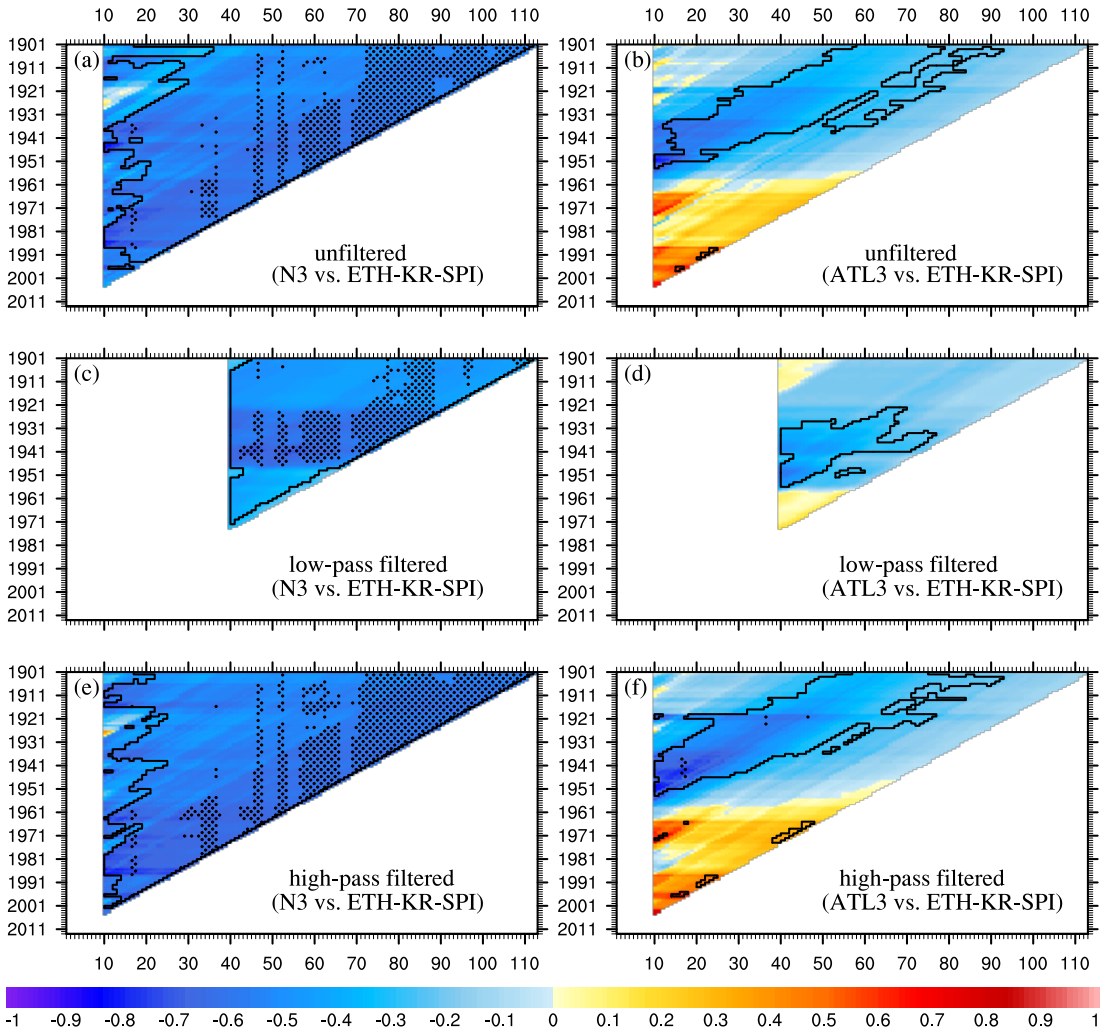

Figure 4.7: As Fig. 5, but for correlation coefficients between ETH-KR-SPI and the standardized N3 index (right panels) and ATL3 (left panels). From Bahaga *et al.* (2019). © 2019 Bahaga et al. International Journal of Climatology published by John Wiley & Sons Ltd on behalf of the Royal Meteorological Society.

4.3.4 Changes associated with Kiremt Rains teleconnections in triangle representation

The sliding correlation in Fig. 4.6 suggests instabilities of the links between Kiremt Rains and remote climate indices. In this subsection, further in-depth analyses performed to examine the non-stationary in triangle representations. Figure 4.7a demonstrates the correlation patterns between the N3 index and ETH-KR-SPI with the unfiltered data. No significant connection could be derived between the N3 and the Kiremt Rains for time windows less than 20 years for starting years between 1901 and 1934, with an exception

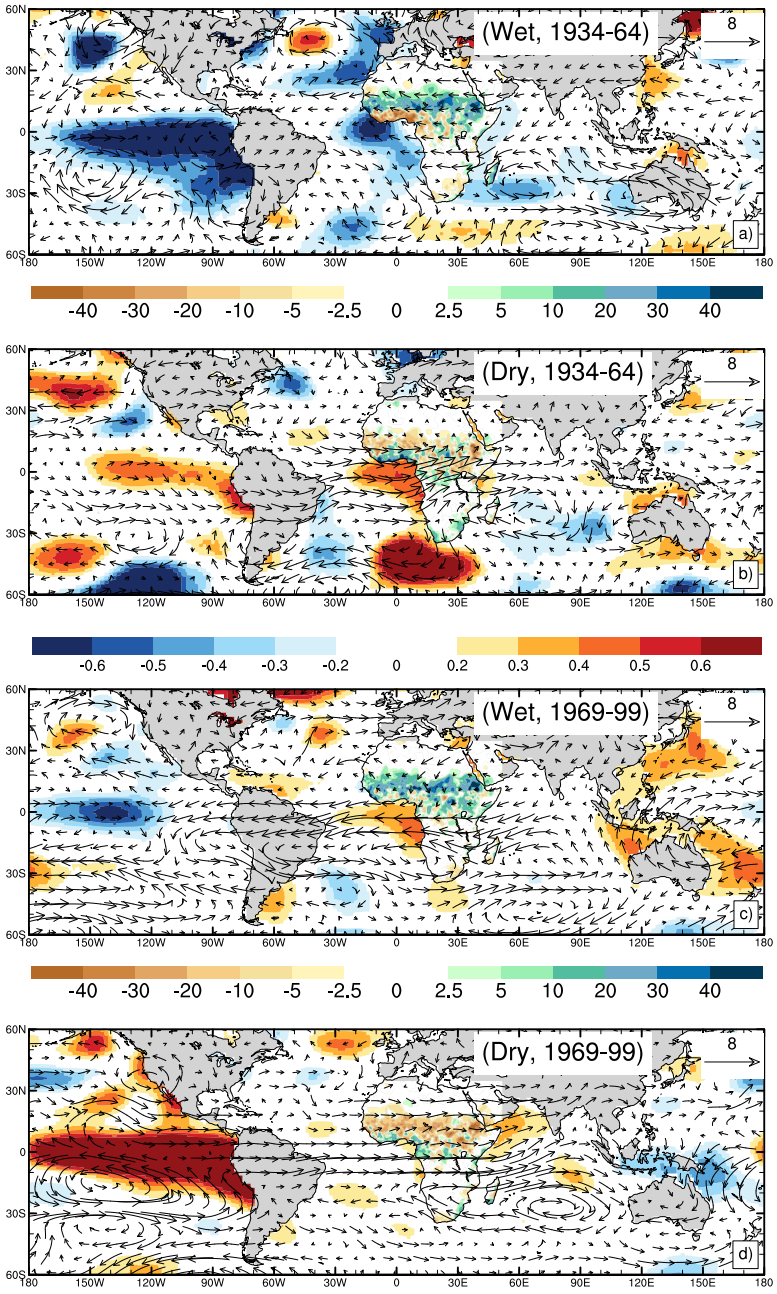

Figure 4.8: Composite of JJAS mean precipitation anomalies (color over Africa), SST anomalies (color), and 200-hPa wind anomalies (vector): a) wet years in 1934–1964, b) dry years in 1934–1964, c) wet years in 1969–1999, d) dry years in 1969–1999. Units are mm for precipitation (top and bottom color bar), ^{o}C for SSTA (middle color bar), and ms^{-1} for wind. Vector scale of 8 ms^{-1} is shown in the top right corner. From Bahaga *et al.* (2019). © 2019 Bahaga et al. International Journal of Climatology published by John Wiley & Sons Ltd on behalf of the Royal Meteorological Society.

for starting years near 1908. However, a relatively strong coupling between the two occurred after the starting year 1935, and between 1980 and 1990. These shifts were associated with warm IPO phases, and ENSO variability

was in phase with the IPO/PDO (Fig. S2). For N3, a significant positive correlation for time windows longer than 30 years is seen for all starting years. Ethiopian Highlands receives above (below) normal rainfall during La Niña (El Niño) years (Fig. 4.7a). This correlation is significant, stable with PVEs larger than 50%, and mainly based on high-frequency variability (<8 years). A similar pattern with a pronounced background decadal change is identified for high-pass filtered time series, exhibits that N3 explains the interannual variability of the Kiremt Rains (Fig. 4.7e). Moreover, there is also significant correlation for low-pass filtered time series (Fig. 4.7c), suggesting a potential decadal link between ENSO and the Kiremt Rains. Similarly, a linear correlation between the ATL3 SSTs and the Kiremt Rains for all combinations of starting years and time window lengths is illustrated in Fig. 4.7b. On the interannual timescales, ATL3 is negatively correlated with the Kiremt Rains for starting years between 1931 and 1960 (Fig. 4.7b), though the negative correlation coefficients are smaller and less significant. This correlation changes from negative to positive in the late 1960s, while being insignificant after this reversal. What causes the significant non-stationarity correlation between ATL3 and ETH-KR-SPI?

In order to answer this question, to further investigate and understand the mechanism by which ATL3 influences the interannual variability of the Kiremt Rains, a composite analysis is performed. Similar to the approach followed in Suárez-Moreno *et al.* (2018), the composites of atmospheric fields and SSTs for the six wettest and six driest years in two epochs of high and low correlations between ATL3 and ETH-KR-SPI are constructed. The years taken for composites can be seen in Table A1.1 in the Supplement. Figure 4.8 demonstrates the result for JJAS mean GPCC gridded precipitation over Africa, HadISST, and 200-hPa wind from ECWMF 20^{th} Century Re-Analysis (ERA-20C) representing patterns for: (a) wet years in 1934–1964, (b) dry years in 1934–1964, (c) wet years in 1969–1999, and (d) dry years in 1969–1999. Wet Kiremt Rains in the 1934–1964 period occurred simultaneously to WAM dipole years with a cold ATL3 (Fig. 4.8a), and vice versa (Fig. 4.8b). On the other hand, Kiremt wet years co-occurred with warmer ATL3 during 1969–1999, but without coherent dipole pattern (Fig. 4.8c). A corresponding regime shift in 1968 within the WAM system has apparently changed the influence of the Atlantic Niño on Kiremt Rains at same time (e.g., Diatta and Fink, 2014; Nicholson *et al.*, 2018). Notably, most wet years

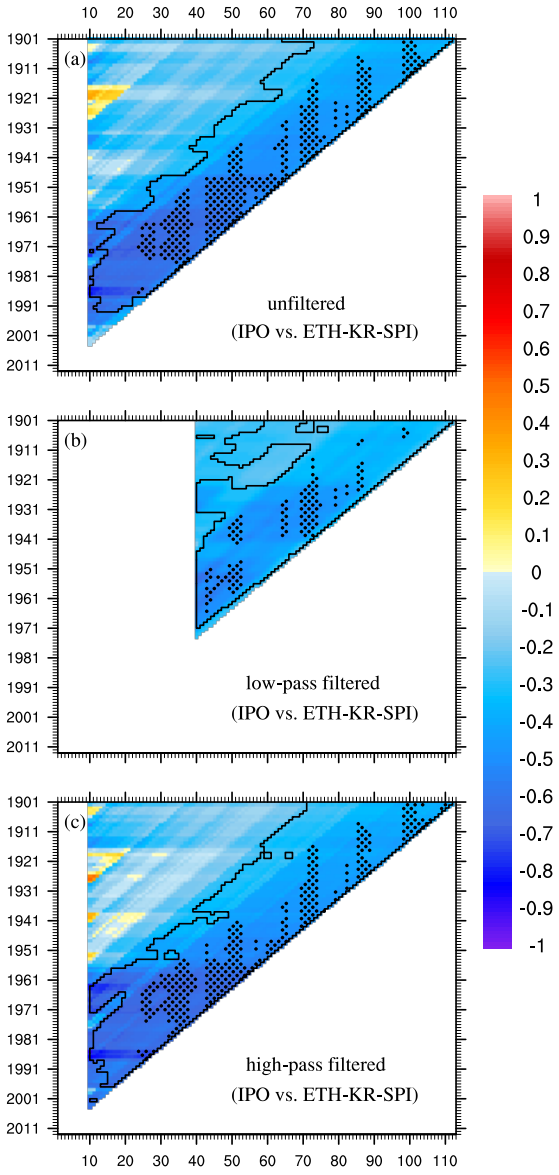

Figure 4.9: As Fig. 5, but for correlation coefficients between ETH-KR-SPI and the standardized IPO index. From Bahaga *et al.* (2019). © 2019 Bahaga et al. International Journal of Climatology published by John Wiley & Sons Ltd on behalf of the Royal Meteorological Society.

did occur with weak La Niña in conjunction with warmer ATL3 but most dry years were strongly associated with El Niño (Figs. 4.8c, 4.8d). This is consistent with Fig. 4.6, showing a clear change in the relation to ENSO. In addition, it can clearly be seen that there are easterly wind anomalies at 200-hPa in excess Kiremt Rain years and a westerly anomalies in deficit Kiremt Rain composites (Fig. 4.8). The corresponding 850 hPa wind composites are shown in the Figure S3 in the Supplement. As to be expected, they show that easterly (westerly) low-level anomalies over northern tropical

Africa are related to dry (wet) Kiremt seasons. Corresponding to the well-known shift in the relation between ATL3 and West African rainfall in the late 1960s (e.g., Nicholson *et al.*, 2018), viz. a dipole (monopole) response to warm ATL3 before (after) this date (Figs A1.3b, A1.3c), the low-level winds did change direction during warm ATL3 years between these periods. This zonal wind change, the reason of which remains elusive, went along with the changed response of the Kiremt Rains to ATL3 forcing.

To further examine the evolution of the linear statical relationship between IPO and the Kiremt Rains, correlation in triangle representation are shown in Fig. 4.9. The IPO index is negatively correlated with ETH-KR-SPI for long sample periods starting between the 1900s and 1950s and more recently also for shorter sample period lengths (Fig. 4.9). Significant association between IPO and ETH-KR-SPI in the low-pass filtered correlation pattern (Fig. 4.9b) is similar to N3 (Fig. 4.7c), with N3 having the most pronounced signal. This might be an indication of interdecadal modulation of the IPO upon the impact of ENSO on the Kiremt Rains. For instance, the frequent dry Kiremt Rains during 1982–84 appears to have occurred when El Niño events coincide during warm phases of IPO (Fig. 4.1, A1.2; Lyon, 2014). Thus, the robust and significant correlation between IPO and the Kiremt rainfall index in a longer time window may reflect ENSO-induced variability of the IPO or superposition of these two variability modes (Figs 4.1, 4.7a, 4.7e, 4.9, 4.10; Newman *et al.*, 2016). In summary, despite the increase in ENSO influence on Kiremt Rains in recent decades, our simple statistical analysis of century-long observations do not exclude that this increase is due to yet short sampling period and that the underlying teleconnection is not changed.

4.3.5 Changes associated with Long Rains teleconnections

As mentioned in the Introduction, understanding interannual variability and predictability of the Long Rains has been a challenge for researchers and forecasters. In this study, all SST-based remote climate anomalies suggested by previous studies are considered and explored (Table 3.1). Consistent with Hastenrath *et al.* (1993) and Camberlin and Philippon (2002), no significant correlation found between indices representing ENSO interannual variability

and Long Rains over GHA (not shown). Recently, Funk *et al.* (2014) suggested western Pacific SST gradient and SSTs in the central Indian Ocean (Table 3.1) as a predictor of the first and the second principal components of the interannual variability of MAM Long Rains. As a consequence, the evolution of the concurrent correlation coefficients between mean GHA-LR-SPI and WPG and CIO are analysed (cf. Table 3.1) for a 31-year sliding window. However, no significant correlations are found (not shown). This is consistent with Liebmann *et al.* (2014) who have highlighted that the sources of interannual variability of the Long Rains have been difficult to pin down, in part because of MAM rainfall appears to be only weakly constrained by SST anomalies on interannual time scales.

4.3.6 Changes associated with Long Rains teleconnections in triangle representation

Consistent with previous studies, no SST-based indices significantly correlated to Long Rains are found and hence it is difficult to identify the sources of interannual variability. In this section, further analyses will be discussed to examine Long Rains decadal variability and teleconnections. As stated in the Introduction, there has been more frequent drought in Long Rains regions over GHA in recent years. So far there are three hypotheses developed in order to explain the recent decline. One of those suggestion attributed this with decadal variability in the PO, however, no specific indices of decadal ocean variability were suggested. Here the definition of Deser *et al.* (2004) is used to create PDO and IPO time series (Table 3.1) and present further evidence on the significant decadal relationship between indices of Pacific multidecadal variability and the MAM Long Rains. Figure 4.10 shows detrended PDO and IPO time series and detrended GHA MAM rainfall anomalies from GPCC. The time series cover our investigation period and all indices have been smoothed using a 9-year running average. The detrended Long Rains time series exhibits significant correlation with both PDO and IPO indices (Fig. 4.10). This is in agreement with Lyon (2014) and Yang *et al.* (2014). Figure 4.10 reaffirms that during warm PDO phases, for instance, 1924–1945 and 1977–1998, GHA received above normal precipitation, while during cold phases from 1914–1925, 1947–1976, and 1999–present precipitation over the

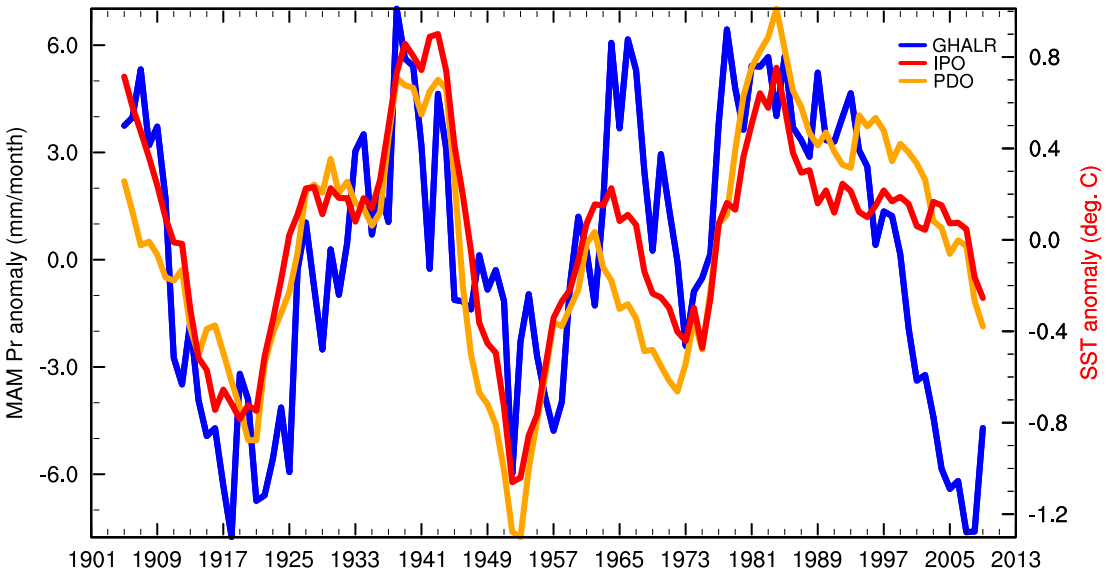

Figure 4.10: Time series of PDO (orange), IPO (red) (°C, right scale; Table 3.1), and the detrended GHA-LR-SPI (blue, mm, left scale) for MAM. A 9-yr moving average has been applied to both series. The temporal correlation between Long Rains time series and PDO (IPO) index is r = 0.65 (0.67) over the full period (1905–2009). All correlation coefficients are calculated with linearly de-trended time series. From Bahaga *et al.* (2019). © 2019 Bahaga et al. International Journal of Climatology published by John Wiley & Sons Ltd on behalf of the Royal Meteorological Society.

GHA was below normal.

To further elucidate the decadal relationship between Pacific Ocean SST anomalies and the MAM Long Rains anomalies, Fig. 4.11 shows the regression pattern of SST anomaly onto the GHA Long Rains anomaly relative to 1950 – 1979 climatological base in MAM over the period of 1901 – 2013. The long-term trends for the whole investigation period in both SST and precipitation were removed before the regression calculation. To show teleconnections at a decadal time scale a 9-year running average has also been applied to both the observed SST and the precipitation, and dotted shading stands for the regression coefficients significant at the 5% level. The regression coefficients spatial pattern shows a typical horseshoe shape characterized by cold SST anomalies in the western North Pacific encircled by warm SST anomalies in the eastern part of the basin extending to the central and eastern tropical Pacific (Fig. 4.11), corresponding the positive phase of PDO spatial pattern (Deser *et al.*, 2012; Farneti, 2017). As can be clearly identified from Fig. 4.11, the wet phase of the Long Rains is associated with a pattern of the positive phase of PDO, while the dry phase of the Long Rains is related to a pattern of the negative phase of PDO (Fig. 4.10, 4.11;

Lyon, 2014; Yang *et al.*, 2014). Overall, the regression analysis further supports Fig. 4.10 and previous suggestion that the post-1998 MAM Long Rains decline is a part of decadal climate variability over GHA, remotely driven and associated with the negative phase of the PDO.

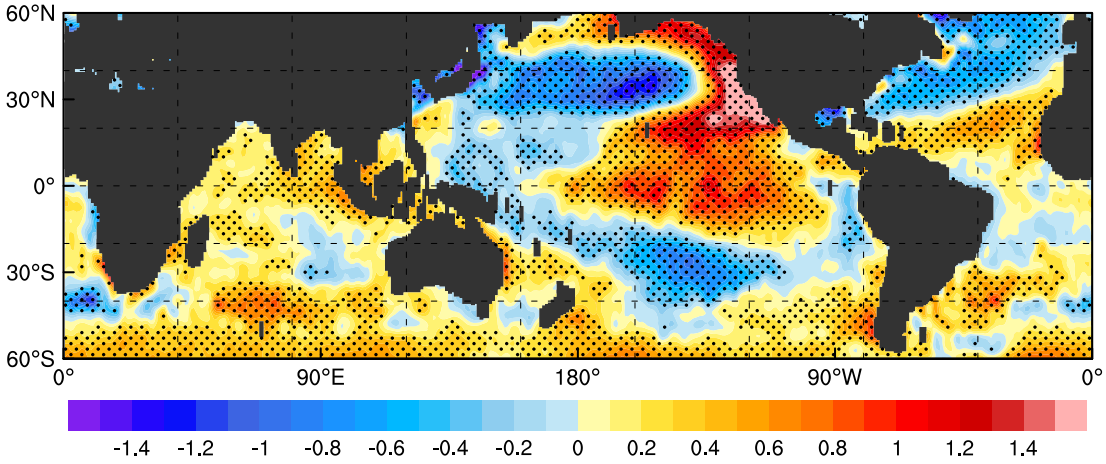

Figure 4.11: The regression maps of HadISST anomaly onto the GHA Long Rains anomaly relative to 1950 – 1979 climatological base in MAM over the period of 1901 – 2013. The long-term trends for the whole investigation period in both SST and precipitation were removed before regression analysis. To show teleconnections at a decadal time scale a 9-year running average has been applied to both the SST and the precipitation. Dotted shading stands for the regression coefficients significant at 5% level and the units are given in $^oC/(mmday^{-1})$. From Bahaga *et al.* (2019). © 2019 Bahaga et al. International Journal of Climatology published by John Wiley & Sons Ltd on behalf of the Royal Meteorological Society.

To illustrate the evolution of Long Rains decadal teleconnection, the correlations in triangle representation are used. for PDO (Fig. 4.12a) and IPO (Fig. 4.12b) and the GHA-LR-SPI. For all starting years, the correlations between the GHA Long Rains and Pacific SSTAs represented by PDO and IPO are positive and significant based on both SDOF and EDOF tests. Consistent with the relation shown in Fig. 4.10 and Fig. 4.11, there are relatively high correlation coefficients greater than 0.6. PVE ranges from 25 to 64% and the association stems from low-frequency variability (>8 years) for both PDO and IPO (Figs. 4.12a and b). Thus, our analysis support that the recent Long Rains decline is part of natural decadal fluctuation and strongly associated with multidecadal variability in the PO. In addition, the significant correlation between the rainfall and indices of decadal variability in the PO hint at useful predictors of rainfall variability on decadal timescales.

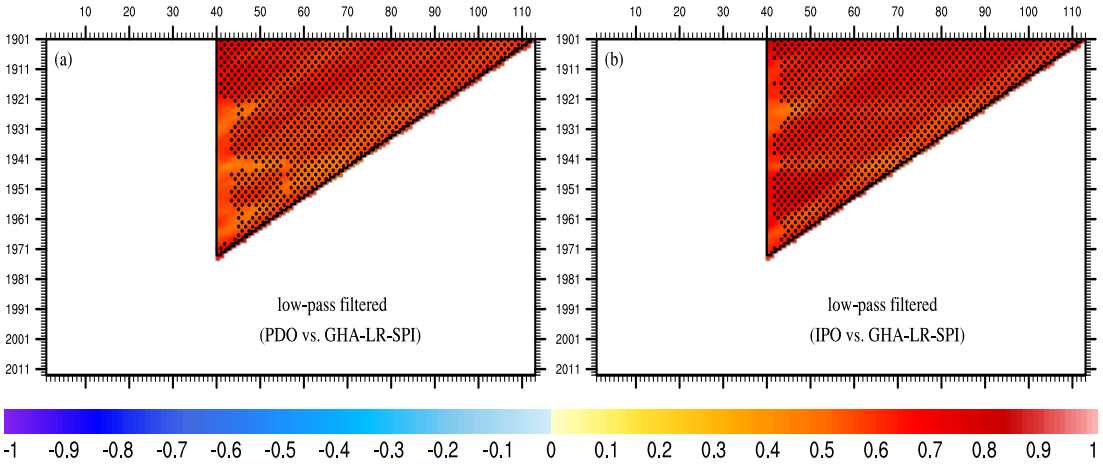

Figure 4.12: As Fig. 5, but for correlation coefficients between low-frequency component of GHA-LR-SPI and standardized PDO index (a) and IPO (b). From Bahaga *et al.* (2019). © 2019 Bahaga et al. International Journal of Climatology published by John Wiley & Sons Ltd on behalf of the Royal Meteorological Society.

Chapter 5

Interannual Variability of the Ethiopian Kiremt Rains as Simulated by ICON

5.1 Introduction

This Chapter focuses on the variability of the Ethiopian Kiremt Rains during the JJAS season, as this is the main rainy season with 65–95% of Ethiopian annual rainfall associated with the Kiremt Rains (Segele and Lamb, 2005). The impact of ENSO on Kiremt Rains' interannual variability has been well documented in the literature (see Chapter 2). Generally, Kiremt Rains and the concurrent central eastern tropical Pacific SSTs show negative correlation and El Niño years are associated with drought in Ethiopia. Previous studies have also examined the relationship between the Kiremt Rains and circulation anomalies. Robust relationships with the TEJ, AEJ, ITCZ, low-level westerly anomalies from the Atlantic Ocean and Congo Basin, high-pressure systems over Mascarene and St Helena, an anomalously deep monsoon trough over the Arabian Peninsula, and the strength of the SLLJ have been documented (see Chapter 2).

The results in the previous Chapters provided useful information about the non-stationary teleconnections associated with the Kiremt Rains over the Ethiopian Highlands. It is also indicated that SST variability in the central eastern tropical Pacific and the Atlantic Ocean plays a significant

role in driving the Kiremt Rains' interannual variability while suggesting dynamical modeling to investigate the physical mechanisms (Bahaga *et al.*, 2019). Subsequently, in this Chapter the capability of the Deutscher Wetterdienst numerical weather prediction ICON model in simulating the Ethiopian Kiremt Rains is evaluated. The ICON climate mode is configured according to the AMIP protocol with a typical global horizontal grid spacing of 100 km, while over the GHA two two-way nests with grid spacings of 50 and 25 km, respectively, are introduced to capture the orographic forcing of the complex terrain in this region, such as the Ethiopian Highlands, more realistically. Three sets of experiments are performed, where each has been forced with observed SSTs over the ocean basin of interest and set to monthly varying climatology elsewhere. To the best of our knowledge, such fine-grid two-way nests over the GHA has been used for the first time. The brief description of the ICON including the physical parameterizations, grid structure, grid nesting, the AMIP type experimental design, the forcing data used, observation datasets used, and various statically methods applied are explained in Chapter 3.

In the light of those previous studies and the results found in Chapter 4, three sets of model experiments were configured and named as GOGA, POGA, and AIOGA (see Chapter 3). The GOGA simulation is required to validate the model in reproducing the observed rainfall climatology in the GHA and to examine the atmospheric response in terms of the Kiremt Rains' interannual variability associated with the SST forcing. The POGA experiment is used to investigate the influence of Pacific SST anomalies in driving the Kiremt Rains anomalies. On the other hand, the AIOGA experiment has been performed to estimate and understand the effects of the Atlantic and Indian SST forcing on the Kiremt Rains by removing the Pacific Ocean anomalous forcing. Runs are initiated on November 1^{st} 1980 and run up to December 31^{st} 2017. The first two months are treated as spin up, thus the model outputs are analyzed for the period 1981–2017. The focus of this Chapter is to evaluate the climatology of the higher-resolution ICON two-way nest in the GHA, to investigate the mechanism for the impact of ENSO variability on the Kiremt Rains variability, and in particular, the following questions are addressed:

- How well can the SST-forced ICON represent the climatology and interannual variability of rainfall, and large-scale circulation patterns during the Kiremt Rains season?

- What are the key features which characterize the ENSO-Kiremt Rains teleconnection?

- How and to what extent does the Pacific Ocean interfere with the Atlantic and Indian Ocean forced Kiremt Rains' variability?

- What are the physical mechanisms by which the SST anomalies in the Pacific Ocean impact on the Ethiopian Kiremt Rains, with a focus on the implication for seasonal predictability?

The rest of the Chapter is organized as follows. In section 2, the ability of ICON to simulate the climatological features of the JJAS rainfall over the GHA and the atmospheric circulation over the regions surrounding Africa is evaluated. The responses of the atmosphere for individual ICON experiments and anomalies associated with the Ethiopian Kiremt Rains' interannual variability are explored in section 3, while in section 4, the physical mechanisms by which SSTs in the Pacific Ocean influences the Kiremt Rains anomalies are investigated. Finally, the results are summarized in section 5.

5.2 Evaluation of ICON During the Kiremt Rains Season

In this section, the spatial patterns and annual cycle of rainfall over the GHA, and the dynamical features of large-scale circulations in the model and reanalysis datasets are analyzed. The analysis concentrates on the JJAS season for the period 1981–2017. The ICON resolution implemented in our experimental setups were inconsistent with the ERA-Interim reanalysis (ERAI) and the CHIRPS2 dataset used and, therefore, interpolated onto a common 0.25^o x 0.25^o and 0.75^o x 0.75^o grid for rainfall and all other variables, respectively. The rainfall, wind, and Mean Sea Level Pressure (MSLP) climatologies derived from the GOGA simulation are compared with observations.

As expected, all other experiments have very similar climatologies and are not shown.

5.2.1 Rainfall and 850hPa wind climatology

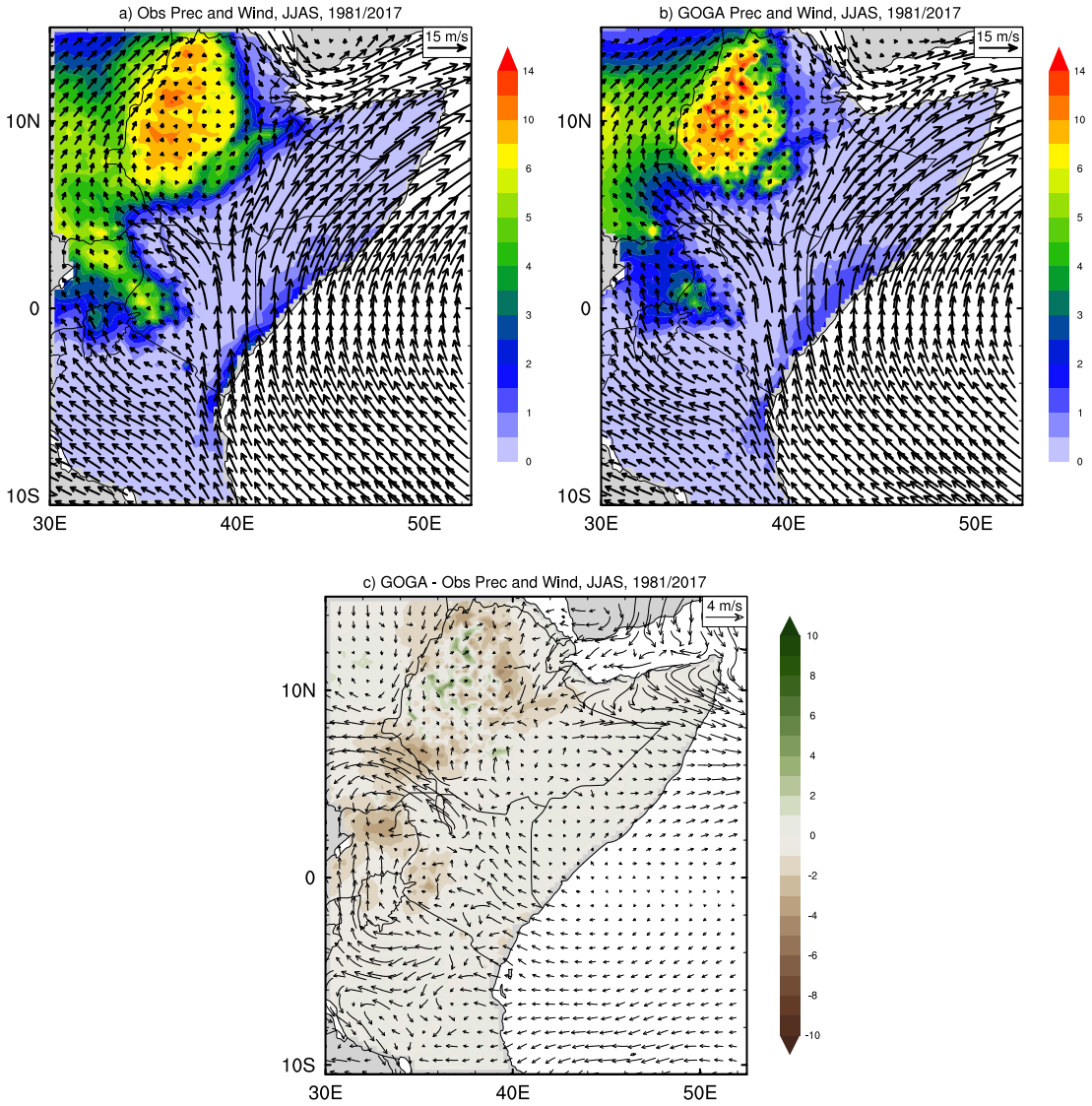

Figure 5.1: The spatial distributions of seasonal (JJAS) mean climatology of rainfall (colored shaded) and 850-hPa winds for the period 1981–2017. (a) CHIRPS2 rainfall and ERAI wind, (b) GOGA, and (c) climatological biases relative to observations for rainfall (colored shading) and 850-hPa wind (vectors). Units are $mm(day)^{-1}$ for rainfall and $m(s)^{-1}$ for wind.

Before evaluating the model performance in representing atmospheric response in terms of the Kiremt Rains' interannual variability, a brief appraisal of the model climatologies for summer (JJAS) rainfall and 850-hPa wind distribution are given. Figure 5.1 shows the JJAS mean rainfall (shading)

and 850-hPa wind (vectors) in observations (Fig. 5.1a) and model simulation (Fig. 5.1b) in the GHA. The corresponding model biases (GOGA minus observations) are given in Figure 5.1c. Qualitatively, the seasonal characteristics of wind and rainfall distribution are reasonably well reproduced. For example, the rainfall distribution over the Ethiopian Highlands, southwestern Kenya, South Sudan and the coastal regions in the narrow strip extending from Kenya to south Somalia is well represented . However, the model shows a negative bias over northeastern Ethiopia, northern Uganda, southeastern South Sudan (Fig. 5.1c). There is also a patchy wet bias, evident over the Ethiopian Highlands; this might be attributed to underestimation of higher rainfall amounts in CHIRPS2 (Dinku *et al.*, 2018). Moreover, the northeastern, eastern, southeastern and southern regions, which are semiarid, receive comparably less rainfall during this season. These climatological rainfall patterns are well replicated in the model.

The model also captures the features of the 850-hPa circulation fairly well when compared to the ERAI climatology (Fig. 5.1a). For instance, the Somali low-level jet is fully formed, placing southeasterly flow over East Africa and the Indian Ocean in the Southern Hemisphere and southwesterly flow over the Horn of Africa. Winds extend into the continental interior over Kenya and Ethiopia, and also flow through the Turkana Channel. Moreover, the Turkana jet is reproduced in the model (Fig. 5.1b). However, the model shows a narrow Turkana channel and strong divergence at the entrance and the jet's core. This might be attributed less moisture transport, and thus dry bias over southeast South Sudan and southwest Ethiopia (Fig. 5.1c). In general, the model rainfall and low-level wind simulation over the GHA are comparable to the state of the science regional climate models (e.g., Zeleke *et al.*, 2013; Segele *et al.*, 2015).

5.2.2 The seasonal cycle of rainfall in the Ethiopia Highlands

In addition to capturing the spatial pattern of rainfall, climate models should be able to provide a reasonable simulation of the seasonal cycle of rainfall. Figure 5.2 shows mean and standard deviation of the annual cycle of the Ethiopian Highlands Kiremt Rains index (ETHKRI), defined as an area averaged rainfall in the region (6^o–14^oN, 35^o–40^oE; orange box in Fig. 3.1) for

the period 1981–2017. It is verified that the results presented in this study are robust with respect to small variations in size and position of this index. The index includes the central and northwestern parts of Ethiopia characterized by the Kiremt Rains (Segele and Lamb, 2005). In CHIRPS2 the rainfall reaches a seasonal maximum of roughly 8 $mm(day)^{-1}$ in July and August. Similar to most parts of North Africa, the seasonal maximum of rainfall over the Ethiopian Highlands coincides with the northernmost migration point of the ITCZ in summer (Kassahun, 1987). The model simulates the seasonal rainfall and its variability reasonably well, yet it is important to note a reduced standard deviations in the model. It is also clear that the model captures the June and July maximum of rainfall correctly and has realistic representation with respect to observation despite small negative biases in the August and September. The seasonal cycle in the model is comparable with the results shown in previous studies (Diro *et al.*, 2011a; Zeleke *et al.*, 2013).

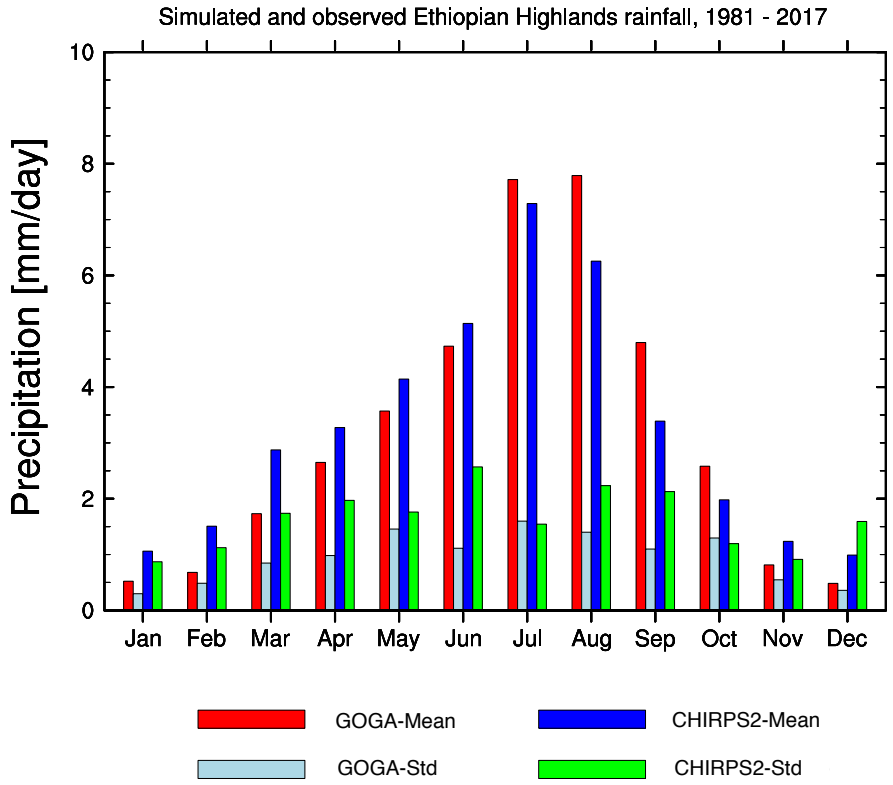

Figure 5.2: Seasonal cycles of total monthly rainfall averaged over the Ethiopian Highlands (6^o–14^oN, 35^o–40^oE; orange box in Fig. 3.1) along with monthly standard deviations for the period 1981–2017. CHIRPS2 climatology/standard-deviation is shown as blue/lightgreen bars, while the GOGA experiment climatology/standard-deviation is plotted as red/lightblue bar. Unit is $mm(day)^{-1}$.

5.2.3 Characteristics of large-scale circulation

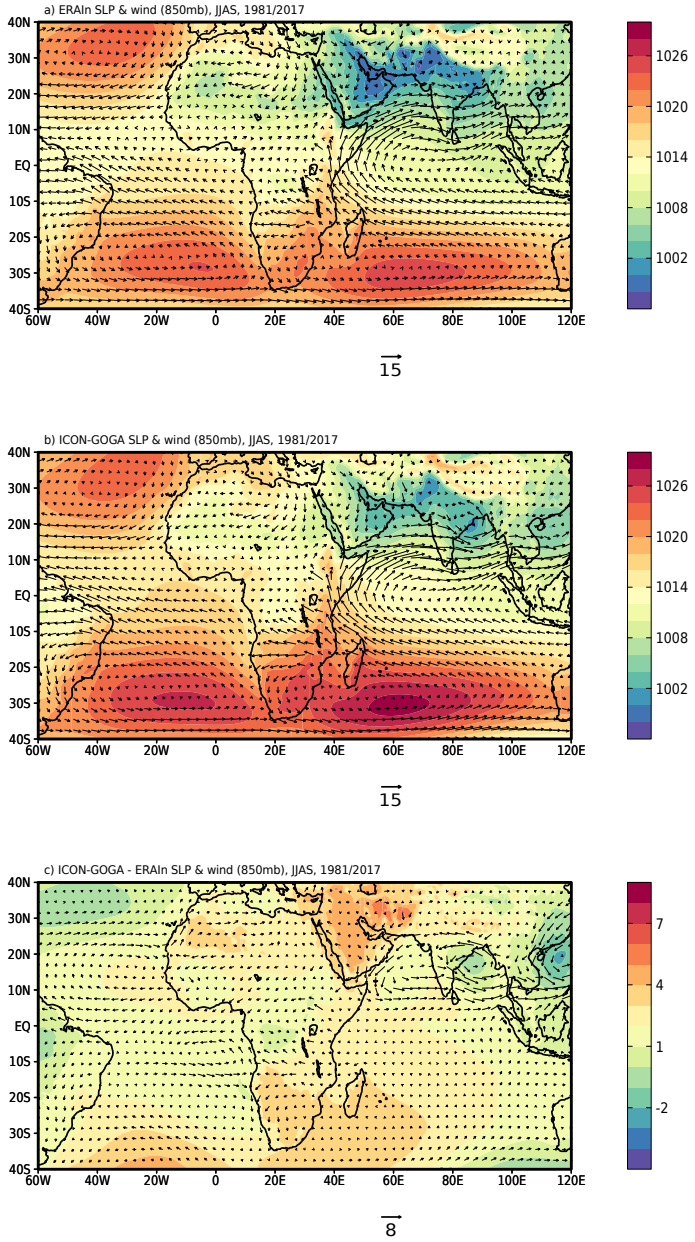

Figure 5.3: The spatial distributions of the seasonal (JJAS) mean climatology of MSLP (colored shaded) and 850-hPa wind (vectors) for the period 1981–2017. (a) ERAI, and (b) GOGA. (c) The climatological biases relative to ERAI for MSLP (colored shaded) and 850-hPa wind (vectors). Units are hPa for MSLP and $m(s)^{-1}$ for wind.

To determine the influence of the large-scale atmospheric circulation anomalies on the ENSO-Kiremt Rains teleconnection, the mean climate of important circulation features and patterns in the model first needs to be assessed. Figure 5.3 presents ERAI and model simulated JJAS averaged MSLP patterns and 850-hPa winds for the period 1981–2017, together with

the difference between GOGA and ERAI. The model is able to reproduce the major summer season circulation features associated with the Kiremt Rains, for example, the Mascarene high over the south Indian Ocean, the St. Helena high over the south Atlantic Ocean, and the subtropical Azores high over the northeast Atlantic Ocean (Fig. 5.3b). The outflow from the St. Helena high in the south Atlantic results in winds turning into southwesterlies to enter West Africa, further east over the northwestern Ethiopia and Eritrea it appears as an asymptotic wind confluence between the moist southwesterlies and the much drier northwesterly winds. Thus, the wind convergence over Eritrea and extreme northern Ethiopia is largely associated with the ITCZ (Fig. 5.3b, Kassahun, 1987; Segele *et al.*, 2009a; Diro *et al.*, 2011a). Moreover, the near-equatorial trough of low pressure spanning North Africa, the Arabian Peninsula, and the Indian subcontinent are well represented. While the model reproduces the main MSLP features ERAI, there are positive and negative biases over subtropical regions, e.g. the MSLP bias up to negative 6-hPa seen over the Arabian Peninsula (Fig. 5.3c). Over the Indian Ocean sector the main features of the low-level flow are reasonably well simulated by the model (Fig. 5.3b). The strength and position of the SLLJ and the diffluent southerlies over southern Ethiopia are captured, but the westerly flow across the Arabian Sea, India and the southern Bay of Bengal is rather strong (Fig. 5.3c). The cyclonic wind bias around the Arabian Sea and Bay of Bengal might be generated by the negative MSLP bias over these regions.

In Chapter 2 it is reviewed that the large-scale features associated with the Ethiopian Highlands Kiremt Rains variability are the TEJ, the AEJ, and the SLLJ among others (Segele *et al.*, 2009a; Diro *et al.*, 2011a,b). It is interesting to see if these large-scale climatological features are also represented in the GOGA simulation before analyzing interannual variability. The model wind climatology at 150, 600 and 925-hPa are compared with ERAI in Figure 5.4. The TEJ maximizes at 150-hPa over Ethiopia (Segele and Lamb, 2005), this is evident in (Fig. 5.4a). At this level, the TEJ core lies to the southwest of India around 8^{o}N, favoring strong divergence over the western Indian Ocean and further west primarily from western Ethiopia to West Africa. Although the GOGA climatology (Fig. 5.4b) qualitatively reproduces the TEJ over southwest India, Ethiopia, and West Africa, the model TEJ has a magnitude approximately 1–4 m/s lower than that of the ERAI over the North Africa region between 0–20^{o}N (Fig. 5.4c).

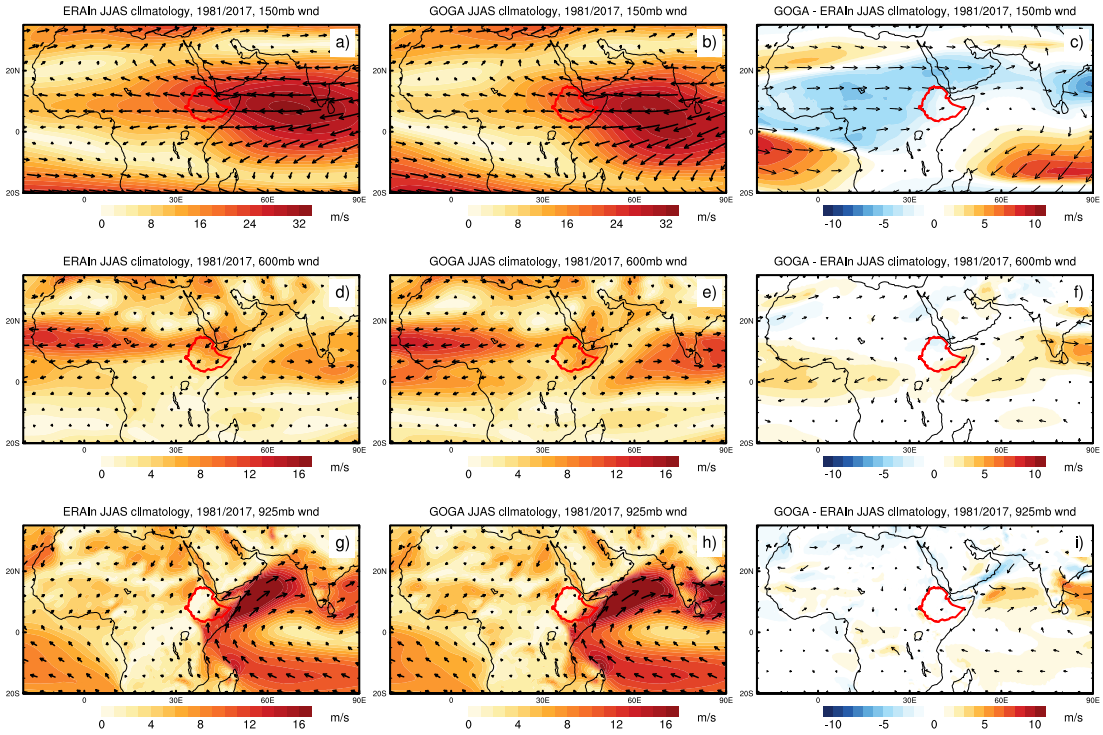

Figure 5.4: Spatial distributions of the seasonal (JJAS) mean climatology of horizontal wind speed (colored shaded) and direction (vectors) at: (a) 150-hPa, (d) 600-hPa, and (g) 925-hpa for the period 1981–2017 in ERAI. (b, e, h) As (a, d, g), but for GOGA. (c, f, i) Bias (difference) between GOGA and reanalysis. The border of Ethiopia is shown in red solid line. Unit is $m(s)^{-1}$ for wind.

Figure 5.4 also shows the 600-hPa wind climatology; at this level the AEJ is a prominent mid-tropospheric jet located over tropical north Africa during northern hemisphere summer as depicted by ERAI (Fig. 5.4d). The entrance of the AEJ extends to northeastern Africa and reaches a maximum over West Africa at about 16^{o}N. The intensity and position of the AEJ are known to influence the amount and variability of rainfall over West Africa. For example over the Sahel, a more equatorward position of the AEJ often corresponds with drought conditions (e.g., Nicholson *et al.*, 2008). Similarly, Diro *et al.* (2011b) have shown that the southward shift of the AEJ related to warm SST anomalies in the Pacific and the Kiremt Rains deficit. Compared to ERAI, it is evident that the model is able to reproduces the correct spatial extent and strength of the AEJ (Fig. 5.4e), although there are a significant overestimation of 600-hPa winds over southern Indian, the Bay of Bengal, and the eastern tropical Atlantic Ocean (Fig. 5.4f).

The model also captures the 925-hPa wind climatology reasonably well compared with ERAI over Africa and the Indian Ocean basin during boreal

summer. As shown in Figure 5.4h, the model simulates a realistic inter-hemispheric monsoon circulation in the lower atmosphere, composed of the easterlies over the south Indian Ocean, the SLLJ and the westerly winds passing through the Indian subcontinent. Moreover, the model captures the zonal location of convergence over the West African region with sufficient accuracy. One minor discrepancy is that the model simulates strong low-level westerlies over the Arabian Sea and the Bay of Bengal (Fig. 5.4i). The other two experiments have very similar climatologies of wind at 150, 600 and 925-hPa and are not shown. In general, ICON simulates the JJAS climatology of zonal and meridional wind patterns at the levels of the primary jets over the African-Indian Ocean area reasonably well, but with a slight underestimation of wind speeds at 150-hPa. This model bias may be ignored here, as the main objective of this study is to investigate the mechanisms for the Kiremt Rains interannual variability associated with the Pacific SSTs.

5.3 Interannual Variability of Kiremt Rains

As discussed in previous Chapters, the Ethiopian Kiremt Rains are subject to large year-to-year variations. These variations are related to SSTs and changes in the atmospheric circulation at regional and planetary scales (Segele *et al.*, 2009a; Diro *et al.*, 2011a,b). In this section, the SST-forced Kiremt Rains variability, and the atmospheric responses to the regional and large-scale circulation patterns are explored.

5.3.1 Kiremt Rains time-series

To explain the interannual variability of JJAS rainfall and its relation with ENSO, many studies focused on area-averaged rainfall which encompasses the crop-growing region of the Ethiopian Highlands (e.g., Jury, 2013; Gissila *et al.*, 2004; Korecha and Barnston, 2007). The ETHKRI used in this section is defined over the same region as in Jury (2013) and Bahaga *et al.* (2019). Figure 5.5a shows the negative of the JJAS ETHKRI time series (given in green and yellow bars) from CHIRPS2 for the period 1981 to 2017 as well as the N34 index (i.e. the area average JJAS SST anomalies in the region 170^o–120^{o}W, 5^{o}S–5^{o}N, given in red and blue bars). Most seasons with excessive rainfall occur during La Niña years. Similarly, the

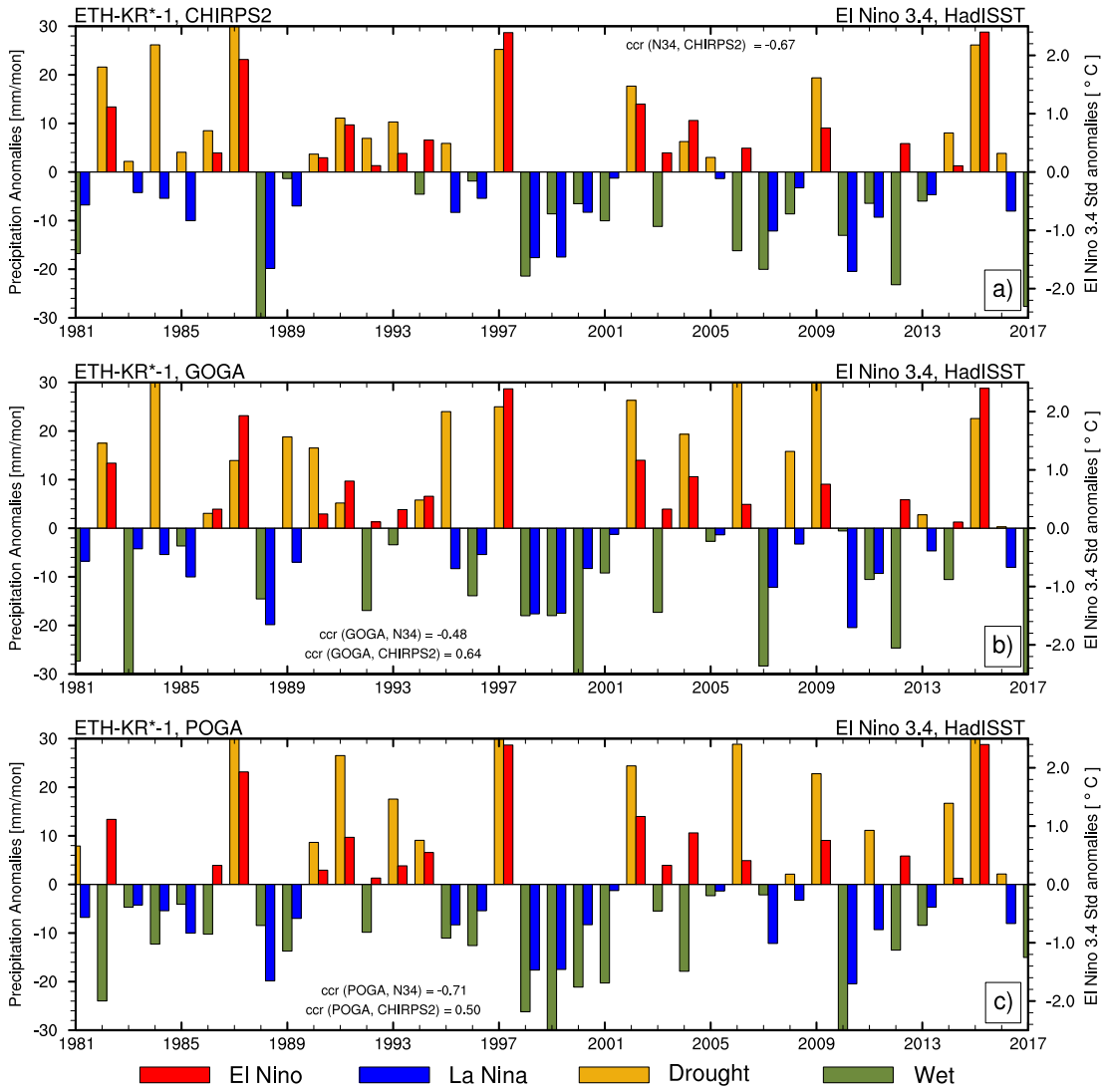

Figure 5.5: Time series of the interannual variability of Kiremt Rains shown in green and yellow bars; and N34 index (i.e. the area average JJAS SST anomalies in the region 170^o–120^oW, 5^oS–5^oN) in red and blue bars. (a) CHIRPS2, (b) GOGA, and (c) POGA. The correlation coefficient (ccr) among the three rainfall indices and with N34 index is given in the top and bottom. Units are $mm(mon)^{-1}$ for rainfall and ^{o}C for SSTs.

majority of droughts occur during El Niño years. The observed concurrent correlation between the Kiremt Rains time series and the N34 index is -0.65; this is significant at the 1% level, consistent with Bahaga *et al.* (2019). The corresponding model rainfall time series are given in Figure 5.5b and 5.5c for the GOGA and the POGA experiments, respectively. The extreme drought years (1982, 1987, 1991, 1997, 2002, 2009, and 2015) and excess years (1981, 1988, 1998/99, 2010, and 2017) are well captured. Moreover, the observed and the GOGA rainfall are statistically significantly correlated at the 1% level, with a correlation coefficient of 0.64. This indicates that a substantial

portion of the Ethiopian Kiremt Rains variability is SST-forced and that the model is reproducing this. In addition, the modeled Kiremt Rains and N34 are statistically significantly correlated at the 1% level, with a correlation coefficient of -0.48 in GOGA, while POGA shows a higher correlation of -0.71, which is closed to the observed correlation. These results further suggest that much of Kiremt Rains variability in the POGA simulation are induced by ENSO, while in the GOGA simulation, the SSTs influence from other ocean basins possibly counteracts the ENSO impact on the Kiremt Rains.

5.3.2 Leading mode of Kiremt Rains and its connection with ENSO

Because of complex topographical features, seasonal rainfall patterns over Ethiopia exhibit high spatial variation as discussed in Chapter 2. Previous studies delineated homogeneous rainfall regions and showed that different mechanisms are linked to SST-forced rainfall variations (Diro *et al.*, 2008; Tsidu, 2012; Zeleke *et al.*, 2013; Bahaga *et al.*, 2019). Such delineation can help to characterize the seasonal fluctuation in rainfall climatology and spatial distributions. However, this might limit the inclusion of the dominant mode of SST-forced Kiremt Rains year-to-year variability and decrease the coherent signal. To avoid such limitations and maximize the dominant mode of variability, an empirical orthogonal function (EOF) analysis is performed over the larger domain (32^o–49^oE, 4^o–15^oN), covering most parts of Ethiopia. The EOF analysis is applied to JJAS averaged monthly anomalies of CHIRPS2 and ICON simulated rainfall to extract the temporal variability that maximize the fraction of total variability that they represent. The analysis hereafter focuses only on the first leading modes of Principal Component (PC1) due to the high percentage (more than 50% in the model) of rainfall variability associated with it. Figure 5.6i depicts the PC1s of CHIRPS2 (green curve), GOGA (black curve), POGA (blue curve), and AIOGA (purple curve). These temporal variations explain 42%, 69%, 64%, and 55% of the total variance, respectively. The PC1s will be used to represent the interannual variability of the Ethiopian Highlands Kiremt Rains, and will be referred to as PC1. It is found that the correlation coefficient between the standardized PC1s and the JJAS N34 index are similar to the correlation between JJAS ETHKRI and N34 (Fig. 5.5, and 5.6i). Note however that the correlation between PC1 in AIOGA and N34 index is 0.42, which is positive

and significant at the 1% level. This implies that Atlantic and Indian Ocean SST forcing, while isolating the effects of Pacific SST, enhances summer rainfall across much of Ethiopia.

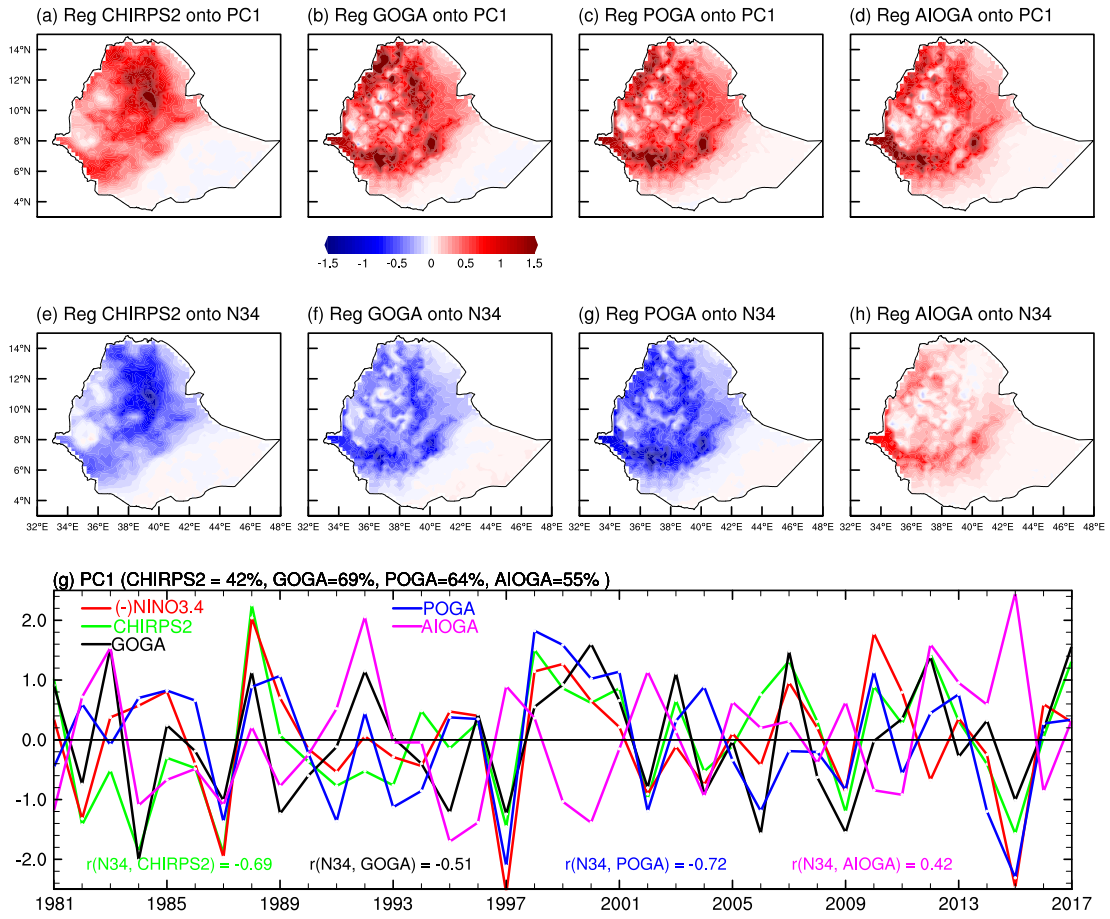

Figure 5.6: Regressions of JJAS rainfall anomalies onto the standardized leading principal components (PC1s) for the period 1981–2017. (a) CHIRPS2, (b) GOGA, (c) POGA, (d) AIOGA. (e, f, g, h) As (a, b, c, d), but regression onto N34. (g) Year-to-year variation of PC1s in the CHIRPS2 and the ICON experiments, along with the negative of the JJAS N34 index. Units are $mm(day)^{-1}$ for rainfall in (a)–(h).

To elucidate the relationship between ENSO and the Ethiopian Kiremt Rains variabilities in observations and in the model outputs, Figure 5.6 shows the regression pattern of the CHIRPS2 (Fig. 5.6e), GOGA (Fig. 5.6f), POGA (Fig. 5.6g), and AIOGA (Fig. 5.6h) JJAS rainfall anomalies onto the standardized N34 index for the 1981–2017 period. As can be clearly identified from Figures 5.6e, 5.6f and 5.6g, ENSO leads to a substantial reduction of Ethiopian Kiremt Rains (e.g., up to 1.5 $mm(day)^{-1}$ in CHIRPS2, particularly over drought prone regions of northeastern Ethiopia). The correspondence between model (GOGA and POGA) and observations is overall very good,

with the exception of south and southwestern parts of the country, where a larger than observed decrease in rainfall is simulated in response to El Niño events. In the AIOGA (Fig. 5.6h) the regression patterns are rather opposite with a tendency for enhanced rainfall over parts of Ethiopia, especially in the southwest. It is also found that amplitude and structure of regression patterns of JJAS rainfall anomalies over Ethiopia onto the corresponding standardized PC1 in the Figures 5.6a, 5.6b and 5.6c are similar but opposite in sign when rainfall anomaly are regressed onto N34. The regression patterns in AIOGA (Fig. 5.6d) produce marked enhanced rainfall over most parts of Ethiopia (thus counteract the effect of the usual contemporaneous SST anomalies in the Pacific Ocean), the reason behind this is examined in the later section. Overall, the model Kiremt Rains regression patterns are consistent with the observed rainfall in Ethiopia; El Niño (La Niña) episodes events are related to enhanced (reduced) summer rainfall across much of the country. This is also consistent with previous works (Segele *et al.*, 2009a; Diro *et al.*, 2011a,b; Zeleke *et al.*, 2013). Notably, the regression of Kiremt Rains anomalies on N34 (Fig. 5.6h) illustrates that the AIOGA experiment produces positive rainfall anomalies. Rather than showing reduced rainfall over Ethiopia, as seen in the observations (Fig. 5.6e), and in both the GOGA (Fig. 5.6f) and the POGA (Fig. 5.6g) results, the AIOGA results show a markedly enhanced rainfall over much Ethiopia. This opposite regression pattern in AIOGA relates to the elimination of the reducing effect typical of ENSO forcing on the Ethiopian Kiremt Rains. In other words, SST influence from the Atlantic and Indian Oceans on Ethiopian Kiremt Rains oppose the ENSO impact in the model. The next subsection will discuss the link between SSTs and the Kiremt Rains in terms of large-scale circulation anomalies both in observation and the modelling experiments.

5.3.3 Atmospheric features and SSTs associated with the Kiremt Rains PCs

The discussion above is based on correlation and regression results produced from the leading mode of Ethiopian Kiremt Rains and N34 time series, using gridded seasonal rainfall anomalies. Now the focus of this section is to examine and see the structure of the patterns of SST and large-scale atmospheric circulation anomalies that are associated with Ethiopian rainfall by

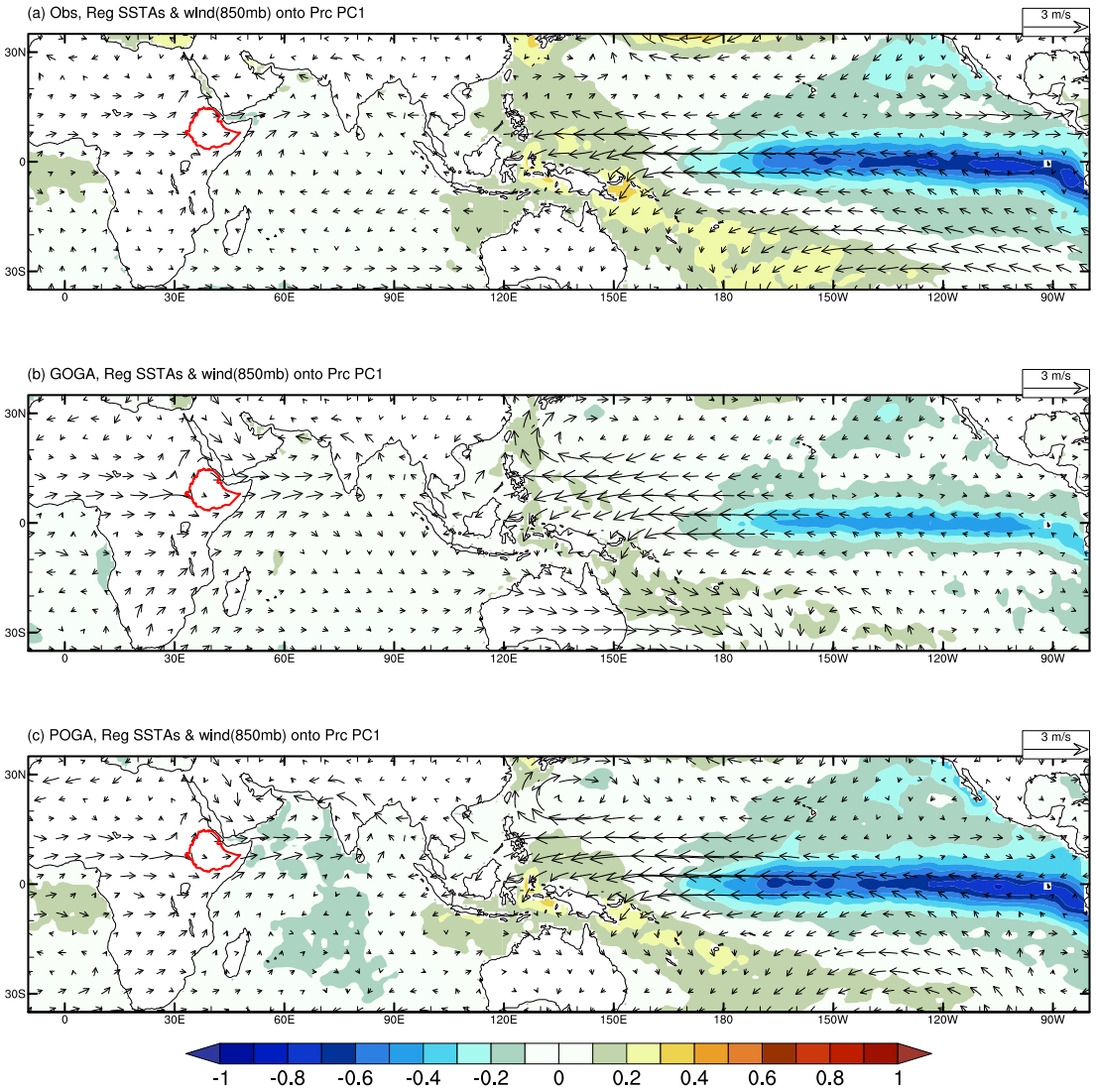

Figure 5.7: Regressions of JJAS anomalies of HadISST1 (colored shade) and 850-hPa wind (vectors) onto the standardized leading principal components (PC1s) for the period 1981 to 2017. (a) CHIRPS2 and ERAI, (b) GOGA, and (c) POGA. Units are ^oC for SSTs and $m(s)^{-1}$ for wind. The border of Ethiopia is delineated by a solid red line.

regressing the leading mode of the year-to-year variability of Kiremt Rains onto the JJAS SST, geopotential height (GH), and wind at 925, 850, 600, and 150-hPa. Such analysis can be used as an indicator of how well rainfall couples to SST, which in the ICON experiments are imposed. This is relevant because the year-to-year variability of rainfall is more related to phenomena like El Niño, and the question is whether the model rainfall is associated with SST in the same way as the observed rainfall. In Figure 5.7 the JJAS SST and 850-hPa wind anomalies are regressed against standardized PC1 for the period 1981 to 2017. Consistent with previous studies (Diro *et al.*, 2011b;

Segele *et al.*, 2009a; Bahaga *et al.*, 2019), La Niña like pattern appears in observation, characterized by prominent SSTs cooling over the equatorial Pacific Ocean (Fig. 5.7a). This indicates that the wet rainfall events in Ethiopia during the Kiremt Rains season are associated with decreasing SSTs in the central and eastern equatorial Pacific, typical of the ENSO phenomenon. As is the case of high anticorrelation between the PC1 and N34 index, the SST anomalies regressed onto the PC1 in POGA (Fig. 5.7c) accurately reflect the observed characteristics. For instance, La Niña like pattern with the cold SST anomalies in the central and eastern Equatorial Pacific, and relatively the warm SST anomalies southwest Equatorial Pacific represented reasonably well. The regression pattern of the SST anomalies onto the PC1 in GOGA (Fig. 5.7b) also shows significant cold anomalies in the equatorial Pacific, albeit weaker and not extended further into the West Pacific. This is consistent with relatively lower negative correlations with N34 (Fig. 5.6i).

Figure 5.7 further shows the regression pattern of the JJAS 850-hPa wind anomalies onto the PC1s both in observation and model. Consistent with the cooling of the equatorial Pacific (Fig. 5.7a), the atmosphere responds with enhanced low-level easterly wind anomalies from the central eastern to the western Pacific. Moreover, ERAI shows southwesterly anomalies along the East African coast and therefore an enhancement of the SLLJ, and the strength of westerly winds from the Atlantic ocean and Congo basin (Fig. 5.7a). Both the GOGA (Fig. 5.7b) and POGA (Fig. 5.7c) experiments are able to reproduce low-level wind regression patterns, such as the band of strong easterly anomalies from the central eastern Pacific, westerly anomalies over Africa, and the strengthening of the SLLJ. Although both experiments capture the anomalous low-level wind spatial structure qualitatively, they show stronger westerly bias over the Arabian Sea, in particular, the GOGA experiment simulates unrealistic westerly anomalies over Australia and the southwest Pacific Ocean. In brief, the result indicates the low-level link between cool Pacific SSTs and the wet Kiremt Rains via the strengthening of SLLJ and enhanced westerlies from the Atlantic region and Congo basin. This is in agreement with Diro *et al.* (2011b).

To investigate further the relationship between the modeled Kiremt Rains variability and circulation anomalies at the levels of the major jets, Figure 5.8b, 5.8d, and 5.8f shows regression pattern of GH and wind anoma-

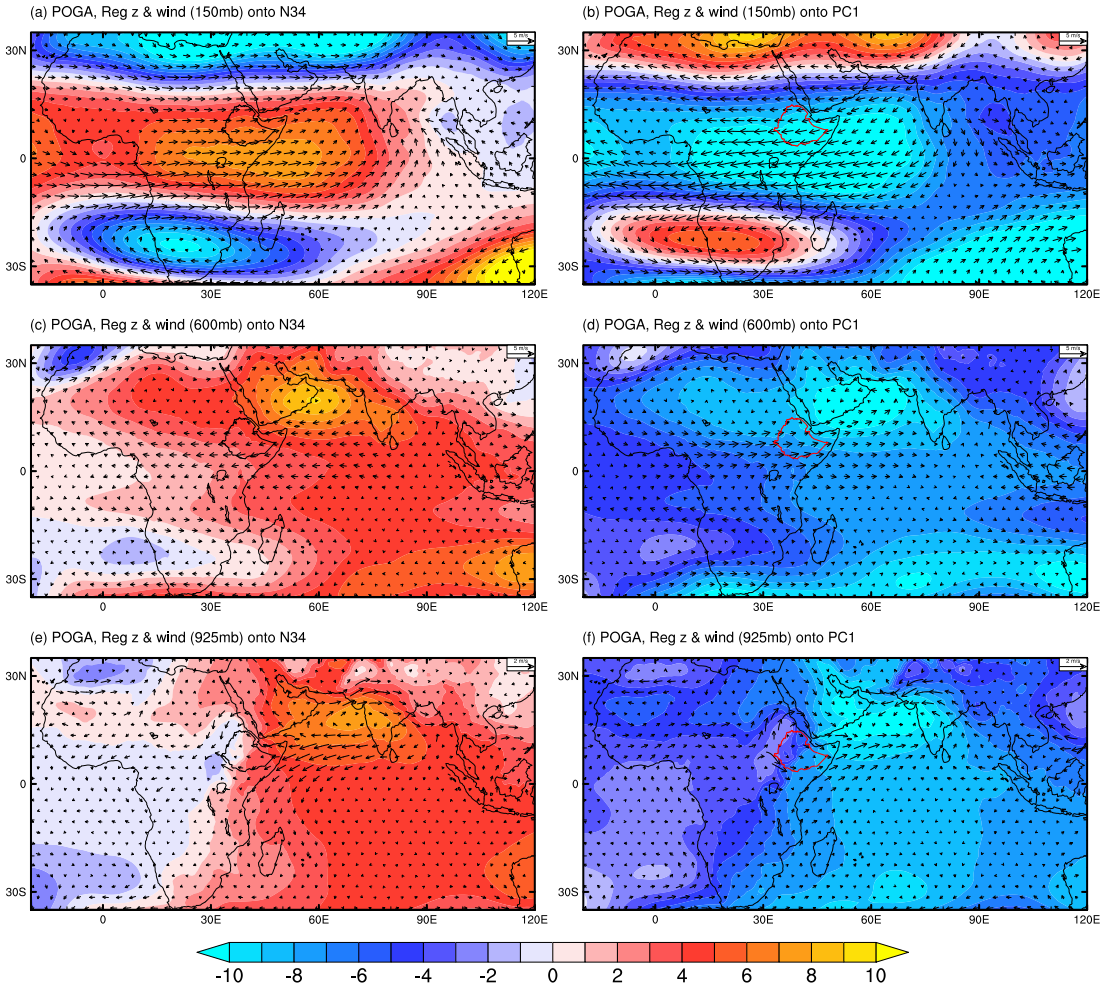

Figure 5.8: Regressions of JJAS seasonal anomalies of geopotential height (colored shade) and wind (vectors) at (a) 150-hPa, (c) 600-hPa and (e) 925-hPa onto the standardized N34 index for the period 1981 to 2017. (b, d, f) As in (a, c, e) but onto standardized PC1. All regressions patterns are derived from POGA. The border of Ethiopia is delineated by a solid red and black line. Units are m for geopotential height and $m(s)^{-1}$ for wind.

lies onto PC1 in the POGA at 150-hPa, 600-hPa, and 925-hPa, respectively. Consistent with the anomalous low SST in the central eastern tropical Pacific associated with PC1 in POGA (Fig. 5.7c), it is clear to see that negative GH anomalies at the surface cover virtually the whole Indian Ocean and Africa (Fig. 5.8f), which is the typical signature of the Southern Oscillation (Trenberth and Shea, 1987). Furthermore, there are marked negative GH anomalies in the Indian monsoon trough region over the Arabian Peninsula, western coast of India, and Arabian Sea; along with a gradient of GH anomalies between the Arabian Peninsula and the Gulf of Guinea and negative GH anomalies increasing up to 600-hPa (Fig. 5.8d). This contributes to a strengthening of the SLLJ over the Arabian Sea and enhanced lower-to-

mid tropospheric moist westerlies from the Atlantic Ocean and Congo basin into Ethiopia (Fig. 5.8d, 5.8f). These results suggest that the POGA experiment correctly captures the relationship between the wet Kiremt Rains and cold equatorial Pacific SST anomalies via local circulation changes, in agreement with ERAI (not shown). This is also consistent with previous works (Camberlin, 1997; Segele *et al.*, 2009a; Diro *et al.*, 2011b).

The climatological pattern of upper-level horizontal winds, specifically the TEJ is discussed in section 1.3, and well represented in the model (Fig. 5.4b). The Kiremt Rains variability is also associated with the TEJ via enhancing (suppressing) of the vertical motion (Segele *et al.*, 2009a; Diro *et al.*, 2011b). To see if these features are present in the POGA experiment, Figure 5.8b shows the regression of 150-hPa horizontal wind and GH anomalies onto PC1. It is clear that there are strong easterly wind anomalies over the northwestern Indian Ocean and tropical Africa, suggesting that a strengthening of the TEJ is strongly associated with wet Kiremt Rains over Ethiopia, which reaffirms the previous studies. This in turn is associated with La Niña like negative SST anomalies over the equatorial eastern Pacific (Fig. 5.7c). Besides, there are negative GH anomalies over the northwestern Indian Ocean and tropical Africa, and positive GH anomalies at high latitudes over northern and southern Africa which is conducive for the strengthening of the TEJ (Fig. 5.8b). This supports the idea of the upper-level teleconnection between Pacific SST anomalies and the Kiremt Rains year-to-year variability via a strengthening of the TEJ. Overall, investigation of the SSTs forced model response based on regression patterns of the leading mode of JJAS Kiremt Rains shows that the wet Kiremt Rains events in the model are associated with a stronger TEJ, enhanced westerly influx from the Atlantic Ocean and Congo basin, and a stronger SLLJ (Figs. 5.8b, 5.8d, and 5.8f). These results suggest that the model successfully captures the relationship between Pacific SSTs and the Kiremt Rains variability via large-scale atmospheric circulation changes.

5.3.4 Atmospheric features and SSTs associated with ENSO

The above results are based on the dominant mode of the Ethiopian Kiremt Rains variability. The patterns for other variables are investigated from concurrent regressions against PC1 both in the model and observation.

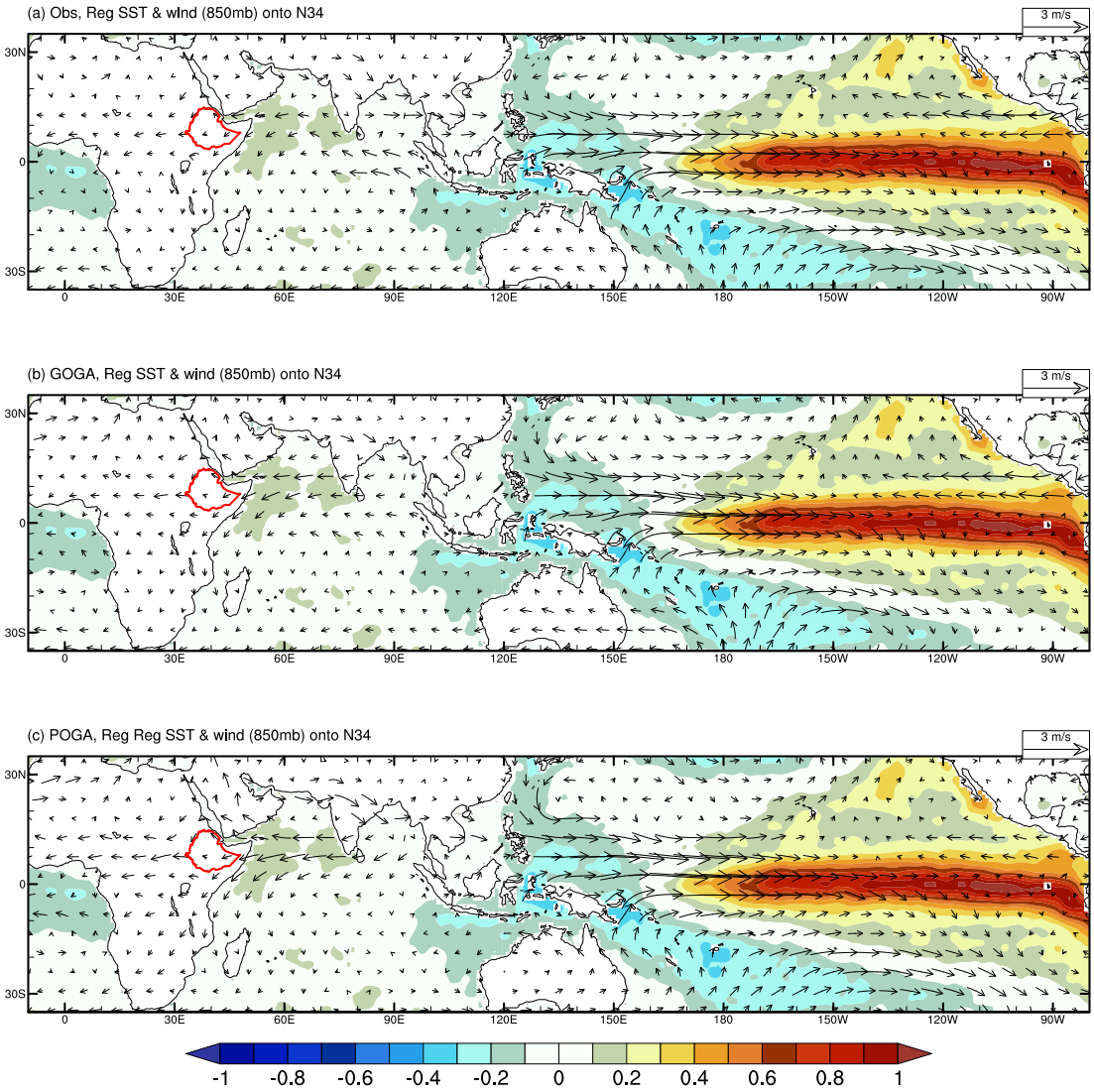

Figure 5.9: Regressions of JJAS anomalies of HadISST1 (colored shade) and 850-hPa wind (vectors) onto the standardized N34 for the period 1981 to 2017. (a) ERAI, (b) GOGA, and (c) POGA. Units are ^oC for SSTs and $m(s)^{-1}$ for wind. The border of Ethiopia is delineated by a solid red line.

On the contrary, it is shown that there is maximum negative correlation (-0.72) between the PC1 in POGA and N34 index (Fig. 5.6i), and thus the regressions against N34 might lead to the opposite large-scale atmospheric circulation patterns. To verify this, the regression analysis is further performed against the N34 index, as in Figure 5.9. The pattern in HadISST1 shows a warm SST anomalies extending broadly over the east and central equatorial Pacific, along with a pattern of cold SST anomalies over the western and southwestern Pacific region. The slightly cold SST anomalies in the Gulf of Guinea might indicate the result of atmospheric teleconnections with

El Niño (see, e.g., Rodríguez-Fonseca *et al.*, 2009). Figure 5.9a further shows a linear regression analysis of the JJAS anomalies of 850-hPa winds onto the N34 in ERAI. Due to anomalously warm SSTs in the central eastern Pacific, the atmosphere responds with the weakening of the low-level easterlies suggested by the reversal of the wind directions. In contrast to the regression pattern against PC1 (Fig. 5.7a), the N34 regression shows northeasterly anomalies along the East African coast and the Arabian Sea, and therefore a weakening of the SLLJ, and reduced westerly wind anomalies across western and central Africa (Fig. 5.9a). Both the GOGA (Fig. 5.9b) and POGA (Fig. 5.9c) experiments are able to reproduce low-level wind regression patterns, for instance, the weakening of the low-level easterlies anomalies from the central eastern Pacific, reduced westerly anomalies across western and central Africa, and the weakening of SLLJ. These results suggest the low-level link between El Niño and the dry Kiremt Rains events via the weakening of SLLJ and westerlies across western and central Africa. Corresponding observation studies revealed similar evidence (Camberlin, 1997; Segele *et al.*, 2009a).

The ENSO-Kiremt Rains relation in the POGA is further evaluated by computing regression of atmospheric circulation anomalies against N34. Figure 5.8a, 5.8c, and 5.8e shows regression pattern of GH and wind anomalies onto N34 in the POGA at 150-hPa, 600-hPa, and 925-hPa, respectively. The regression pattern in the Pacific is characterized by warm SST anomalies over the central eastern tropical sector and cold SST anomalies on the western side (Fig. 5.9a). The anomalous high SSTs in the central eastern tropical Pacific leads to large scale positive GH anomalies over the Indian Ocean, the Arabian Peninsula, East Africa, and the Indian monsoon trough region at 600 and 925-hPa (Figs. 5.8c and 5.8e). Consequently, the N34 regression of low-level wind in the POGA produces a reduced SLLJ and weakened westerly winds from the Atlantic and central Africa. This is clear from the northeasterly wind anomaly vectors over the East African coast and the Arabian Sea (Fig. 5.8e), and the easterly anomalies over west and central Africa (Fig. 5.8c). The weakening of these low-to-mid level winds will directly reduce the moisture influx to Ethiopia from both the Atlantic and Indian Ocean and hence would be expected to give rise to reduced rainfall (Fig. 5.6g). To further demonstrate the relationship between ENSO and the Kiremt Rains variabilities via an upper-level link in the POGA output,

Figure 5.8a shows the regression pattern 150-hPa horizontal wind and GH anomalies onto the N34 index. As can be clearly identified in Figure 5.8a, El Niño leads to positive GH anomalies over the northwestern Indian Ocean and tropical Africa, and negative GH anomalies at high altitude over northern and southern Africa, which is a reverse atmospheric condition compared to the regression pattern onto PC1 (Fig. 5.8b). Moreover, the regression of 150-hPa horizontal wind anomalies onto N34 shows a decrease in strength of the TEJ. This can be seen in westerly wind anomaly vectors at 150-hPa over tropical Africa and the northwest Indian Ocean (Fig. 5.8a). These results strongly suggest that the Ethiopian Kiremt Rains are modulated by the effect of the equatorial Pacific SST anomaly on the TEJ, with a warm anomaly leading to weakening of the TEJ and thus reducing rainfall over Ethiopia.

Overall, the circulation anomalies associated with El Niño events in the POGA experiment lead to weaker low-to-mid level westerlies across western and central Africa, which are produced by a GH gradient resulting from negative anomalies over the Gulf of Guinea and weakening of the monsoon trough across the Arabian Peninsula. Furthermore, El Niño events further lead to a weak TEJ at the upper levels and a weak SLLJ near the surface. Consistent with previous studies these results reaffirm that Pacific only SST-forced ICON simulation can reproduce observed circulation changes associated with El Niño, thus induced the dry Kiremt Rains events.

5.4 Physical Mechanism for the ENSO Influence on Kiremt Rains

In this section, the physical mechanisms by which the Pacific Ocean influences the Ethiopian Kiremt Rains' interannual variability are further analyzed both in the model and ERAI. The focus is on the Pacific ocean. Therefore, here results from the POGA experiment is presented, but results for the GOGA experiment are very similar. On the other hand, the PC1 in the AIOGA experiment shows positive correlation with N34 (Fig. 5.6); this imply that Atlantic and Indian Ocean SST forcing, while isolating the effects of Pacific SSTs, enhances summer rainfall across much of Ethiopia. Why do the PC1 in the AIOGA experiment produce significant positive correlation with N34 on the contrary to the anticorrelation in the POGA and GOGA?

In order to answer this question, composite analyses are performed. Based on the definition of ENSO from Trenberth (1997), composites of atmospheric fields for the five El Niño and five La Niña events are constructed. The years used as an input for composite analysis are shown in Table 5.1.

Table 5.1: Years of ENSO events considered in the composite analysis of atmospheric fields

El Niño	La Niña
1982	**1988**
1987	**1998**
1997	**1999**
2009	**2007**
2015	**2010**

Figure 5.10 shows the result for the composite analysis of MSLP and 850-hPa wind anomalies associated with the ENSO events in: ERAI (Fig. 5.10a), GOGA (Fig. 5.10b), POGA (Fig. 5.10c), and AIOGA (Fig. 5.10a) for the JJAS season. The positive anomalies of MSLP over Africa, the Arabian Peninsula, and the Indian Ocean, and the negative anomalies over the central and eastern Pacific Ocean are a distinctive signature of Southern Oscillation associated with the ENSO response in the observations (Fig. 5.10a; Trenberth and Shea, 1987). Consistent with this result, the composite pattern of JJAS anomalies of wind at 850-hPa (Fig. 5.10a) shows weakening of easterly wind anomalies over the central western Pacific ocean, along with a cyclonic structure over subtropical Pacific Ocean. This supports the regression of 850-hPa wind anomalies onto N34 index (Fig. 5.9a). The ENSO composite also shows a northeast-southwest pressure gradient between the Gulf of Guinea and Arabian Peninsula, which is consistent with the weakening of the monsoon trough over the Arabian Sea (Fig. 5.8c and 5.8e). The weakening of the monsoon trough can be seen as reduced westerlies over Africa, an anticyclonic anomaly, and the weakening SLLJ over the Arabian Sea. Furthermore, the low-level easterly anomalies over the eastern Pacific, Atlantic, and Africa are related to a Gill-type response to the central eastern tropical Pacific Ocean heating as described by Gill (1980). The weakening of the SLLJ (easterly) anomalies over the west and central Africa means less moisture being advected to the GHA from Indian (Atlantic) Ocean, which in

turn reduces the Kiremt Rains over Ethiopia. These results are in agreement with Figs. 5.8c, 5.8e, and 5.9a.

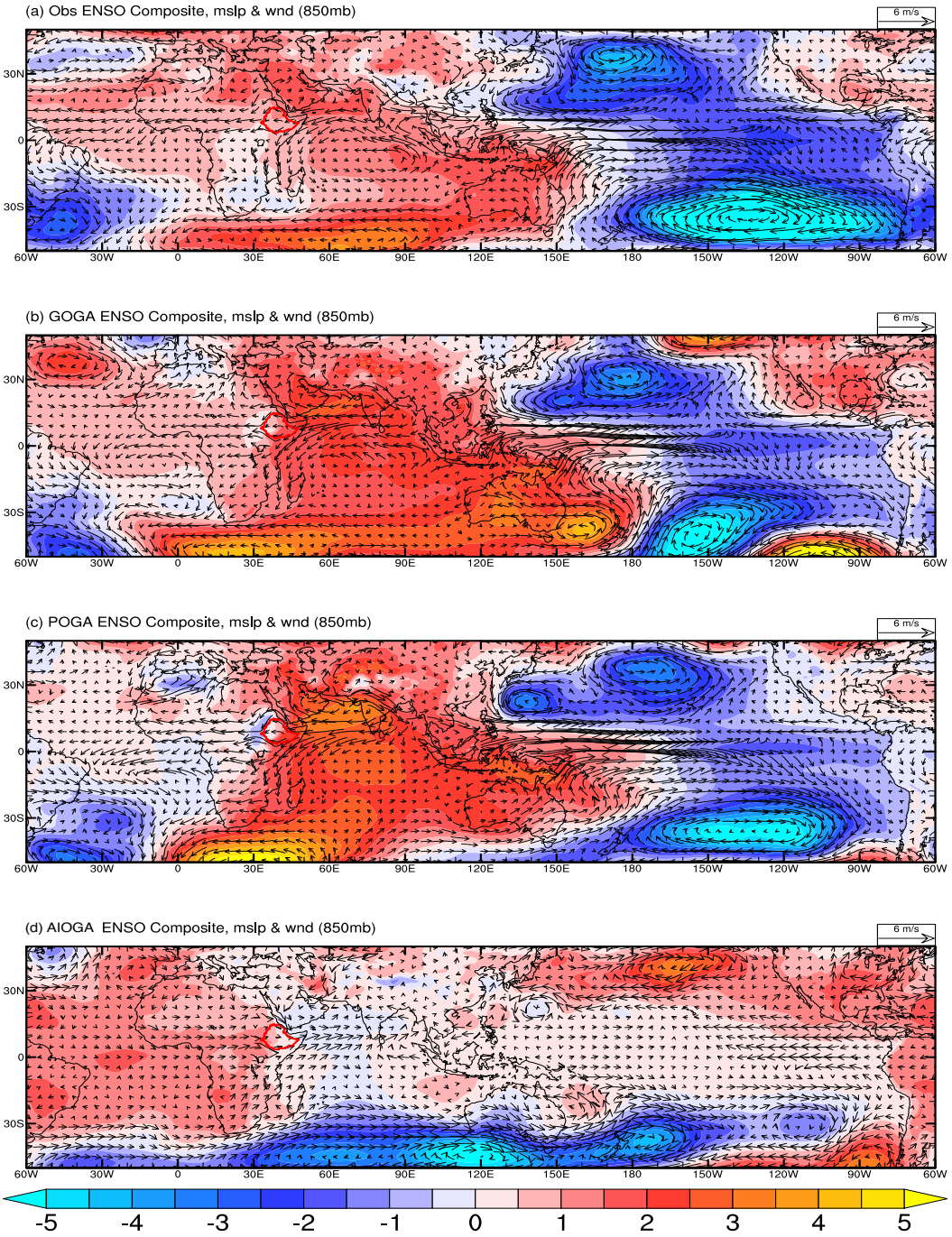

Figure 5.10: Composite of ENSO events for JJAS mean MSLP (colored shade) and 850-hPa wind anomalies (vector) derived from: (a) ERA-Interim, (b) GOGA, (c) POGA, and (d) AIOGA. Units are hPa for MSLP and $m(s)^{-1}$ for wind.

The distribution of the MSLP composite derived from the GOGA (Fig. 5.10b) and the POGA (Fig. 5.10c) experiments reproduces the positive anomalies over Africa, the Arabian Peninsula, and the Indian Ocean, and negative

anomalies over the central and eastern Pacific Ocean; despite unrealistic positive MSLP anomalies around 35^{o}S, 135^o–80^{o}W in the GOGA. Simulated low-pressure anomalies over the central and eastern Pacific Ocean may be interpreted as a response induced by the warm ENSO events (Fig. 5.9b, and 5.9c). These simulations are also able to reproduce the weakening of easterly wind anomalies over the central western Pacific Ocean; easterly anomalies over the eastern Pacific, Atlantic, and Africa as well as anticyclonic anomaly and weakening SLLJ over the Arabian Sea. The change in circulation anomalies are associated with the warm ENSO episodes and thus reflected in a deficit rainfall composite over Ethiopia (not shown), which is consistent with a significant negative correlation between N34 and PC1 in the GOGA and POGA (Fig. 5.6i). The AIOGA experiment (Fig. 5.10d), on the other hand, shows an extensive area of positive MSLP anomalies over the tropical and north Pacific Ocean, in contrast to the negative anomalies both in the POGA and GOGA. It is also clear that there are positive MSLP anomalies over the Atlantic Ocean, and Africa, and an area of negative anomaly over the central Indian Ocean, and the Arabian Sea. This leads to strong low-level westerly wind anomalies from the Atlantic Ocean and central Africa to Ethiopia. Furthermore, a strong SLLJ over the East African coast and Arabian Sea is associated with the MSLP gradient resulting from intensification over the Gulf of Guinea and deepening of the monsoon trough across the Arabian Sea (Fig. 5.10d). Thus, enhanced westerlies across western and central Africa and a strong SLLJ lead to above normal Ethiopian Kiremt Rains in the AIOGA (not shown). This excess Kiremt Rains composites for ENSO events and a positive correlation between PC1 in AIOGA and N34 are comparable with the result shown by Segele *et al.* (2015), based on regional modeling experiments for the period of 1971–2000, who showed that warmer Atlantic Ocean SSTs generally brought wetter conditions to northern Ethiopia. In addition, Srivastava *et al.* (2018) showed that after 1980, El Niño (La Niña) tends to occur simultaneously with negative (positive) ATL3 and this in turn reduced (enhanced) the WAM by increased south-westerly moisture flux. Generally, the results from the AIOGA experiment, compared to GOGA and POGA, indicate that the Southern Oscillation center shifts westward, creating pressure gradient between the Atlantic and Indian Ocean, which lead to enhanced westerlies and a strong SLLJ and thus wetter Kiremt Rains over Ethiopia.

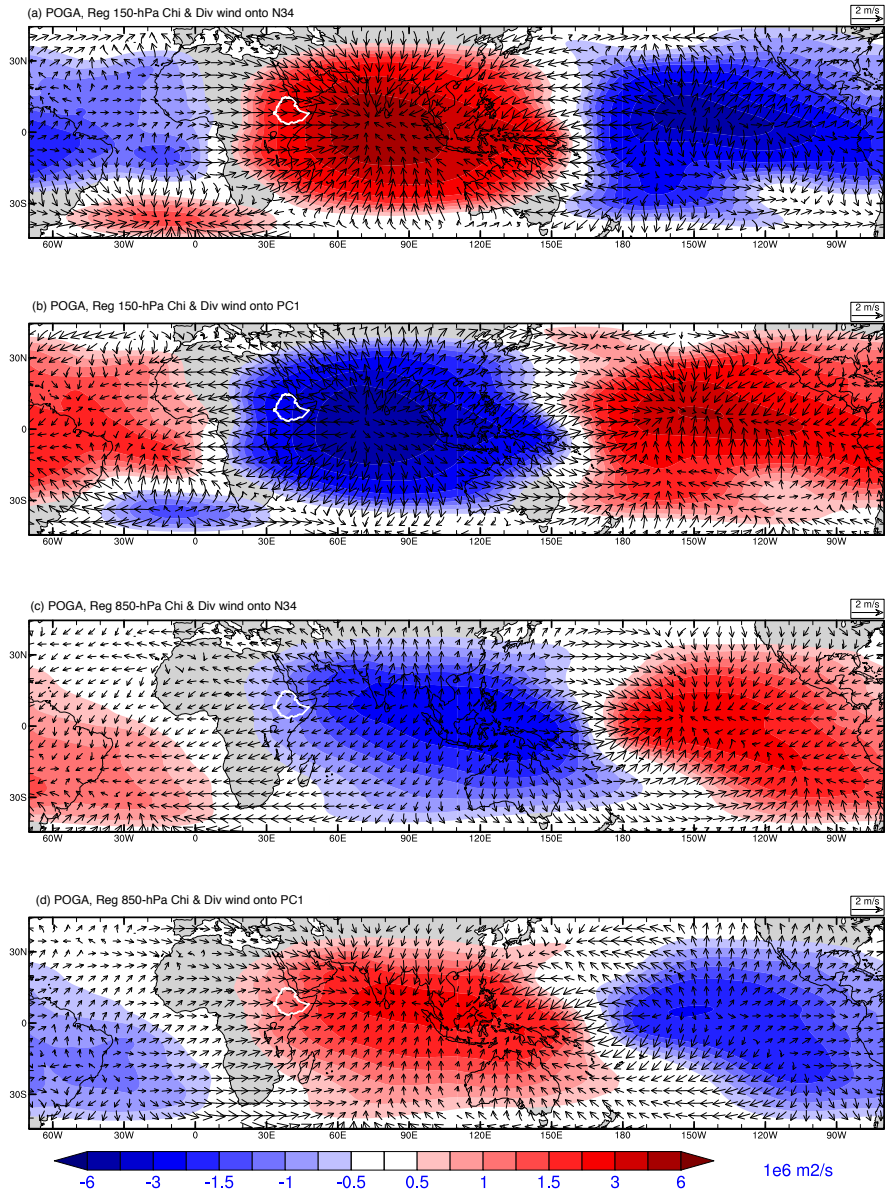

Figure 5.11: Regressions of JJAS velocity potential (colored shade) and corresponding divergent wind (vectors) obtained from the POGA experiment onto: (a) N34, at 150-hPa, (b) PC1, at 150-hPa; (c) As a, but at 850-hPa, and (d) as b, but at 850-hPa. Units are $10^6 m^2(s)^{-1}$ for velocity potential and $m(s)^{-1}$ for wind. The border of Ethiopia is delineated by a solid white line.

In order to further substantiate the presented results, the lower and upper-level circulation changes associated with N34 and PC1 are investigated. Velocity potential at 850 and 150-hPa can be used as an indicator of large-scale circulations that reflect lower (upper) level convergence (divergence), and vice versa (e.g., Tanaka *et al.*, 2004). A positive velocity

potential indicates large-scale convergence, which at 150-hPa can be related to sinking motion, while negative values indicate divergence and upward motion. To explore the mechanism of the ENSO-Kiremt Rains teleconnection in the POGA experiment, Figure 5.11 demonstrates the regression of JJAS velocity potential and the corresponding divergent wind anomalies at 150-hPa (Fig. 5.11a) and 850-hPa (Fig. 5.11c) onto N34. Consistent with the MSLP response shown in Figure 5.10c, there are low-level convergence and upper-level divergence anomalies associated with El Niño over the equatorial central and eastern Pacific Ocean. A reverse pattern of lower-level divergence and upper-level convergence occurs over the Maritime Continent, the Indian Ocean, and the GHA, indicating a Walker-Cell like response to ENSO with upward anomalies over the warm SST in the east and central Pacific and balancing downward anomalies over the whole Indian Ocean region. ERAI shows a very similar circulation anomaly (not shown). The upper (lower) level positive (negative) velocity potential anomalies directly over Ethiopia and the corresponding westerly (easterly) divergent wind associated with the N34 index indicate the influence of ENSO on the Kiremt Rains via suppression of convection ;the weakening of the TEJ (Fig. 5.8a) (reducing moist westerlies (Fig. 5.8e)) from the Atlantic Ocean and Congo basin and, thus reducing rainfall over Ethiopia (Fig. 5.6g). Some of these are in agreement with the mechanisms proposed by Diro *et al.* (2011b).

To further examine the mechanism of ENSO-Kiremt Rains teleconnection, the Walker circulation is computed. Figure 5.12 shows longitude-height cross-sections of regression of the JJAS vertical wind speed (colored shade), and zonal and vertical wind anomalies (vectors) for ERAI onto N34 (Fig. 5.12a) and PC1 (Fig. 5.12b). The anomalously warm SSTs in the central and eastern equatorial Pacific during El Niño years favor convection, which reorganizes the Walker circulation throughout the tropics, with anomalous rising motion over the central and eastern equatorial Pacific, descending motion over the far western Pacific, Atlantic, west Africa, Indian subcontinent, and Ethiopia (Fig. 5.12a). The situation is quite similar but opposite sign during the wet Kiremt Rains events, which shows enhanced vertical ascending motion over the western Pacific, Atlantic, West Africa, Indian Ocean, and Ethiopia, and therefore intensified convective activity (Fig. 5.12b).

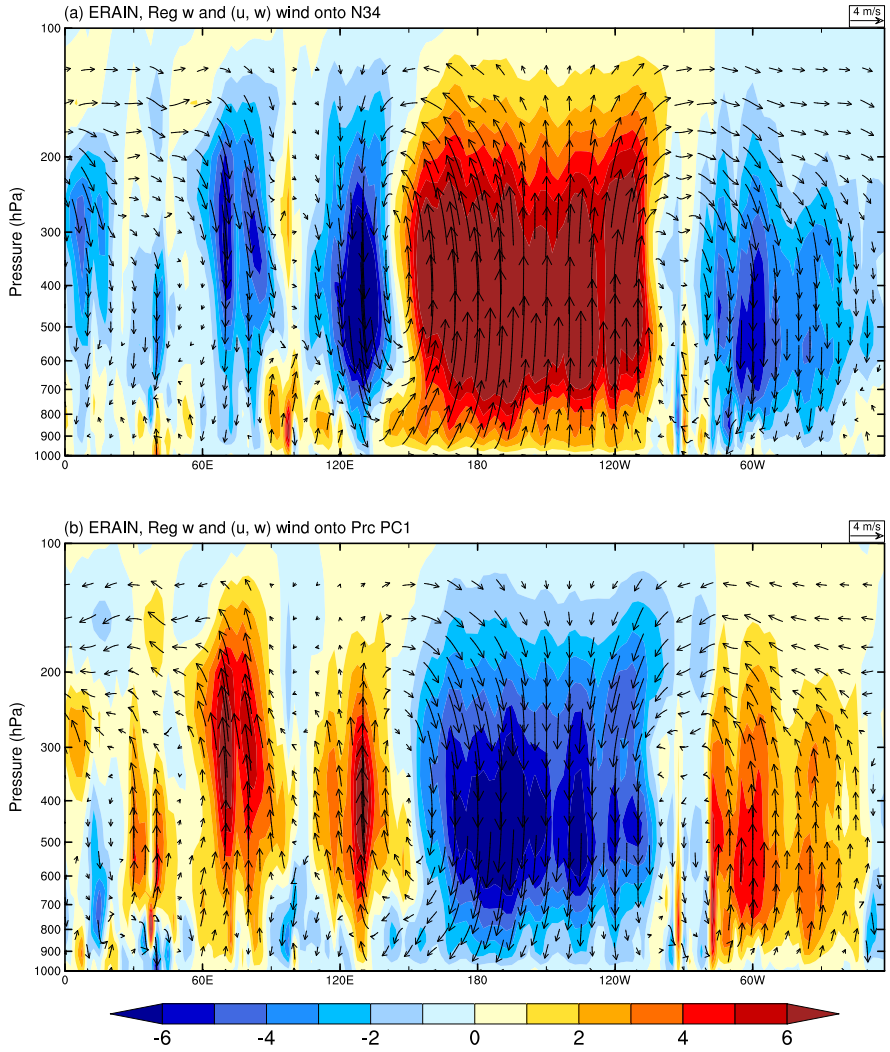

Figure 5.12: Height-longitude cross-section of regressions of JJAS vertical wind speed (colored shade; positive values indicate ascending motion), and vertical and zonal wind (vectors) obtained from ERAI onto: (a) N34, and (b) PC1. All variables are averaged from 5 to 15 N on 20 pressure levels. Unit is $m(s)^{-1}$ both for horizontal and vertical wind.

Additionally, the regression of velocity potential and corresponding divergent wind at 150-hPa (Fig. 5.11b) and 850-hPa (Fig. 5.11d) onto PC1 displays a pattern quite similar but of opposite sign to the one regressed onto N34. In the upper (lower) level negative (positive) anomalies are seen in the Indian Ocean region and GHA leading to divergence (convergence), this favors enhanced ascending motion (Fig. 5.12b). Consistent with the 150-hPa (850-hPa) negative (positive) velocity potential anomalies there are easterly (westerly) divergent wind anomalies over Africa. These results support the idea that the wet Kiremt Rains events are strongly linked to a strengthening TEJ (Fig. 5.8a) via upper-level divergence and anomalous ascending motion.

Therefore, the teleconnection between cold Pacific SSTs (Fig. 5.7c) and the wet Kiremt Rains is an upper-level link via a strengthening of the TEJ.

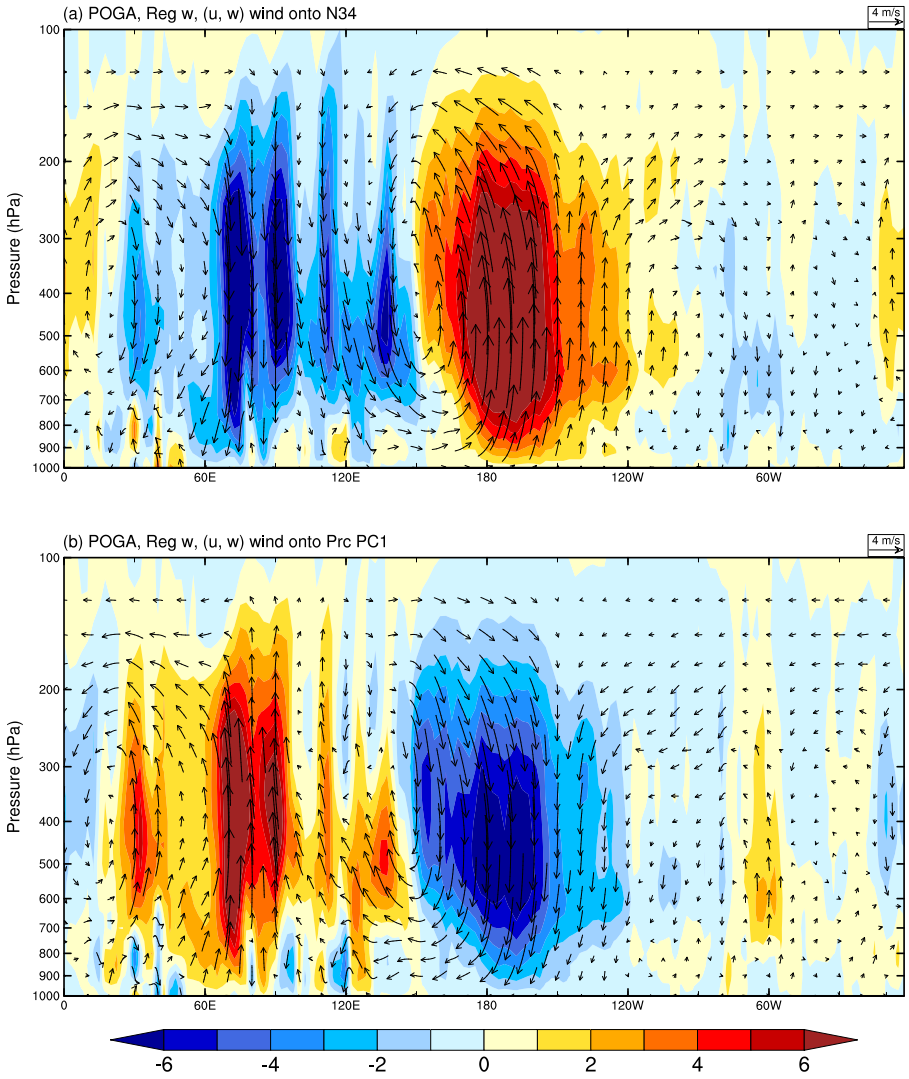

Figure 5.13: As Figure 5.12, but obtained from the POGA experiment regressed onto: (a) N34, and (b) PC1.

The POGA experiment reproduces the observed equatorial Walker circulation anomalies associated with the ENSO-Kiremt Rains teleconnection very well, as seen in Figure. 5.13. Changes in the model longitude-height cross-sections of vertical wind anomalies associated with N34 (PC1) show anomalous ascending (descending) motion over the equatorial central and eastern Pacific and anomalous descending (ascending) motion over the western Pacific and Indian Ocean region (Figs. 5.13a and 5.13b). The anomalous Walker circulation in the POGA is typical of an ENSO response and consistent with the result in ERAI (Fig. 5.12), albeit with weaker sinking (rising)

branches of the Walker circulation associated with N34 (PC1) located in the equatorial Atlantic.

On the whole, these results indicate that El Niño (La Niña) phase of ENSO drives anomalous dry (wet) Kiremt Rains (Figs. 5.6c, 5.6g, 5.7c, and 5.9c) through modification of the Walker circulation. This leads to sinking (rising) and upper-level convergence (divergence) motion right over Ethiopia and rising (sinking) motion and upper-level divergence (convergence) in the central eastern tropical Pacific region (Figs. 5.11a, 5.11b, 5.13a, and 5.13b). The sinking motion over the GHA region instigates upper (lower) level westerly (easterly) wind anomalies over Africa leading to weakening TEJ (reducing moist westerlies) from the Atlantic and Congo basin and, thus a reduction of the Kiremt Rains over Ethiopia (Figs. 5.6g, Fig. 5.8a, Fig. 5.8e); but the response for wet Kiremt Rains events show opposite circulation anomaly. In brief, a high-resolution ICON configuration might be the best choice for such large-scale model experimental study, as it reproduces the Kiremt Rains variability and realistically simulates the physical mechanism which ENSO influences the Ethiopian Kiremt Rains' interannual variability.

Chapter 6

Evaluation of the MiKlip Decadal Hindcasts Systems over Tropical Africa

6.1 Introduction

Tropical Africa is highly vulnerable to rainfall variabilities at interannual-to-decadal time-scale. These variabilities are dominated by the changes on a large-scale, with a clear link to modes of the oceanic variability. Therefore, seasonal-to-decadal prediction of rainfall variability and the evolution of these modes of oceanic variability, if skillful, can be beneficial to the society to avoid humanitarian disasters, mitigate climate-related risks, and establish long-term adaptation plans for agriculture, water management, etc. Currently, seasonal forecasts of rainfall are considered the priority timescale by many users in tropical Africa. For instance, in the GHA the primary operational seasonal forecast for the region is produced by the GHACOF and issued ahead of each rainfall season. The GHACOF seasonal forecast skill is generally derived from teleconnections with slowly evolving ocean variability, particularly SST anomalies. The persistence of SST anomalies forms the basis of seasonal forecasts either as a predictor in a statistical model or as boundary conditions to dynamic seasonal forecasts using general circulation models.

While seasonal climate predictions and projections have made great ad-

vancements, decadal climate prediction is still in its early stages. Only in the last few years, predictions over a few decades have become feasible due to the availability of large observational data sets and progresses in climate modelling. Decadal prediction lies between seasonal/interannual forecasting and longer-term climate change projections and focuses on time evolving regional climate conditions over the next l0-30 year (Meehl *et al.*, 2009b). Similar to the seasonal forecast, the skill of decadal predictions stems from good representation of slowly acting parts of the climate system (e.g., the oceans). The transport of skill towards the atmosphere over land is one main challenge of decadal predictions. Though there are known sources for decadal predictability, particularly slow ocean variability, e.g. AMO, the implications for atmospheric variables, e.g. rainfall, over land are not necessarily straight forward. For a brief literature review on decadal climate variability, significant internal sources of decadal predictability, predictions, and the MiKlip project see Chapter 2 and Chapter 3.

The MiKlip project aims to investigate and understand the climate systems controlling decadal climate variability and predictability, then incorporate these processes to establish and develop an operational ensemble decadal climate prediction system. As part of MiKlip, Process Evaluation of the MiKlip decadal forecast system in Tropical Africa (PROMISA), dedicated to exploiting interannual to decadal predictability of the WAM and GHA climate systems. The PROMISA regions are known to be linked to interannual to decadal variations in SSTs in adjacent and remote ocean basins (see Chapter 4, and Chapter 5; Diatta and Fink, 2014; Bahaga *et al.*, 2019). Nonetheless, this Chapter presents teleconnection-oriented evaluation focus on GHA.

The ability of decadal forecast to predict the atmospheric teleconnections provides an important basis for the use of decadal predictions. Therefore, a potentially predictable variable on the decadal scale includes a strong expression of teleconnections. Thus, the MiKlip decadal hindcast experiments are assessed on their ability to predict the observed teleconnection patterns. Besides, the predictability of climate drivers (e.g., ENSO, IPO, AMO, and IOD) providing interannual and decadal skill, are evaluated. The skill of a comprehensive set of decadal hindcast experiments, including baseline0, baseline, prototype, and preop are analyzed (see Table 3.3). The pre-

diction data contain ten ensemble members, with each simulation integrated for 10 lead years, and are initialized every year starting from 1961 to 2013. Rainfall and SST anomalies with respect to 1981–2010 climatological base period are calculated for both predictions and observations. Here, the main focus is on the skill of individual experiment ensemble mean, minima, and the maxima throughout the common hindcast period. The predictive skill of these individual ensembles is evaluated through simple correlation and regression analysis. This Chapter will address the following questions:

- How well do the Miklip systems predict the principal drivers of seasonal-to-decadal climate variability?
- How well do the MiKlip decadal predictions represent the observed teleconnection patterns?

6.2 MiKlip Skill for Climate Drivers

The skill of climate predictions stems from good representation of the evolution of modes of variability in the oceans. Besides, the result in Chapter 4 and Chapter 5 have shown the relationship between seasonal rainfall over the GHA and SST anomalies in the Pacific, the Indian, and the Atlantic Ocean, in particular highlighting the importance of IOD, ENSO, and PDO (Bahaga *et al.*, 2019). This section will assess the predictive skills of a different configuration of MiKlip decadal prediction experiments for these SST-based remote climate indices. The following two datasets are used as an observational reference to assess the predictive skills of decadal prediction experiments: (1) Gridded monthly SST obtained from the Hadley Centre Sea Ice and SST dataset (HadISST; Rayner *et al.*, 2003) and (2) Global Precipitation Climatology Centre (GPCC) gridded monthly precipitation dataset (Schneider *et al.*, 2014). For more details on these datasets, the readers are referred to Chapter 3.

6.2.1 Predictive skill for the drivers of interannual variability

Here, the performance of individual systems, including baseline0, baseline, prototype, preop, and preop-DCPP are examined, and the prediction

for the evolution of SST-based remote climate indices are also assessed. Figure 6.1 shows correlation coefficients as a function of lead time for different remote climatic indices: (a) N34, (b) PDO, (c) DMI, and (d) AMO. January–March (JFM) mean SSTA from the HadISST is used to evaluate the Miklip hindcast experiment in predicting these remote climate anomalies up to lead year-10. The bold curve represents ensemble mean and dashed curve indicates ensemble min and max, which are determined after concatenating each lead year together. It is seen from Figure 6.1a that there is a substantial skill for N34 index prediction in all experiments at the lead year-1, as reflected in the highly significant correlation coefficients above 0.85 with observations. However, this skill quickly decreases to marginally significant correlations in the lead year-2. It is also worth noting that the of skill all experiments systematically declines below significant levels at lead year-3 and beyond. The skill of SST hindcasts for DMI index (Fig. 6.1c) is lower than for the N34 index (Figure 6.1a). Only four experiments show significant correlation skill for the lead year-1, with a marked decline in skill in the lead year-2 and then after (Fig. 6.1c). In brief, baseline1 shows improved correlation skill for both N34 and DMI, compared to baseline0. This improvement in tropical SST indices skill is attributed to a higher-resolution ocean simulation in baseline1 (Pohlmann *et al.*, 2009; Marotzke *et al.*, 2016). Though the JFM seasonal mean N34 prediction skill in the MiKlip hindcast shows considerable skill in lead year-1, the skill for the JJAS N34 index is substantially decreased (not shown), indicating that the MiKlip systems can only predict ENSO events at a few months advance after initialization. This poor performance in predicting tropical SST-based indices may have arisen from initialization or other factors and requires substantial future improvements.

6.2.2 Predictive skill for the drivers of multidicadal variability

AMO and PDO are known to be the leading decadal phenomena. They are linked to rainfall variations over land and the relationship is particularly strong for low-frequency variations (e.g., Cassou *et al.*, 2018). In the following, the predictive skill for both AMO and PDO is evaluated. The AMO (Fig. 6.1d) appears to be predictable within a time-scale that depends strongly on the particular MiKlip experiments, ranging from 2- up to 10-years. The substantial AMO index skill demonstrated here is consistent with

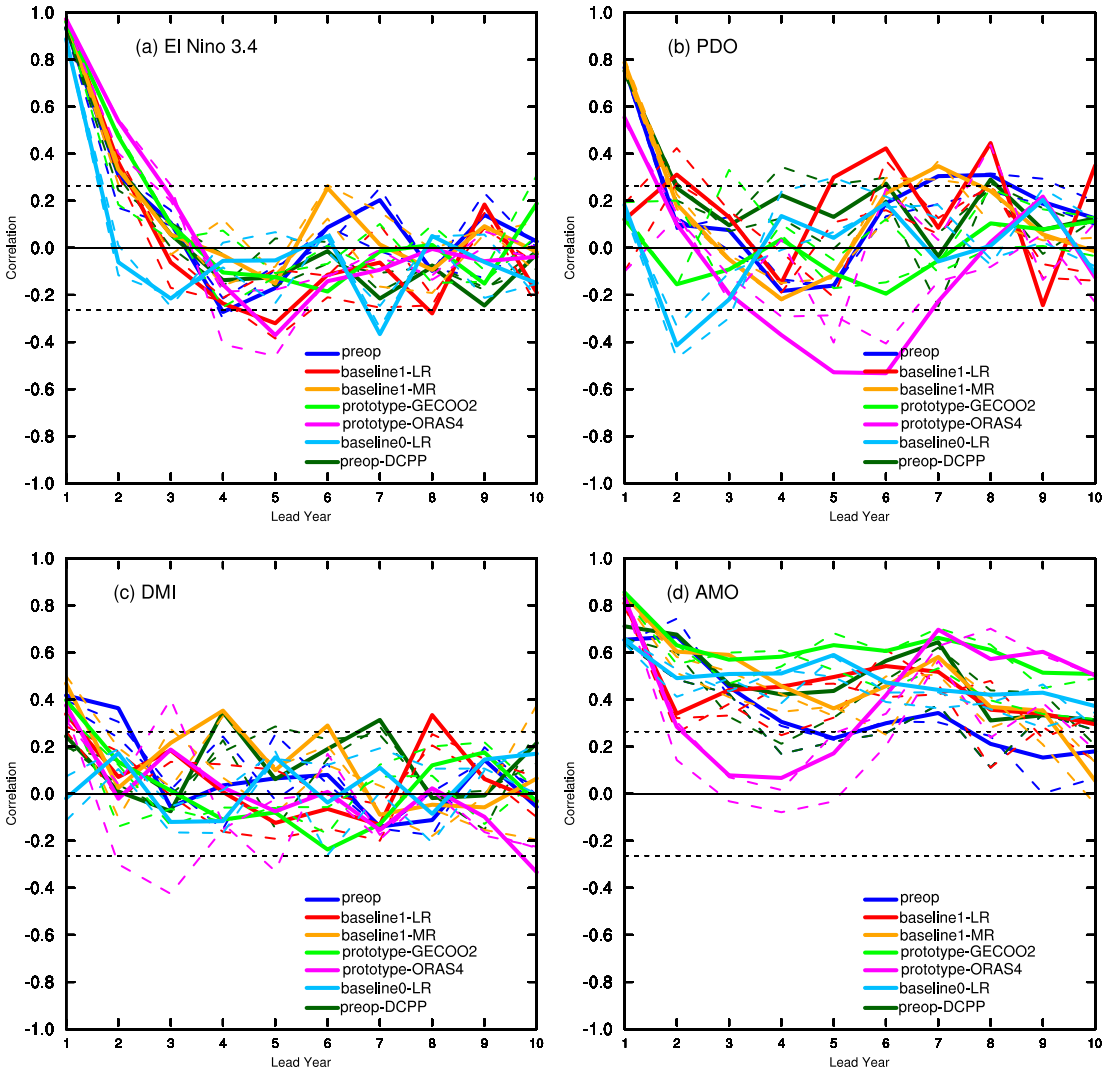

Figure 6.1: The correlation coefficients as a function of the lead year, for area average JFM mean remote climatic indices derived from MiKlip hindcast experiments for the period of 1961–2013. (a) N34, (b) PDO, (c) DMI, and (d) AMO. The ensemble mean for each model is represented by solid colored lines, while ensemble min and max are depicted by dashed lines. High correlations indicate better predictive skill. The horizontal dashed lines represent the 5% significance levels.

Marotzke *et al.* (2016) and Kröger *et al.* (2018). The new generation MiKlip, CMIP6 forced experiment, preop Decadal Climate Prediction Project (preop-DCPP) was configured using a higher-resolution version of the coupled MPI-ESM1.2-HR. Further details of the MPI-ESM1.2-HR system are discussed in (Müller *et al.*, 2018). The preop-DCPP shows improved skill with lead years for AMO (Fig. 6.1d), which is better than the preop. Nonetheless, compared with preop, no significant improvement was found in the preop-DCPP in predicting N34, PDO, and DMI (Fig. 6.1). The pronounced drop in the AMO

correlation skill for the lead years 2-5 in the prototype-ORAS4 experiment (full-field initialization) compared to the baseline1 (anomaly initialization) from ORAS4 is attributed to poor initialization of the ocean flow Kröger *et al.* (2018).

Figure 6.1b shows the lead year correlation skill for PDO. It appears that the high resolution MiKlip experiments, baseline1-MR, preop, and preop-DCPP, show significant prediction skill for PDO for the lead year-1, as indicated in the high correlation coefficients near 0.8 with observation. However, consistent with N34, the PDO skill quickly drops below a significant level after lead year-2 (Fig. 6.1a and 6.1b). Overall performance of MiKlip prediction skill for PDO is inferior to the AMO case, in agreement with the result from other decadal forecast systems contributing to CMIP5 (Doblas-Reyes *et al.*, 2013). This is due, in part, to the Pacific being inherently more sensitive to initial state uncertainty as well as to uncertainty in the mechanisms of internally generated decadal climate variability in the Pacific (Cassou *et al.*, 2018).

6.3 Teleconnection Evaluation of MiKlip Decadal Systems

Interannual-to-decadal prediction skill over land originates from high-to-low frequency climate variations in the oceans. Therefore, interannual-to-decadal predictability of teleconnections that couple the different parts of the climate system provide an important basis for the use and application of decadal predictions. This section evaluates the teleconnection predictive skill in the MiKlip decadal experiments.

6.3.1 The predictability of PDO and AMO characteristics

To assess the performance of preop, basline1, preop-DCPP experiments for the spatial characteristics of the PDO, lead year-1 data from each initialization are concatenated to create monthly SST datasets for the period of 1961–2013. A PDO pattern is created as EOF1 of monthly SST anomalies after removing the global mean SSTs anomalies. The EOF is computed over 20^{o}S–65^{o}N, 120^{o}E–100^{o}W. The PDO spatial pattern, obtained by regress-

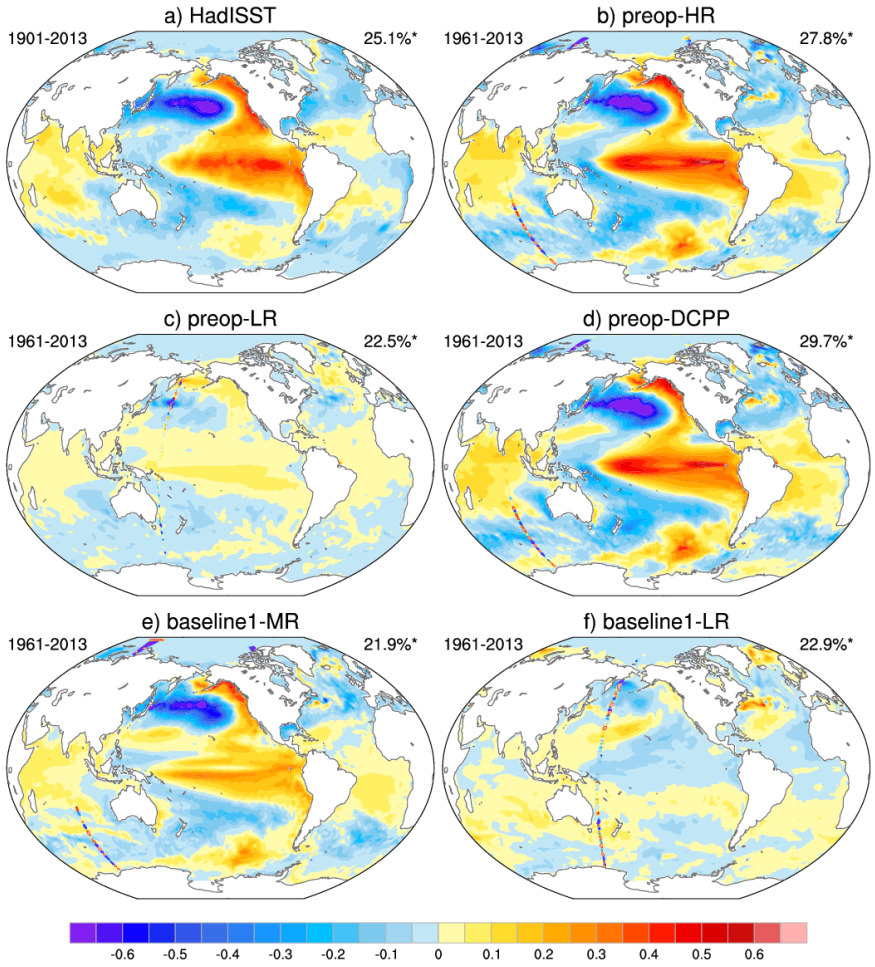

Figure 6.2: The spatial structure of the PDO, regression of JFM mean global SST anomalies onto the PDO time series for a period of 1961–2013: (a) HadISST, (b) preop-HR, (c) preop-LR, (d) preop-DCPP, (e) baseline1-MR, and (f) baseline1-LR. The global-mean SSTA was removed prior to computing the EOF analysis, and PC1 represents the PDO index. All indices were standardized prior to computing the regression maps. Units is ^oC.

ing global SST anomalies onto the normalized leading principal component time series, has a typical horseshoe shape connecting tropical and extratropical anomalies. In its "warm phase," the PDO is characterized by cold SST anomalies in the western north Pacific encircled by warm SST anomalies in the eastern part of the basin extending to the central and eastern tropical regions (Fig. 6.2a; Deser *et al.*, 2012). The cold phase is characterized by an opposite pattern with negative equatorial SST anomalies. In general, the preop-HR and the preop-DCPP produce excellent predictions of the spatial pattern of observed PDO teleconnections behavior for the lead year-1 (Fig. 6.2b and 6.2d). Although observed percent variance explained in EOF1 is moderately represented, the predictability of the PDO telecon-

nection pattern over the tropical region is weak in the preop-LR and the baseline1-LR (Fig. 6.2c and 6.2f). On the other hand, high-resolution MiKlip systems, preop, baseline1-MR, and preop-DCPP able to predict observed PDO global teleconnections. It is clear to note a warming over the Indian Ocean and a cooling over the northern Atlantic Ocean. Generally, observed percent variance explained in EOF1 is moderately represented, and it is also demonstrated that an increased horizontal ocean model resolution improved the prediction of PDO teleconnections in lead year-1. This is consistent with the study of Schuster *et al.* (2019), who assessed the MiKlip system and showed improved prediction skill of the northern hemisphere extra-tropical atmospheric circulation with an increase in resolution.

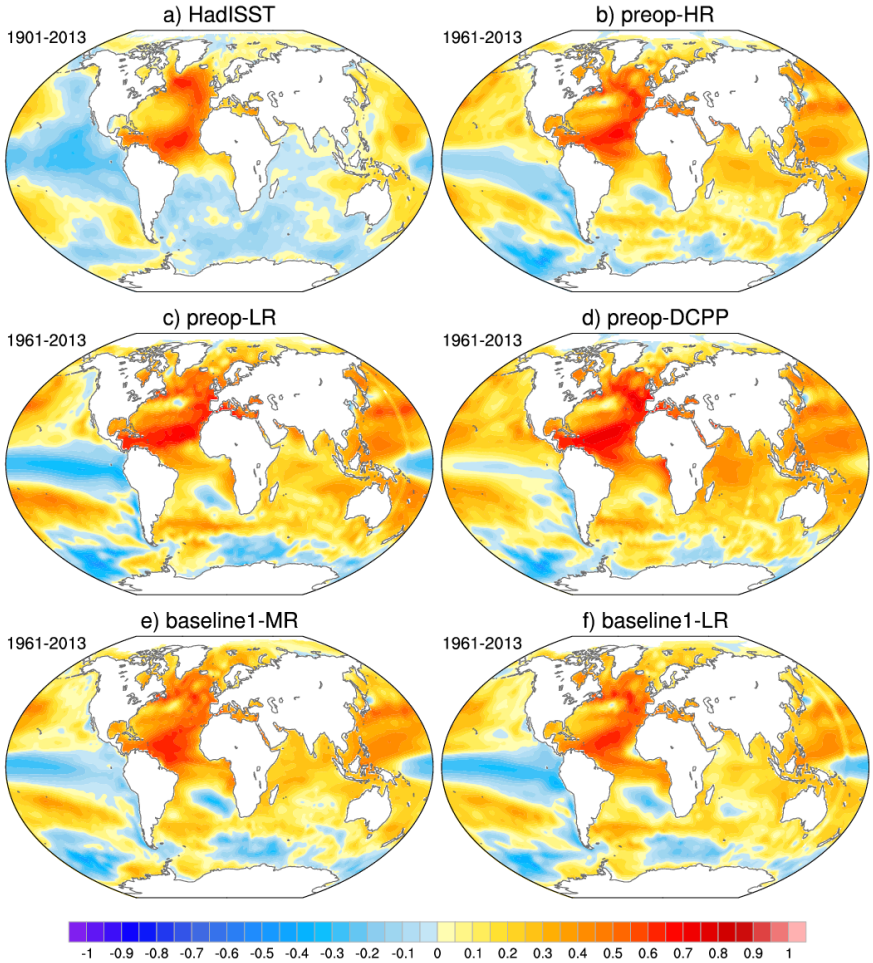

Figure 6.3: The spatial structure of the AMO, regression of JFM mean SST anomalies onto the AMO index for the period 1961–2013: (a) HadISST, (b) preop-HR, (c) preop-LR, (d) preop-DCPP, (e) baseline1-MR, and (f) baseline1-LR. The AMO index is defined as the area average JFM mean SST anomaly over the North Atlantic (0^o–70^oN, 80^oW–0^o) after romoving the global mean monthly SST anomaly. All indices were standardized prior to computing the regression maps. Units is ^oC.

In the previous section, the predictability of AMO discussed. The forecast horizon depends strongly on the considered MiKlip system (Fig. 6.1d). Here the performance of the decadal hindcasts is further assessed for AMO teleconnection. Figure 6.3 shows the pattern of JFM SST anomalies regressed onto the standardized AMO index derived from observation and MiKlip experiments: (a) HadISST, (b) preop-HR, (c) preop-LR, (d) preop-DCPP, (e) baseline1-MR, and (f) baseline1-LR. The observed spatial patterns associated with the AMO index are characterized by a horseshoe pattern (Fig. 6.3a), and exhibit positive values over the entire North Atlantic, with the largest magnitudes south of Greenland, over the northeastern Atlantic, and over the tropical Atlantic. In addition, a positive AMO leads to a cooling in the eastern Pacific Ocean and the western Indian Ocean compared to the warming in the western Pacific as well as tropical Indo-Pacific regions (Fig. 6.1a), a pattern similar to the negative phase of PDO over the Pacific. This is consistent with previous studies (e.g., Kucharski *et al.*, 2016; Cassou *et al.*, 2018). In general, the MiKlip experiments predict remarkably similar global teleconnections (Figs. 6.3b, 6.3c, 6.3d, and 6.3e). Consistent with observation, it is clear to note a considerable warming over the North Atlantic Ocean associated with the AMO. Moreover, the baseline and the preop also predict a warming of the tropical Indo-Pacific regions and the negative phase of PDO over the Pacific Ocean. However, there are significant differences in that the western Indian and the northeastern parts of the Pacific Ocean show positive SST anomalies, while in the observation weak negative anomalies are observed. The above results suggest that the east-west Pacific SST gradient (i.e, negative phase of PDO) is strengthened during the positive and weakened during the negative phase of AMO. In particular, the multi-decadal variability of SST in the North Atlantic basin appears to be skillfully reproduced by the MiKlip decadal experiments. These results are in agreement with Marotzke *et al.* (2016) and Kröger *et al.* (2018).

6.3.2 Predictive skill for rainfall teleconnections

In the previous section, we have analyzed the predictability of SST-based remote climate drivers, and here we show predictive skill for rainfall teleconnection in the MiKlip experiments. Figure 6.4 shows correlations between the JJAS standardized N34 index against concurrent grid-point rainfall, in-

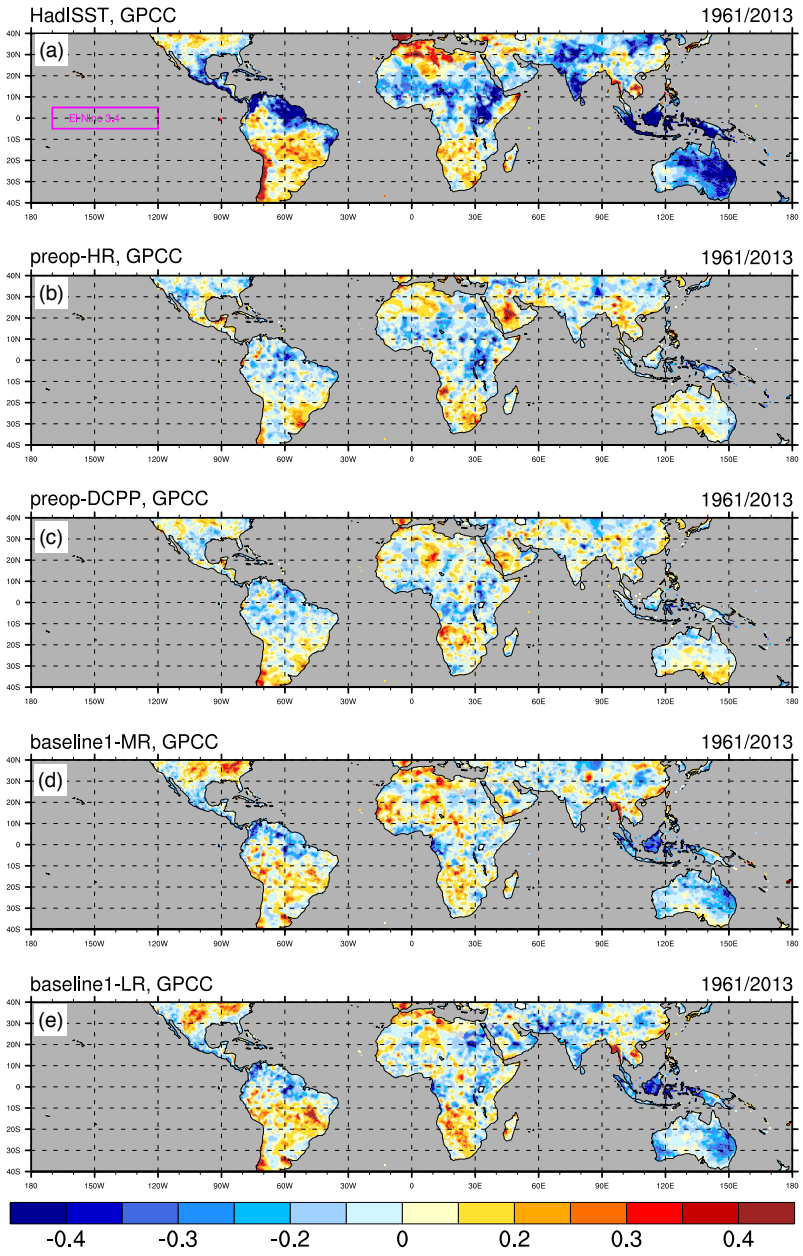

Figure 6.4: Correlation map between JJAS seasonal mean standardized precipitation anomalies derived from GPCC over land and JJAS seasonal mean N34 index, derived from observations and individual MiKlip decadal hindcasts ensemble mean: (a) HadISST, (b) preop-HR, (c) preop- DCPP, (d) baseline1-MR, and (e) baseline1-LR. The N34 index regions is outlined by a purple box.

dicating that the SST anomalies in the central eastern tropical Pacific Ocean drive interannual rainfall variations over the tropical regions. The observed dataset (HadISST) demonstrates that JJAS N34 has a concurrent correlation with summer rainfall anomalies over Australia, India, northern South America, and Africa (Fig. 6.4a). A wetter (drier) summer across much of the

northwestern parts of the GHA region tends to occur during the cold (warm) phase of ENSO (i.e., El Niño (La Niña)). This is consistent with the results found in Chapter 4 and Chapter 5. The corresponding correlation maps are created using the JJAS N34 index calculated from the MiKlip decadal hindcasts for lead year-1, then each N34 time series is correlated with the JJAS GPCC rainfall at a grid-point (Figs. 6.4b, 6.4c, 6.4d, and 6.4e). The results show that the latest MiKlip experiments failed to predict the main teleconnection patterns. For instance, the negative correlation is very low over the Maritime Continent, Australia, India, northern Brazil, and East and West Africa (Figs. 6.4b, and 6.4c). However, in contrast to preop, baseline1 shows better correlation skill for ENSO teleconnection over the Maritime content and Australia (Figs. 6.4d and 6.4e). The newly generated CMIP6 forced experiment failed to reproduce observed teleconnection, in fact the correlation is spatially non-coherent and reversed over tropical West Africa (Fig. 6.4c). Although the MiKlip decadal hindcasts are able to predict interannual variations of ENSO in the lead year-1 (Fig. 6.1a), they have imperfect skill and weak summer ENSO-rainfall teleconnections over most parts of tropical regions.

ENSO is also known to be important for the prediction of Ethiopian Kiremt Rains (e.g., Korecha and Barnston, 2007; Diro *et al.*, 2011b; Bahaga *et al.*, 2019). The predictability of this teleconnection is further elucidated in the MiKlip decadal hindcasts. Figure 6.5 show areal average GPCC rainfall SPI over purple box correlated with SST anomalies over the tropical region both in observations and Miklip decadal hindcasts. The observed dataset (GPCC) shows that the JJAS rainfall in the northwestern part of Ethiopia has a strong negative correlation with SSTs in the eastern equatorial Pacific. A positive rainfall anomaly tends to occur during the cold phase of ENSO while dry conditions prevail during the warm phase ENSO (Fig. 6.5a). This is consistent with previous studies of Segele *et al.* (2009a) and Diro *et al.* (2011b), which use rain gauge rainfall data, and observed SST. Overall, the MiKlip decadal hindcast have relatively little or no skill and are unable to produce observed correlation patterns in the Pacific Ocean (Figs. 6.5b, 6.5c, 6.5d, and 6.5e). On the whole, although the MiKlip decadal hindcasts are able to predict interannual variations of ENSO for lead year-1 (Fig. 6.1a), they have low skill and weak summer ENSO-rainfall teleconnections over most parts of tropical regions. This might be related to the unrealistic rep-

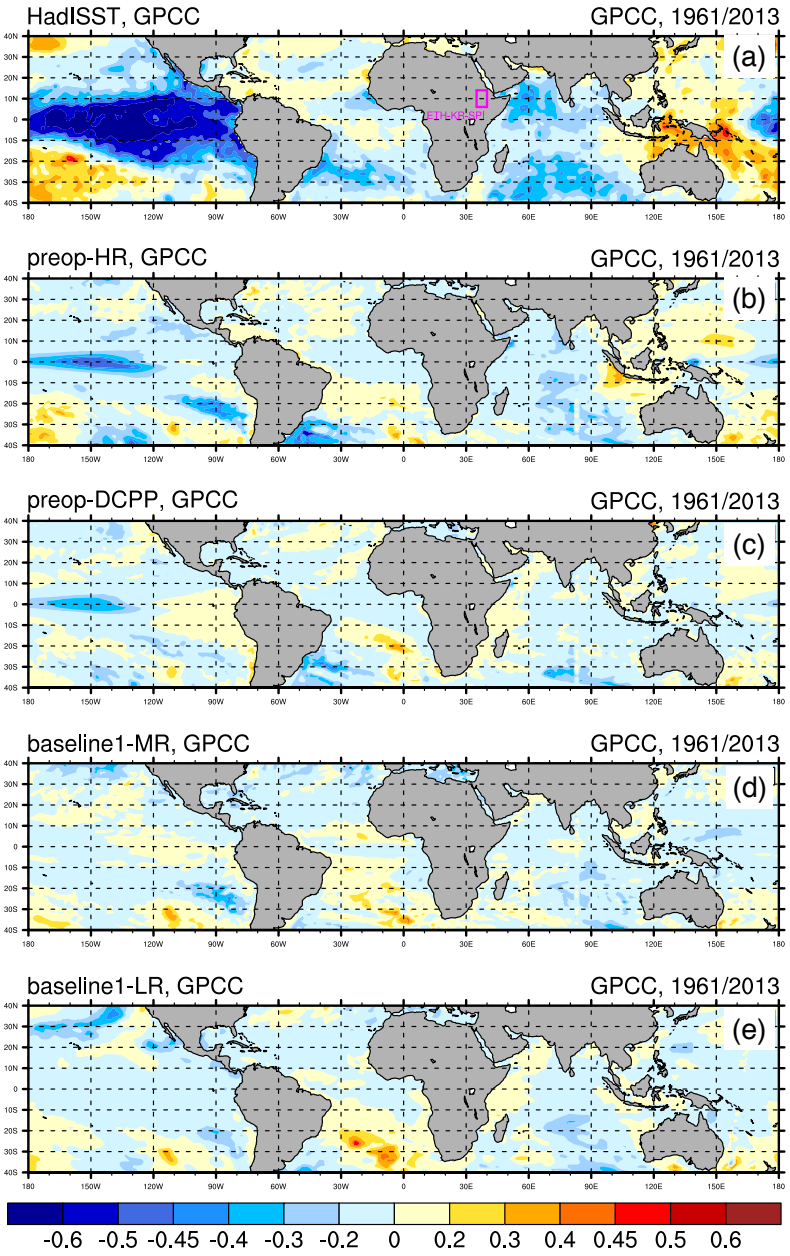

Figure 6.5: Correlation map between JJAS ETH-KR-SPI derived from GPCC and JJAS seasonal mean SSTAs derived from observations and individual MiKlip decadal hindcasts ensemble mean and estimated over the tropical region: (a) HadISST, (b) preop-HR, (c) preop-DCPP, (d) baseline1-MR, and (e) baseline1-LR. The rainfall index regions is outlined by a purple box.

resentation of atmospheric circulations anomalies that link slowly evolving SSTs and seasonal rainfall anomalies over the land regions.

Chapter 7

Conclusions and Outlook

This Chapter provides the main conclusions that were drawn from previous Chapters. Some recommendations and direction are also given for future work.

7.1 Summary and Conclusions

Livelihoods, food security, and development processes in the GHA region are highly dependent on rainfall. Nonetheless, interannual to decadal rainfall fluctuations and a series of severe droughts, such as the humanitarian crises of 2011 and 2015 threaten the livelihood of millions. Moreover, in recent decades, a continuous decline in precipitation is observed, while the majority of climate models from CMIP3/5 project indicated that precipitation will increase in the future. Therefore, understanding the mechanisms that produce this variability and developing both dynamical and statistical approaches for sub-seasonal to decadal forecasts and climate information is urgently needed.

Therefore, the main objectives of this thesis are to understand the drivers of interannual to decadal rainfall variability over the GHA, to detect non-stationary teleconnections, to explore the dynamical processes instigating multidecadal changes, to conduct Sea Surface Temperature (SST)-forced icosahedral Nonhydrostatic (ICON) model experiments, to investigate the physical mechanisms that govern the influence of SST on Kiremt Rains, and to assess the skill of MiKlip decadal forecast systems over GHA. In order to achieve these objectives, a thorough literature review made in Chapter 2, followed by comprehensive statistical analyses in Chapter 4, and multi-

decadal changes in SST-rainfall teleconnections were examined. The underlying dynamical mechanisms for SST-rainfall teleconnections were analyzed with higher-resolution SST-forced ICON experiments in Chapter 5, while the MiKlip decadal hindcast experiments were evaluated on their ability to predict the observed teleconnections in Chapter 6. In the following, the main conclusions drawn from Chapter 4 to Chapter 6 are presented.

Non-stationary teleconnections and dynamical processes instigating multidecadal changes

Chapter 2 presented a thorough literature review on the large-scale factors that are known to influence Short, Kiremt, and Long Rains interannual to decadal variability over GHA. It reviewed the progress of observational and modeling understanding about the role of tropical ocean-atmosphere variability on these seasonal rainfall variabilities, and these work immensely contributed for improvement of seasonal forecasting in the region. However, the seasonal forecasts based on empirical data might be constrained by overfitting, usage of unphysical predictors, and non-stationary teleconnections. One way to improve these forecasts is to check the validity of the statistical predictors used, the teleconnection may change over time, and better define them accordingly.

To detect if such non-stationary relationship between Short, Kiremt, and Long Rains and SST-based climate anomalies exist over 1901–2013 period, Chapter 4 used observational data and applied comprehensive analyses to review the evolution of statistical relationships. The evolution of statistical relationships between remote climate anomalies and rainfall indices are examined both over varying time window lengths for fixed starting years and varying starting years for fixed time window length in triangle representation. Focusing on the stationarity, linear correlations were studied for unfiltered, low-pass (larger than 8 years), and high-pass (less than 8 years) filtered detrended time series. In addition, a composite analysis was used to investigate the physical mechanisms explaining the non-stationary behaviour of the correlation between ATL3 and Kiremt Rains. To this end, monthly precipitation datasets were used to create standardized precipitation indices over homogeneous rainfall regimes in the respective sub-regions. SST datasets were used to construct indices for remote climate anomalies (Table 3.1). The major findings related to the three rainy season are:

- Consistent with previous studies, the interannual variability of the Short Rains is more closely linked to the IOD than to ENSO. The East Africa region receives above (below) normal rainfall during positive (negative) IOD events. It is found that there is abrupt changes in the relation between the Short Rains and IOD, particularly around 1918, 1951, 1983, and 1987. The non-stationarity test applied for 11-year window length further reaffirmed that this non-stationarity in the link is significant at the 1% level. This is consistent, but expands the findings of Camberlin and Philippon (2001), Clark *et al.* (2003), and Nicholson (2015). Moreover, ENSO shows strong correlation with the Short Rains year-to-year variability, yet the ENSO influence is mediated by the co-occurrence of in-phase oscillation of the IOD. The result further reveals that the low-frequency variations of the Short Rains are most likely explained by decadal variability in the PO, as it is demonstrated by significant correlations to the low-pass filtered time series of ENSO and IPO indices.

- The Atlantic Niño 3 (ATL3) influence in the Ethiopian Highlands Kiremt Rains is found be non-stationary. It changed from significantly negative to positive after in the 1960s. This is in agreement with a WAM regime change in 1968 (e.g., Diatta and Fink, 2014; Nicholson *et al.*, 2018). The composite analysis also revealed that in the 1934–1964/1969–1999 period, wet Kiremt Rains over the Ethiopian Highlands tend to simultaneously occur with cold/warm ATL3 region (Fig. 4.8; Diro *et al.*, 2011a; Segele *et al.*, 2015). The analysis also revealed that interannual variability of the Ethiopian Kiremt Rains is strongly correlated with the ENSO indices. This association is significant and stable with PVEs larger than 50% in recent periods and mainly based on high-frequency variability (<8 years). From simple time series analysis, a statistically significant larger influence of ENSO on Kiremt Rains in recent decades cannot be inferred.

- On the other hand, the IPO index is negatively correlated with Kiremt Rains for long sample periods. The negative (positive phase) of IPO corresponds to frequent occurrence of wet (dry Kiremt Rains), and might reflect the interannual ENSO events occur in phase with the IPO. For instance, the frequent dry Kiremt Rains during 1982–84 appears to have occurred when El Niño events coincide during warm phases of IPO (Fig. 4.1, A1.2; Lyon, 2014). This might further suggest a potential modulation of ENSO forced

interannual teleconnections by the background Pacific decadal variability (Wang *et al.*, 2014; Newman *et al.*, 2016).

- The recent Long Rains decline over GHA is part of natural decadal fluctuations and significantly associated with indices representing multidecadal variability in the PO. Both the PDO and IPO show a positive and significant correlation to the Long Rains. PVE ranges from 25 to 64% and the association stems from low-frequency variability (>8 years) for both PDO and IPO. The result presented is in agreement with Lyon (2014) and Yang *et al.* (2014). This significant correlation between the Long Rains and IPO/PDO might offer a useful inference in predicting the Long Rains at the decadal timescale.

Reasons for non-stationary behaviour in interannual teleconnections can be manifold. Apart from data inhomogeneities, changes in the background climate state at interdecadal time scales is another potential cause. For example, Suárez-Moreno *et al.* (2018) suggest this is one reason for non-stationary teleconnections between the Eastern Mediterranean SSTs and WAM rainfall. Alternatively, the amplitude of ENSO is suggested as a reason for variations in the link to WAM rainfall. Changes in the East African Short Rains teleconnections have been discussed by Camberlin and Philippon (2001), Clark *et al.* (2003), and Nicholson (2015). Camberlin and Philippon (2001) suggested the change in large-scale circulation anomalies and inclusion/exclusion of extreme years as justifications for the changes in the apparent strength of the teleconnections. The results found here suggest that the multidecadal background state of the Pacific Ocean (i.e., IPO, PDO) is one possible explanation for the non-stationary of Short Rains interannual teleconnections. The correlation between the Short Rains and N34/DMI appears to be modulated and enhanced during the cold phase of IPO, while the impact is insignificant during the warm IPO phase. This is consistent with the damping effect discussed in Wang *et al.* (2014). Some of the abrupt changes found in the present study may also coincide with 1976–1977 climate shift (Trenberth and Hurrell, 1994).

Physical mechanisms for ENSO-Kiremt Rains teleconnection and SST-forced ICON experiments

The multidecadal changes with ATL3 and recent increase in ENSO influence on Kiremt Rains raises questions about how and to what extent does the PO interfere with the Atlantic and the Indian Ocean forced Kiremt Rains' variability, and what are the physical mechanisms for ENSO-Kiremt Rains teleconnection. This motivated a modeling study, and the Kiremt Rains interannual variability analyzed using observational data and higher-resolution SST-forced ICON experiments for the period of 1981–2017. Such fine-grid global and two-way nests over the GHA were carried out here for the first time. The physical mechanisms that link ENSO influence on the Kiremt Rains in the model and the ERA-Interim reanalysis were also investigated.

To this end, three separate ICON experiments were performed, where each member was forced with observed SST over the Ocean basin of interest and set to monthly varying climatology elsewhere for the period of 1981–2017. EOF analysis was applied both in observations and model data. Besides, composite, correlation and regression analyses are used to show the dynamical response generated by SST-forced experiments, and to understand the physical mechanisms behind the ENSO-Kiremt Rains teleconnections. It is found that the model reasonably simulates the main features of the JJAS rainfall climatology over GHA and also reproduces horizontal wind intensity and patterns at $150, 600, 850, 925 - hPa$ levels over Africa. In general, the model climatology over GHA is comparable to the state of the science with respect to regional climate model performances (e.g., Zeleke *et al.*, 2013; Segele *et al.*, 2015).

The modeled Kiremt Rains PC1s and N34 indices are statistically significantly correlated at the 1% level, with a correlation coefficient of -0.48 in the GOGA, while the POGA showed a higher correlation of -0.71, which is closed to the observed correlation. This indicates that a substantial portion of the Kiremt Rains variability is SST forced and that the model is reproducing this. However, the positive and significant correlation between PC1 in AIOGA and N34 imply that Atlantic and Indian Ocean SST forcing, while isolating the effects of Pacific SSTs, enhances summer rainfall across much of Ethiopia. These results further support the idea that SST effects from other regions on the Ethiopian Kiremt Rains counteracted ENSO impact in the

model, and thus ENSO is probably the only SST pattern that impact on the POGA rainfall. The model Kiremt Rains regression patterns against N34 are consistent with the observed rainfall in Ethiopia; El Niño (La Niña) episodes events are related to enhanced (reduced) summer rainfall across much of the country (Fig. 5.6; see also Segele *et al.*, 2009a; Diro *et al.*, 2011b; Zeleke *et al.*, 2013). In brief, it is shown that there is a substantial skill in reproducing the leading modes of Kiremt Rains interannual variability ($r = 0.64$) given the SSTs are known. The result suggests that the majority ($> 50\%$) of Kiremt Rains anomalies are driven by equatorial Pacific SST variability, while the SST effects from other regions counteract the ENSO impact in the model.

In terms of anomalous atmospheric circulation features associated with Kiremt Rains variability, regression pattern against PC1 in the POGA experiment leads to enhanced low-to-mid-level westerlies across western and central Africa and a strengthening of the SLLJ, which are produced by anomalously high GH in the Gulf of Guinea and deepening of monsoon trough across the Arabian Peninsula. Moreover, the wet Kiremt Rains events in the POGA run are associated with a stronger TEJ. The anomalous atmospheric circulation features are quite similar but reverse during dry Kiremt Rains. On the other hand, the composite analysis of ENSO events revealed that the AIOGA experiment, compared to the GOGA and POGA, shift Southern Oscillation center westward, creating pressure gradient between the Atlantic and Indian Oceans, which lead to enhanced westerlies and a strong SLLJ, and thus wetter Kiremt Rains over Ethiopia.

Consistent with previous studies, it is found that the El Niño phase of the ENSO drives a corresponding large-scale circulation anomaly, which weakens the monsoon trough over the Arabian Peninsula, enhances descending motion, and upper-level convergence right over Ethiopia. The subsidence over the GHA region induces upper (lower) level westerly (easterly) wind anomalies over North Africa leading to weakening the Tropical Easterly Jet, Somali Low-Level Jet, and reducing the moist westerlies from the Atlantic and Congo basin, and thus lead to a reduction of Kiremt Rains over Ethiopia. The opposite pattern is observed during La Niña events with enhanced surface westerlies leading to a wetter Kiremt Rains. This mechanism represents an anomalous Walker-type circulation for the ENSO-Kiremt Rains teleconnection.

On the whole, a high-resolution ICON configuration might be the best choice for such large-scale model experimental study, as it captures the Kiremt Rains producing systems, the Kiremt Rains amounts, and variability; and realistically simulates the physical mechanism through which ENSO influences the Ethiopian Kiremt Rains.

Process and teleconnection evaluation MiKlip decadal hindcast experiments.

The result in Chapter 6 analyzed the MiKlip decadal hindcast systems, and it also evaluated the predictability of climate drivers (e.g., ENSO, IPO, AMO, and IOD) providing interannual and decadal skill. In addition, the MiKlip experiments were assessed with respect to their ability to predict the observed teleconnection patterns. Ensemble means for each decadal hindcast experiments were created, and forecast skill was analyzed using simple correlation and linear regression analyses.

It is shown that Atlantic Multidecadal Oscillation (AMO) is predictable within a time-scale that depends strongly on the particular MiKlip experiments, ranging from 2 up to 10 years, while the SST interannual variability in the North Atlantic basin appears to be skillfully reproduced at 1 year lead. Nonetheless, overall performance of the MiKlip prediction skill for PDO is found to be lower than that for AMO. The predictive skill for ENSO is dependent on the lead time. It is shown that the January–March El Niño 3.4 (N34) index has considerable prediction skill ($r > 0.85$) for 1 year lead, but the skill for the JJAS N34 index is substantially decreased. These results suggest that the MiKlip system can only predict ENSO events at a few months advance after initialization. Moreover, the MiKlip decadal hindcasts failed to reproduce ENSO-Kiremt Rains teleconnection patterns during the JJAS season, and in general, the prediction skill for SST and rainfall is weak over most parts of the tropical regions. This might be related to the unrealistic representation of atmospheric circulations anomalies that link slowly evolving SSTs and seasonal rainfall anomalies over the land regions. Additionally, the prediction skill for DMI is inferior to N34, which is ascribed to the the fact that the MiKlip hindcast experiments have degraded performance for SSTs in the Indian Ocean.

On the whole, the MiKlip hindcast exhibited a substantial prediction skill for SSTs over the North Atlantic Ocean, while they failed to predict the

evolution of SSTs and associated teleconnections that communicate tropical ocean signals to the continents. This poor performance in predicting tropical SSTs may have arisen from initialization or other factors and requires substantial future improvements.

7.2 Outlook and Recommendation

The results of this PhD thesis aid improved understanding of the drivers of interannual to decadal rainfall variability, non-stationary teleconnections, physical mechanisms, and predictability over the GHA. But at the same time, it also highlights that non-stationary behaviour as well as correlations between indices on interannual and decadal times scales needs to be taken into account. A similar finding has been noted by Diatta and Fink (2014) for the WAM. As outlined in the introduction, the statistical model based seasonal prediction is a widely used approach among countries in the GHA. These forecasts might be constrained by overfitting, usage of unphysical predictors, and non-stationary teleconnections. Therefore, the results found in this thesis will feed into real-time monitoring of seasonal drought forecasting in the region, and enhance early warning and disaster preparedness activities.

Further studies should consider individual months (e.g., Vigaud *et al.*, 2017) and the spatial coherence of the signals within the three regions considered (e.g., Camberlin and Philippon, 2002). Bahaga *et al.* (2019) has proposed the multidecadal background state of the Pacific Ocean (i.e., IPO, PDO) as one possible explanation for the non-stationary of seasonal rainfall interannual teleconnections. Nevertheless, further analysis of decadal variability of the regional climate in observations and model simulation is needed, as a background to understanding seasonal to interannual predictability. Besides, further work needed to quantify the role of internal decadal variability and external forcing on decadal climate variability over the GHA.

There are also limitations of literature on how different ENSO flavors and intensity impact climate variability in the region. On the other hand, understanding interannual variability and predictability of the Long Rains has been a challenge for researchers as no oceanic or atmospheric predictor has so far been found. There are strong signals of Long Rains decadal variability remotely driven and strongly associated with Pacific decadal oscillation.

Nonetheless, no detailed research conducted focusing physical explanation of this link.

Given considerable errors in coupled climate models' skill to simulate the current climate, it remains an open question as to whether or not the future climate in the GHA will become wetter as a result of anthropogenic forcing. It is, therefore, necessary to improve these validation products by evaluating them against available field observations. There is also no clear consensus regarding climate changes far-reaching impact on the mean precipitation and interannual variability and how these will be driven by potential changes in ENSO.

To fill these gaps, the intended future work expected to address the following questions:

- How and to what extent does Pacific Ocean interfere in the Indian Ocean forced interannual to decadal Short Rains variability and predictability?
- How do changes in multidecadal background state of the global Ocean modulate the interannual teleconnections between IOD/Short Rains and ENSO/Kiremt Rains relations?
- What are the mechanisms and predictability of the recent Long Rains decline over GHA as part decadal fluctuations and associated to Pacific Decadal Oscillation?
- How well do CMIP6 models improve the errors identified in CMIP5 models in representing GHA climatology and interannual to decadal rainfall variability?
- How well do the CMIP6 decadal hindcast predict the principal drivers of seasonal to decadal climate variability over the GHA and represent the observed teleconnection patterns?
- What are the relative contributions of natural variability and anthropogenic forcing driving the 19th, 20th, and 21st-century GHA decadal drought variability?

Appendix A

Non-stationarity Teleconnections

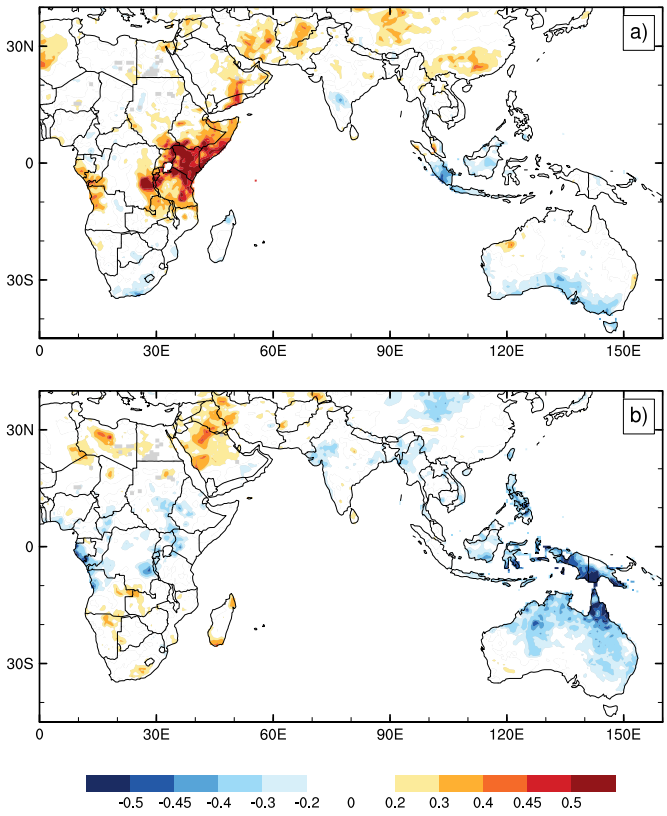

Figure A.1.1: The partial correlation between Short Rains index and DMI anomalies after partialing out the El Niño 3.4 influence (a). The partial correlation between short rains index and El Niño 3.4 anomalies after partialing out the DMI influence (b). The Short Rains index is derived from GPCC and the correlations are computed over the 1901–2013 period. From Bahaga *et al.* (2019), supplementary material. © 2019 Bahaga et al. International Journal of Climatology published by John Wiley & Sons Ltd on behalf of the Royal Meteorological Society.

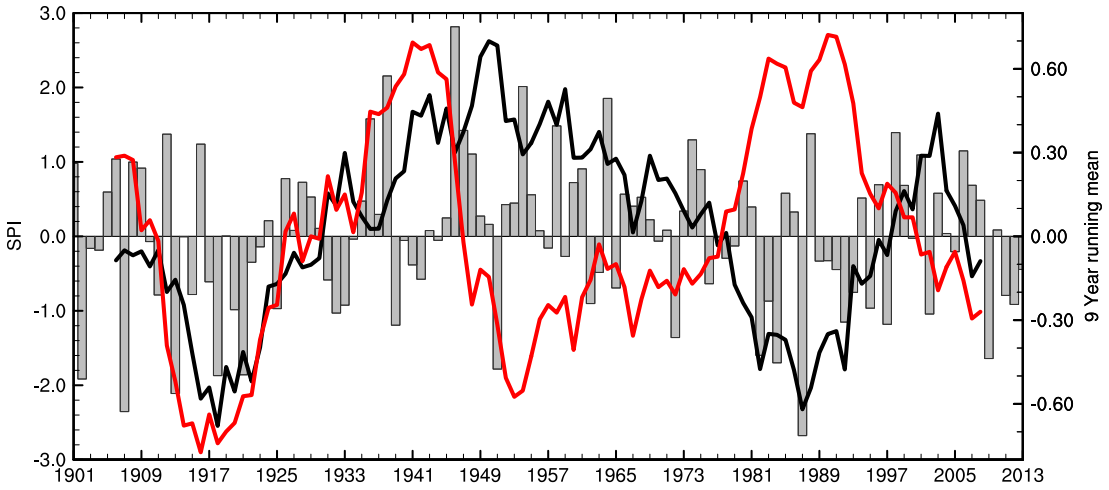

Figure A.1.2: Interannual and decadal variability of the seasonal JJAS mean Standardized Precipitation Index and IPO indices for 1901–2013: interannual variability averaged over Ethiopian Highlands (bar), decadal variability Ethiopian Highlands (black curve), and decadal variability IPO (red curve). The smooth curves are representing 9 years running mean indicating potential decadal variability. Note that the right and left Y-axis scale are different. From Bahaga *et al.* (2019), supplementary material. © 2019 Bahaga et al. International Journal of Climatology published by John Wiley & Sons Ltd on behalf of the Royal Meteorological Society.

Table A.1.1: Six wettest and six driest years considered in the composite analysis of atmospheric fields and SSTs; composite is constructed for the two periods where we found high and low correlations between ATL3 and ETH-KR-SPI. From Bahaga *et al.* (2019), supplementary material. © 2019 Bahaga et al. International Journal of Climatology published by John Wiley & Sons Ltd on behalf of the Royal Meteorological Society.

Early Period (1934–1964)		**Recent Period (1969–1999)**	
Wettest Years	Driest Years	Wettest Years	Driest Years
1936	1939	1974	1972
1938	1941	1975	1982
1946	1942	1980	1984
1947	1951	1981	1987
1954	1962	1988	1992
1964	1963	1998	1997

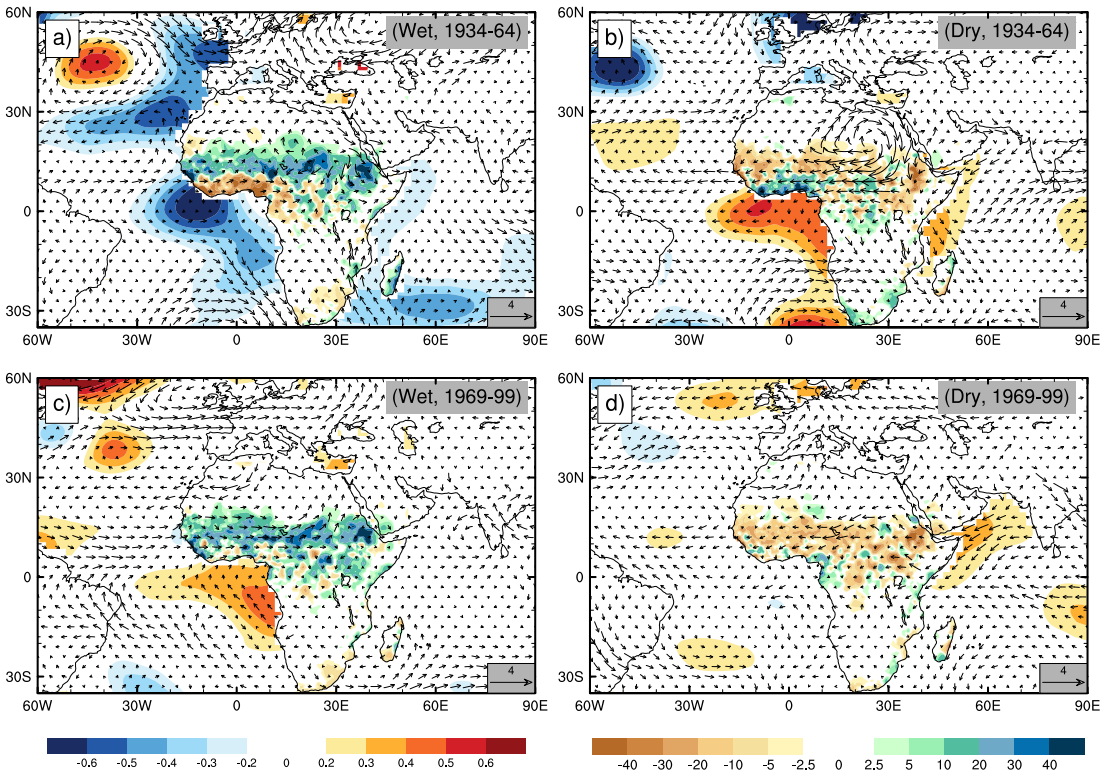

Figure A.1.3: Composite of JJAS mean precipitation (colour over Africa), SST anomalies (colour), and 850-hPa wind anomalies (vector): a) wet years in 1934–1964, b) dry years in 1934–1964, c) wet years in 1969–1999, d) dry years in 1969–1999. Units are mm/month for precipitation (top and bottom colour bar), °C for SSTA (middle colour bar), and m/s for wind. Vector scale of 4 m/s is shown in the top right corner. From Bahaga *et al.* (2019), supplementary material.

Bibliography

Annamalai H, Potemra J, Murtugudde R, McCreary JP. 2005. Effect of preconditioning on the extreme climate events in the tropical indian ocean. *Journal of Climate* **18**: 3450–3469. 25, 66

Anyah RO, Semazzi FHM. 2006. Climate variability over the Greater Horn of Africa based on NCAR AGCM ensemble. *Theoretical and Applied Climatology* **86**: 39–62. 14

Anyamba EK. 1984. Some aspects of the origin of rainfall deficiency in East Africa. *Proceeding of the WMO Regional Scientific Conference on GATE, WAMEX and Tropical Meteorology, Dakar, Senegal* : 110–112. 14

Äthiopien Wirtschaft. 2018. Auswäartiges amt-deutschland. accessed april 2019. *https://www.auswaertiges-amt.de/de/aussenpolitik/laender/aethiopien-node/-/209506* . 1

Bahaga TK, Fink AH, Knippertz P. 2019. Revisiting interannual to decadal teleconnections influencing seasonal rainfall in the Greater Horn of Africa during the 20th century. *International Journal of Climatology* doi:10.1002/joc.5986. iii, xiii, xiv, xv, xvi, 5, 30, 32, 34, 35, 36, 42, 45, 63, 65, 67, 69, 72, 73, 75, 76, 78, 81, 82, 83, 86, 94, 95, 96, 100, 116, 117, 125, 134, 137, 138, 139

Bahaga TK, Mengistu Tsidu G, Kucharski F, Diro GT. 2015. Potential predictability of the Sea Surface Temperature forced equatorial East African short rains interannual variability in the 20^{th} century. *Quarterly Journal of the Royal Meteorological Society* **141**: 16–26. 26, 31, 32, 46, 66, 69

Baquero-Bernal A, Latif M, Legutke S. 2002. Notes and correspondence on dipole like variability of sea surface temperature in the tropical Indian Ocean. *Journal of Climate* **15**: 1358–1368. 26, 27, 28

Bechtold P, Köhler M, Jung T, Doblas-Reyes F, Leutbecher M, Rodwell MJ, Vitart F, Balsamo G. 2008. Advances in simulating atmospheric variability with the ecmwf

model: From synoptic to decadal time-scales. *Quarterly Journal of the Royal Meteorological Society* **134**(634). 49

Behera SK, Luo JJ, Masson S, Delecluse P, Gualdi S, Navarra A, Yagamata T. 2005. Paramount impact of the Indian Ocean Dipole on the East African short rains: ACGCM study. *Journal of Climate* **18**: 4514–4530. 18, 25, 26, 31, 46, 66

Behera SK, Yamagata T. 2003. Influence of the Indian Ocean Dipole on the Southern Oscillation. *Journal of the Meteorological Society of Japan* **81**: 169–177. 28

Berhane F, Zaitchik B, Dezfuli A. 2014. Subseasonal Analysis of Precipitation Variability in the Blue Nile River Basin. *Journal of Climate* **27**: 325–344. 20

Bjerknes J. 1966. A possible response of the atmospheric Hadley circulation to equatorial anomalies of ocean temperature. *Tellus* **18**: 820–829. 24

Bjerknes J. 1969. Atmospheric teleconnections from the equatorial pacific. *Monthly Weather Review* **97**: 163–172. 23

Black E, Slingo J, Sperber KR. 2003. An observational study of the relationship between excessively strong short rains in coastal East Africa and Indian Ocean SST. *Monthly Weather Review* **131**: 74–94. 11, 12, 24, 26, 28, 31, 66, 70, 71

Burpee R. 1972. The origin and structure of easterly waves in the lower troposphere of north Africa. *Journal of the Atmospheric Sciences* **29**: 77–90. 19

Butterworth S. 1930. On the theory of filter amplifiers. *Wireless Engineer* **7**: 536–541. 60

Camberlin P. 1997. Rainfall anomalies in the source region of the Nile and their connection with the Indian summer monsoon. *Journal of Climate* **10**: 1380–1392. 4, 16, 20, 32, 102, 104

Camberlin P. 2018. Climate of Estern Africa. *Oxford Research Encyclopedia of Climate Science* . 7, 13, 14

Camberlin P, Moron V, Okoola R, Philippon N, Gitau W. 2009. Components of rainy seasons' variability in equatorial East Africa: onset, cessation, rainfall frequency and intensity. *Theoretical and Applied Climatology* **98**: 237–249. 14, 16

Camberlin P, Philippon N. 2001. The stationarity of lead-lag teleconnections with East Africa rainfall and its incidence on seasonal predictability. In detecting and modelling regional climate change. *Springer, Berlin, Heidelberg* : 291–307. 35, 62, 66, 129, 130

Camberlin P, Philippon N. 2002. The East African March-May rainy season: associated atmospheric dynamics and predictability over the 1968–97 period. *Journal of Climate* **15**: 1002–1019. 33, 79, 134

Cassou C, Kushnir Y, Hawkins E, Pirani A, Kucharski F, Kang IS, Caltabiano N. 2018. Decadal climate variability and predictability: Challenges and opportunities. *Bulletin of the American Meteorological Society* **99**: 479–490. 118, 120, 123

Checchi F, Robinson WC. 2013. Mortality among populations of southern and central somalia affected by severe food insecurity and famine during 2010–2012. FAO and FEWS NET,87 pp. *Available online at http://www.fsnau.org/in-focus/study-report-mortality-among-populations-southernand-central-somalia-affected-severe-food-*. . 1

Clark CO, Webster PJ, Cole JE. 2003. Interdecadal variability of the relationship between the Indian Ocean zonal mode and East African coastal rainfall anomalies. *Journal of Climate* **16**: 548–554. 24, 31, 32, 35, 62, 68, 129, 130

Conway D, Lisa E, Schipper F. 2011. Adaptation to climate change in africa: challenges and opportunities identified from Ethiopia. *Global Environ Change* **21**: 227–237. 1

Cook KH. 1999. Generation of the African Easterly Jet and its Role in determining West African Precipitation. *Journal of Climate* **12**: 1165–1184. 19

Dee D, Uppala SM, Simmons AJ, Berrisford P, Poli P, Kobayashi S, Andrea A. 2011. The era-interim reanalysis: Configuration and performance of the data assimilation system. *Quarterly Journal of the Royal Meteorological Society* **137**((656)): 553–597. 47, 54

Degefu MA, Rowell DP, Bewket W. 2016. Teleconnections between ethiopian rainfall variability and global SSTs: observations and methods for model evaluation. *Meteorology and Atmospheric Physics* **129**: 173–186. 32

Deser C, Phillips AS, Hurrell JW. 2004. Pacific interdecadal climate variability: Linkages between the tropics and the north Pacific during boreal winter since 1900. *Journal of Climate* **17**: 3109–3124. 36, 46, 70, 80

Deser C, Phillips AS, Tomas RA, Okumura YM, Alexander MA, Capotondi A, Ohba M. 2012. ENSO and Pacific decadal variability in the community climate system model version 4. *Journal of Climate* **25**: 2622–2651. 46, 81, 121

Diatta S, Fink AH. 2014. Statistical relationship between remote climate indices and West African monsoon variability. *International Journal of Climatology* **34**(12): 3348–3367. 3, 30, 35, 46, 56, 62, 74, 77, 116, 129, 134

Diaz HF, Markgraf V. 2000. El niño and the Southern Oscillation: multiscale variability and global and regional impacts. *Cambridge University Press, UK* . 21

Ding H, Keenlyside NS, Latif M. 2010. Equatorial Atlantic interannual variability: Role of heat content. *Journal of Geophysical Research: Oceans* **115**. 29

Dinku T, Funk C, Peterson P, Maidment R, Tadesse T, Gadain H, Ceccato P. 2018. Validation of the chirps satellite rainfall estimates over eastern africa. *Quarterly Journal of the Royal Meteorological Society* **144**: 292–312. 89

Diro GT, Black E, Grimes DIF. 2008. Seasonal forecasting of Ethiopian spring rains. *Meteorological Applications* **15**: 73–83. 32, 96

Diro GT, Grimes DIF, Black E. 2011a. Large scale features affecting Ethiopian rainfall. In: Williams cjr, kniveton DR (ed). Springer, Dordrecht. *Advances in global change research Springer, Netherlands* **43**: 13–50. xii, 11, 14, 16, 18, 20, 32, 33, 46, 74, 90, 92, 94, 98, 129

Diro GT, Grimes DIF, Black E. 2011b. Teleconnections between Ethiopian summer rainfall and sea surface temperature: Part-I observation and modelling. *Climate Dynamics* **37**: 103–119. 4, 19, 20, 32, 92, 93, 94, 98, 99, 100, 102, 110, 125, 132

Doblas-Reyes FJ, Andreu-Burillo I, Chikamoto Y, García-Serrano J, Guemas V, Kimoto M, Mochizuki T, Rodrigues LRL, van Oldenborgh GJ. 2013. Initialized near-term regional climate change prediction. *Nature Communications* **4**: 1715. 120

Dommenget D, Latif M. 2002. A cautionary note on the interpretation of eofs. *Journal of Climate* **15**: 216–225. 59

Doms G, Schättler U. 2004. A description of the nonhydrostatic regional model lm. part ii: Physical parameterization. *Technical report, Deutscher-Wetterdienst, Offenbach, Germany.* : (available from http://www.cosmo–model.org/public/documentation.htm). 49

Endris HS, Lennard C, Hewitson B, Dosio A, Nikulin G, Panitz HJ. 2016. Teleconnection responses in multi-GCM driven CORDEX RCMs over eastern Africa. *Climate Dynamics* **46**: 2821–2846. 31

Enfield DB, Mestas-Nuñez AM, Trimble PJ. 2001. The Atlantic multidecadal oscillation and its relation to rainfall and river flows in the continental U.S. *Geophysical Research Letters* **28**: 2077–2080. 36, 46, 47, 74

Farneti R. 2017. Modelling interdecadal climate variability and the role of the ocean. *Wiley Interdisciplinary Reviews: Climate Change* **8**: e441. 46, 81

FEWS-NET. 2011. East Africa: Past year one of the driest on record in the eastern horn. famine early warning system network report. *Available online at http://reliefweb.int/report/ethiopia/east-Africa-past-year-one-driest-record-eastern-horn-june-14-2011.* . 1, 30

FEWS-NET. 2015. Large-scale food security emergency projected for 2016. *Available online at http://www.fews.net/east-Africa/ethiopia/food-security-outlook/october-2015/* . 1, 30

FEWS-NET, WFP. 2016. Ethiopia food security out look report. *Available online at http://www.fews.net/sites/default/files/documents/reports/* . 1, 30

Findlater J. 1971. Mean monthly airflow at low levels over the Western Indian Ocean. *Geophys. Mem, HMSO, London* **115**: 53. 16

Fink A, Speth P. 1997. Some potential forcing mechanisms of the year- to-year variability of the tropical convection and its intraseasonal (25–70-day) variability. *International Journal of Climatology* **17**: 1513–1534. 56

Fink AH, Schrage JM, Kotthaus S. 2010. On the potential causes of the nonstationary correlations between West African precipitation and Atlantic hurricane activity. *Journal of Climate* **23**: 5437–5456. 56

Flohn H. 1987. Rainfall teleconnections in northern and northeastern Africa. *Theoretical and Applied Climatology* **38**: 191–197. 14

Folland CK, Palmer TN, Parker DE. 1986. Sahel rainfall and worldwide sea temperatures. *Nature* **320**: 602–607. 36

Funk C, Dettinger MD, Michaelsen JC, Verdin JP, Brown ME, Barlow M, Hoell A. 2008. Warming of the Indian Ocean threatens eastern and southern African food security but could be mitigated by agricultural development. *Proceedings of the National Academy of Sciences* **105**(32): 11 081–11 086. 33

Funk C, Hoell A. 2015. The leading mode of observed and CMIP5 ENSO-residual Sea Surface Temperatures and associated changes in indo-Pacific climate. *Journal of Climate* **28**(11): 4309 – 4329. 35

Funk C, Hoell A, Shukla S, Bladé I, Liebmann B, Roberts JB, Husak G. 2014. Predicting East African spring droughts using Pacific and Indian Ocean sea surface temperature indices. *Hydrology and Earth System Sciences* **18**(12): 4965–4978. 35, 46, 80

Funk C, Nicholson SE, Landsfeld M, Klotter D, Peterson P, Harrison L. 2015a. The Centennial Trends Greater Horn of Africa precipitation dataset. *Scientific Data* **2**: 15 005. 40

Funk C, Peterson P, Landsfeld M, Pedreros D, Verdin J, Shukla S, Michaelsen J. 2015b. The climate hazards infrared precipitation with stations a new environmental record for monitoring extremes. *Scientific Data* **2**: 1–21. 40

Gassmann A, Herzog HJ. 2008. Towards a consistent numerical compressible non-hydrostatic model using generalized hamiltonian tools. *Quarterly Journal of the Royal Meteorological Society* **134**(635): 1597–1613. 48

Gates WL, Boyle JS, Covey C, Dease CG, Doutriaux CM, Drach RS, Fiorino M. 1999. An overview of the results of the atmospheric model intercomparison project (amip i). *Bulletin of the American Meteorological Society* **80**: 29–56. 52

Gill AE. 1980. Some simple solutions for heat-induced tropical circulations. *Quarterly Journal of the Royal Meteorological Society* **106**: 447–462. 31, 106

Gill AE. 1982. Atmosphere-Ocean Dynamic. *Academic Press* **30**: 978–0–12–283 522–3. 22

Giorgetta MA, Jungclaus J, Reick CH, Legutke S, Bader J, Böttinger M, Brovkin V, Crueger T, Esch M, Fieg K, Glushak K, Gayler V, Haak H, Hollweg HD, Ilyina T, Kinne S, Kornblueh L, Matei D, Mauritsen T, Mikolajewicz U, Mueller W, Notz D, Pithan F, Raddatz T, Rast S, Redler R, Roeckner E, Schmidt H, S R, S J, S KD, Stockhause M, Timmreck C, Wegner J, Widmann H, Wieners KH, Claussen M, Marotzke J, Stevens B. 2013. Climate and carbon cycle changes from 1850 to 2100 in mpi-esm simulations for the coupled model intercomparison project phase 5. *Journal of Advances in Modeling Earth Systems* **5**(3): 572–597. 55

Gissila T, Black E, Grimes DIF, Slingo JM. 2004. Seasonal forecasting of the Ethiopian summer rains. *International Journal of Climatology* **24**: 1345–1358. 4, 32, 94

Glantz MH. 1988. Drought and hunger in Africa. *Cambridge University Press, UK* . 13

Glantz MH. 2001. Currents of change: Impacts of El Niño and la niña on climate and society. *second edition. Cambridge University Press, Cambridge, UK.* . 21

Goddard L, Graham NE. 1999. Importance of the Indian Ocean for simulating rainfall anomalies over eastern and southern Africa. *Geophysical Research Letters* **104**: 99–116. 31, 66

Goldenberg SB, Landsea CW, Mestas-Nuñez AM, Gray WM. 2001. The recent increase in atlantic hurricane activity: causes and implications. *Science* **293**: 474–479. 36

Hastenrath S. 1991. Climate dynamics of the tropics. *Kluwer Academic Publishers* : 302–309. 13, 19

Hastenrath S, Nicklis A, Greischar L. 1993. Atmospheric - hydrospheric mechanisms of climate anomalies in the western equatorial Indian Ocean. *Geophysical Research Letters* **98**: 20 219–20 235. 11, 12, 18, 31, 33, 79

Hastenrath S, Polzin D, Camberlin P. 2004. Exploring the predictability of the $'short-rains'$ at the coast of East Africa. *International Journal of Climatology* **24**: 1333–1343. 11, 25

Hastenrath S, Polzin D, Mutai C. 2007. Diagnosing the 2005 drought in equatorial East Africa. *Journal of Climate* **20**: 4628–4637. 11

Hastenrath S, Polzin D, Mutai C. 2011. Circulation Mechanisms of Kenya Rainfall Anomalies. *Journal of Climate* **24**: 404–412. 18, 31, 66

Heise E, Ritter B, Schrodin E. 2006. Operational implementation of the multilayer soil model terra', technical report. . *Deutscher Wetterdienst: Offenbach, Germany* : http://www.cosmo–model.org. 49

Hession SL, Moore N. 2011. A spatial regression analysis of the influence of topography on monthly rainfall in East Africa. *International Journal of Climatology* **31**(10): 1440–1456. 8

Hoell A, Hoerling M, Eischeid J, Quan WX, Liebmann B. 2017. Reconciling theories for human and natural attribution of recent East Africa drying. *Journal of Climate* **30**: 1939–1957. 35

Holton JR, Hakim GJ. 2013. Chapter 10–the general circulation. In: An introduction to dynamic meteorology, 5th edn. *Academic Press, Boston* : 325–375. 19

Hsiang SM, Meng KC, Cane MA. 2011. Civil conflicts are associated with the global climate. *Nature* **476**: 438–441. 24

Huang B, *et al.* 2015. Extended reconstructed sea surface temperature version 4 (ersst.v4). part I: upgrades and inter-comparisons. *Journal of Climate* **28**: 911–930. 44

IPCC. 2007. Climate change 2007: Impacts, Adaptation and Vulnerability — contribution of working group ii to the third assessment report of the intergovernmental panel on climate change. *Cambridge University Press, Cambridge, United Kingdom and New York, NY, USA* . 1, 2

Jury MR. 2010. Ethiopian decadal climate variability. *Theoretical and Applied Climatology* **101**: 29–40. 33, 36, 46, 74

Jury MR. 2013. Ethiopian Highlands crop-climate prediction: 1979–2009. *Journal of Applied Meteorology and Climatology* **52**: 1116–1126. 94

Jury MR, Enfield DB, Jean-Luc M. 2002. Tropical monsoons around africa: Stability of El Nino southern oscillation associations and links with continental climate. *Journal of Geophysical Research: Oceans* **107**: 15–1–15–17. 46

Kassahun B. 1987. Weather systems over Ethiopia. proceedings of first technical conference on meteorological research in eastern and southern Africa. *Kenya Meteorological Department, Nairobi, Kenya* **135**: 53–57. 14, 17, 90, 92

Keenlyside N, Ba J, Mecking J, Omrani NE, Latif M, Zhang R, Msadek R. 2015. North Atlantic Multi-decadal Variability Mechanisms and Predictability. *Climate Change: Multidecadal and Beyond* **9**: 141–157. 36

Keenlyside N, Latif M. 2007. Understanding Equatorial Atlantic Interannual Variability. *Journal of Climate* **20**: 131–142. 29, 30

Keenlyside N, Latif M, Jungclaus J Kornblueh L, Roeckner E. 2008. Advancing decadal-scale climate prediction in the North Atlantic sector. *Nature* **453**: 84–88. 36

Knight JR, Folland CK, Scaife AA. 2006. Climate impacts of the Atlantic Multidecadal Oscillation . 36

Korecha D, Barnston A. 2007. Predictability of June–September Rainfall in Ethiopia. *Monthly Weather Review* **135**: 628–650. 9, 32, 46, 74, 94, 125

Krishnamurti TN, Stefanova L, Misra V. 2013. Tropical meteorology, an introduction. *Springer, New York* : 109–119. 16

Kröger J, Pohlmann H, Sienz F, Marotzke J, Baehr J, Köhl A, Modali K, Polkova I, Stammer D, Vamborg FSE, Müller WA. 2018. Full-field initialized decadal predictions with the mpi earth system model: an initial shock in the north atlantic. *Climate Dynamics* **51**: 2593–2608. 119, 120, 123

Kucharski F, Ikram F, Molteni F, Farneti R, Kang IS, No HH, King MP, Giuliani G, Mogensen K. 2016. Atlantic forcing of pacific decadal variability. *Climate Dynamics* **46**: 2337–2351. 123

Kushnir Y. 1994. Interdecadal Variations in North Atlantic Sea Surface Temperature and Associated Atmospheric Conditions. *Journal of Climate* **7**(1): 141–157. 36

Latif M, Dommenget D, Dima M, Grotzner A. 1999. The role of Indian Ocean sea surface temperature in forcing East African rainfall anomalies during December-January 1997/98. *Journal of Climate* **12**: 3497–3504. 31

Leuenberger D, Koller M, Fuhrer O, Schär C. 2010. A generalization of the sleve vertical coordinate. *Monthly Weather Review* **138**(9): 3683–3689. 51

Liebmann B, Hoerling M, Funk C, Blade I, Dole R, Allured D, Eischeid J. 2014. Understanding the Eastern Horn of Africa rainfall variability and change. *Journal of Climate* **27**: 8630–8645. 3, 33, 35, 80

Losada T, Rodriguez-Fonseca B, Janicot S, Gervois S, Chauvin F, Ruti P. 2010. A multimodel approach to the Atlantic equatorial mode: impact on the West African monsoon. *Climate Dynamics* **35**: 29–43. 30

Lott F, Miller MJ. 1997. A new subgrid-scale orographic drag parametrization: Its formulation and testing. *Quarterly Journal of the Royal Meteorological Society* **123**(537): 101–127. 49

Lyon B. 2014. Seasonal drought in the greater horn of Africa and its recent increase during the March – May Long Rains. *Journal of Climate* **27**(21): 7953–7975. 33, 34, 46, 64, 79, 80, 82, 129, 130

Lyon B, Barnston A, DeWitt DG. 2014. Tropical Pacific forcing of a 1998–99 climate shift: Observational analysis and climate model results for the boreal spring season. *Climate Dynamics* **43**: 893–909. 33, 34, 70

Lyon B, DeWitt DG. 2012. A recent and abrupt decline in the East African long rains. *Geophysical Research Letters* **39**. 1, 30, 33, 34

Manatsa D, Behera SK. 2013. On the epochal strengthening in the relationship between rainfall of East Africa and IOD. *Journal of Climate* **26**: 5655–5673. 32, 35, 62, 66, 68

Manatsa D, Chipindu B, Behera SK. 2012. Shifts in IOD and their impacts on association with East Africa rainfall. *Theoretical and Applied Climatology* **110**: 115–128. 35, 62, 68

Mantua NJ, Hare SR, Zhang Y, Wallace JM, Francis RC. 1997. A Pacific interdecadal climate oscillation with impacts on salmon production. *Bulletin of the American Meteorological Society* **78**: 1069–1079. 36, 46, 71

Marotzke J, Müller WA, Vamborg FSE, Becker P, Cubasch U, Feldmann H, Kaspar F, Kottmeier C, Marini C, Polkova I, Prömmel K, Rust HW, Stammer D, Ulbrich U, Kadow C, Köhl A, Kröger J, Kruschke T, Pinto JG, Pohlmann H, Reyers M, Schröder M, Sienz F, Timmreck C, Ziese M. 2016. Miklip: A National Research Project on Decadal Climate Prediction. *Bulletin of the American Meteorological Society* **97**(12): 2379–2394. xxi, 5, 37, 55, 56, 118, 119, 123

McKee TB, Doesken NJ, Kleist J. 1993. The relationship of drought frequency and duration to time scales. *Proceedings of the 8th Conference on Applied Climatology* : 179–183. 41

Meehl GA, Goddard L, Boer G, Burgman R, Branstator G, Cassou C and Yeager S. 2014. Decadal climate prediction: An update from the trenches. *Bulletin of the American Meteorological Society* **95**(2): 243–267. 37

Meehl GA, Goddard L, Murphy J, Stouffer RJ, Boer G, Danabasoglu G, Stockdale T. 2009a. Decadal prediction: can it be skillful? *Bulletin of the American Meteorological Society* **90**(10): 1467–1486. 37

Meehl GA, Goddard L, Murphy J, Stouffer RJ, Boer G, Danabasoglu G, Dixon K, Giorgetta MA, Greene AM, Hawkins E, Hegerl G, Karoly D, Keenlyside N, Kimoto M, Kirtman B, Navarra A, Pulwarty R, Smith D, Stammer D, Stockdale T. 2009b. Decadal prediction. *Bulletin of the American Meteorological Society* **90**: 1467–1486. 116

Meehl GA, Hu A. 2006. Megadroughts in the Indian monsoon region and southwest North America and a mechanism for associated multi-decadal Pacific sea surface temperature anomalies. *Journal of Climate* **19**: 1605–1623. 36

Meehl GA, Hu A, Santer BD. 2009c. Climate shift in the Pacific and the relative roles of forced versus inherent decadal variability. *Journal of Climate* **22**: 780–792. 36, 66, 70

Mlawer EJ, Taubman SJ, Brown PD, Iacono MJ, Clough SA. 1997. Radiative transfer for inhomogeneous atmospheres: Rrtm, a validated correlated-k model for the longwave. *Journal of Geophysical Research: Atmospheres* **102**(D14): 16 663–16 682. 49

Mohino E, Janicot S, Bader J. 2011. Sahel rainfall and decadal to multi-decadal sea surface temperature variability. *Climate Dynamics* **37**: 419–440. 36

Müller WA, Jungclaus JH, Mauritsen T, Baehr J, Bittner M, Budich R, Bunzel F, Esch M, Ghosh R, Haak H, Ilyina T, Kleine T, Kornblueh L, Li H, Modali K, Notz D, Pohlmann H, Roeckner E, Stemmler I, Tian F, Marotzke J. 2018. A higher-resolution version of the max planck institute earth system model (mpi-esm1.2-hr). *Journal of Advances in Modeling Earth Systems* **10**: 1383–1413. 119

Mutai CC, Ward MN, Colman AW. 1998. Towards the prediction of the East Africa short rains based on sea-surface temperature atmosphere coupling. *International Journal of Climatology* **18**: 975–997. 31

Nakamura N, Kayanne H, Iijima H, McClanahan TR, Behera S, Yamagata T. 2009. Mode shift in the Indian Ocean climate under global warming stress. *Geophysical Research Letters* : 36. 32, 35, 62

Newman M, Alexander AM, Ault RT, Cobb KM, Deser C, Lorenzo ED, Smith CA. 2016. The Pacific decadal oscillation, revisited. *Journal of Climate* **29**: 4399–4427. 79, 130

Nicholson SE. 1996. A review of climate dynamics and climate variability in eastern Africa. *The Limnology, Climatology and Paleoclimatology of the East African Lakes, T. C. Johnson and E. O. Odada, Eds., Gordon and Breach* : 25–56. 9

Nicholson SE. 2008. The intensity, location and structure of the tropical rainbelt over west africa as factors in interannual variability. *International Journal of Climatology* **28**: 1775–1785. 19

Nicholson SE. 2014. The Predictability of Rainfall over the Greater Horn of Africa. Part I: Prediction of seasonal rainfall. *Journal of Hydrometeorology* **15**: 1011–1027. 32

Nicholson SE. 2015. Long-term variability of the East African Short Rains and its links to large-scale factors. *International Journal of Climatology* **35**: 3979–3990. 3, 18, 31, 32, 35, 61, 62, 66, 67, 68, 129, 130

Nicholson SE. 2016. The Turkana low-level jet: mean climatology and association with regional aridity. *International Journal of Climatology* **36**: 2598–2614. 9

Nicholson SE. 2017. Climate and climatic variability of rainfall over eastern Africa. *Reviews of Geophysics* **55**: 590–635. xiii, 3, 31, 32, 33, 35, 61, 62, 64, 68

Nicholson SE. 2018. The ITCZ and the Seasonal Cycle over Equatorial Africa. *Bulletin of the American Meteorological Society* **99**: 337–348. 9

Nicholson SE, Barcilon AI, Challa M. 2008. An analysis of west african dynamics using a linearized gcm. *Journal of Atmospheric Science* **64**: 1182–1203. 93

Nicholson SE, Fink AH, Funk C. 2018. Assessing recovery and change in West Africa's rainfall regime from a 161-year record. *International Journal of Climatology* doi: 10.1002/joc.5530. 77, 79, 129

Nicholson SE, Hoopingarner J, Kim E. 1988. Atlas of African rainfall and its interannual variability. *Dept. of Meteorology, The Florida State University, Tallahassee* : 237 pp. xi, 11, 13

Ogallo L, Bessemoulin, P Ceron JP, Mason S, Connor S. 2008. Adapting to climate variability and change the climate outlook forum process. *WMO Bulletin* **57**: 93–102. 2

Ogallo LJ. 1988. Relationship between seasonal rainfall in East Africa and the southern oscillation. *Journal of Climate* **8**: 31–43. 31

Omondi P, Awange J, Ogallo L, Okoola R, Forootan E. 2012. Decadal rainfall variability modes in observed rainfall records over East Africa and their relations to historical sea surface temperature changes. *Journal of Hydrology* **464**: 140–156. 32, 46

Omondi P, Ogallo LA, Anyah RO, Muthama JM, Ininda J. 2013. Linkages between global sea surface temperatures and rainfall variability over East Africa region. *International Journal of Climatology* **33**: 2082–2104. 33, 69

Orr A, Bechtold P, Scinocca J, Ern M, Janiskova M. 2010. Improved middle atmosphere climate and forecasts in the ecmwf model through a nonorographic gravity wave drag parameterization. *Journal of Climate* **23**(22): 5905–5926. 49

Philander SGH. 1985. El Niño and La Niñ. *Journal of the Atmospheric Sciences* **42**: 2652–2662. 24

Philander SGH. 1990. El Niño, La Niñ and the Southern Oscillation. *Academic Press, Science* . 21

Pohl B, Camberlin P. 2011. Intraseasonal and interannual zonal circulations over the equatorial Indian Ocean. *Climate Dynamics* **104**: 175–191. 1, 18, 31, 33

Pohlmann H, Jungclaus JH, Köhl A, ;; D, Marotzke J. 2009. Initializing decadal climate predictions with the GECCO Oceanic Synthesis: Effects on the North Atlantic. *Journal of Climate* **22**(14): 3926–3938. 5, 36, 37, 118

Poli P, Hersbach H, Dee DP, Berrisford P, Simmons AJ, Vitart F, Thépaut JN. 2016. ERA-20C: An atmospheric reanalysis of the twentieth century. *Journal of Climate* **29**(11): 4083–4097. 47

Power S, Tseitkin F, Mehta V, Torok S, Lavery B. 1999a. Decadal climate variability in Australia during the 20th century. *International Journal of Climatology* **19**: 169–184. 36

Power SB, Casey T, Folland C, Colman A, Mehta V. 1999b. Interdecadal modulation of the impact of ENSO on Australia. *Climate Dynamics* **15**: 319–324. 36, 46

Raschendorfer M. 2001. The new turbulence parameterization of lm, cosmo newsl. *Available at http://www.cosmo-model.org.* **1**: 89–97. 49

Rayner NA, Parker DE, Horton EB, Folland CK, Alexander LV, Rowell DP, Kaplan A. 2003. Global analyses of sea surface temperature, sea ice, and night marine air temperature since the late nineteenth century. *Geophysical Research Letters* **108**. 44, 54, 117

Rodríguez-Fonseca B, Polo I, Garcá-Serrano J, Losada T, Mohino E, Mechoso CR, Kucharski F. 2009. Are atlantic Niños enhancing acific ENSO events in recent decades? *Geophysical Research Letters* **36**. 30, 104

Ropelewski CF, Halpert MS. 1987. Global and regional scale precipitation patterns associated with the El Niño/Southern oscillation. *Monthly Weather Review* **115**: 1606–1626. 24, 31, 46

Rowell DP, Booth BB, Nicholson ES, Good P. 2015. Reconciling past and future rainfall trends over East Africa. *Journal of Climate* **28**(24): 9768–9788. 3, 35, 64

Sadourny R, Arakawa A, Mintz Y. 1968. Integration of the nondivergent barotropic vorticity equation with an icosahedral-hexagonal grid for the sphere. *Monthly Weather Review* **96**(6): 351–356. 50

Saji HN, Yamagata T. 2003. Structure of sst and surface wind variability during Indian Ocean dipole mode events: COADS observations. *Journal of Climate* **16**: 2735–2751. 28

Saji NH, Goswami BN, Vinayachandran PN, Yamagata T. 1999. A dipole mode in the tropical Indian Ocean. *Nature* **401**: 360–363. xii, 24, 25, 26, 27, 28, 31, 46

Salami A, Kamara AB, Brixiova Z. 2010. Smallholder agriculture in east africa: Trends, constraints, and opportunities. african development bank working papers series no. 105. african Development Bank, Tunis, Tunisia. *Available online*

at https://www.commdev.org/wp-content/uploads/2015/06/Smallholder-Agriculture-East-Africa-Trends-Constraints-Opportunities.pdf **52**. 1

Schär C, Leuenberger D, Fuhrer O, Lüthi D, Girard C. 2002. A new terrain-following vertical coordinate formulation for atmospheric prediction models. *Monthly Weather Review* **130**(10): 2459–2480. 51

Schneider U, Andrea B, Peter F, Meyer-Christoffer A, Ziese M, Rudolf B. 2014. GPCC's new land surface precipitation climatology based on quality-controlled in situ data and its role in quantifying the global water cycle. *Theoretical and Applied Climatology* **115**: 15–40. 39, 117

Schuster M, Grieger J, Richling A, Schartner T, Illing S, Kadow C, Müller WA, Pohlmann H, Pfahl S, Ulbrich U. 2019. Improvement in the decadal prediction skill of the northern hemisphere extra-tropical winter circulation through increased model resolution. *Earth System Dynamics Discussions* **2019**: 1–21. 122

Segele ZT, Lamb PJ. 2005. Characterization and variability of Kiremt rainy season over ethiopia.. *Meteorol Atmos Phys* **89**: 153–180. 85, 90, 92

Segele ZT, Lamb PJ, Leslie LM. 2009a. Large-scale atmospheric circulation and global sea surface temperature associations with horn of Africa june-september rainfall. *International Journal of Climatology* **29**: 1075–1100. 14, 17, 18, 20, 32, 64, 74, 92, 94, 98, 100, 102, 104, 125, 132

Segele ZT, Lamb PJ, Leslie LM. 2009b. Seasonal-to-interannual variability of Ethiopia/Horn of Africa monsoon. Part I: Associations of wavelet-filtered large-scale Atmospheric circulation and global sea surface temperature. *Journal of Climate* **22**: 3396–3421. 11, 13, 14, 33, 74

Segele ZT, Leslie LM, Tarhule AA. 2015. Sensitivity of horn of Africa rainfall to regional Sea Surface Temperature forcing. *Climate* **3**(2): 365–390. 11, 30, 33, 73, 89, 108, 129, 131

Smith DM, Cusack S, Colman AW, Folland CK, Harris GR, Murphy JM. 2007. Improved surface temperature prediction for the Coming Decade from a Global Climate Model **317**(5839): 796–799. 36, 37

Srivastava G, Chakraborty A, Nanjundiah RS. 2018. Multidecadal see-saw of the impact of ENSO on Indian and West African summer monsoon rainfall. *Climate Dynamics* doi:10.1007/s00382-018-4535-2. 73, 108

Staniforth A, Thuburn J. 2012. Horizontal grids for global weather and climate prediction models: a review. *Quarterly Journal of the Royal Meteorological Society* **138**(662): 1–26. 50

Stratton RA, Stirling AJ. 2012. Improving the diurnal cycle of convection in gcms. *Quarterly Journal of the Royal Meteorological Society* **138**(666): 1121–1134. 49

Suárez-Moreno R, Rodríguez-Fonseca B, Barroso JA, Fink AH. 2018. Interdecadal changes in the leading ocean forcing of Sahelian rainfall interannual variability: Atmospheric dynamics and role of multidecadal SST background. *Journal of Climate* **0**: null, doi:10.1175/JCLI-D-17-0367.1. 3, 35, 62, 74, 77, 130

Sutton RT, Hodson DLR. 2005. Atlantic ocean forcing of North American and European summer climate. *Science* **309**: 115–118. 36

Tanaka H, Ishizaki N, Kitoh A. 2004. Trend and interannual variability of walker, monsoon and hadley circulations defined by velocity potential in the upper troposphere. *Tellus A* **56**: 250–269. 109

Taubenheim J. 1969. *Statistische auswertung geophysikalischer und meteorologischer daten*. Leipzig, Germany (In German): Akadem. Verlag. 56

Taylor K, Stouffer RJ Meehl G. 2012. An overview of CMIP5 and the experiment design. *Bulletin of the American Meteorological Society* **93**: 485–498. 5, 37

Thom H. 1966. Some methods of climatological analysis. wmo, 415, nota tecnica 81, geneve thornthwaite cw (1948) an approach towards a rational classification of climate. *Geographical Review* **38**: 55–94. 41, 43

Thorncroft CD, Blackburn M. 1999. Maintenance of the African Easterly Jet. *Quarterly Journal of the Royal Meteorological Society* . 19

Tiedtke M. 1989. A comprehensive mass flux scheme for cumulus parameterization in large-scale models. *Monthly Weather Review* **117**(8): 1779–1800. 49

Tierney JE, Ummenhofer C, deMenocal P. 2015. Past and future rainfall in the horn of Africa. *Science Advances* **1**: e1500 682. 35

Trenberth KE. 1997. The definition of El Niño. *Bulletin of the American Meteorological Society* **78**: 2771–2777. 45, 46, 106

Trenberth KE, Branstator GW, Karoly D, Kumar A, Lau N, Ropelewski C. 1998. Progress during TOGA in understanding and modeling global teleconnections associated with tropical sea surface temperatures. *Journal of Geophysical Research: Oceans* **103**: 14 291–14 324. 24

Trenberth KE, Hurrell JW. 1994. Decadal atmosphere-ocean variations in the Pacific. *Climate Dynamics* **9**: 303–309. 36, 65, 70, 130

Trenberth KE, Shea DJ. 1987. On the evolution of the southern oscillation. *Monthly Weather Review* **115**: 3078–3096. 101, 106

Tsidu GM. 2012. High-resolution monthly rainfall database for Ethiopia: Homogenization, Reconstruction, and Gridding. *Journal of Climate* **25**: 8422–8443. 96

Ummenhofer CC, Gupta AS, England MH, Reason CJC. 2009. Contributions of Indian Ocean sea surface temperatures to enhanced East African rainfall. *Journal of Climate* **22**: 993–1013. 31

Ummenhofer CC, Kulüke M, Tierney JE. 2018. Extremes in East African hydroclimate and links to indo-Pacific variability on interannual to decadal timescales. climate dynamics. *Climate Dynamics* **50**: 2971–2991. 33, 34

UN-OCHA. 2011. Eastern africa drought. humanitarian rep. 4, United Nations Organization for the coordination of humanitarian affairs, 10 pp. *Available online at http://reliefweb.int/ sites/reliefweb.int/files/resources/* . 1

Van Oldenborgh GJ, Burgers G. 2005. Searching for decadal variations in enso precipitation teleconnections. *Geophysical Research Letters* **32**: 1944–8007. 57

Vigaud N, Lyon B, Giannini A. 2017. Sub-seasonal teleconnections between convection over the Indian Ocean, the East African long rains and tropical Pacific surface temperatures. *International Journal of Climatology* **37**: 1167–1180. 33, 34, 134

Viste E, Sorteberg A. 2013. The effect of moisture transport variability on ethiopian summer precipitation. *International Journal of Climatology* **33**(15): 3106–3123. 9

von Storch H, Zwiers FW. 1999. Statistical analysis in climate research. *Cambridge, UK: Cambridge Univ. Press* . 59

Walker GT. 1924. Correlation in seasonal variations of weather, IX: A further study of world weather. *Memoirs of the Indian Meteorological Department XIV* . 21

Wang S, Huang J, He Y, Guan Y. 2014. Combined effects of the pacific decadal oscillation and El Niño southern oscillation on global land dry–wet changes. *Scientific Reports* **4**: 6651. 130

Webster PJ, Moore AM, Loschnigg JP, Leben RR. 1999. Coupled ocean-atmosphere dynamics in the indian ocean during 1997-98. *Nature* **401**: 356–360. 24, 25, 31

Williams AP, Funk C. 2011. A westward extension of the warm pool leads to a westward extension of the walker circulation, drying eastern Africa. *Climate Dynamics* **37**: 2417–2435. 33, 35

Williams AP, Funk C, Michaelsen J, Rauscher SA, Robertson I, Wils THG, Loader NJ. 2012. Recent summer precipitation trends in the greater horn of Africa and the emerging role of Indian Ocean sea surface temperature. *Climate Dynamics* **39**(9): 2307–2328. 33

World-Bank. 2006. Managing water resources to maximise sustainable growth: A country water resources assistance strategy for Ethiopia. *World Bank, Washington, DC.* . xi, 1, 2

Xie SP, Annamalai H. 2002. Structure and mechanisms of south Indian Ocean climate variability. *Journal of Climate* **15**: 864–878. 25, 27, 28, 70, 71

Xie SP, Carton JA. 2013. Tropical Atlantic Variability: Patterns Mechanisms and Impacts. *American Geophysical Union* : 121–142. 29

Yamagata T, Behera SK, Luo JJ, Masson S, Jury M, Rao SA. 2004. Coupled ocean-atmosphere variability in the tropical Indian Ocean. earth climate: The ocean - atmosphere interaction, geophys. monogr. *American Geophysical Union* **147**: 189–212. 25, 31

Yang W, Seager R, Mark CA, Lyon B. 2014. The East African long rains in observations and models. *Journal of Climate* **27**(19): 7185–7202. xiii, 3, 34, 36, 64, 80, 82, 130

Yang W, Seager R, Mark CA, Lyon B. 2015. The annual cycle of East African precipitation. *Journal of Climate* **28**: 2385–2404. 8, 9, 11, 17

Yule GU. 1907. On the theory of correlation for any number of variables treated by a new system of notation. *Proceedings of the Royal Society* **79**: 182–193. 58

Zängl G, Reinert D, Rípodas P, Baldauf M. 2015. The icon (icosahedral non-hydrostatic) modelling framework of dwd and mpi-m: Description of the non-hydrostatic dynamical core. *Quarterly Journal of the Royal Meteorological Society* **141**(687): 563–579. 48

Zebiak SE. 1993. Air-sea interaction in the Equatorial Atlantic Region. *Journal of Climate* **6**: 1567–1586. 29

Zeleke T, Giorgi F, G MT, Diro GT. 2013. Spatial and temporal variability of summer rainfall over ethiopia from observations and a regional climate model experiment. *Theoretical and Applied Climatology* **111**: 665–681. 89, 90, 96, 98, 131, 132

Zhang R, Delworth TL. 2006. Impact of Atlantic Multidecadal Oscillations on India/Sahel rainfall and Atlantic hurricanes . 36

Zhang Y, Wallace JM, Battisti DS. 1997. ENSO-like interdecadal variability: 1900-93. *Journal of Climate* **10**: 1004–1020. 36, 45, 66

Zhou G, Minakawa N, Githeko A, Yan G. 2004. Association between climate variability and malaria epidemics in the East African highlands. *Proceeding of the National Academy of Sciences of the USA* **101**. 2

Acknowledgements

First and foremost, I would like to thank my supervisors, Prof. Dr. Andreas H. Fink and Prof. Dr. Peter Knippertz, for their valuable insight, direction, patience, and guidance throughout these years. In particular, thank you to Peter for providing sound feedback, corrections, and suggestions. Thank you to Andreas for your knowledge, constant support, constructive criticism, and useful discussion.

I gratefully acknowledge support by the "MIKLIP PRO-MISA" project funded by the German Federal Ministry of Education and Research (BMBF) under Grant 01 LP1520D. I also thank the Institute of Meteorology and Climate Research (IMK), Karlsruhe Institute of Technology (KIT) for providing me a PhD position opportunity, which allows my family and me to have an enjoyable time in Karlsruhe. I am also thankful to Atmospheric Dynamics group at IMK for offering me the opportunity, providing infrastructure, research facilities and fascinating research environment. I acknowledge the three-month financial support from German Academic Exchange Service (DAAD) and International Scholars and Welcome Office (IScO) - STIBET Final Scholarships.

I also acknowledge all respective centres providing datasets: Deutscher Wetter-dienst (DWD) and Climate Hazards Group (CHG) at the University of California at Santa Barbara (USC) for gridded precipitation, ECMWF for reanalysis fields, NOAA for ERSSTv4, and Hadley Center for the HadISST. Most of the figures were created using National Center for Atmospheric Research (NCAR) Command Language (NCL).

For ICON climate modeling I would like to thank Gregor Pante, Jennifer Schröter, and Florian Pantillon. A special thanks must go to Gregor for your generous time and help during ICON integration and any issue related to computing facilities.

Finally, thanks to my colleagues and all members of the Atmospheric Dynamics group. Among these members, thanks in particular to office mates: Anke Kniffka, Enrico Di Muzio, Michael Maier-Gerber, Joseph Njeri–you made the last few years so much fun. A special thanks must go Anke Kniffka for always being there for me–without your translation, the beginning would have been difficult.

But most of all I want to thank my wife and son. Thank you Meron, you are my gift every day. Thank you for your loving support, patience, and tolerance, from the early beginning of my academic endeavor. To Mikael, thank you for the immense joy you brought into our lives. Thank you for enduring my ignorance and the patience you showed during my thesis writing.